DTU Mechanical Engineering
Department of Mechanical Engineering

Aerodynamic Stability of Long Span Bridges

Randi Nøhr Møller

PhD Thesis

Aerodynamic Stability of Long Span Bridges

Randi Nøhr Møller

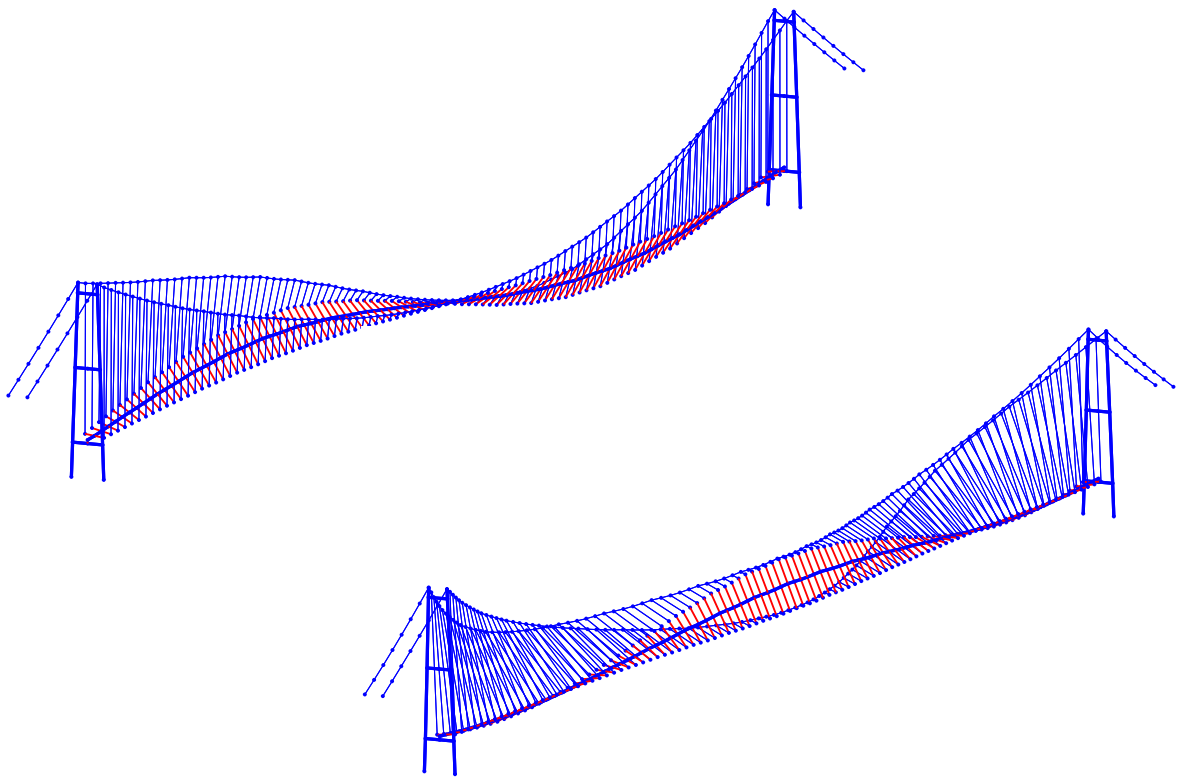

Department of Mechanical Engineering
Section of Solid Mechanics
Technical University of Denmark
June 2019

Section of Solid Mechanics
Department of Mechanical Engineering
Technical University of Denmark
Nils Koppels Alle, Building 404
DK-2800 Kongens Lyngby,
Denmark

Preface

This thesis is submitted in partial fulfilment of the Ph.D. degree from the Technical University of Denmark. The work has been carried out in collaboration between Rambøll and the Department of Mechanical engineering at the Technical University of Denmark with funding from the Rambøll Foundation and the Innovation Fund Denmark. The work has been conducted during the project period from June 2016 to May 2019 with professor, Dr.techn. Steen Krenk as the main supervisor and Martin Nymann Svendsen as the company supervisor.

I would like to express my sincere gratitude towards Steen for sharing his expertise and extensive technical knowledge over the past three years and for always being generous with his time. Also, I would like to thank Martin for providing a practical perspective, for valuable discussions, and for always being stable and supportive. I also wish to extend my thanks to Professor Ole Øiseth and the rest of the structural dynamics group for welcoming me at the Norwegian University of Science and Technology for a research exchange stay in the fall of 2017. I found my stay in Trondheim both enjoyable and educating.

Furthermore, I would like to thank my colleagues at Rambøll and my fellow Ph.D. students at the university for interesting discussions and especially for being really good company and for making my time as a Ph.D. student memorable. Finally, I wish to thank my family and friends for moral support.

Kgs. Lyngby, June 2019

Randi Nøhr Møller

Abstract

With a desire to build even longer bridges, it is of interest to improve the numerical tools for aerodynamic response calculations as well as the flutter limit assessment, and to investigate the possibilities for increasing the stability limit. The work conducted within the field of aerodynamic stability and response of long-span bridges is summarised in three parts: wind field simulation, bridge aerodynamics, and external damping of suspension bridges.

The first part describes the conditional mean field wind simulation method as an efficient and flexible alternative to existing wind simulation methods. The mean field method is an auto-regressive process allowing for a stepwise update of the turbulence components based on a relatively compact memory. Hereby, the data storage requirements are limited even for large scale problems and long simulation records. The coefficient matrices of the auto-regressive model are determined directly from the wind field covariance relations, and examples show that an exponential distribution of the memory steps included in the model provides high quality results with a minimal number of auto-regressive terms. The statistical properties in terms of the auto-spectral density and the cross-field coherence estimated from simulated records are shown to correspond well with the target results.

The second part focuses on the representation of aero-elastic forces for bridge response evaluation and flutter assessment. The aero-elastic forces are represented as additional state-variables in a compact first-order state-space form of the equation of motion. The aerodynamic matrices used in the representation of the aero-elastic forces are identified from the aerodynamic derivatives by a simple identification procedure based on a least squares solution of an over-determined equation system. Furthermore, a second order momentum based time integration procedure is described and the modelling and quasi-static reduction of a long-span suspension bridge are discussed. Finally, the established model was used to obtain results for full structural loading including the bridge deck, pylons, and cables and to evaluate the influence of the wind load correlation on the response based on a consistent anisotropic turbulence representation. It was found that the magnitude of the load depends significantly on the the ratio of the along-wind and transverse turbulence length scales.

The final part describes a damping system for suspension bridges. The damping system consists of four equally calibrated, symmetrically located devices working on the relative displacement between the pylons and the main suspension cables. Each device consists of a viscous damper and a spring in parallel connected to the structure via a pre-tensioned cable. The tuning of the damper system is based on the asymptotic results to a two-component subspace approximation with still-air modes as calibration input, and the simple procedure is shown to provide very accurate results. The damping system targets the modes of interest for unstable flutter motion and it can be observed that the double symmetrical system of equally tuned dampers is able to provide damping to all modes of interest. Finally, the ability of the damping system to increase the stability limit is illustrated numerically on a full aero-elastic model of a long-span suspension bridge which shows a significant increase of the critical wind speed for the unset of flutter.

Resumé

Ud fra et ønske om at bygge længere broer er det nødvendigt at forbedre de numeriske værktøjer til aerodynamiske respons- og flutterberegninger samt at undersøge mulighederne for at øge stabilitetsgrænsen. Arbejdet, der er udført inden for området aerodynamisk stabilitet og respons af lange broer er opsummeret i tre dele: vindfeltsimulering, aerodynamik af broer og ekstern dæmpning af hængebroer.

Den første del beskriver en sekventiel vindsimuleringsmetode hvor vindhastighedsfeltet i det kommende tidsskridt opnås som sum af en betinget middelværdi og en stokastisk komponent. Denne metode er et effektivt og fleksibelt alternativ til eksisterende metoder. 'Mean field'-metoden er en autoregressiv proces, der muliggør en trinvis opdatering af turbulens komponenterne baseret på en relativt kort hukommelse. Derved er kravene til datalagring begrænsede, selv for store problemer og lange simulerede tidshistorier. Koefficient matricerne i den autoregressive model bestemmes direkte af vindfeltets kovariansstruktur og eksempler viser, at en eksponentiel fordeling af hukommelses leddene giver resultater af høj kvalitet med et minimalt antal autoregressive led. De statistiske egenskaber i form af spektraltæthed og koherens funktioner er dels bestemt analytisk og desuden estimeret fra simulerede tidshistorier med god overensstemmelse.

Den anden del fokuserer på repræsentationen af aeroelastiske kræfter i bro respons og flutter beregninger. De aeroelastiske kræfter, der i udgangspunktet foreligger som foldnings integraler, repræsenteres som ekstra tilstandsvariable i en udvidet første-ordens state-space repræsentation af bevægelsesligningerne. De aerodynamiske matricer, der indgår i repræsentationen af de aeroelastiske kræfter, identificeres ud fra de aerodynamiske afledte via en simpel identifikationsprocedure baseret på en mindste kvadraters løsning af et overbestemt ligningssystem. En anden-ordens tidsintegrationsmetode baseret på en integreret form af bevægelsesligningerne er beskrevet, og implementeringen af en lang hængebro inklusiv kvasi-statisk reduktion er diskuteret. Endelig er den etablerede model anvendt til respons beregninger baseret på en konsistent anisotrop turbulens repræsentation med fuld vindbelastning af brodæk, pyloner og kabler. Forholdet mellem den transversale og aksielle længdeskala viser sig af stor betydning for det resulterede respons.

Den sidste del beskriver et dæmpningssystem til hængebroer. Dæmpningssystemet består af fire ens symmetrisk placerede enheder, der virker gennem den relative flytning mellem pyloner og hovedkabler. Hver enhed består af en parallelkoblet viskos dæmper og fjeder, som er forbundet til konstruktionen med et forspændt kabel. Kalibreringen af dæmpersystemet er baseret på en reduceret to-komponent repræsentation for hver af de behandlede svingningsformer, hvor egenværdi løsninger til det strukturelle problem uden aeroelastiske kræfter er anvendt som kalibreringsinput, og det demonstreres, at denne enkle metode giver meget nøjagtige resultater. Dæmpersystemet er målrettet flutter svingninger og det bemærkes, at det dobbeltsymmetriske system med ens kalibrering af alle fire enheder er i stand til at dæmpe de svingningsformer, der indgår i flutter svingerne. Ved hjælp af en fuld aeroelastisk hængebro model er det illustreret numerisk, at dæmpersystemet kan øge stabilitetsgrænsen markant.

Publications

Journal papers

[P1] S. Krenk, R.N. Møller, Turbulent wind field representation and conditional mean simulation, *Proceedings of the Royal Society A*, **475**: 20180887, 2019.

[P2] R.N. Møller, S. Krenk, M.N. Svendsen, Time simulation of turbulent wind response and flutter of long-span bridges, (*submitted for publication*).

[P3] R.N. Møller, S. Krenk, M.N. Svendsen, Damping system for long-span suspension bridges, (*submitted for publication*).

Conference papers

[C1] R.N. Møller, S. Krenk, M.N. Svendsen, Bridge response analysis with ARMA simulated wind field. Proceedings of the 12th international Conference on Structural Safety and Reliability, Vienna, Austria, August 6–10, 2017.

[C2] R.N. Møller, S. Krenk, M.N. Svendsen, Quasi-static condensation of aeroelastic suspension bridge model. Proceedings of the 30th Nordic Seminar on Computational Mechanics, Kongens Lyngby, Denmark, October 25–27, 2017.

Additional contributions

[A1] R.N. Møller, Aerodynamic stability of long span bridges, Abstract and poster, DCAMM 16th Internal Symposium, March 13–15, Middelfart, Denmark, 2017.

[A2] R.N. Møller, S. Krenk, M.N. Svendsen, Long suspension bridge response to anisotropic turbulent wind, Abstract and presentation, 8th Conference on Computational Stochastic Mechanics, June 10–13, Paros, Greece, 2018.

[A3] R.N. Møller, Damping system for long-span suspension bridges, Abstract and presentation, DCAMM 17th Internal Symposium, March 11–13, Vejle, Denmark, 2019.

Contents

1 Introduction **1**

2 Wind field simulation **5**
2.1 Conditional mean-field simulation 6
2.2 Line field simulation 7

3 Bridge aerodynamics **11**
3.1 Aero-elastic load representation 12
3.2 Parameter identification 13
3.3 Time integration 15
3.4 Suspension bridge model 16
3.5 Aerodynamic response 18

4 Suspension bridge damping system **23**
4.1 Suspension bridge stability 23
4.2 Damping system concept 25
4.3 Device calibration 27
4.4 Effect of the damping system 29

5 Conclusions **33**

References **36**

1. Introduction

Aerodynamic stability is an important factor in the design of long-span bridges and in many cases it sets the limit for the maximum span length. A structural system is considered aerodynamically stable if the dynamic response is bounded. This will be the case for wind speeds up to a certain critical limit where the wind-structure interaction will cause the system to become unstable. At this point, the dynamic response is unbounded which will ultimately cause structural failure. Different factors including the general dynamic properties of the structure and the outer shape of the structural elements determine the wind speed that will cause the system to become unstable. Aerodynamic stability is an issue for a number of structural and mechanical systems exposed to wind. This includes for example wind turbine blades, airplane wings, and racing cars as well as bridges. In this context, bridges and especially long-span bridges are a special case as they are unique structures where failure will be catastrophic for the surrounding transport infrastructure. Furthermore, it is a special challenge to ensure aerodynamic stability of long-span bridges as they are ultra large-scale and extremely costly structures which makes real-scale testing prior to construction impossible. For this reason, it is important that computational models used in the design of long-span bridges account for the aero-elastic effects correctly. These effects are caused by the interaction between the wind flow surrounding the structure and the vibrating structure itself and cause the aerodynamic response to go from stable at low wind speeds to unstable at higher wind speeds.

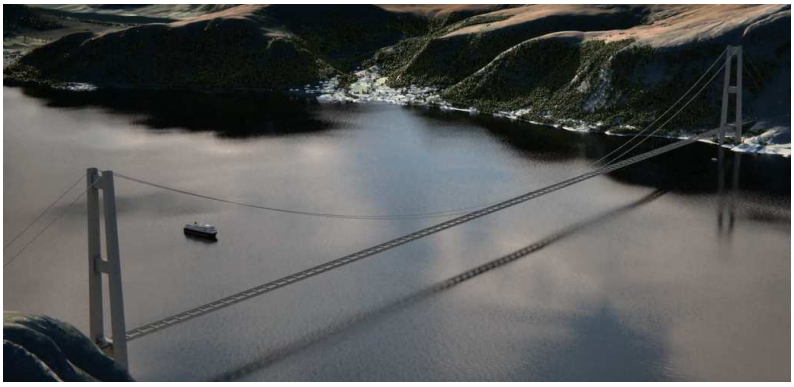

Figure 1.1. The Sulafjord Bridge, single span concept, rendering [61].

The aerodynamic response of long-span bridges is caused by the dynamic loading due to turbulent wind. Long-span bridges are characterized by a long and slender bridge girder supported by a cable structure which makes up a system with very low vibration frequencies, which is particularly susceptible to low frequency loading as in the case of large-scale wind turbulence. The representation of the wind field constitutes a second

major design issue related to long-span bridges. The wind turbulence is a stochastic phenomenon, which means that it is described by statistical properties rather than known incidents. The statistical properties describe the probability that the wind loading will be of a certain amplitude, spacial extent, and frequency. These probability distributions can be obtained by site measurements or described by mathematical models. The turbulence characteristics are site specific as the surrounding landscape affects the wind which implies that site measurements are necessary when planing the construction of long-span bridges. However, the quality of the data depends on the time spent measuring and as storms rarely occur, high quality measurements at winds speeds relevant for the design of the bridge are not easily obtained. Therefore, in practice, a combination of measurements and a mathematical description of the wind field turbulence is applied.

Currently, the three longest suspension bridges in the world are the Akashi Kaikyō Bridge in Japan with a span length of 1991 metres, the Xihoumen Bridge in China with a span length of 1650 metres, and The Great Belt Bridge in Denmark with a span length of 1624 metres. However, a desire to build even longer spans is present for example in relation to the Coastal Highway E39 project in Norway where several major fjord crossings are planned. One of the planned crossings is the Sulafjord, where different bridge concepts are considered, one of which is a 3000 metre span suspension bridge depicted in Figure 1.1. Alternatively, a suspension bridge concept with two spans and a supporting pylon in the middle founded at 450 metres water depth is proposed. A rendering of this concept is shown in Figure 1.2. Both concepts are ultra long-span bridge structures pushing the limit of the maximum span length. Hence, the aerodynamic design constitutes a key element in realizing the construction of either of them, which was the motivation for the present study.

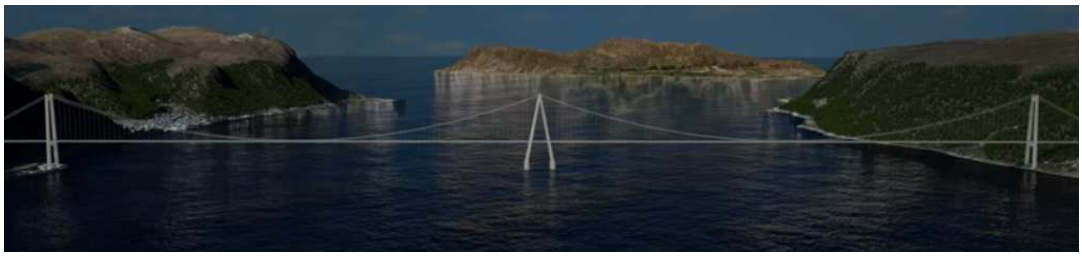

Figure 1.2. The Sulafjord Bridge, double span concept, rendering [61].

The present work has focused on three different subareas within the field of aerodynamic stability and the response of long-span bridges. The first part is concerned with the development of an efficient and accurate wind field simulation method. This is essential for time simulation of the wind loading, serving as input for a time domain response simulation. In [C1], preliminary work on wind field simulation and its application to bridge response evaluation were presented. A considerably more detailed simulation method for three-dimensional wind fields is presented in [P1] and applied for the wind loading of a full suspension bridge structure in [P2]. The second part of the project is concerned with the implementation of an efficient aero-elastic model for time domain response calculations. An investigation of model reduction via quasi-steady condensation was presented in [C2] and the full aero-elastic implementation is presented in [P2]. The model is used for simulation of bridge response due to wind loading based on the full three-dimensional turbulence

model developed in [P1]. The third and final part of the project was about the suppression of unstable aerodynamic response by use of external dampers. In [P3] an external damping system is presented and the effect on the stability limit and the aerodynamic response is illustrated numerically by using the aero-elastic model developed in [P2].

The following presentation constitutes a comprehensive summary of the work conducted and presented in papers and at conferences during the three-year project period. The presentation is divided into three chapters. The first chapter describes the conditional mean field wind simulation method and illustrates the performance of the method with an example. Chapter 2 describes the aero-elastic model and calibration of the aerodynamic derivatives and summarises the results for full structural loading and the influence of the wind load correlation on the response based on a full-field turbulence representation. Finally, chapter 3 introduces the damping system together with a tuning concept and the effect of the damping system on the stability limit. The summary includes figures and results from the included papers and is rounded off with some main conclusions on the presented work.

2. Wind field simulation

Turbulent wind constitutes an important aspect of the structural loading of long and slender structures as long-span bridges. A turbulent wind field can be understood as elliptic vortices of different sizes and intensities, and the statistical distribution of these vortices is what characterises the turbulence. In relation to wind loading of bridges, two aspects are relevant: the modelling of the turbulent field, and time simulation of the turbulence components. The turbulent wind field is represented by the wind velocity components in a fixed three-dimensional coordinate system. For bridge application the wind field is most often represented by the auto-spectral density of the component of interest in combination with a cross-field coherence formulation to provide the transverse field properties, typically chosen on an empirically exponential form as suggested by Davenport [17]. However, the Davenport formulation implies a positive correlation at any cross-field separation. This yields a non-zero mean flow at any particular time and also violates the underlying incompressibility condition. An alternative three-dimensional field formulation has been developed in [49] and [41] based on homogeneous isotropic turbulence and a von Kàrmàn representation of the along wind spectral density [37, 3].

In general, wind field simulation methods can be divided into two categories: One is the so-called Fourier methods, based on the spectral density of the wind velocity components. These methods are based on an inverse Fourier transformation of a factored form of the spectral representation of the turbulence field often making use of the Fast Fourier Transform (FFT). A basic formulation was introduced in [73], but for wind loading of large scale structures where a large correlated field needs to be simulated, the decomposition of the spectral density matrix is challenging. This issue has been addressed in various forms, e.g. by eigenvector decomposition [51, 19, 20, 14], Proper Orthogonal Decomposition [75, 9] or Karhunen-Loève expansion techniques [81]. Ultra fast simulations can be carried out on regular grids by taking advantage of the cross-field periodicity [86, 6, 34], and inclusion of unevenly spaced simulation points by interpolation has been discussed in [67]. An alternative to the spectrally based Fourier simulations are the direct time-domain procedures: the auto-regressive (AR), the moving-average (MA), and the combined auto-regressive moving-average (ARMA) processes. These are step-by-step processes in which the wind velocity field at each time step is generated from the velocity field at some of the previous time steps and suitable random components, making them computationally efficient and flexible. The quality of an ARMA simulated wind fields depends on the specific format of the model. In principle, the model coefficients can be calibrated based on existing time records. However, this approach is typically incomplete and may be cumbersome for large scale problems. Alternatively, the calibration can be based on the field spectral properties [59, 78, 21, 36] or based on the field covariance [47],[P1].

2.1 Conditional mean-field simulation

The conditional mean-field simulation method presented in [P1] is a multi-variate auto-regressive process. The simulation procedure is closely related to the concept of convected frozen turbulence and illustrated in Figure 2.1. Each of the rectangular planes represent the turbulence components at a set of fixed points, and the planes are separated by the distance $\Delta x = Uh$, where U is the mean wind speed and h is the time step. The front plane contains the wind components at the current step n and the light blue planes contain the corresponding wind components at previous steps used as input for the current step, and therefore referred to as memory steps. The quality of the simulated field depends on the number of auto-regressive terms as well as on the distribution of these. In combination this is referred to as the memory layout. In contrast to standard auto-regressive procedures, the memory steps are not necessarily found at k previous steps $n-1, ..., n-k$, or even equally spaced steps. An advantageous memory layout will be discussed in relation to a simulation example in section 2.2. It is noted that even though the wind components in a single step are illustrated with a two-dimensional rectangle, the wind components can be located in a three-dimensional pattern. This is important e.g. when loading a full bridge structure including the bridge deck, cables and pylons.

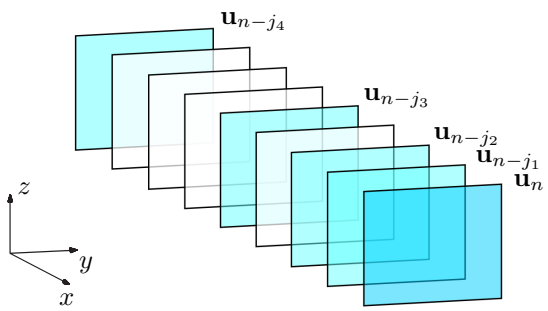

Figure 2.1. Conditional mean-field simulation procedure [P1].

The sequential simulation procedure can be written on the following compact form

$$\mathbf{u}_n \;=\; \mathbf{A}\,\mathbf{w}_n \;+\; \mathbf{B}\,\boldsymbol{\xi}_n, \qquad n = 1, 2, \cdots . \tag{2.1}$$

Here, $\mathbf{u}_n$ is the wind component vector at step n, $\mathbf{A}$ is a compound coefficient matrix and $\mathbf{w}_n$ is a compound vector consisting of the wind component vectors at the memory time steps

$$\mathbf{A} \;=\; [\mathbf{A}_1, \cdots, \mathbf{A}_j]\,, \qquad \mathbf{w}_n^T \;=\; [\mathbf{u}_{n-i_1}^T, \cdots, \mathbf{u}_{n-i_j}^T]\,. \tag{2.2}$$

The second term in (2.1) constitutes a zero-mean stochastic input, where $\mathbf{B}$ is a coefficient matrix and $\boldsymbol{\xi}_n$ is a random vector with uncorrelated normalized zero-mean normal components, whereby $\mathrm{E}[\boldsymbol{\xi}_i, \boldsymbol{\xi}_j] = \delta_{ij}\mathbf{I}$. The coefficient matrices can now be determined based on the field covariance relations. To ease the notation, the covariance matrices are introduced as

$$\mathbf{C}_{\mathbf{uu}} \;=\; \mathrm{E}[\mathbf{u}_n\mathbf{u}_n^T]\,, \quad \mathbf{C}_{\mathbf{uw}} \;=\; \mathrm{E}[\mathbf{u}_n\mathbf{w}_n^T]\,, \quad \mathbf{C}_{\mathbf{ww}} \;=\; \mathrm{E}[\mathbf{w}_n\mathbf{w}_n^T]\,. \tag{2.3}$$

The matrix $\mathbf{A}$ is now determined by post-multiplying (2.1) by $\mathbf{w}^T$ and by subsequently considering the expected value of each side of the equation. As the expected value is a linear operator, the two terms on the right hand side can be evaluated independently.

Observing that $\boldsymbol{\xi}_n$ is independent from $\mathbf{w}_n$, the second term vanishes and the following relation can be obtained,

$$\mathbf{A} \;=\; \mathbf{C}_{\mathbf{uw}}\mathbf{C}_{\mathbf{ww}}^{-1}. \tag{2.4}$$

The second coefficient matrix $\mathbf{B}$ can now be determined. By moving the term $\mathbf{A}\mathbf{w}_n$ to the left hand side of equation (2.1) it can be observed that the expected value of both sides of the equation must be zero. Evaluation of the covariance on both sides of the equation, using that $\mathrm{E}[\boldsymbol{\xi}_n, \boldsymbol{\xi}_n] = \mathbf{I}$, then yields the relation

$$\mathbf{B}\,\mathbf{B}^T \;=\; \mathbf{C}_{\mathbf{uu}} \;-\; \mathbf{A}\mathbf{C}_{\mathbf{ww}}\mathbf{A}^T. \tag{2.5}$$

The solution $\mathbf{B}$ can then be found by a LU decomposition or an eigenvalue analysis.

2.2 Line field simulation

To illustrate the performance of the conditional mean-field method, a simulation example from [P1] is summarized. The simulated wind field is a three-dimensional isotropic field described by the field covariance tensor $\mathbf{R}(\mathbf{r})$ for the turbulence component vector $\mathbf{v}$ at two different points separated by the vector $\mathbf{r}$ [3],

$$\mathbf{R}(\mathbf{r}) \;=\; \mathrm{E}\big[\,\mathbf{v}(\mathbf{r}_0+\mathbf{r})\,\mathbf{v}(\mathbf{r}_0)^T\big] \;=\; \sigma_v^2\Big(\big[\,f(r)-g(r)\,\big]\frac{\mathbf{r}\,\mathbf{r}^T}{\mathbf{r}^T\mathbf{r}} \;+\; g(r)\,\mathbf{I}\Big), \tag{2.6}$$

where σ_u^2 is the variance of a single component at a point, and $r = |\mathbf{r}|$ is the distance between the two points. The functions $f(r)$ and $g(r)$ are the correlation in the lengthwise direction and transverse direction, respectively. Hereby, the correlation of two vertically separated vertical components is given by $f(r)$ while the correlation of two horizontally separated vertical components are given by $g(r)$. In the current example, the correlation functions are taken corresponding to the von Kàrmàn spectral density [41],

$$f(r) = \frac{\mathrm{Ai}(z)}{\mathrm{Ai}(0)}, \qquad g(r) \;=\; f(r) \;+\; \frac{z}{3}\,\frac{\mathrm{Ai}'(z)}{\mathrm{Ai}(0)}. \tag{2.7}$$

where,

$$z = \Big(\frac{3r}{2\ell}\Big)^{2/3}. \tag{2.8}$$

The length parameter ℓ is directly related to the integral length scale λ as $\ell = 1.339\lambda$, where the integral length scale is found as the integral of the correlation function $f(r)$. The functions $\mathrm{Ai}(z)$ and $\mathrm{Ai}'(z)$ are the Airy function and its derivative, respectively. The covariance matrices given in (2.3) used as input for the calibration of the simulation model are composed explicitly from the two-point covariance in (2.6).

The cross-section of the simulated field is a horizontal line of $N_y = 201$ simulation points with three components at each point, i.e. a total number of 603 components. The simulation points are equally distributed with distance $\Delta y = 9.0$, whereby the total width of the simulation field is $L_y = 1800$ and the step length is $\Delta x = 5.0$. The integral length scale is set to $\lambda = 300$, much shorter than the width of the line field, and the standard deviation of a turbulence in a single point is $\sigma_u = 1$. A large number of steps $N_x = 10^6$ are simulated in order to reduce the uncertainty related to the field property estimates.

In [P1] an investigation of different memory layouts has been carried out. Initial tests showed that a simple memory layout $j = 1, .., k$ provides improved accuracy of low

wavenumber content for increasing memory depth. However, high wavenumber content was seen to be well-represented even with few memory steps. This observation suggests an alternative distribution of the memory steps where the resolution of high and low wavenumber content is more even. This is obtained by an exponential layout $j = m^{i-1}$, $i = 1, 2, ...$, where the base m is chosen appropriately: choosing $m = 2$ will provide the optimal representation of high wavenumbers while $m > 2$ will compromise the representation of high wavenumber content, while obtaining a larger memory depth with fewer auto-regressive terms, which will benefit the representation of the low wavenumber content. For reference, the wavenumber κ relates to the angular frequency ω via the relation $\kappa = \omega/(2\pi U)$. However, for illustrating the performance of the simulation method, it is convenient to use the spacial representation.

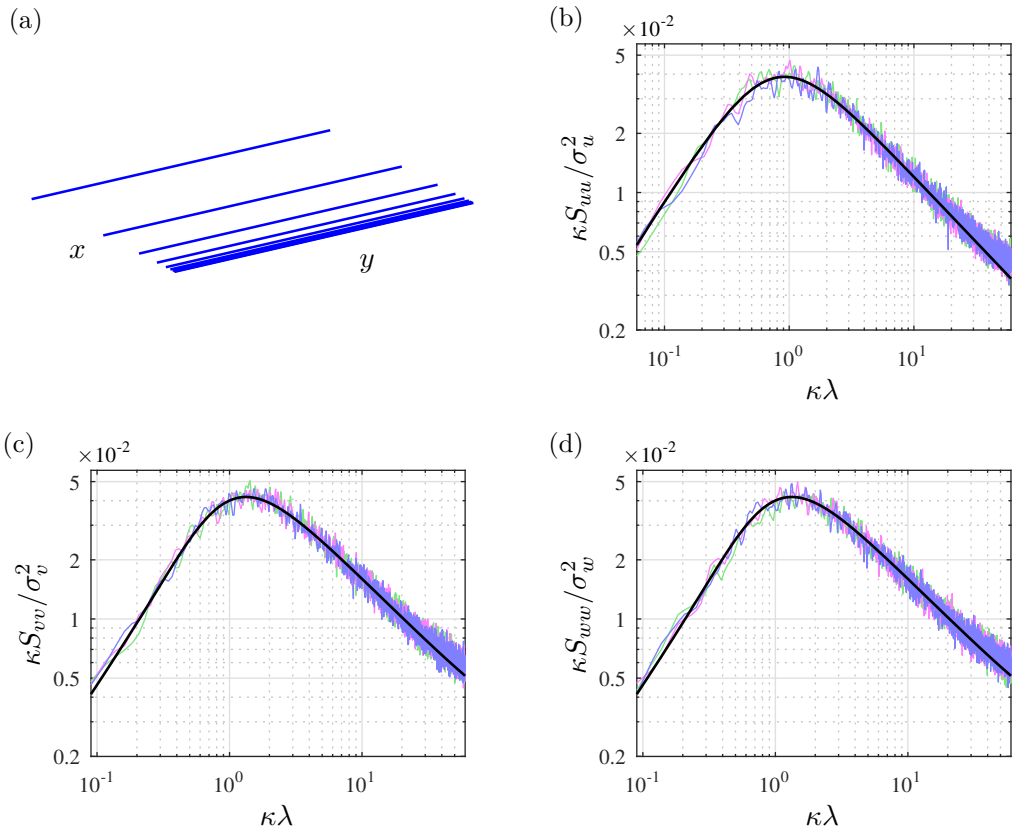

Figure 2.2. Estimated spectral densities at end point (−), quarter point (−), and mid-point (−), target spectrum (−).

Figure 2.2a shows the memory layout of the simulated line field with each of the lines representing a memory step found at $j = 2^{i-1}$, $i = 1, 2, ..., 9$. It can be observed that the memory depth is comparable with the width of the field. To obtain a comparable depth with a single step layout, a number of 256 auto-regressive terms should be included. As the simulation time is proportional to the number of auto-regressive terms, the exponential layout offers an almost 30 times faster simulation of equal quality. The quality of the simulated record is illustrated by comparing estimated statistical properties to target results. Two properties are of special interest: firstly, the power spectral density which provides a measure of the wavenumber content of a single component in a single simulation point. Secondly, the field coherence which provides the correlation of wavenumber content of

two spatially separated turbulence components. Figure 2.2b-d shows the estimated power spectral densities of the along wind component u, the horizontal cross field component v and the vertical wind component, w. The three colored graphs show the estimated power spectral density at an end point, a quarter point and a mid point and it is found that the distribution is indifferent to the location of the simulation point within the simulated field. The black curve represents the target power spectral densities found as the Fourier transform of the correlation function $f(x)$ for the u-components and $g(x)$ for the v- and w-components. For all three components, it can be observed that the estimated spectral properties correspond very well with the target results.

The coherence functions of horizontal cross-field separation of each of the three wind components are derived in [P1] for a generalized von Kàrmàn field [41]. These are used as target for the estimated coherence functions from the simulated field. Figure 2.3a and 2.3b show the coherence functions ψ_{11} and ψ_{33} of two u-components and two w-components, respectively, with a fixed horizontal separated of 0.75λ, 1.5λ and 3λ. The estimated coherence functions for the different separations correspond well with theoretical results. Also, it is noted that for a consistent three-dimensional turbulence representation, the coherence does not go towards one for the wavenumber going towards zero, which is in accordance with recent site measurements [24, 87, 68].

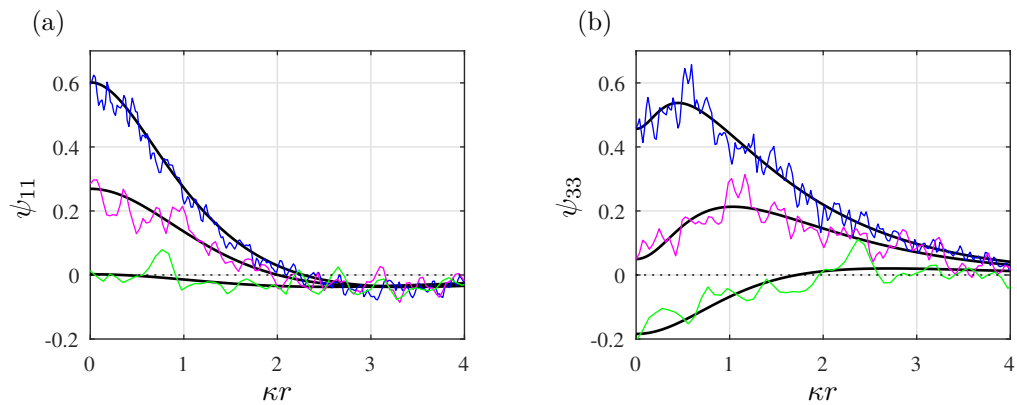

Figure 2.3. Estimated coherence: (a) ψ_{11}, (b) ψ_{33}. Separation 0.75λ (−), 1.5λ (−), 3λ (−). Target coherence (−).

Both the power spectral density and the coherence are wavenumber functions in contrast to the field covariances that were used as input for the simulation model. In [P1], correlations estimated from the simulated field are also shown to correspond well with the input correlation functions. The performance of the conditional mean-field simulation method was also illustrated in relation to a field with a square cross-section and dimensions comparable to the integral length scale as a case relevant for wind turbine application. In [P2], the simulation method was applied to a long-span suspension bridge for loading of the full structure including the deck, pylons and cables.

3. Bridge aerodynamics

The aerodynamic response of long-span bridges depends on both the turbulent wind loading as well as the forces caused by the structural motions in the surrounding flow. The latter are most often referred to as self-excited forces, motion-induced forces, or aero-elastic forces and depend on the structural response, the wind speed, the air density, and the cross-sectional shape of the structure. Figure 3.1 shows a bridge girder with cross-section forces $\mathbf{f} = [f_x, f_z, f_\theta]^T$, the mean wind speed U, the along wind turbulence component u, and the vertical turbulence component w. The bridge girder is depicted as a twin-box girder as an example of a modern aerodynamically shaped bridge girder designed to optimise the wind stability conditions of long-span bridges.

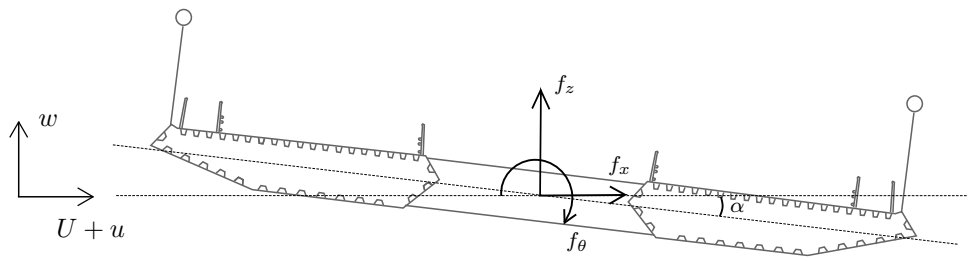

Figure 3.1. Aerodynamic forces.

The basic principles in the representation of aero-elastic forces are carried over from Theodorsen's classic airfoil theory [84] which describes the actions on an oscillating flat plate in a homogeneous stationary fluid flow. The application to bridge deck flutter was introduced by Scanlan and Tomko [71]. The aero-elastic forces are typically described by the frequency dependent aerodynamic derivatives. These can either be derived from the Theodorsen flat plate theory, or they can be measured in a wind tunnel on scaled cross section models. For time domain response simulations, it is necessary to transform the frequency dependent formulation of the aero-elastic force. This can be done either by indicial functions [72] or by a rational function approximation [12, 32, 33, 63]. The current chapter summarizes the aero-elastic implementation presented in [P2] which deviates from other implementations by a compact first order differential state-space format of the equation of motion, a simple algorithmic approach for parameter identification and a momentum-based unconditionally stable time integration scheme. The established model is applied to investigate the influence of full structural loading versus the commonly applied deck loading. Finally, the influence of the transverse turbulence length scale on the structural response will be discussed based on the aerodynamic response due to consistent wind loading based on a full-field turbulence representation.

3.1 Aero-elastic load representation

The equation of motion of the aero-elastic system is written with the structural terms on the left-hand side and with the aerodynamic loading on the right-hand side of the equation

$$\mathbf{M}_s\ddot{\mathbf{q}}(t) + \mathbf{C}_s\dot{\mathbf{q}}(t) + \mathbf{K}_s\mathbf{q}(t) = \mathbf{f}_a(t) + \mathbf{f}_e(t), \tag{3.1}$$

where $\mathbf{M}_s$, $\mathbf{C}_s$ and $\mathbf{K}_s$ are the structural mass, damping and stiffness matrices, respectively, and $\mathbf{q}(t) = [q_x(t), q_z(t), q_\theta(t)]^T$ is the time dependent displacement vector. The displacement entries correspond to the cross-sectional forces defined in Figure 3.1. The vectors $\dot{\mathbf{q}}(t)$ and $\ddot{\mathbf{q}}(t)$ are the first and second time derivatives of the displacements, i.e. the velocities and accelerations. The aerodynamic load appears as the aero-elastic contribution $\mathbf{f}_a(t)$ and the external forces $\mathbf{f}_e(t)$, referred to as the buffeting load. The implementation of the buffeting load is based on standard buffeting theory, see e.g. [82] or a brief summary in [P2]. The aero-elastic forces depend on the displacement history as expressed by the convolution integral

$$\mathbf{f}_a = \int_0^\infty \mathbf{Q}(\tau)\mathbf{q}(t-\tau)\, d\tau, \tag{3.2}$$

where $\mathbf{Q}(\tau)$ is the kernel function. Assuming harmonic force and response, $\mathbf{f}_a = \bar{\mathbf{f}}_a e^{i\omega t}$ and $\mathbf{q} = \bar{\mathbf{q}}e^{i\omega t}$, where the bar denotes the complex amplitude and ω is the angular frequency, the relation between the aero-elastic force and response is given by the Fourier transform of the kernel function. The Fourier transform of the kernal function is most often given in terms of the geometry-specific, non-dimensional aerodynamic derivatives P_n^*, H_n^*, A_n^*, $n = 1, 2, ..., 6$, [71],

$$\frac{\bar{\mathbf{Q}}}{\frac{1}{2}\rho U^2 B} = \frac{\omega_*^2}{B}\begin{bmatrix} P_4^* + iP_1^* & P_6^* + iP_5^* & B(P_3^* + iP_2^*) \\ H_6^* + iH_5^* & H_4^* + iH_1^* & B(H_3^* + iH_2^*) \\ B(A_6^* + iA_5^*) & B(A_4^* + iA_1^*) & B^2(A_3^* + iA_2^*) \end{bmatrix}. \tag{3.3}$$

Here, $\omega_* = \omega B/U$ is the reduced frequency and B and ρ are the reference width of the bridge deck and the air density.

The convolution integral in (3.2) is computationally inefficient and a rational function implementation is therefore considered. The idea is to represent the motion-dependent aero-elastic forces in terms of instantaneous contributions proportional to the displacement, velocity, and acceleration as well as one or more memory contributions representing the non-instantaneous contributions. Thereby, the aero-elastic forces can be written as

$$\mathbf{f}_a = -\mathbf{M}_a\ddot{\mathbf{q}}(t) - \mathbf{C}_a\dot{\mathbf{q}}(t) - \mathbf{K}_a\mathbf{q}(t) + \sum_{j=1}^{J}\mathbf{f}_j. \tag{3.4}$$

The coefficient matrices $\mathbf{M}_a$, $\mathbf{C}_a$ and $\mathbf{K}_a$ are referred to as the aerodynamic mass, damping and stiffness and $\mathbf{f}_j$ are the memory force contributions. The number of memory contributions included in the representation of the aero-elastic forces determines the accuracy of the approximation. Each of the contributions can be described by its own convolution integral similar to (3.2). The kernel function of each convolution integral $\mathbf{Q}_j(t)$ is assumed on a decaying exponential form described by a time scale factor γ_j and a coefficient matrix $\mathbf{D}_j$ which determines the size of the contribution

$$\mathbf{Q}_j = \mathbf{D}_j e^{-\gamma_j \tau}, \quad \tau \geq 0. \tag{3.5}$$

The decaying exponential form indicates that more recent events have larger influence. By evaluating the convolution integral with the kernel function expressed by the exponential assumption, a first order differential relation between a single memory force contribution $\mathbf{f}_j$ and the displacements can be derived

$$\dot{\mathbf{f}}_j + \gamma_j \mathbf{f}_j = \mathbf{D}_j \mathbf{q}. \tag{3.6}$$

Each of the included memory contributions can conveniently be included as an additional state-variable in the equation of motion by introducing an extended state-space format. A first order format is obtained by further introducing the velocity $\mathbf{v}$ as a state-variable via the relation $\mathbf{M}\mathbf{v} = \mathbf{M}\dot{\mathbf{q}}$, ensuring a symmetric form of the still-air system,

$$\begin{bmatrix} \mathbf{C} & \mathbf{M} & \mathbf{0} \\ \mathbf{M} & \mathbf{0} & \mathbf{0} \\ \mathbf{0} & \mathbf{0} & \mathbf{I}_{J\times J} \end{bmatrix} \begin{bmatrix} \dot{\mathbf{q}} \\ \dot{\mathbf{v}} \\ \dot{\mathbf{f}} \end{bmatrix} + \begin{bmatrix} \mathbf{K} & \mathbf{0} & -\mathbf{I}_{1\times J} \\ \mathbf{0} & -\mathbf{M} & \mathbf{0} \\ -\mathbf{D} & \mathbf{0} & \mathbf{\Gamma} \end{bmatrix} \begin{bmatrix} \mathbf{q} \\ \mathbf{v} \\ \mathbf{f} \end{bmatrix} = \begin{bmatrix} \mathbf{f}_e \\ \mathbf{0} \\ \mathbf{0} \end{bmatrix}, \tag{3.7}$$

where

$$\mathbf{D} = \begin{bmatrix} \mathbf{D}_1 \\ \vdots \\ \mathbf{D}_J \end{bmatrix}, \quad \mathbf{\Gamma} = \begin{bmatrix} \gamma_1 \mathbf{I} & \cdots & \mathbf{0} \\ \vdots & \ddots & \vdots \\ \mathbf{0} & \cdots & \gamma_J \mathbf{I} \end{bmatrix}, \quad \mathbf{f} = \begin{bmatrix} \mathbf{f}_1 \\ \vdots \\ \mathbf{f}_J \end{bmatrix}. \tag{3.8}$$

The system matrices are now the sum of the structural and the aerodynamic contribution: $\mathbf{M} = \mathbf{M}_s + \mathbf{M}_a$, $\mathbf{C} = \mathbf{C}_s + \mathbf{C}_a$, and $\mathbf{K} = \mathbf{K}_s + \mathbf{K}_a$. The first order state-space format is convenient for derivation of a momentum-based, unconditionally stable time integration scheme as presented in [P2] and summarised in Section 3.3. Also, for linear systems, the modal properties in terms of the frequencies, damping ratios, and mode shapes are easily acquired by solving the generalised eigenvalue problem obtained by assuming a harmonic representation of the state-variables.

3.2 Parameter identification

The relation between the aerodynamic derivatives and the aerodynamic system matrices can be established by comparing the Fourier transform of the kernel function in (3.3) with the Fourier transform of the kernel function of the rational function approximation of the aero-elastic forces. The derivation of the Fourier transform of the rational approximation is found in [32] and also shown in [P2]. The comparison leads to the following relations

$$\mathbf{M}_a^* - \frac{1}{\omega_*^2}\mathbf{K}_a^* + \frac{1}{\omega_*^2}\sum_j \frac{\gamma_j^*}{\gamma_j^{*2} + i\omega_*^2}\mathbf{D}_j^* = \frac{1}{B}\begin{bmatrix} P_4^* & P_6^* & BP_3^* \\ H_6^* & H_4^* & BH_3^* \\ BA_6^* & BA_4^* & B^2A_3^* \end{bmatrix} \tag{3.9}$$

and

$$-\frac{1}{\omega_*}\mathbf{C}_a^* - \frac{1}{\omega_*}\sum_j \frac{1}{\gamma_j^{*2} + i\omega_*^2}\mathbf{D}_j^* = \frac{1}{B}\begin{bmatrix} P_1^* & P_5^* & BP_2^* \\ H_5^* & H_1^* & BH_2^* \\ BA_5^* & BA_1^* & B^2A_2^* \end{bmatrix}. \tag{3.10}$$

Here, $\mathbf{M}_a^*$, $\mathbf{C}_a^*$ and $\mathbf{K}_a^*$ are the normalised aerodynamic system matrices, and $\mathbf{D}_j^*$ and γ_j^* are normalised memory parameters. The normalization can be found in [P2]. To identify the aerodynamic system matrices and memory parameters from the relations in (3.9) and (3.10), an identification procedure is required. The identification can be done by non-linear

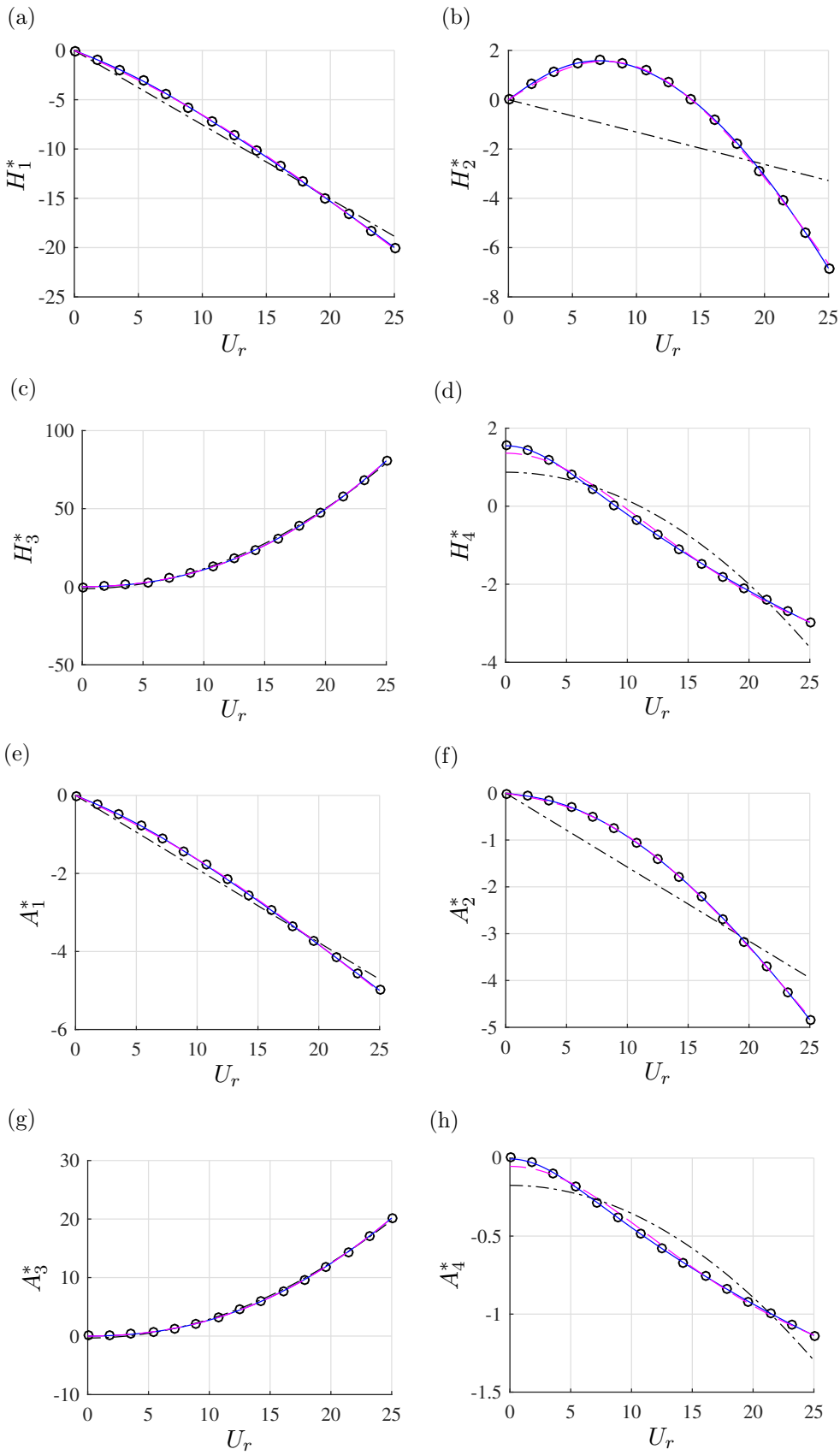

Figure 3.2. Aerodynamic derivatives, flat plate: (○) analytic plate, (·—,– –,—) 0,1,2 memory terms.

least squares fitting [72, 7] or iterative parameter fitting [88]. In [P2], a simple identification procedure is presented based on the least squares solution of an over-determined equation system. The equally weighted minimisation process is written as

$$\min_{\gamma_j \in \mathbb{R}_+} \{(\mathbf{A}\mathbf{x} - \mathbf{b})^T (\mathbf{A}\mathbf{x} - \mathbf{b})\} \tag{3.11}$$

where $\mathbf{A}$ is the non-square system matrix containing the relations between the aerodynamic derivatives and the aerodynamic system matrices as they appear in (3.9) and (3.10). The number of columns in $\mathbf{A}$ depends on the number of memory terms included in the aero-elastic force representation and the number of rows is determined by the number of data points available for the aerodynamic derivatives. It the case of 18 derivatives, each represented with m data points, the number of rows is $18m$. The vector $\mathbf{b}$ consists of the data points of the aerodynamic derivative and finally, the vector $\mathbf{x}$ contains the entries of the normalized aerodynamic matrices $\mathbf{M}_a^*$, $\mathbf{C}_a^*$, $\mathbf{K}_a^*$ and $\mathbf{D}_j^*$ and is found by solving the over-determined linear system $\mathbf{A}\mathbf{x} = \mathbf{b}$. Thus, the identification of the aerodynamic matrices can be carried out with an over-determined linear system solver as well as a basic minimisation algorithm.

The identification procedure is applied to a flat plate example and is illustrated in Figure 3.2, where the aerodynamic derivatives are shown as functions of the reduced mean wind speed $U_r = U/(\omega B)$. The circular markers indicate the aerodynamic derivatives obtained by Theodorsen's theory [84] and the black dash-dotted curve, the magenta dashed curve, and the blue solid curve represent the approximated results obtained with zero, one, and two memory terms respectively. Only the aerodynamic derivatives related to vertical and torsional motions of the structure are included, as the derivatives related to drag motions are described by instantaneous terms exclusively, see e.g. [82]. The representation of the aero-elastic forces without memory terms is also referred to as a quasi-steady representation and offers the most efficient evaluation of the aero-elastic forces [5, 62]. However, this representation is seen to provide a linear representation of H_1^*, H_2^*, A_1^* and A_2^* whereby the approximation is highly dependent on the interval covered by the the data. The representation with one memory term, and especially the representation with two memory terms, can be observed to provide a very good fit for all eight derivatives in the case of a flat plate. For aerodynamic derivatives measured in a wind tunnel the data will be scattered, and for practical application it can be of interest to introduce a weighted minimisation process to provide an improved fit in a reduced range of the mean wind speed. Alternatively, the data points outside an interval of interest can be left out completely.

3.3 Time integration

In [P2] the momentum-based time integration procedure presented e.g. in [44] is extended to the system including aero-elastic forces. The derivation of a discrete form is based on integration of the state-space equation of motion in (3.7) over the time-step h. For the linear system, the system matrices are constant, whereby only the state variable, their derivatives, and the external load are integrated

$$\begin{bmatrix} \mathbf{C} & \mathbf{M} & \mathbf{0} \\ \mathbf{M} & \mathbf{0} & \mathbf{0} \\ \mathbf{0} & \mathbf{0} & \mathbf{I}_{J\times J} \end{bmatrix} \begin{bmatrix} \int_h \dot{\mathbf{q}}\, dt \\ \int_h \dot{\mathbf{v}}\, dt \\ \int_h \dot{\mathbf{f}}\, dt \end{bmatrix} + \begin{bmatrix} \mathbf{K} & \mathbf{0} & -\mathbf{I}_{1\times J} \\ \mathbf{0} & -\mathbf{M} & \mathbf{0} \\ -\mathbf{D} & \mathbf{0} & \mathbf{\Gamma} \end{bmatrix} \begin{bmatrix} \int_h \mathbf{q}\, dt \\ \int_h \mathbf{v}\, dt \\ \int_h \mathbf{f}\, dt \end{bmatrix} = \begin{bmatrix} \int_h \mathbf{f}_e\, dt \\ \mathbf{0} \\ \mathbf{0} \end{bmatrix} \tag{3.12}$$

A second-order accurate discretized form is obtained by evaluating the integrals using the trapezoidal rule. Thereby, the integral of the displacement vector can be determined as the interval mean value $\bar{\mathbf{q}} = \frac{1}{2}(\mathbf{q}_n + \mathbf{q}_{n+1})$ times the step-length h, and the integral of its derivative can be found as the increment $\Delta\mathbf{q} = \mathbf{q}_{n+1} - \mathbf{q}_n$. The subscript n and $n+1$ refer to the end points of the time interval. The integral of the external load as well as the other state-variables and their derivatives are evaluated similarly, whereby

$$\begin{bmatrix} \mathbf{C} & \mathbf{M} & \mathbf{0} \\ \mathbf{M} & \mathbf{0} & \mathbf{0} \\ \mathbf{0} & \mathbf{0} & \mathbf{I}_{J\times J} \end{bmatrix} \begin{bmatrix} \Delta\mathbf{q} \\ \Delta\mathbf{v} \\ \Delta\mathbf{f} \end{bmatrix} + h \begin{bmatrix} \mathbf{K} & \mathbf{0} & -\mathbf{I}_{1\times J} \\ \mathbf{0} & -\mathbf{M} & \mathbf{0} \\ -\mathbf{D} & \mathbf{0} & \mathbf{\Gamma} \end{bmatrix} \begin{bmatrix} \bar{\mathbf{q}} \\ \bar{\mathbf{v}} \\ \bar{\mathbf{f}} \end{bmatrix} = h \begin{bmatrix} \bar{\mathbf{f}}_e \\ \mathbf{0} \\ \mathbf{0} \end{bmatrix}. \tag{3.13}$$

The discrete form can be rearranged to provide the state-variables at time $n+1$ based on the state-variables at time n. However, it is undesirable to solve a system with dimensions equal to the block coefficient matrices in the state-space format. This can be avoided by a break down of the state-space representation to an algorithmic form where a system the size of the number of structural degrees of freedom can be solved to find the displacement increment at the particular time-step. This is followed by an individual update of the state variable. The time integration algorithm is presented in [P2] together with a more detailed explanation of the derivation. The application of the time-stepping algorithm requires a single matrix inversion of an equivalent stiffness matrix followed by pure matrix-vector multiplications, whereby the computational speed is proportional to the number of structural degrees of freedom squared. The integration algorithm is second-order accurate which means the error introduced is proportional to the non-dimensional frequency ωh squared, wherefore the time-step size should be chosen relative to the modal period of interest. In [P2], the energy balance equation of the discrete equations of motion is shown to be the direct counterpart of the differential form and finally an elaborate discussion on algorithmic damping is carried out.

3.4 Suspension bridge model

The aerodynamic response is evaluated for a 3000 m single-span suspension bridge proposed for crossing the Sulafjord in Norway as part of the Coastal Highway E39 project [61]. The considered structural model is depicted in Figure 3.3 and is modelled with three-dimensional aero-elastic beam elements for the deck, using the implementation presented in [P2], and summarised in Section 3.1. The towers are modelled with basic three-dimensional beam elements and the cables are modelled using non-linear Green strain elements to ease the cable calibration, whereupon a linearised model is used for response simulations. The geometry as well as structural and aerodynamic properties are found in [69] and summarised in [P2] and [P3].

The response model is reduced by quasi-static condensation to increase the computational speed. This is relevant for time domain as well as frequency domain response calculations and for stability analysis, where the eigenvalue problem is solved numerous times in order to evaluate the modal damping at different wind speeds. The reduction method is based on a master-slave principle, where the displacement of the slave degrees of freedom, here referred to as the static degrees of freedom, is determined directly from the displacements of the master degrees of freedom, referred to as the dynamic degrees of

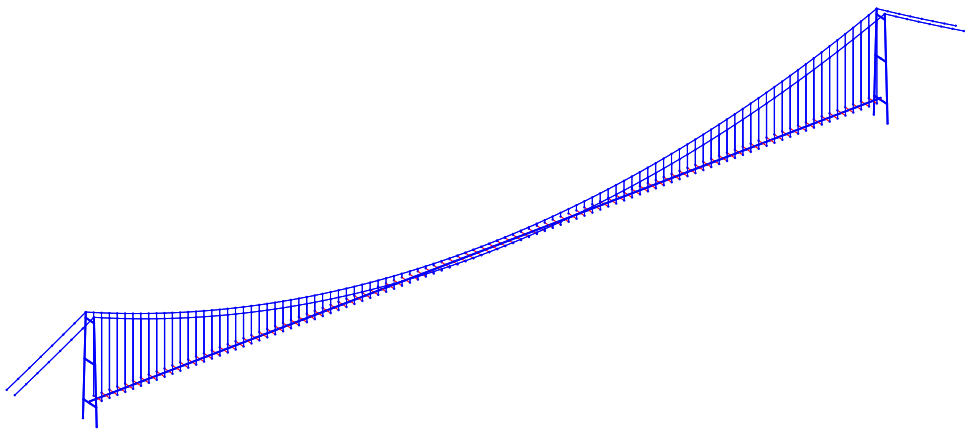

Figure 3.3. Suspension bridge model.

freedom, via the relation

$$\mathbf{q} = \begin{bmatrix} \mathbf{q}_d \\ \mathbf{q}_s \end{bmatrix} = \begin{bmatrix} \mathbf{I} \\ \mathbf{S} \end{bmatrix} \mathbf{q}_d \,, \quad \mathbf{S} = -\mathbf{K}_{ss}^{-1}\mathbf{K}_{sd}, \tag{3.14}$$

Subscripts d and s refer to static and dynamic degrees of freedom respectively. Extending the condensation method to include self-excited forces suggests to treat the state proportional aero-elastic terms as the structural mass, damping, and stiffness, while the memory part of the aero-elastic forces is reduced by considering the rate of work. The reduced mass matrix and force vector are found as

$$\bar{\mathbf{M}} = \mathbf{M}_{dd} + \mathbf{S}^T\mathbf{M}_{sd} + \mathbf{M}_{ds}\mathbf{S} + \mathbf{S}^T\mathbf{M}_{ss}\mathbf{S} \,, \quad \bar{\mathbf{f}} = \mathbf{f}_d + \mathbf{S}^T\mathbf{f}_s. \tag{3.15}$$

Other system matrices are reduced by the same methodology. The quality of the reduced system depends on the chosen ratio between dynamic and static degrees of freedom as well as on the distribution of them. For the suspension bridge, the distribution pattern shown in Figure 3.4 is applied, where nodes with dynamic degrees of freedom are indicated with black dots and nodes with static degrees of freedom are indicated with white dots. The dynamic nodes are distributed evenly along the bridge deck and the corresponding nodes on the suspension cables are also chosen as dynamic nodes, providing a direct relation

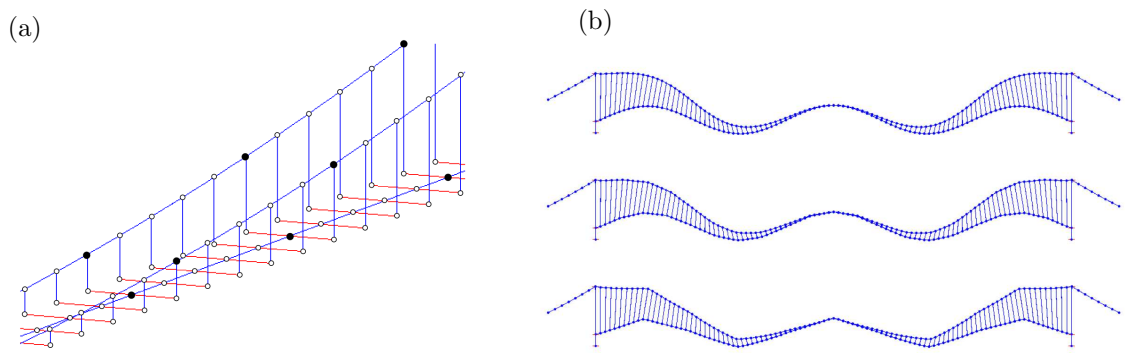

Figure 3.4. (a) Reduced system nodes, (b) second mode for reduction of 1:1, 1:5, 1:10.

between the suspension cables and the deck. Figure 3.4b shows the mode shape of the second symmetric vertical mode obtained by the original model as well as with a reduced model where every fifth node along the bridge deck is chosen as a dynamic node and for another reduced model where every tenth node is a dynamic node. It can be observed that the model with a reduction ratio of 1:5 reproduces the mode shape fairly accurate, while the 1:10 reduction results in a very coarse representation. This indicates that modes with a complexity level corresponding to the second vertical mode or simpler will be well-represented with a reduction ratio of 1:5.

From Figure 3.4 it was understood that the amount of dynamic nodes needed for a decent modal representation depends on the complexity of the mode shapes of interest. In [P2], the frequencies of the reduced models were compared to the frequencies of the original model, which shows that the frequencies obtained with the 1:10 model start to deviate around mode 9, while the frequencies obtained with the 1:5 model correspond well with the frequencies of the original system up until around mode 16. Furthermore, the frequencies obtained with the reduced models were seen to be equally good at zero mean wind speed and at the critical wind speed $U_{cr} = 57\,\mathrm{m/s}$, which is the wind speed that causes the aero-elastic system to become unstable. This implies that the reduction method is indeed applicable to the aero-elastic system.

3.5 Aerodynamic response

The response is evaluated for turbulent wind loading of the full bridge structure including the deck, pylons and cables. The load is evaluated based on the wind speeds at the nodal locations and is assumed linearly distributed over the elements. The wind field is represented as stretched isotropic turbulence as introduced in [P1], and the along-wind component is represented by the von Kàrmàn spectral density with the integral length scale $\lambda_x = 300\,\mathrm{m}$ and the two transverse length scales $\lambda_y = \lambda_z = 0.5\lambda_x$. The turbulence intensity is $I_u = 0.135$ and the standard deviation of the along-wind turbulence component is found as $\sigma_u = I_u/U$ where U is the mean wind speed. The time simulations are carried out by the conditional mean-field method as presented in [P1] and summarized in Chapter 2, with an exponential memory layout $j = 2^{i-1}$, $i = 1, 2, ..., 8$. In [P2], the simulated wind field is shown to provide a rather accurate representation of the statistical properties of the

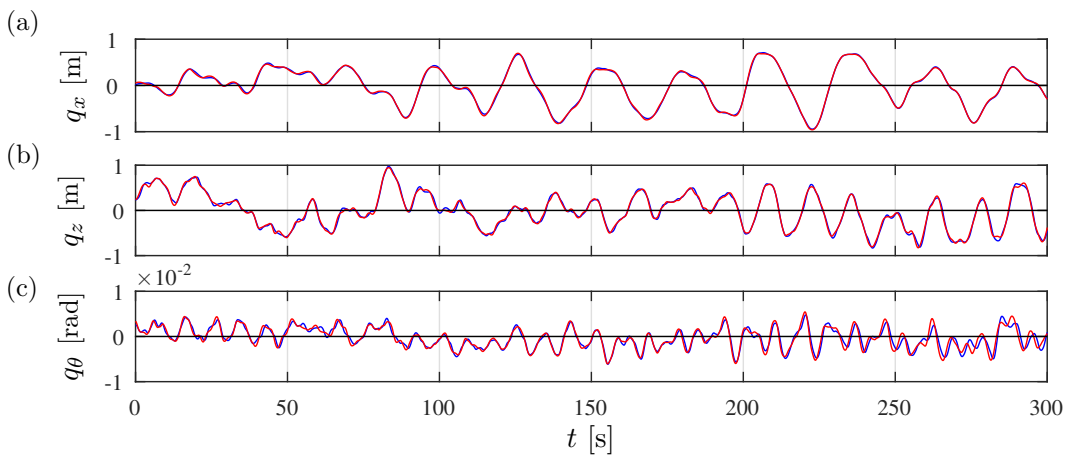

Figure 3.5. Time response at quarter span: full model (–), 1:5 reduction (–).

wind field. Furthermore, the computational speed of the sequential mean-field simulation method is compared to a FFT simulation method [1] demonstrating the efficiency and applicability to large scale problems.

A five-minute time record of a steady-state lateral, vertical, and torsional response at quarter span is shown in Figure 3.5a–c. The response is obtained for a mean wind speed of $U = 0.6U_{cr}$ using a time step size of $h = 0.166\,\mathrm{s}$. The blue graphs are results obtained by the original full bridge model, while the red graphs are results obtained with the 1:5 model. It can be observed that all three response records are well-represented by the reduced model. Furthermore, the low frequency content dominating the lateral and the vertical response is seen to be virtually perfectly reproduced, while minor deviations appear in the torsional response. The number of unconstrained degrees of freedom in the original model is 1284, while the reduced model is represented by 264 degrees of freedom. Hereby the computational time it takes to obtain a five minute response history is reduced significantly from 59.3 s to 0.7 s.

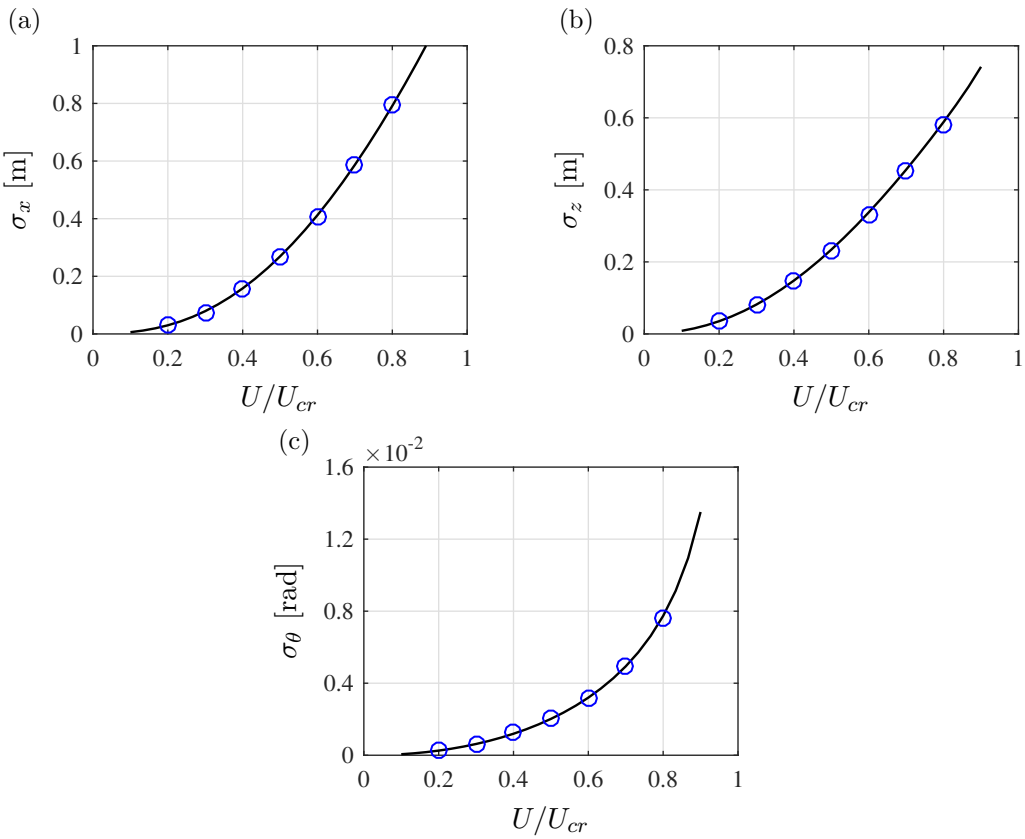

Figure 3.6. Response at quarter-span: frequency domain (−), time domain (○).

The accuracy of time domain response is dependent on the approximation related to the auto-regressive simulation of the wind load as well as the time-step size chosen for the time integration. A validation of the time domain results can be carried out by comparing the time simulation response with results obtained with a frequency domain calculation, which for a linear system should give the same results. Figure 3.6a–c shows the lateral, vertical, and torsional response σ_x, σ_z and σ_θ at quarter span as a function of the normalised mean wind speed. The solid black curve represents the response obtained with the

frequency domain calculation based on the spectral representation of the isotropic turbulence field given in [41]. For both time domain and frequency domain loading, stretching the wind field is equivalent to inverse stretching of the structural model. The accuracy of the frequency domain results is only determined by the considered frequency interval as well as the discretisation of this interval. The response is evaluated in the interval $\omega = [0.001; 2]$ rad/s at evenly distributed frequencies separated by $\Delta\omega = 0.0014$ rad/s. For lightly damped systems, a relatively fine resolution is needed around the system frequencies and improved efficiency of the frequency response calculation can be gained by evaluating the frequency response with a high resolution near the peaks and with a coarser resolution elsewhere. The blue circles mark the time domain results evaluated based on 20 hours of steady-state response. An estimate of the length of the transient period can be based on the free decay function of the lowest modes. In the case of long-span bridges, the transient period is long due to low vibration frequencies and extremely low damping of the drag modes corresponding to the structural damping. In the particular case, the transient period of the drag response is estimated to 1.7 hours. Note that the transient period is much lower for vertical and torsional responses due to the higher frequency content and the presence of aerodynamic damping. As expected, the results obtained by the two methods appear consistent based on the quality of the simulated wind field, the simulation length, the time-step size, and the frequency domain resolution.

Figure 3.7a–c shows the standard deviation of the drag, heave, and torsional response at quarter span as a function of the mean wind speed. The blue curves represent results

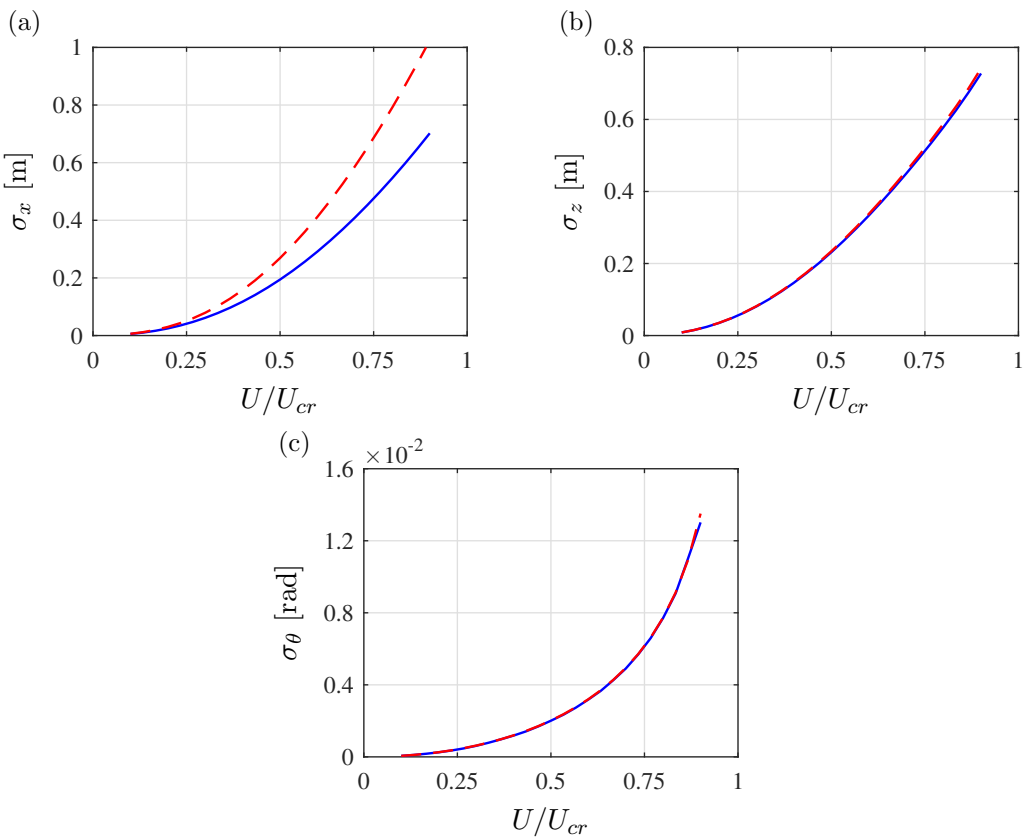

Figure 3.7. Response at quarter-span: deck loading (—), full bridge loading (– –).

obtained loading the bridge deck only and the red dashed curve represents results obtained loading the full structure. It is observed that the drag response is significantly lower when loading the bridge deck only, while the lateral and vertical responses are very similar. Time domain loading of the full structure constitutes a significant computational cost which can be reduced significantly if only the vertical and torsional responses are of interest.

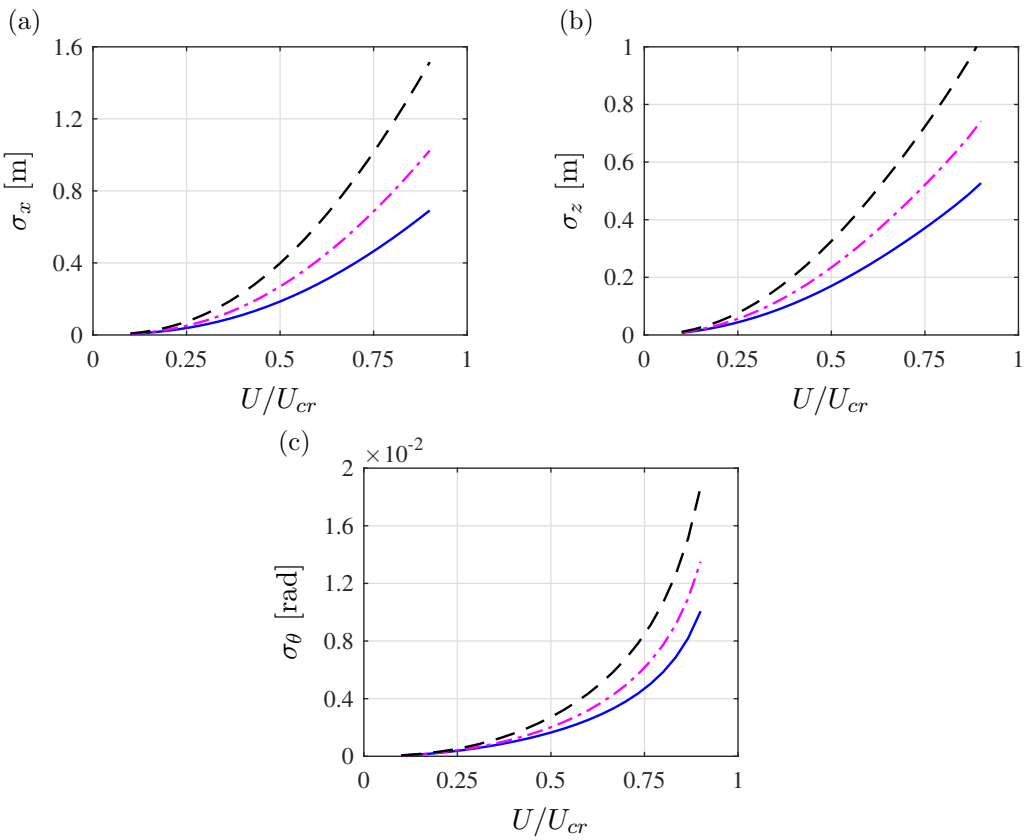

Figure 3.8. Response at quarter-span: $\lambda_y = 75\,\mathrm{m}$ (—), $\lambda_y = 150\,\mathrm{m}$ (·–), $\lambda_y = 300\,\mathrm{m}$ (- -).

Finally, the structural response is evaluated for different integral length-scales along the bridge deck. For fully correlated components, the response corresponds to the response found by a harmonic analysis, whereas the magnitude of the response to uncorrelated components is accumulated via what amounts to a root-mean-square analysis. This means that limited correlation of the loading results in a reduced response. Figure 3.8a–c shows the lateral, vertical, and torsional responses at quarter span for different across-wind turbulence length scales. The solid blue curves, the dash-dotted magenta curves, and the dashed black curves represent results obtained for turbulent length scale $\lambda_y = 75\,\mathrm{m}$, $\lambda_y = 150\,\mathrm{m}$, and $\lambda_y = 300\,\mathrm{m}$, respectively. As expected, a shorter across wind length-scale leads to a lower response as the wind field is less correlated. The effect is quite noticeable, and it is found that doubling the length scale results in approximately a 50% increase of the response. This emphasises that a representative value of the transverse turbulence length-scale is important in the design of long-span bridges.

4. Suspension bridge damping system

For long-span bridges, the stability limit is determined by the aero-elastic forces that occur due to the structural motions in a surrounding wind flow. To increase the aerodynamic stability limit, the shape of the deck cross-section is a key design element. The Tacoma Narrows suspension bridge that collapsed in 1940 due to unstable flutter response is a historical example that underlines the importance of the cross-sectional shape. For reference, the span length of the Tacoma Narrows bridge was 853 m, while currently the longest span suspension bridge in the world is the Akashi Kaikyō bridge with a span length of 1991 m. However, even for bridges with highly optimized aerodynamically shaped bridge girders, the flutter limit still sets the limit for the maximum span length in many cases. Therefore, it is of interest to introduce external damping to the bridge structure to further increase the aerodynamic stability limit. A study of the effect of increased modal damping on the aero-elastic behaviour showed improved stability as well as a lowered buffeting response [35]. Different methods for suppressing flutter motions have been suggested. Two concepts are prevalent: suppression of flutter motions by tuned mass dampers, where appropriately tuned resonant dampers are attached to the deck, or suppression of the flutter motions by movable flaps or winglets that control the flow around the bridge deck. The application of tuned mass dampers has been discussed both in the form of passive systems [28, 13, 10, 55], semi-active systems [29] and active systems [39]. All with a positive influence on the aerodynamic bridge response as well as the stability limit. However, a concern related to the weight penalty that comes with the installation of additional masses are limiting their use. Structural control via movable flaps has been proven very effective for active control systems [38, 85, 52, 2], however less effective for semi-active systems and passive systems [65, 66, 79]. The active systems require high maintenance and concerns are related to their reliability, thus limiting their use for flutter control. An alternative system with liquid column dampers has also been proposed [83]. In [P3], a passive damping system for suspension bridges is presented. The concept, the device calibration procedure, and the effect on the stability limit are summarized in this chapter.

4.1 Suspension bridge stability

The damping system targets the flutter motions which are governed by the low frequency torsional and vertical structural modes. For a typically configured single-span suspension bridge, here exemplified by the same 3000 m bridge considered in Chapter 3, these modes are the first antisymmetric and symmetric heave modes and the first antisymmetric and symmetric torsional modes as shown in Figure 4.1a–d. These modes are still-air modes, while the mode shapes shown in Figure 4.1e–f are the antisymmetric and symmetric flutter mode shapes, respectively, found at the critical wind speed, where the damping ratio of the particular mode is zero. It can be observed that these mode shapes appear to be

primarily a combination of the similar shaped vertical and torsional modes. In general, the asymmetric flutter mode is the critical mode for a suspension bridge without mid-span cable clamps, while the symmetric flutter mode is critical when cable clamps are used. The cable clamp is a stiff connection between the main suspension cables and the bridge girder and is a well-established method to increase the stability limit of a suspension bridge as it prevents lateral displacement of the cable relative to the girder thereby significantly increasing the frequency of the first asymmetric cable mode and the combination frequency. In the following, the bridge structure without and with mid-span cable clamps will be considered, referred to as System 1 and 2 respectively.

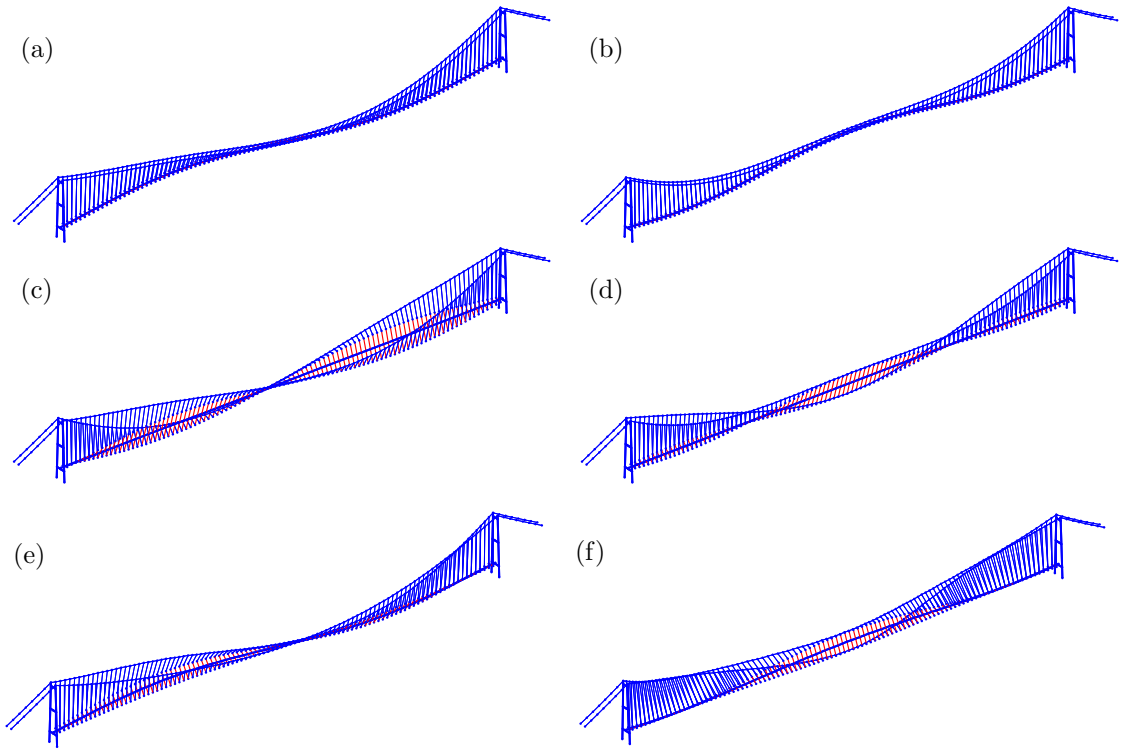

Figure 4.1. Mode shapes: (a) Asymmetric heave, (b) Symmetric heave, (c) Asymmetric torsion, (d) Symmetric torsion, (e) Asymmetric flutter, (f) Symmetric flutter.

The evolution of the modal angular frequency ω and the modal damping ratio ζ are shown as function of the mean wind speed U in Figure 4.2a–b for System 1 without a cable clamp. The modal parameters are shown for wind speeds in the interval around the critical wind speed $U_{cr,1} = 57.4\,\mathrm{m/s}$, which is the wind speed where the damping ratio of the most critical mode becomes zero and the system becomes unstable. The first antisymmetric and first symmetric vertical modes are referred to as AH1 and SH1 and the first antisymmetric and first symmetric torsional modes are referred to as AT1 and ST1. The frequencies of the heave modes are lower than the frequencies of the torsional modes and the frequencies of the antisymmetric modes are lower than the symmetric modes. Considering the damping ratios, the modes starting out as heave modes at zero wind speed experience higher damping for increasing wind speeds. However, original torsional modes are experiencing very low damping corresponding to the structural damping [30], and at the critical wind speed the damping coefficient of the original antisymmetric torsional

mode is zero. Finally, it is found that the symmetric mode becomes unstable at a wind speed 20% higher than the critical wind speed. This shows that a damping system needs to target both the antisymmetric and the symmetric modes in order to increase the stability limit of the system by more than 20%.

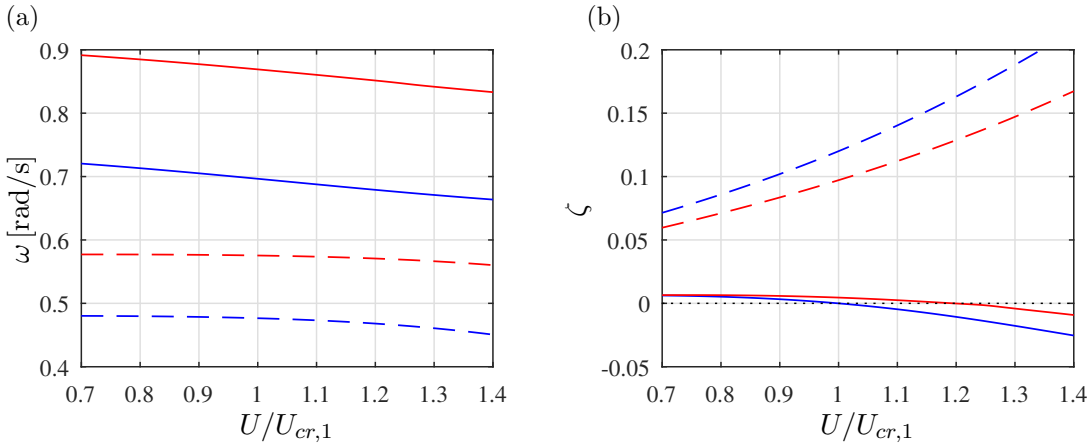

Figure 4.2. System 1: (a) Frequencies, (b) Damping ratio. — — AH1, — — SH1, — AT1, — ST1.

The evolution of the modal parameters of System 2 with mid-span cable clamps are shown in Figure 4.3a–b. For System 2 the modes have shifted so the frequencies and damping ratios of the symmetric modes are now lower than the frequencies and damping ratios of the antisymmetric modes. Thereby, the symmetric flutter mode is now the critical mode experiencing zero damping at a critical wind speed $U_{cr,2} = 1.2U_{cr,1}$, while the asymmetrical motions become unstable at a wind speed 40% higher than the critical wind speed.

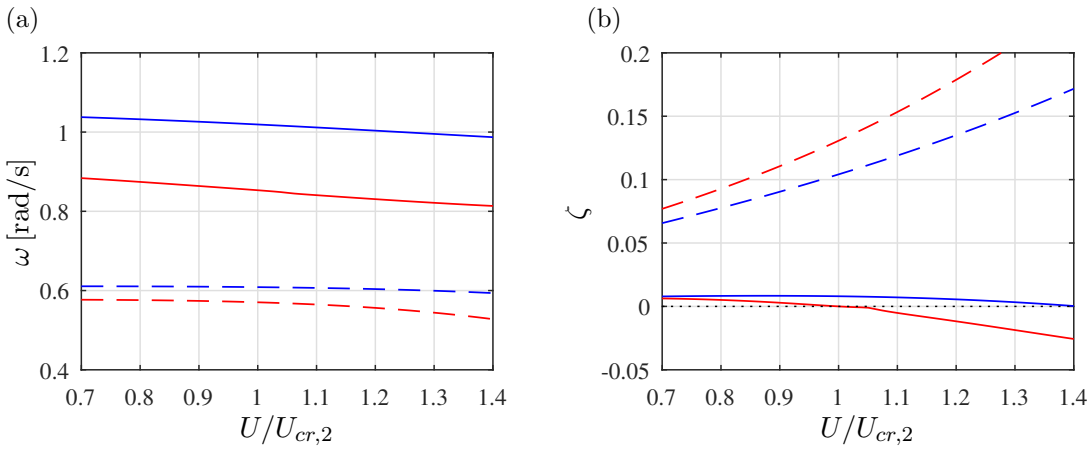

Figure 4.3. System 2: (a) Frequencies, (b) Damping ratio. — — AH1, — — SH1, — AT1, — ST1.

4.2 Damping system concept

Considering the four still-air modes shown in Figure 4.1a–d, the vertical deck motions are related to in-phase motion of the suspension cables while the torsional deck motions are related to out-of-phase motions of the suspension cables. Thereby, both the antisymmetric vertical and torsional deck motions are governed by the first antisymmetric cable mode,

shown in Figure 4.4a, and both the symmetric vertical and torsional deck motions are governed by the first symmetric cable mode, shown in Figure 4.4b. All modes of main interest in relation to aerodynamic instability of the bridge can thereby be addressed by four dampers placed in a double-symmetric setup, working on the relative motion of the main suspension cables and the pylons. The distance between the attachment point on the pylon and on the suspension cable is relatively long wherefore a connection via a pre-tensioned cable is considered. The cable connection only transfers tension forces and thus the viscous damper needs to be placed in parallel with a pre-tensioned spring.

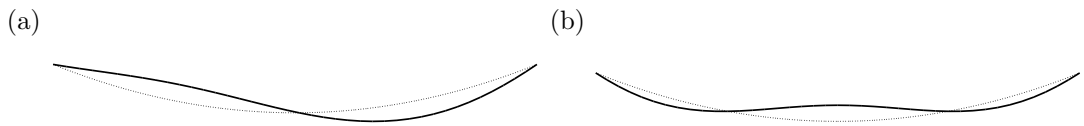

Figure 4.4. Cable modes: (a) Antisymmetric mode, (b) Symmetric mode.

A conceptual sketch of the single-span suspension bridge including the external spring-dampers is shown in Figure 4.5. The system consists of four equally tuned and symmetrically located devices with spring stiffness k and damping coefficient c. The pre-tensioned cable connecting the device to the suspension cable is not shown in the sketch.

Figure 4.5. External device positioning (distorted geometry).

In [P3], a detailed explanation of the interaction between the external devices and the structural model is provided and the result is here summarized. The external spring-damper devices can in the numerical model be introduced via an additional damping matrix $\mathbf{C}_d$ and an additional stiffness matrix $\mathbf{K}_d$ found as a sum of the damping and stiffness contribution of each of the four devices

$$\mathbf{C}_d = c \sum_j \mathbf{w}_j \mathbf{w}_j^T, \quad \mathbf{K}_d = k \sum_j \mathbf{w}_j \mathbf{w}_j^T. \tag{4.1}$$

Here $\mathbf{w}_j$ is the connectivity vector of device $j = 1, ..., 4$ providing the location of the external device in the global model. The connectivity vectors contain zeros at all degrees of freedom unrelated to the device attachment nodes and can be found in terms of the nodal connectivity vectors $\mathbf{w}_A$ and $\mathbf{w}_B$, where index A and B refer to the structural nodes connected by the device as shown in Figure 4.5

$$\mathbf{w}_j^T = \left[\cdots, \mathbf{w}_{A_j}^T, \cdots, \mathbf{w}_{B_j}^T, \cdots \right], \quad \mathbf{w}_A = -\mathbf{w}_B = \frac{\mathbf{x}_{AB}}{\|\mathbf{x}_{AB}\|}. \tag{4.2}$$

The dots in the global connectivity vectors indicate zeros. The nodal connectivity vectors have unit length and provide the direction of the damper force in the particular structural node. The damper force at the points A and B are of opposite sign and the direction

are found by the vector connecting the two points $\mathbf{x}_{AB}$. The efficacy of the damping system now depends on the device configuration giving the position of the dampers and a subsequent calibration of the parameters c and k.

4.3 Device calibration

The calibration of the damping and stiffness parameters c and k is based on the two-component subspace method developed in [54]. The method provides a direct expression for tuning of the damping system for optimal damping of a single mode and is applicable when the included external devices do not introduce substantial changes to the considered mode. The presented damping system is targeting the four modes of main interest in relation to unstable flutter motions and a simple tuning procedure is to target optimal tuning of a single mode and subsequently check the utilization of the damping potential of the other modes of interest. The two-component subspace method rests upon the assumption that the modal displacements $\mathbf{q}(t)$ can be expressed as a linear combination of the mode shape vector of the free system without any external damping $\mathbf{u}_0$ and the mode shape of the system including external devices in a locked state $\mathbf{u}_\infty$ obtained by either letting the spring stiffness or the damping coefficient go toward infinity

$$\mathbf{q}(t) = \mathbf{u}_0\xi_0(t) + \mathbf{u}_\infty\xi_\infty(t). \tag{4.3}$$

The response variable ξ_0 and ξ_∞ determine the magnitude of the contribution from each mode. The representation is illustrated in Figure 4.6 for the first antisymmetric cable mode.

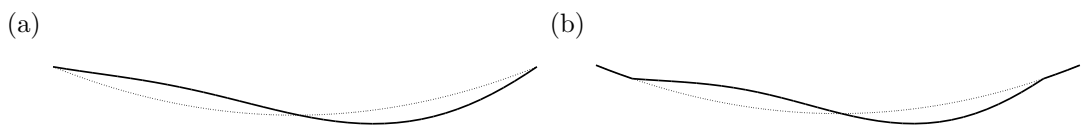

Figure 4.6. First antisymmetric mode shape: (a) Without dampers $\mathbf{u}_0$, (b) Clamped dampers $\mathbf{u}_\infty$.

The derivation of a relation between the system frequency ω and the frequency response function $H(\omega)$ of the damping system is found in [54] and given in a short form in [P3]. For small damping ratios where $\Delta\omega_\infty \ll \omega_0$ an asymptotic relation can by applied with good accuracy [54]. Here ω_0 is the angular frequency of the free system and $\Delta\omega_\infty = \omega_\infty - \omega_0$ is the frequency shift between the clamped mode and the free mode. The asymptotic relation is given as

$$\frac{\Delta\omega}{\Delta\omega_\infty} \simeq \frac{i\eta}{1+i\eta}, \quad \eta = \frac{1}{i}\frac{H(\omega)}{\omega_\infty^2 - \omega_0^2}. \tag{4.4}$$

Here $\Delta\omega = \omega - \omega_0$ is the frequency change from the free mode to the damped mode and η is a non-dimensional damping parameter. For the parallel spring-damper the frequency response function is found as a contribution from the viscous damper and from the spring. For tuning of the external devices, the structural damping is neglected whereby the frequencies ω_0 and ω_∞ as well as their corresponding mode shapes are real valued. As discussed in [43] the tuning of the viscous damper in a parallel spring-damper setup can be carried out by including the spring as part of the free structure as this will only introduce a frequency shift of ω_0 to new real valued frequency ω_k now serving as the new

free mode frequency. For viscous dampers, the damping parameter η can be written in terms of the damping coefficient c as

$$\eta = \frac{\omega}{\omega_\infty + \omega_0} \frac{c \sum_j u_j^2}{\Delta\omega_\infty} \simeq \frac{c \sum_j u_j^2}{2\Delta\omega_\infty}, \tag{4.5}$$

where $u_j = \mathbf{w}_j^T \mathbf{u}_0$ is the relative modal displacement of the attachment nodes of device j for a unit modal mass normalization. For this result, the frequency is characterized by a semicircular trace in the complex plan as illustrated in Figure 4.7a. The dashed semi-circle represents the system with viscous damping, and the solid semi-circle represents a system with a parallel spring-damper. In this particular case, the stiffness of the spring is set to provide a 10% reduction of the frequency interval $\Delta\omega_\infty$. Figure 4.7b shows the corresponding damping curves. Reduction of the frequency interval $\Delta\omega_\infty$ yields a reduction of the maximal imaginary part, whereby a smaller damping ratio $\zeta = \mathrm{Im}[\omega]/|\omega|$ of a particular mode can be obtained. The chosen stiffness of the springs in the damping system is thereby a trade-off between an acceptable reduction of the maximal damping ratio and an appropriate stiffness to account for the pre-tensioning of the system.

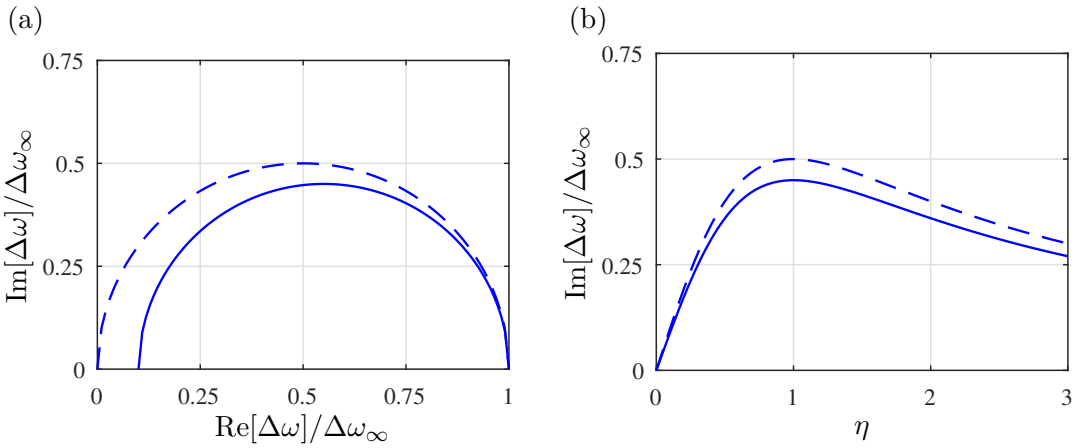

Figure 4.7. (a) Complex root locus, (b) Normalized damping. Without spring (– –), parallel spring (–).

The maximal damping is found approximately at the top of the semi-circle corresponding to $\eta = 1$, and can be found from geometrical considerations as

$$\zeta^{\max} \simeq \frac{\omega_\infty - \omega_0}{\omega_\infty + \omega_0}, \tag{4.6}$$

The semi-circular shape of the frequency trace yields a rather high utilization of a particular mode for $0.25 \lesssim \mathrm{Re}[\Delta\omega]/\Delta\omega_\infty \lesssim 0.75$. The damping ratios of other modes can be estimated by $\zeta = \mathrm{Im}[\omega]/|\omega| \simeq \mathrm{Im}[\omega]/\omega_0$ with the frequency ω expressed by (4.4), whereby

$$\zeta \simeq \frac{\Delta\omega_\infty}{\omega_0} \frac{\eta}{1+\eta^2}. \tag{4.7}$$

The maximum damping potential of each mode is thereby determined by the frequency shift introduced by locking of the spring-damper devices relative to the model frequency, while the utilization of the damping potential is determined by the damping parameter η.

4.4 Effect of the damping system

The efficacy of the damping system is here discussed based on results obtained for the idealized damping system assuming a rigid connecting cable. The devices are attached to the suspension cable at a horizontal distance from the pylon equal to 3% of the span length, which for a cable with sag would provide a damping ratio of approximately 3% for the first antisymmetric mode [42]. Figure 4.8a shows the frequency traces of all four still-air modes of System 1, normalized by the undamped frequency of the respective mode and thereby providing an estimate of the damping ratios. Figure 4.8b shows the corresponding damping curves. The different sizes of the frequency traces and damping curves illustrate the varying damping potential of the four modes with the antisymmetric modes having the highest and the symmetric modes having the lowest damping potential. The asymptotically estimated frequencies are marked with blue circles for a spring stiffness $k = 1.091 \cdot 10^6$ N/m corresponding to a frequency shift of 10% and a damping coefficient $c = 14.556 \cdot 10^6$ kg/s providing optimal damping of the first asymmetric torsional mode. It is found that the damping ratio obtained for each of the four modes are close to the maximum damping of the particular mode. The red crosses mark the frequencies obtained with the numerical model, indicating that the explicit two-component calibration approach is indeed sufficiently accurate for the considered problem.

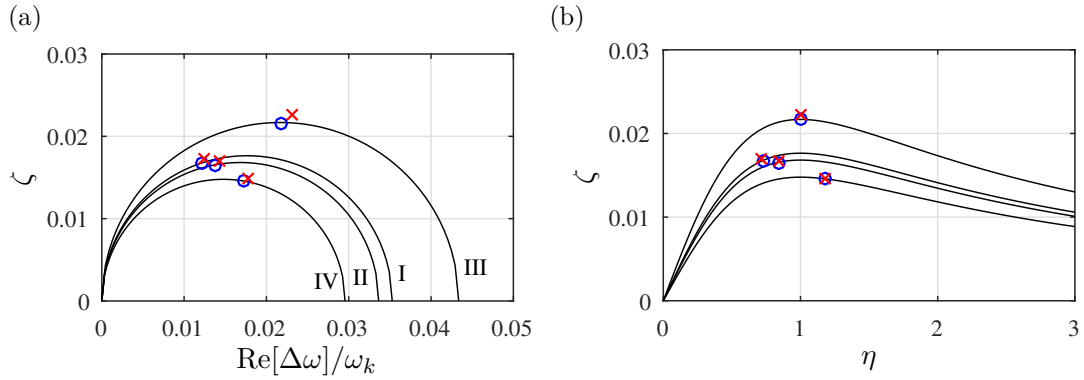

Figure 4.8. Common normalization of design curves: (a) Frequency trace (b) Damping curve. AH1(I), SH1(II), AT1(III), ST1(IV).

The evolution of the frequency and the damping ratio as function of the normalized mean wind speed of the first antisymmetric torsional mode of System 1 without mid-span cable clamps is shown in Figure 4.9. The black dashed curves indicate the reference results of the undamped system and the blue and gray curves are the frequencies and damping ratios obtained for the system including external damping, with optimal tuning of each of the four still-air modes. As expected, the frequency of the system with external damping is shifted relative to the reference frequency. Also, the damping ratio is shifted significantly which results in an increase of the critical wind speed of around 41% to 43% depending on the calibration input. The blue curve corresponds to optimal tuning of the first symmetric heave mode and provides the largest stability increase. However, optimal tuning of each of the four modes provides almost equal stability improvement, corresponding well with the results shown in Figure 4.8, where the damping ratio of all four modes was relatively close to optimal.

The effect of the damping system on the stability limit on System 2 with mid-span cable clamps is shown in Figure 4.10a–b. The black dashed curves mark the frequency

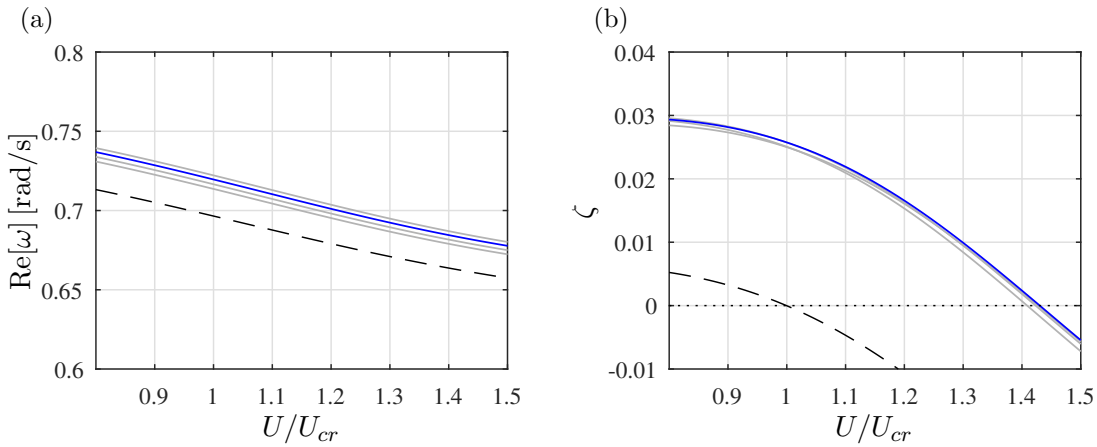

Figure 4.9. System without cable clamp: (a) Frequency, (b) Damping ratio of mode AT1 (III) as function of mean wind speed. (−−) undamped, (−,−) damped.

and damping evolution of the first symmetric mode for the reference system without external damping. The red and gray curves represent the corresponding results for the system including external damping with optimal tuning of each of the four still-air modes. These curves are split into two due to an aero-elastic phenomenon, where the frequency of two modes approach each other for increasing wind speeds. Close to an actual intersection the modes start to behave similarly whereupon they switch roles for higher wind speed. The second mode that appears in the plot is unaffected by the damping system indicating that it is a drag mode. As for System 1 the damping ratio is seen to be shifted significantly resulting in an increase of the critical wind speed of around 27% to 28% depending on the tuning. The red curve corresponds to optimal tuning of the first antisymmetric mode and provides optimal stability conditions, but again the chosen tuning has little influence on the stability increase.

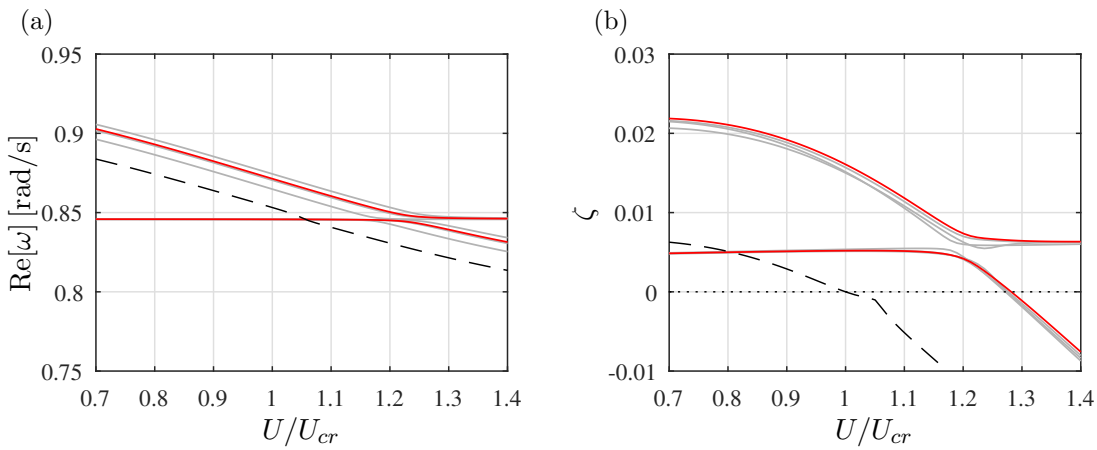

Figure 4.10. System with cable clamp: (a) Frequency, (b) Damping ratio of mode ST1 (IV) as function of mean wind speed. (−−) undamped, (−,−) damped.

The presented results show that the damping system of four symmetrically located, equally tuned spring-damper devices is indeed capable of damping the modes included in unstable flutter motions. The system without mid-span cable clamps experienced a larger relative increase of the stability limit, which corresponds well with the damping

potential of each of the four still-air modes shown in Figure 4.8. Here it was found that the damping potential of the antisymmetric modes, which are the most critical modes for flutter instability of the system without mid-span cable clamps, was higher than the symmetric modes most critical for the instability motions of the system with mid-span cable clamps.

In [P3] more perspectives of the damping system efficacy are considered. This includes a parametric study of the configuration of the system devices in terms of their attachment point on the suspension cables and on the pylons. The different configurations considered are shown in Figure 4.11. The study showed that attaching the device to the suspension cable with a larger distance to the pylon would improve the effectiveness of the damping system, as expected. However, this comes at a cost of a longer connecting cable, which requires a larger cross-section area as well as a larger pre-tension force in order to provide a large cable stiffness relative to the spring stiffness. Shifting the attachment point on the pylon was seen to have a limited effect on the effectiveness of the damping system, wherefore it was concluded that the damper attachment point on the pylon should be chosen to limit the length of the connecting cable while still providing an effective system.

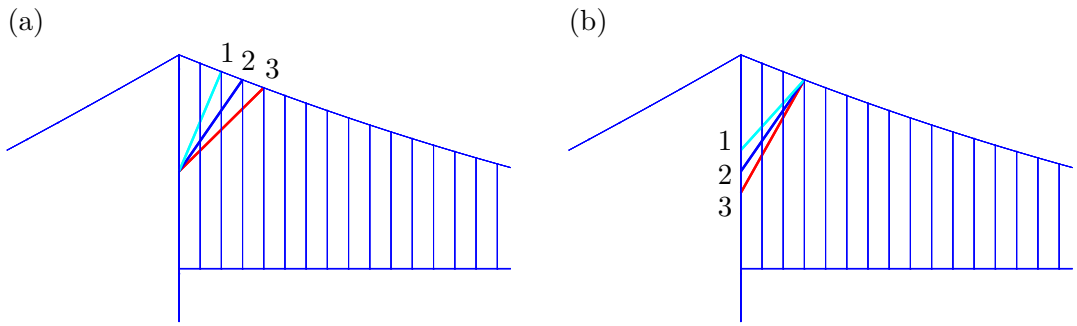

Figure 4.11. Damper configuration: (a) cable attachment, (b) tower attachment.

The influence of cable flexibility was also considered for a realistic design case. The idealized system with an infinitely stiff connecting cable can be considered as an upper limit result. Taking the cable flexibility into account will therefore lower the effectiveness of the damping system. However, a higher ratio between the stiffness of the connecting cable and the spring will improve the effectiveness. The stiffness of the connecting cable was considered by the so-called Dischinger formula [22, 16], where an equivalent stiffness modulus of the cable is evaluated based on the weight of the cable, the horizontal length, and the pre-tension. Attaining a high cable stiffness thereby demands a certain amount of pre-tension which is obtained by an initial deformation of the spring. In the case of a stiffness ratio of 20 between the connecting cable and the spring, a reduction of the stability limit of 7.4% was found compared to the stability limit of the damped system with an infinitely stiff cable. The design parameters of the connecting cable and the spring-damper devices are presented in [P3]. Here, the efficacy of the damping system is also evaluated in relation to the buffeting response. The response is evaluated based on a realistic turbulence representation [P1], and taking into account the self-excited forces [P2]. The damping system was found to provide a significant reduction of the torsional response, while the vertical and lateral response were only slightly affected.

5. Conclusions

The work conducted within the field of aerodynamic stability and the response of long-span bridges has been summarised. The presentation was divided into three chapters addressing: wind field simulation, bridge aerodynamics, and external damping of long-span suspension bridges. The first chapter described the conditional mean field wind simulation procedure presented in [P1] as an efficient and flexible alternative to existing simulation methods. The conditional mean field method is an auto-regressive procedure, where the coefficient matrices are calibrated explicitly from the covariance relations of the wind field. The quality of the simulated wind field depends on the 'memory layout' chosen for the calibration. The memory layout, which is the number of auto-regressive terms and the distribution of these, spatially and time-wise, is discussed in [P1] for a square area as well as a line-like configuration used as focus in the present summary with a simulation example with 603 simulated components. It was shown that an exponential memory layout with exponential base 2 and a modest number of nine memory terms were appropriate to obtain a very accurate representation of the target spectral properties of the wind field. Simulation results presented in [P1] show that a simulated wind field with a simple single-step memory layout with equal depth provides results of equal quality. However, this simulation needs a number of 256 auto-regressive terms, and as the computational speed is proportional to the number of auto-regressive terms, the exponential memory layout offers an approximately 30 times faster simulation. The simulation example provides the estimated auto-spectral densities for all three wind components at three different locations in the simulation cross plane, and it was found that all components independent of the location were equally well represented. The cross-field coherence estimated from simulation records of horizontally separated along wind and vertical components for three different separation length was shown to correspond well with the theoretical results. The simulated wind field was thereby shown to reproduce a consistent turbulence format where the coherence even for low frequencies is less than one.

Chapter 2 described the representation of aero-elastic forces via a rational function approximation. The aero-elastic forces were represented on a form with instantaneous terms proportional to the displacement, velocity, and acceleration as well as a number of non-instantaneous terms, referred to as memory terms and described by their own convolution integrals with an exponential kernel. Hereby, the memory terms can be included as additional state-variables in the equation of motion on a first order state-space format. Also, a procedure presented in [P2] for identification of the aerodynamic coefficient matrices in the representation of the aero-elastic forces from the aerodynamic derivatives was described. The identification procedure is based on a least squares solution of an over-determined equation system. The representation of the aero-elastic forces with zero, one, and two memory terms was compared to flat plate results. It was found that a representation with a single memory term and especially with two memory terms reproduced the flat plate

results very accurately. Furthermore, the generalisation of the momentum-based time integration method to include aero-elastic forces was discussed, and the implementation and the model condensation of a 3000 metre suspension bridge was described. The model was reduced by quasi-static condensation and it was shown that in the present model a 1:5 reduction was able to reproduce a five-minute time response record with high accuracy and a significant time saving. The established model was used to obtain results for full structural loading and to evaluate the influence of the wind load correlation on the response based on an anisotropic full-field turbulence representation obtained by equivalent stretching of an isotropic field [P1,P2]. It was found that full structural loading in comparison with deck loading resulted in a significantly higher lateral response, while the vertical and torsional response were similar. Finally, as expected, the response was found to be strongly dependent on the along bridge turbulence length scale, and it was found that a doubling of the length scale would result in an approximately 50% response increase.

In Chapter 3 the damping system presented in [P3] was described. The damping system consists of four equally tuned symmetrically located devices working on the relative displacement between the pylons and the main suspension cables. Each device consists of a viscous damper and a spring in parallel connected to the structure via a pre-tensioned cable. The tuning of the damping system is based on the asymptotic results to a two-component subspace approximation with still-air modes as calibration input and the simple procedure was seen to provide very accurate results. Furthermore, it was shown that the system of four symmetrically located identical dampers is able to damp all the four modes related to instability of the bridge effectively. The damping system was considered for two different suspension bridge concepts: firstly, a single span suspension bridge without mid-span cable clamps where the critical flutter mode is governed primarily by the first antisymmetric torsional and vertical modes, and, secondly, a single span suspension bridge including a mid-span cable clamp, where the critical flutter mode is governed primarily by the first symmetric torsional and vertical modes. It was shown that the damping system is able to provide a 40% increase of the stability limit for the system without cable clamps and a 28% increase for the system including cable clamps, when assuming an infinitely stiff connecting cable attached to the suspension cable at a distance from the pylon equal to 3% of the span length. Finally, the influence of the device configuration and the cable flexibility on the stability limit were discussed, and it was concluded that higher damping could be obtained by shifting the anchorage point on the suspension cable further away from the pylon. However, this comes at a cost of a longer connection which requires a thicker connecting cable and larger pre-tension forces. Shifting the anchorage point on the pylon has limited effect.

The developed wind field simulation method as well as the computational methods described in relation to bridge aerodynamics constitute essential contributions in an efficient numerical evaluation of the time domain response of long-span bridges. The wind simulation method is based on a full-field description of the wind turbulence in which the correlations between various points in a three-dimensional field are described. In [P1], a stretched isotropic turbulence field is presented, by which a consistent three-dimensional field with three different length scales and corresponding turbulence intensities can be represented and simulated. For practical application it is of interest to develop a full anisotropic turbulence description that allows for independent scaling of three length scales and three turbulence intensities. However, for a horizontal line field simulation, which in many cases

is appropriate for loading of bridge structures as discussed in [P2], the along wind and vertical wind components are most often considered uncorrelated, whereby single component field simulations can be applied to obtain independent scaling of the relevant length scales and turbulence intensities. The described damping system was shown to provide a significant increase of the stability limit of long-span suspension bridges, and in [P3] realistic design parameters of the connecting cable and the spring-damper units were presented, and it was demonstrated that the damping system is indeed a viable solution to suppress unstable flutter motion. It is likely that this damping system can be further improved by replacing the damping units by resonant damping devices including an inerter element.

References

[1] K. Aas-Jakobsen, E. Strømmen, Time domain buffeting response calculations of slender structure. *Journal of Wind Engineering and Industrial Aerodynamics*, **89**, 341–364, 2012.

[2] K.N. Bakis, M. Massaro, M.S. Williams, D.J.N. Limebeer, Aeroelastic control of long-span suspension bridges with controllable winglets, *Structural Control and Health Monitoring*, **23**, 1417–1441, 2016.

[3] G.K. Batchelor, *The Theory of Homogeneous Turbulence*, Cambridge University Press, Cambridge, UK, 1953.

[4] B.A. Benowitz, G. Deodatis, Simulation of wind velocity on long span structures: A novel stochastic wave based model, *Journal of Wind Engineering and Industrial Aerodynamics*, **147**, 154–163, 2015.

[5] C. Borri, C. Costa, Quasi-steady analysis of a two-dimensional bridge deck element, *Journal of Computers and Structures* **82**, 993–1006, 2004.

[6] Y. Cao, H. Xiang, Y. Zhou, Simulation of stochastic wind velocity field of long-span bridges, *Journal of Enginering Mechanics*, **126**, 1–6, 2000.

[7] L. Caracoglia, N.P. Jones, Time domain vs. frequency domain characterization of aeroelastic forces for bridge deck sections, *Journal of Wind Engineering and Industrial Aerodynamics*, **91**, 371–402, 2003.

[8] L. Carassale, G. Solari, Monte Carlo simulation of wind velocity fields on complex structures, *Journal of Wind Engineering and Industrial Aerodynamics*, **94**, 323–339, 2006.

[9] L. Carassale, G. Solari, F. Tubino, Proper orthogonal decomposition in wind engineering. Part 2: Theoretical aspects and some applications, *Wind and Structures*, **10**, 177–208, 2007.

[10] A. Casalotti, A. Arena, W. Lacarbonara, Mitigation of post-flutter oscillations in suspension bridges by hysteretic tuned mass dampers, *Engineering Structures*, **69**, 62–71, 2014.

[11] F. Casciati, F. Giuliano, Performance of multi-TMD in the towers of suspension bridges, *Journal of Vibration and Control*, **15**, 821–847, 2009.

[12] X. Chen, M. Matsumoto, A. Kareem, Time domain flutter and buffeting response analysis of bridges, *Journal of Engineering Mechanics*, **126**, 7–16, 2000.

[13] X. Chen, A. Kareem, Efficacy of tuned mass dampers for bridge flutter control, *Journal of Structural Engineering - ASCE*, **129**, 1291–1300, 2003.

[14] X. Chen, A. Kareem, Proper orthogonal decomposition-based modeling, analysis, and simulation of dynamic wind load effects on structures, *Journal of Enginering Mechanics*, **131**, 325–339, 2005.

[15] J. Chung, G.M. Hulbert, A time domain algorithm for structural dynamics with improved numerical dissipation - the generalized-α method. *Journal of Applied Mechanics*, **60**, 371–375, 1993.

[16] P. Croce, Non-linear behavior of heavy stays, *International Journal of Solids and Structures*, **50**, 1093–1107, 2013.

[17] A.G. Davenport, The prediction of the response of structures to gusty wind, in *Safety of Structures under Dynamic Loading*, eds. I. Holand, D. Kavlie, G. Moe and R. Sigbjörnsson, Tapir, Trondheim, 257–284, 1977.

[18] G. Deodatis, Simulation of ergodic multivariate stochastic processes, *Journal of Enginering Mechanics*, **122**, 778–787, 1996.

[19] M. Di Paola, Digital simulation of wind field velocity, *Journal of Wind Engineering and Industrial Aerodynamics*, **74-76**, 91–109, 1998.

[20] M. Di Paola, I. Gullo, Digital generation of multivariate wind field processes, *Probabilistic Engineering Mechanics*, **16**, 1–10, 2001.

[21] M. Di Paola, M. Zingales, Stochastic diferential calculus for wind-exposed structures with auto-regressive continuous (ARC) filters, *Journal of Wind Engineering and Industrial Aerodynamics*, **96**, 2403–2417, 2008.

[22] F. Dischinger, Hängebrücken für schwerste Verkehrslasten (I and II), *Der Bauingenieur*, **24**(3/4), 65–75, 107–113, 1949. (in German)

[23] W. Eversman, A. Tewari, Modified exponential series for the Theodorsen function, *Journal of Aircraft*, **28**, 553–557, 1991.

[24] A. Fenerci, O. Øiseth, Measured buffeting response of a long-span suspension bridge compared with numerical predictions based on design wind spectra, *Journal of Structural Engineering*, **143**, 04017131 (pp. 15), 2017.

[25] A. Fenerci, O. Øiseth, Strong wind chracteristics and dynamic response of a long-span suspension bridge during a storm, *Journal of Wind Engineering and Industrial Aerodynamics*, **172**, 116–138, 2018.

[26] Forth Replacement Crossing (Queensferry Crossing), Principal Contract for the Design, Construction and Completion of the Forth Replacement Crossing, Employer's Requirements, TS/MTRIPS/WKS/2009/02, Transport Scotland (2011).

[27] M. Géradin, D.J. Rixen, *Mechanical Vibrations – Theory and Application to Structural Dynamics, Third Edition*, Wiley, Chichester, U.K. (2015).

[28] M. Gu, C.C. Chang, W. Wu, H.F. Xiang, Increase of critical flutter wind speed of long-span bridges using tuned mass dampers, *Journal of Wind Engineering and Industrial Aerodynamics*, **73**, 111–123, 1998.

[29] M. Gu, S.R. Chen, C.C. Chang, Control of wind-induced vibrations of long-span bridges by semi-active lever-type TMD, *Journal of Wind Engineering and Industrial Aerodynamics*, **90**, 111–126, 2002.

[30] S.O. Hansen, R.G. Srouji, B. Isaksen, K. Berntsen, Vortex-induced vibrations of streamlined single box girder bridge decks. *14th International Conference on Wind Engineering*, Porto Alegra, Brazil, June 21–26, 2015.

[31] P. Hémon, F. Santi, Simulation of a spatially correlated turbulent velocity field using biorthogonal decomposition, *Journal of Wind Engineering and Industrial Aerodynamics*, **95**, 21–29, 2007.

[32] J.R. Høgsberg, J. Krabbenhøft and S. Krenk, State space representation of bridge deck aeroelasticity, 13'th Nordic Seminar on Computational Mechanics (NSCM-13), Oslo University, Norway, 109–112, (2000).

[33] J.R. Høgsberg, *Aerodynamics of Bridge Decks*, M.Sc. thesis, Department of Mechanical Engineering, Technical University of Denmark, 2002.

[34] G. Huang, H. Liao, M. Li, New formulation of Cholosky decomposition and applications in stochastic simulation, *Probabilistic Engineering Mechanics*, **34**, 40–47, 2013.

[35] A. Jain, N.P. Jones, R.H. Scanlan, Effect of modal damping on bridge aeroelasticity, *Journal of Wind Engineering and Industrial Aerodynamics*, **77-8**, 421–430, 1998.

[36] A. Kareem, Numerical simulation of wind effects: A probabilistic perspective, *Journal of Wind Engineering and Industrial Aerodynamics*, **96**, 1472–1497, 2008.

[37] T. von Kàrmàn, Progres in the statistical theory of turbulence, *Proceedings of the National Academy of Science*, **34**, 530–539, 1948.

[38] H. Kobayashi, H. Nagaoka, Active control of flutter of a suspension bridge, *Journal of Wind Engineering and Industrial Aerodynamics*, **41**, 143–151, 1992.

[39] R. Körlin, U. Starossek, Wind Tunnel test of an active mass damper for bridge decks, *Journal of Wind Engineering and Industrial Aerodynamics*, **95**, 267–277, 2007.

[40] S. Krenk, Wind field coherence and dynamic wind forces. *IUTAM Symposium on Advances in Nonlinear Stochastic Mechanics*, (eds. A. Naess, S. Krenk), Kluwer, Dordrecht, 269–278, 1996.

[41] S. Krenk, Wind field coherence and dynamic wind forces. *IUTAM Symposium on Advances in Nonlinear Stochastic Mechanics*, (eds. A. Naess, S. Krenk), Kluwer, Dordrecht, 269–278, (1996).

[42] S. Krenk, S.R.K. Nielsen, Vibration of a shallow cable with a viscous damper, *Proceedings of the Royal Society A*, **458**, 339–357, 2001.

[43] S. Krenk, J.R. Høgsberg, Damping of cable by a transverse force, *Journal of Engineering Mechanics – ASCE*, **131**, 340–348, 2005.

[44] S. Krenk, Extended state-space time integration with high-frequency energy dissipation, *International Journal for Numerical Methods in Engineering*, **73**, 1767–1787, 2008.

[45] S. Krenk, *Non-linear Modeling and Analysis of Solids and Structures*, Cambridge University Press, Cambridge, U.K. (2009).

[46] S. Krenk, Explicit calibration and simulation of stochastic fields by low-order ARMA processes. *COMPDYN 2011. ECCOMAS Thematic Conference on Computational Methods in Structural Dynamics and Earthquake Engineering*, (eds. M. Papadrakakis, M. Fragiadakis, V. Plevris), paper 550, 1–10, 2011.

[47] S. Krenk, Explicit calibration and simulation of stochastic fields by low-order ARMA processes. *COMPDYN 2011. ECCOMAS Thematic Conference on Computational Methods in Structural Dynamics and Earthquake Engineering*, (eds. M. Papadrakakis, M. Fragiadakis, V. Plevris), paper 550, 1–10, 2011.

[48] S. Krenk, R.N. Møller, Turbulent wind field representation and conditional mean simulation, Proceedings of the Royal Society A, **475**: 20180887, 2019.

[49] L. Kristensen, N.O. Jensen, Lateral coherence in isotropic turbulence and in the natural wind, *Boundary Layer Meteorology*, **17**, 353–373, 1979.

[50] Y. Li, A. Kareem, ARMA systems in wind engineering, *Probabilistic Engineering Mechanics*, **5**, 50–59, 1990.

[51] Y. Li, A. Kareem, Stochastic decomposition and application to probabilistic dynamics, *Journal of Enginering Mechanics*, **119**, 162–174, 1995.

[52] K. Li, Y.J. Ge, Z.W. Guo, L. Zhao, Theoretical framework of feedback aerodynamic control of flutter oscillation for long-span suspension bridges by the twin-winglet system, *Journal of Wind Engineering and Industrial Aerodynamics*, **145**, 166–177, 2015.

[53] Y. Li, P. Hu, X. Xu, J. Qiu, Wind characteristics at bridge site in a deep-cutting gorge by wind tunnel tests, *Journal of Wind Engineering and Industrial Aerodynamics*, **160**, 30–46, 2017.

[54] J.A. Main, S. Krenk, Efficiency and tuning of viscous dampers on discrete systems, *Journal of Sound and Vibration*, **286**, 97–122, 2005.

[55] B. Mokrani, Z. Tian, D. Alaluf, F. Meng, A. Preumont, Passive damping of suspension bridges using multi-degree of freedom tuned mass dampers, *Engineering Structures*, **153**, 749–756, 2017.

[56] J. Mann, S. Krenk, Fourier simulation of non-isotropic wind field model. *Proceedings of ICOSSAR '93*, Innsbruck, Austria, August 9-13, 1993, Eds. G.I. Schueller, M. Shinozuka, J.T.P. Yao, Balkema, Rotterdam, Vol.3, pp. 1669-1674, 1994.

[57] J. Mann, Wind field simulation, *Probabilistic Engineering Mechanics*, **13**, 269–282, 1998.

[58] M.P. Mignolet, P.D. Spanos, Recursive simulation of stationary multivariate random processes – Part I, *Journal of Applied Mechanics*, **54**, 674–680, 1987.

[59] M.P. Mignolet, P.D. Spanos, Simulation of homogeneous two-dimensional random fields: Part I – AR and ARMA models, *Journal of Applied Mechanics*, **59**, 260–269, 1992.

[60] R.N. Møller, S. Krenk, M.N. Svendsen, Turbulent wind response of long-span bridges including flutter, Department of Mechanical Engineering, Technical University of Denmark, 2018. (submitted for publication)

[61] Norwegian Public Roads Administration, Statens vegvesen – E39 Sulafjorden K1, Elverum, Norway, Link: https://youtu.be/VUUPLido31Q (2015).

[62] O. Øiseth, A. Rönnquist, R. Sigbjörnsson, Simplified prediction of wind-induced response and stability limit of slender long-span suspension bridges, based on modified quasi-steady theory: A case study. *Journal of Wind Engineering and Industrial Aerodynamics*, **98**, 730–741, 2012.

[63] O. Øiseth, A. Rönnquist, R. Sigbjörnsson, Finite element formulation of the self-exited forces for time-domain assessment of wind-induced dynamic response and flutter stability limit of cable-supported bridges. *Finite Elements in Analysis and Design*, **50**, 173–183, 2012.

[64] F.W.J. Olver, D.W. Lozier, R.F. Boisvert, C.W. Clark, *NIST Handbook of Mathematical Functions*, Cambridge University Press, Cambridge, UK, 2010.

[65] P. Omenzetter, K. Wilde, Y. Fujino, Suppression of wind-induced instabilities of a long span bridge by a passive deck-flaps control system Part I: Formulation, *Journal of Wind Engineering and Industrial Aerodynamics*, **87**, 61–79, 2000.

[66] P. Omenzetter, K. Wilde, Y. Fujino, Suppression of wind-induced instabilities of a long span bridge by a passive deck-flaps control system Part II: Numerical simulations, *Journal of Wind Engineering and Industrial Aerodynamics*, **87**, 81–91, 2000.

[67] L. Peng, G. Huang, A. Kareem, Y. Li, An efficient space-time based simulation approach of wind velocity field with embedded conditional interpolation for unevenly spaced locations, *Probabilistic Engineering Mechanics*, **34**, 40–47, 2013.

[68] Y. Peng, S. Wang, J. Li, Field measurement and investigation of spatial coherence for near-surface strong winds in southeast China, *Journal of Wind Engineering and Industrial Aerodynamics*, **172**, 423–440, 2018.

[69] Rambøll, for the Norwegian Public Roads Administration, Konseptrapport Hengebru i Korridor 1, November 2015.

[70] H. Sato, S. Kusuhara, K. Ogi, H. Matsufuji, Aerodynamic characteristics of super long-span bridges with slotted box girder, *Journal of Wind Engineering and Industrial Aerodynamics*, **88**, 297–306, 2000.

[71] R.H. Scanlan, J.J. Tomko, Airfoil and bridge deck flutter derivatives, *Journal of the Engineering Maechanics Division – ASCE*, **97**, 1717–1737, 1971.

[72] R.H. Scanlan, J.-G. Beliveau, K.S. Budlong, Indicial aerodynamic functions for bridge decks, *Journal of the Engineering Maechanics Division – ASCE*, **100**, 657–672, 1974.

[73] M. Shinozuka, C.-M. Jan, Digital simulation of random processes and its applications, *Journal of Sound and Vibrations*, **25**, 111–128, 1972.

[74] M. Shinozuka, G. Deodatis, Simulation of multidimensional Gaussian stochastic fields by spectral representation, *Applied Mechanics Reviews*, **49**, 29–53, 1996.

[75] G. Solari, L. Carassale, F. Tubino, Proper orthogonal decomposition in wind engineering. Part 1: A state-of-the-art and some prospects, *Wind and Structures*, **10**, 153–176, 2007.

[76] Y. Song, J. Chen, Y.Peng, P.D. Spanos, J. Li, Simulation of nonhomogeneous fluctuating wind speed field in two-spatial dimensions via an evolutionary wavenumber-frequency joint power spectrum. *Journal of Wind Engineering and Industrial Aerodynamics*, **179**, 250–259, 2018.

[77] P.D. Spanos, M.P. Mignolet, Recursive simulation of stationary multivariate random processes – Part II, *Journal of Applied Mechanics*, **54**, 681–687, 1987.

[78] P.D. Spanos, M.P. Mignolet, Simulation of homogeneous two-dimensional random fields: Part II – MA and ARMA models, *Journal of Applied Mechanics*, **59**, 270–277, 1992.

[79] U. Starossek, H. Aslan, Passive control of bridge deck flutter using tuned mass dampers and control surface. *EURODYN 2008. 7th Eurepean Conference on Structural Dynamics*, Southampton, England, July 7-9, 2008.

[80] Statens Vegvesen, *N400 Handbook for Bridge Design*, Elverum, Norway (2009).

[81] G. Stefanou, M. Papadrakakis, Assessment of spectral representation and Karhunen–Loève expansion methods for the simulation of Gaussian stochastic fields, *Computer Methods in Applied Mechanics and Engineering*, **196**, 2465–2477, 2007.

[82] E. Strømmen, *Theory of Bridge Aerodynamics*, Springer, Berlin (2006).

[83] X. Suduo, J.M. Ko, Y.L. Xu, Wind-induced vibration control of bridges using liquid column damper, *Earthquake Engineering and Engineering Vibrations*, **1**, 271–280, 2002.

[84] T. Theodorsen, General theory of aerodynamic instability and the mechanism of flutter, *NACA Report*, **496**, Washington, DC (1934).

[85] K. Wilde, Y. Fugino, Aerodynamic control of bridge deck flutter by active surfaces, *Journal of Engineering Mechanics*, **124**, 718–727, 1998.

[86] W.W. Yang, T.Y.P. Chang, C.C. Chang, An efficient wind field simulation technique for bridges, *Journal of Wind Engineering and Industrial Aerodynamics*, **67-68**, 697–708, 1997.

[87] J.D. Zeng, Z.G. Li, M.S. Li, Coherence of simulated atmospheric boundary-layer turbulence, *Fluid Dynamics Research*, **49**, 2017.

[88] Z. Zhang, Z. Chen, Y. Cai, et al., Indicial functions for bridge aeroelastic forces and time-domain flutter analysis, *Journal of Bridge Engineering*, **16**, 546–557, 2011.

P1

Turbulent wind field representation and
conditional mean-field simulation

Steen Krenk & Randi Nøhr Møller

Proceedings of the Royal Society A,
Vol **475**: 20180887, 2019.

PROCEEDINGS A

royalsocietypublishing.org/journal/rspa

Research

Cite this article: Krenk S, Møller RN. 2019 Turbulent wind field representation and conditional mean-field simulation. *Proc. R. Soc. A* **475**: 20180887.
http://dx.doi.org/10.1098/rspa.2018.0887

Received: 18 December 2018
Accepted: 22 February 2019

Subject Areas:
applied mechanics, computer modelling and simulation, computational mechanics

Keywords:
wind field turbulence, conditional mean simulation, generalized von Kàrmàn spectrum, stretched isotropic turbulence

Author for correspondence:
Steen Krenk
e-mail: sk@mek.dtu.dk

Turbulent wind field representation and conditional mean-field simulation

Steen Krenk[1] and Randi N. Møller[1,2]

[1]Department of Mechanical Engineering, Technical University of Denmark, DK-2800 Kongens Lyngby, Denmark
[2]Rambøll, Hannemanns Alle, DK-2300 Copenhagen, Denmark

SK, 0000-0002-8535-294X; RNM, 0000-0001-8836-4623

The covariance structure of a homogeneous isotropic turbulent wind velocity field is derived in terms of modified Bessel functions for an extended form of the Kàrmàn velocity spectrum, including explicit expressions for the transverse coherence functions. A concept of transformed isotropic turbulence is introduced to account for differences in the axial, transverse and vertical fluctuating wind velocities and length scales in natural wind. A special form of the auto-regressive simulation format is developed for convected turbulence with exponentially increasing intervals to the regression planes. In each step, the wind velocity field in a transverse plane is represented by a conditional mean field and a stochastic contribution determined explicitly by the time–space covariances. Simulation results are presented for a square area of dimension less than the integral length scale, representative of buildings and wind turbines, and a horizontal line of length six times the length scale, representative of a long-span bridge. The simulations demonstrate high accuracy of simulated spectral densities, covariance functions and transverse coherence functions. The simulated results do not show visible dependence on the specific points used for the simulated records. The efficiency and the free simulation point configuration suggest high competitiveness compared to fast Fourier transform-based spectral methods.

1. Introduction

Wind load constitutes an important aspect of the loading of many structures like, e.g. bridges, towers and wind turbines. With increasing structural flexibility, the

THE ROYAL SOCIETY PUBLISHING

fluctuating component of the wind load gains increased importance, and as most modern structures require analysis by numerical models, the simulation of realistic wind fields for calculation of structural loads plays a central role. Also, the requirements of the simulated wind field have increased—from the longitudinal component used with stationary structures, over the longitudinal and vertical components used, e.g. for dynamics of bridge decks, to the fully three-dimensional wind fields needed for wind turbine loads. The simulation models fall largely in two categories: spectral methods, often using fast Fourier transform (FFT) techniques; and sequential models, typically of auto-regressive moving-average (ARMA) type. The wind field properties are typically given in terms of a more or less detailed spectral description, suggesting the use of FFT-based spectral methods. However, transform techniques, and in particular the FFT method, place restrictions on the spatial configuration in the form of regular intervals and rectangular grids, and furthermore the underlying discrete Fourier transform leads to periodic time histories that are not directly amenable to extension by restart of the simulation. By contrast, simulations by recurrence techniques, such as the use of ARMA processes, are computationally extremely efficient and can be continued in a fully consistent manner from a rather small amount of stored data. In the recurrence techniques, the main challenge is the development of efficient calibration techniques that select the number of matrices and their optimal calibration from the desired wind field properties.

A survey of the early development of multi-component spectral simulation, using random phase and direct factorization of the spectral density matrix, has been given by Shinozuka & Deodatis [1]. A multi-component form was presented by Deodatis [2], in which the phase of the different components was offset by sub-increments, thereby creating a longer period of the simulated records. The Fourier technique was used to simulate a fully three-dimensional wind velocity vector field with a perturbation-based anisotropic modification of the isotropic spectral density tensor [3], by Mann & Krenk [4,5], introducing an anti-aliasing frequency filter and Gaussian white noise amplitudes. An alternative factorization of the spectral matrix in terms of frequency-dependent eigenvectors was introduced by Li & Kareem [6]. This format identifies the main contributing modes, and it is suitable for reduction of the number of simulated components. It has been used for simulating turbulent wind loads generated by the longitudinal component by Di Paola [7,8], and for a general discussion of wind simulation techniques by Chen & Kareem [9]. Procedures for reduction of the dimension of the independent simulation input, e.g. by proper orthogonal decomposition (POD) and Karhunen–Loève expansion techniques, have been surveyed by Solari and colleagues [10,11] and Stefanou & Papadrakakis [12]. An interesting extension of the typical spectral procedure, in which the wind field is described in terms of convected turbulence, has been presented by Hémon & Santi [13]. In their procedure, the wind field is represented by a combination of eigen-solutions to the spatial covariance problem as well as eigen-solutions for a temporal covariance problem.

In spite of the generality of the spectral representation and simulation methods, only [4,5] use a fully consistent three-dimensional spectral density, whereas the other papers are based on a representative spectral density, e.g. of the longitudinal component, supplemented by an empirically based transverse coherence function, typically of the exponential form $\exp(-C\omega\Delta y/U)$, introduced by Davenport and discussed, e.g., in [14]. The spectrally based simulation techniques require a factorization of the spectral density matrix, typically by an eigenvector decomposition or by direct triangular matrix product decomposition. In the case of equally spaced simulation points on a line, the exponential representation of the transverse coherence offers the possibility of explicit factorization [15–17], and direct simulation of equally spaced points supplemented by a separate set of points has been considered by Peng *et al.* [18]. In [19], the transverse coherence function for line-based separation was used to construct a time–space-based spectral density and a corresponding FFT formulation. In the exponential coherence format, the combination of the frequency ω and the transverse distance Δy implies that low-frequency components exhibit excessive coherence for large separation distances. Recent measurements of the transverse coherence support the lack of full coherence for low frequencies and large separation [20–22]. A resolution of this problem in terms of alternative coherence

representations was presented in [23], based on the work of Kristensen & Jensen [24] using the von Kàrmàn spectral density, [25].

An alternative to spectral FFT-based simulation methods is constituted by the family of sequential filter-based procedures consisting of auto-regressive (AR), moving average (MA) and the combined auto-regressive moving average (ARMA) models. The time is discretized into finite—typically equal—intervals, and each step consists of generation of a random input vector corresponding to the number of velocity components at any given time, and the formation of the new velocity values as a weighted linear combination of the simulated current white noise components, the white noise components at a set of previous times, and the wind velocities from a set of previous times. Early work on sequential stochastic field simulation was presented by Mignolet & Spanos [26,27]. In this work, as well as in later works on wind field simulation, e.g. [28,29], priority was given to AR and ARMA processes and calibration techniques based on underlying spectral distributions. It turns out that the coefficient matrices in auto-regressive time–space processes can be determined directly from the set of covariance matrices for the velocity components of the current and the regression steps. The key point is the availability of the full time–space covariance matrices. A simple single-step procedure for simulation of convected three-dimensional wind turbulence was presented in [30], and the present paper develops a more accurate multi-step auto-regressive format with coefficient matrices determined explicitly in terms of the two-point covariances of the convected turbulence. The wind velocity covariance is based on convected fully three-dimensional isotropic turbulence using the von Kàrmàn spectral density [25], and a simple scaling procedure is presented for adjusting the length scale and velocity intensity in the axial and transverse directions. The turbulence representation also contains explicit formulae for the transverse coherence functions, and simulation examples demonstrate that these are reproduced faithfully by the proposed method.

2. Representation of isotropic turbulence

The turbulent wind field used in the present paper is represented in the form of convected homogeneous isotropic incompressible turbulence as described by Batchelor [3]. The representation is for a three-dimensional homogeneous stochastic turbulent velocity field that is translated by the mean wind velocity U. When observing the wind field from a fixed point in space, the convected velocity field passes by at the speed U, thereby effecting a replacement of the along-wind coordinate by time, $x_1 = -Ut$. This leads to a compact representation in which the time-invariant spatially three-dimensional field effectively is transformed into a two-dimensional time-dependent field. Clearly this representation is most suitable for scenarios where the spatial distribution is closely represented by a cross-sectional plane. It holds the advantage that turbulence can be represented as a three-dimensional isotropic spatial velocity field. However, this representation also imposes the requirement that the covariance functions of the time histories at a point lead directly to the representation of the transverse spatial structure of the field. Thus the spectral density of the time histories also defines properties like transverse coherence. A simple procedure for representing different length scales in the transverse directions or standard deviations of the transverse velocity components via 'stretched isotropic turbulence' is discussed in §4.

(a) Isotropic correlation functions

A concise summary of the representation of isotropic turbulence is now presented for a 'frozen' three-dimensional isotropic velocity field. It follows from invariance to coordinate transformations that the general form of the covariance tensor $\mathbf{R}(\mathbf{r})$ for the velocity components at two points separated by the vector $\mathbf{r}$ must be a linear combination of the unit tensor $\mathbf{I}$ and the tensor $\mathbf{r}\,\mathbf{r}^{\mathrm{T}}$. The classic form is

$$\mathbf{R}(\mathbf{r}) = \mathrm{E}\big[\,\mathbf{v}(\mathbf{r}_0+\mathbf{r})\mathbf{v}(\mathbf{r}_0)^{\mathrm{T}}\big] = \sigma_v^2\left([f(r)-g(r)]\frac{\mathbf{r}\,\mathbf{r}^{\mathrm{T}}}{\mathbf{r}^{\mathrm{T}}\mathbf{r}} + g(r)\mathbf{I}\right), \tag{2.1}$$

where $r = |\mathbf{r}|$ is the distance between the two points, and σ_v^2 is the variance of a single component at a point. The functions $f(r)$ and $g(r)$ describe the lengthwise and transverse correlation, respectively.

At the typical wind speeds in the natural wind, the flow can be assumed to be incompressible. It then follows from the incompressibility condition $\nabla_{\mathbf{r}}^{\mathrm{T}}\mathbf{v} = 0$ that the correlation functions are related by

$$g(r) = f(r) + \frac{r}{2}\frac{\mathrm{d}}{\mathrm{d}r}f(r) = \frac{1}{2r}\frac{\mathrm{d}}{\mathrm{d}r}\left[r^2 f(r)\right]. \tag{2.2}$$

Thus, the isotropic incompressible stochastic field is described entirely in terms of a single scalar correlation function, e.g. the lengthwise correlation function $f(r)$. The local incompressibility condition (2.2) can be reformulated into an integral condition. Multiplication with r and integration gives

$$\int_0^\infty g(r) r \,\mathrm{d}r = \frac{1}{2}\left[r^2 f(r)\right]_0^\infty = 0, \tag{2.3}$$

where the last equality is satisfied when the upper limit does not contribute. This relation has implications of considerable importance for the representation of correlation. If multiplied by 2π, the left side is simply the integral of the transverse correlation function $g(r)$ over an infinite plane. The result states that for any infinite plane the correlation between a normal component at a selected point and the integral of the normal component over the plane vanishes. Thus, an observation of, e.g., a positive normal component at a point does not lead to a positive expectation of the total flux through the infinite plane. This may seem obvious also for non-isotropic turbulence, but nonetheless most representations of the transverse correlation used in wind engineering violate this condition, typically by assuming the transverse correlation function $g(r)$ in the form of an exponential function. It follows from (2.3) that the transverse correlation $g(r)$ must be negative over an interval large enough to satisfy the integral condition.

(b) Generalized von Kàrmàn representation

The longitudinal and transverse correlation functions are represented via the exponential Fourier transform as

$$\sigma_v^2 f(r) = \int_{-\infty}^{\infty} F(k)\mathrm{e}^{ikr}\,\mathrm{d}k \quad \text{and} \quad \sigma_v^2 g(r) = \int_{-\infty}^{\infty} G(k)\mathrm{e}^{ikr}\,\mathrm{d}k, \tag{2.4}$$

where k is the wavenumber corresponding to the spatial separation r. When used for convected turbulence, the 'frozen' turbulence velocity field is convected with the mean wind velocity U downstream. For convection in the x_1-direction, this defines a relation between the spatial x_1-coordinate and the time t of the form $x_1 = -Ut$, and thus the spatial x_1 variation corresponds to a time history and the corresponding spectral densities are easily scaled to frequency form. In the derivation of the theory and in the following simulations, the three-dimensional formulation in terms of wavenumber and coordinate components is used. Frequency and time records can then be obtained by appropriate scaling of the k_1 and x_1 components.

It is convenient to represent the spectral density function $F(k)$ in terms of the normalized form of the generalized von Kàrmàn spectral density [23],

$$F(k) = \frac{1}{\sqrt{\pi}}\frac{\Gamma(\gamma)}{\Gamma(\gamma - 1/2)}\frac{\sigma_v^2 \ell}{[1 + (k\ell)^2]^\gamma}, \tag{2.5}$$

where $\Gamma(\,)$ is the gamma function, and ℓ is a length scale. The parameter γ controls the asymptotic behaviour of the spectral density for $(k\ell) \to \infty$. Integrability of the spectral density requires $\gamma > 1/2$. According to the Kolmogorov cascade theory, the parameter takes the value $\gamma = 5/6$ as used in the von Kàrmàn spectral density, [25]. Here, γ is kept as a parameter to enable a discussion of the generalized exponential format later. This form of the spectral density is analytically tractable and leads to explicit expressions for the correlation functions $f(r)$ and $g(r)$. Substitution of the

spectral density (2.5) into (2.4a) gives

$$f(r) = \frac{2\ell}{\sqrt{\pi}} \frac{\Gamma(\gamma)}{\Gamma(\gamma - 1/2)} \int_{-\infty}^{\infty} \frac{\cos(kr)}{[1 + (k\ell)^2]^{\gamma}} \, \mathrm{d}k, \tag{2.6}$$

and by 10.32.11 [32] this determines the longitudinal correlation function as

$$f(r) = \frac{2}{\Gamma(\gamma - 1/2)} \left(\frac{r}{2\ell}\right)^{\gamma - 1/2} K_{\gamma - 1/2}\left(\frac{r}{\ell}\right), \tag{2.7}$$

where $K_{\gamma-1/2}(\,)$ is the modified Bessel function of the second kind of order $\gamma - 1/2$.

The transverse correlation function $g(r)$ is now conveniently found by use of the incompressibility condition (2.2). By using the differentiation formula for Bessel functions, 10.6.6 [32],

$$\frac{\mathrm{d}}{\mathrm{d}z}\left(z^{\nu} K_{\nu}(z)\right) = -z^{\nu} K_{\nu-1}(z) \tag{2.8}$$

with $\nu = \gamma - 1/2$ it is found that

$$\frac{r}{2}\frac{\mathrm{d}}{\mathrm{d}r} f(r) = \frac{-2}{\Gamma(\gamma - 1/2)} \left(\frac{r}{2\ell}\right)^{\gamma + 1/2} K_{\gamma - 3/2}\left(\frac{r}{\ell}\right). \tag{2.9}$$

Substitution of this into (2.2) then gives the corresponding transverse correlation function as

$$g(r) = f(r) - \frac{2}{\Gamma(\gamma - 1/2)} \left(\frac{r}{2\ell}\right)^{\gamma + 1/2} K_{\gamma - 3/2}\left(\frac{r}{\ell}\right). \tag{2.10}$$

Thus, the two correlation functions corresponding to a velocity field with the generalized von Kàrmàn spectral density (2.5) are given by (2.7) and (2.10), respectively.

The spectral density $G(k)$ of the transverse covariance can be determined by inverting (2.4) and expressing the transverse correlation function $g(r)$ in terms of the longitudinal correlation function $f(r)$ by using (2.2). The result of this operation is

$$G(k) = \frac{1}{2} F(k) - \frac{1}{2} k \frac{\mathrm{d}}{\mathrm{d}k} F(k). \tag{2.11}$$

In the particular case of the generalized von Kàrmàn spectral density (2.5), this leads to

$$G(k) = \left(\frac{1}{2} + \frac{\gamma (k\ell)^2}{1 + (k\ell)^2}\right) F(k) \tag{2.12}$$

In the limit $k\ell \to \infty$, the asymptotic high wavenumber relation is $G(k) \simeq (\gamma + 1/2) F(k)$.

The turbulence length scale is a representative length over which the turbulent velocity field is correlated. It is defined by

$$\lambda = \int_0^{\infty} f(r) \, \mathrm{d}r. \tag{2.13}$$

Substitution of the lengthwise correlation function $f(r)$ from (2.7) gives

$$\lambda = \frac{2\ell}{\Gamma(\gamma - 1/2)} \int_0^{\infty} \left(\frac{r}{2\ell}\right)^{\gamma - 1/2} K_{\gamma - 1/2}\left(\frac{r}{\ell}\right) \mathrm{d}r = \frac{\Gamma(1/2)\Gamma(\gamma)}{\Gamma(\gamma - 1/2)} \ell, \tag{2.14}$$

where the integral formula 10.43.19 [32] has been used.

3. Transverse coherence

The correlation function of the velocity components at two points gives a measure of statistical dependence of the fluctuations. However, more detailed information can be obtained by considering the individual spectral components associated with any particular frequency. This leads to the introduction of the coherence function of any two velocity components at two separate points. The most direct measure is the cross-spectral density normalized by the square root of the product of the spectral densities of the two velocity components. This is sometimes called the root-coherence, reserving the term coherence for the square of this quantity. However,

in the present context, it is convenient to use the term coherence for the normalized cross-spectral density. Its usefulness is closely linked to the fact that the spectral contributions at various frequencies exhibit different spatial distribution. In connection with a representation of the turbulent velocity field in the form of a convected homogeneous spatial field, only velocities at points with transverse separation retain the spatial coherence characteristics, constituting important components in the classic design of slender structures for wind loads [14].

(a) A scalar potential

When extracting the coherence from the convected velocity field, a full spectral representation of the covariance tensor is needed in the form of the three-dimensional wavenumber integral

$$R_{ij}(\mathbf{x}) = \int_{-\infty}^{\infty}\int_{-\infty}^{\infty}\int_{-\infty}^{\infty} \Phi_{ij}(\mathrm{k})\mathrm{e}^{i\mathrm{k}\cdot\mathrm{x}}\,\mathrm{d}\mathrm{k}. \tag{3.1}$$

In the present context, the velocity field is isotropic and incompressible, and therefore of the form

$$\Phi_{ij}(\mathrm{k}) = \frac{E(k)}{4\pi k^4}\left(k^2\delta_{ij} - k_i k_j\right), \tag{3.2}$$

where δ_{ij} is Kronecker's delta, and $E(k)$ is the energy density in the scalar wavenumber interval $[k, k+dk]$. It turns out to be convenient to express the dependence on the individual components via spatial derivatives in the form

$$R_{ij}(\mathbf{x}) = \left(\frac{\partial^2}{\partial x_i \partial x_j} - \delta_{ij}\frac{\partial^2}{\partial x_l \partial x_l}\right)\Psi(\mathbf{x}), \tag{3.3}$$

where the scalar potential

$$\Psi(\mathbf{x}) = \int_{-\infty}^{\infty}\int_{-\infty}^{\infty}\int_{-\infty}^{\infty} \frac{E(k)}{4\pi k^4}\mathrm{e}^{i\mathrm{k}\cdot\mathrm{x}}\,\mathrm{d}\mathrm{k} \tag{3.4}$$

is a triple integral in terms of $E(k)$.

The energy density function $E(k)$ is closely related to the one-dimensional spectral density $F(k)$ introduced in (2.4). The relation is established, as demonstrated by Batchelor [3], by expressing $F(k_1)$ by the inverse of (2.4), and then introducing $\sigma_v^2 f(x_1) = R_{11}(x_1)$ from (3.1) and (3.2). The final result is

$$E(k) = k^3\frac{\mathrm{d}}{\mathrm{d}k}\left(\frac{1}{k}\frac{\mathrm{d}F(k)}{\mathrm{d}k}\right) = \frac{4}{\sqrt{\pi}}\frac{\Gamma(\gamma+2)}{\Gamma(\gamma-1/2)}\frac{(k\ell)^4\sigma_v^2\ell}{[1+(k\ell)^2]^{\gamma+2}}, \tag{3.5}$$

after substitution of the generalized von Kàrmàn spectral density $F(k)$ from (2.5). Substitution of the energy density function $E(k)$ into (3.4) gives the following expression for the scalar potential:

$$\Psi(\mathbf{x}) = \frac{\sigma_v^2\ell}{\pi^{3/2}}\frac{\Gamma(\gamma+2)}{\Gamma(\gamma-1/2)}\int_{-\infty}^{\infty}\int_{-\infty}^{\infty}\int_{-\infty}^{\infty}\frac{\ell^4}{[1+(k\ell)^2]^{\gamma+2}}\mathrm{e}^{i\mathrm{k}\cdot\mathrm{x}}\,d\mathrm{k}. \tag{3.6}$$

The triple integration is divided into two parts: an integration over the k_2k_3-plane, followed by integration over the axial wavenumber component k_1. The first integration is carried out by transformation into polar components with $k_2x_2 + k_3x_3 = \kappa r\cos\theta$, leading to, 10.9.1 [32],

$$\Psi(x_1, r) = \sigma_v^2\ell\frac{2\ell^2}{\pi^{1/2}}\frac{\Gamma(\gamma+2)}{\Gamma(\gamma-1/2)}\int_{-\infty}^{\infty}\mathrm{e}^{ik_1x_1}\mathrm{d}k_1\int_0^{\infty}\frac{J_0(\kappa r)\ell^2\kappa}{[1+(k_1\ell)^2+(\kappa\ell)^2]^{\gamma+2}}\,\mathrm{d}\kappa, \tag{3.7}$$

where $J_0(\kappa r)$ is the Bessel function of the first kind of order zero, and κ and r are the polar radius in the transverse wavenumber plane and in the transverse physical plane, respectively.

The two first terms in the denominator of the integrand are combined into the form $(\kappa_1\ell)^2$ by introducing the equivalent wavenumber κ_1 by

$$\kappa_1^2 = k_1^2 + \ell^{-2}. \tag{3.8}$$

The integral can then be evaluated by the use of the formula, 10.22.46 [32],

$$\int_0^\infty \frac{J_0(a\,t)\,t}{[\,b^2+t^2]^{\mu+1}}\,\mathrm{d}t = \frac{a^\mu b^{-\mu}}{2^\mu\,\Gamma(\mu+1)} K_{-\mu}(a\,b) \tag{3.9}$$

when identifying the parameters $\mu=\gamma+1$, $t=\kappa\ell$, $a=r/\ell$ and $b=\kappa_1\ell$. This gives the scalar potential (3.7) in the form

$$\Psi(x_1,r) = \frac{2}{\Gamma(\gamma)}\int_{-\infty}^{\infty} F(k_1)\,\frac{1}{\kappa_1^2}\left(\frac{\kappa_1 r}{2}\right)^{\gamma+1} K_{\gamma+1}(\kappa_1 r)\mathrm{e}^{ik_1x_1}\,\mathrm{d}k_1, \tag{3.10}$$

when the longitudinal spectral density $F(k_1)$ is introduced from (2.5) as

$$F(k_1) = \frac{1}{\sqrt{\pi}}\,\frac{\Gamma(\gamma)}{\Gamma(\gamma-1/2)}\,\frac{\sigma_u^2\ell}{(\kappa_1\ell)^{2\gamma}}, \tag{3.11}$$

and it is used that the sign of the subscript on the modified Bessel function $K_{\gamma+1}(\,)$ can be changed [32].

(b) Transverse coherence functions

The transverse coherence functions now follow from differentiation of the scalar potential $\Psi(\mathbf{x})$ according to (3.3). The simplest is the coherence of the longitudinal component derived from introduction of polar coordinates in the transverse plane,

$$R_{11}(0,r) = -\left(\frac{\partial^2}{\partial x_2^2}+\frac{\partial^2}{\partial x_3^2}\right)\Psi(0,r) = -\frac{1}{r}\frac{\partial}{\partial r}\left(r\frac{\partial}{\partial r}\right)\Psi(0,r). \tag{3.12}$$

It is seen from (3.10) that the radial coordinate can be combined into the non-dimensional variable $\kappa_1 r$. It then follows from the standard differentiation formula (2.8) that the covariance can be expressed in terms of the wavenumber integral

$$R_{11}(0,r) = \int_{-\infty}^{\infty} F(k_1)\psi_{11}(\kappa_1 r)\,\mathrm{d}k_1, \tag{3.13}$$

where the transverse coherence $\psi_{11}(\kappa_1 r)$ is obtained as

$$\psi_{11}(\kappa_1 r) = \frac{2}{\Gamma(\gamma)}\left[\left(\frac{\kappa_1 r}{2}\right)^{\gamma} K_\gamma(\kappa_1 r) - \left(\frac{\kappa_1 r}{2}\right)^{\gamma+1} K_{\gamma-1}(\kappa_1 r)\right]. \tag{3.14}$$

It follows from the factorization, and is easily verified, that $\psi_{11}(0)=1$. The result was found in asymptotic form with $\kappa_1 \simeq k_1$ and $\gamma=5/6$ in [24] and the present full form in [23].

Now, consider velocity components in the x_2-direction for a separation r in the x_2-direction. It follows from applying the differentiation rule (3.3) to the scalar potential (3.10) that

$$R_{22}(0,r) = \frac{2}{\Gamma(\gamma)}\int_{-\infty}^{\infty}\left(k_1^2 - \frac{1}{r}\frac{\partial}{\partial r}\right)\frac{F(k_1)}{\kappa_1^2}\left(\frac{\kappa_1 r}{2}\right)^{\gamma+1} K_{\gamma+1}(\kappa_1 r)\,\mathrm{d}k_1. \tag{3.15}$$

Application of the differentiation formula (2.8) then gives

$$R_{22}(0,r) = \frac{2}{\Gamma(\gamma)}\int_{-\infty}^{\infty} F(k_1)\left[\frac{k_1^2}{\kappa_1^2}\left(\frac{\kappa_1 r}{2}\right)^{\gamma+1} K_{\gamma+1}(\kappa_1 r) + \frac{1}{2}\left(\frac{\kappa_1 r}{2}\right)^{\gamma} K_\gamma(\kappa_1 r)\right]\mathrm{d}k_1. \tag{3.16}$$

A more compact form of the result is obtained by expressing the function $K_{\gamma+1}(\kappa_1 r)$ in terms of the similar functions of order one and two lower,

$$R_{22}(0,r) = \frac{2}{\Gamma(\gamma)}\int_{-\infty}^{\infty} F(k_1)\left[\left(\frac{1}{2}+\gamma\frac{k_1^2}{\kappa_1^2}\right)\left(\frac{\kappa_1 r}{2}\right)^{\gamma} K_\gamma(\kappa_1 r) + \frac{k_1^2}{\kappa_1^2}\left(\frac{\kappa_1 r}{2}\right)^{\gamma+1} K_{\gamma-1}(\kappa_1 r)\right]\mathrm{d}k_1. \tag{3.17}$$

The first factor in the first term is put outside the square brackets. According to (2.12), combination of this factor with $F(k_1)$ gives the transverse spectral density function $G(k_1)$. It follows from (2.12) that the integral then is of the form

$$R_{22}(0,r)=\int_{-\infty}^{\infty} G(k_1)\,\psi_{22}(\kappa_1 r)\,\mathrm{d}k_1, \tag{3.18}$$

with the coherence of the transverse velocity component for transverse separation $x_2=r$ obtained as

$$\psi_{22}\,(\kappa_1 r,\kappa_1/k_1)=\frac{2}{\Gamma(\gamma)}\left[\left(\frac{\kappa_1 r}{2}\right)^{\gamma} K_{\gamma}(\kappa_1 r)+\frac{1}{\gamma+\frac{1}{2}(\kappa_1/k_1)^2}\left(\frac{\kappa_1 r}{2}\right)^{\gamma+1} K_{\gamma-1}(\kappa_1 r)\right]. \tag{3.19}$$

It is noted that the transverse coherence function ψ_{22} depends on the length scale ℓ, not only via the variable $\kappa_1 r$, but also by κ_1/k_1 in the factor to the second term. It is easily verified that $\psi_{22}(0,\kappa_1/k_1)=1$. The asymptotic result for small separation corresponds to $\ell\to\infty$, whereby the factor to the second term becomes $(\frac{1}{2}+\gamma)^{-1}$. For $\gamma=5/6$, this reproduces the asymptotic result with factor 3/4 from [24].

When denoting the separation in the x_2 direction r, the covariance matrix component $R_{33}(0,r)$ follows from the scalar potential (3.10) and the differentiation formula (3.3) as

$$R_{33}(0,r)=\frac{2}{\Gamma(\gamma)}\int_{-\infty}^{\infty}\left[k_1^2-\left(1+r\frac{\partial}{\partial r}\right)\left(\frac{1}{r}\frac{\partial}{\partial r}\right)\right]\frac{F(k_1)}{\kappa_1^2}\left(\frac{\kappa_1 r}{2}\right)^{\gamma+1} K_{\gamma+1}(\kappa_1 r)\,\mathrm{d}k_1. \tag{3.20}$$

When comparing with the similar integral for the covariance $R_{22}(0,r)$ in (3.15) it is seen that only the last term containing the second derivative has been added. This term leads to a modification of the factor on the second term in (3.17). The coherence function ψ_{33} is defined by normalization with respect to the transverse covariance spectrum $G(k_1)$, leading to

$$\psi_{33}\,(\kappa_1 r,\kappa_1/k_1)=\frac{2}{\Gamma(\gamma)}\left[\left(\frac{\kappa_1 r}{2}\right)^{\gamma} K_{\gamma}(\kappa_1 r)+\frac{1-(\kappa_1/k_1)^2}{\gamma+\frac{1}{2}(\kappa_1/k_1)^2}\left(\frac{\kappa_1 r}{2}\right)^{\gamma+1} K_{\gamma-1}(\kappa_1 r)\right]. \tag{3.21}$$

In the asymptotic solution with $\kappa_1\simeq k_1$the second term vanishes, and for $\gamma=5/6$ the result from [24] is recovered.

The covariances $R_{13}(0,r)$ and $R_{23}(0,r)$ vanish for all values of the separation distance r, as seen from the differentiation formula (3.3), by which the integrand from (3.4) vanishes identically. Thus, also the corresponding coherence functions $\psi_{13}(k_1 r)$ and $\psi_{23}(k_1 r)$ vanish. The covariance $R_{12}(0,r)$ also vanishes. In this case, the integrand does not vanish, but by the differentiation formula (3.3) it contains the factor ik_1, making the general integral a sine-transform with factor $\sin(k_1 x_1)$. For $x=0$, this introduces a factor zero, so although there is an amplitude function that can be subjected to a formal normalization, the corresponding coherence function $\psi_{12}(k_1 r)$ vanishes in the transverse plane $x_1=0$.

The transverse coherence functions $\psi_{11}(k_1 r)$, $\psi_{22}(k_1 r)$ and $\psi_{33}(k_1 r)$ are shown in figure 1 for the parameter value $\gamma=5/6$, representing the Kolmogorov high-frequency behaviour of the spectral density. When considering convected turbulence with mean velocity U, the argument of the covariance functions is $\omega r/U$. There are two sets of curves, one corresponding to a finite length scale ℓ in the von Kàrmàn spectral density and separation $r=\lambda$, and the other set representing the asymptotic case of $\kappa_1\simeq k_1$. It is observed that the asymptotic theory gives full correlation at $r=0$, whereas the finite length ℓ in the spectral density leads to a notable reduction of the correlation functions for $k_1 r\lesssim 2$ for the present separation $r=\lambda$. Recent measurements in turbulent wind [20–22] confirm the general features illustrated in figure 1.

4. Transformed isotropic turbulence

Natural turbulent wind fields are characterized by different turbulence intensities and different turbulence length scales in the along-wind, transverse and vertical directions. These anisotropic

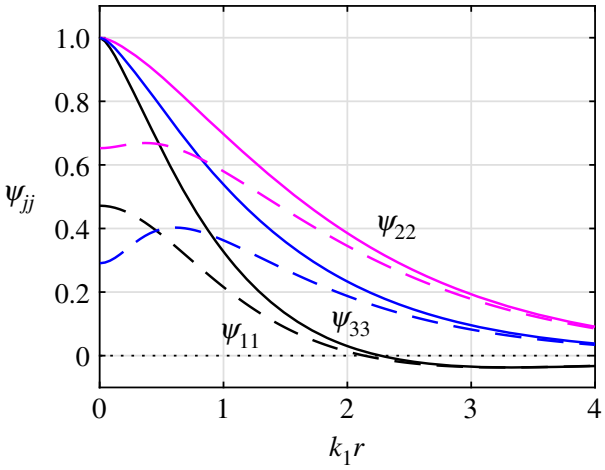

Figure 1. Transverse coherence functions $\psi_{11}(k_1 r)$, $\psi_{22}(k_1 r)$, $\psi_{33}(k_1 r)$. Full lines $\kappa_1 = k_1$, dashed lines $r = \lambda$. (Online version in colour.)

characteristics are different from those developing physically from an isotropic turbulent field, typically analysed as a perturbation building up over time.

The turbulent velocity field representation in §2 is a special case, valid for incompressible isotropic flow. The representation in terms of the two scalar potential functions $f(r)$ and $g(r)$ follows from invariance requirements due to isotropy, and the elimination of $g(r)$ is a consequence of incompressibility. A quite general incompressible anisotropic flow field can be constructed from the three vector components of an incompressible Helmholtz potential, in which there are three intensities and each of these can be given a spatial distribution in terms of scaled coordinates. A more specialized anisotropic turbulence format is that of transformed isotropic turbulence, in which the velocity components $\mathbf{v}'$ and corresponding spatial coordinates $\mathbf{r}'$ are obtained from an isotropic turbulent field by a common transformation matrix $\mathbf{F}$,

$$\mathbf{v}' = \mathbf{F}\mathbf{v} \quad \text{and} \quad \mathbf{r}' = \mathbf{F}\mathbf{r}. \tag{4.1}$$

It follows from the differential increment relation $d\mathbf{v}' = (\partial \mathbf{v}'/\partial \mathbf{r}')d\mathbf{r}'$ that the gradient tensor of the transformed field is

$$\frac{\partial \mathbf{v}'}{\partial \mathbf{r}'} = \mathbf{F}\frac{\partial \mathbf{v}}{\partial \mathbf{r}}\mathbf{F}^{-1}. \tag{4.2}$$

The divergence is given by the trace of the gradient tensor, and when combining the factors $\mathbf{F}$ and $\mathbf{F}^{-1}$ it follows that transformation of an incompressible turbulent field by linear relations of the form (4.1) leads to an incompressible transformed field.

The simple concept of transformed isotropic turbulence enables an approximate representation of the often observed fact in turbulent wind fields that the length scales associated with along-wind, transverse and vertical separation typically satisfy the relations $\lambda_x > \lambda_y > \lambda_z$, with the associated standard deviations of the fluctuating wind velocity components satisfying the similar inequalities $\sigma_u > \sigma_v > \sigma_w$. If selecting σ_u to represent the along-wind component intensity and λ_x, the length scale associated with the measured spectral density, there is one free parameter remaining for each of the transverse directions. This enables, by a suitable compromise, to represent the frequency spectrum together with a reduced transverse length scale and turbulence intensity. The effect of the difference in along-wind and transverse length scales and turbulence intensities has been demonstrated for wind loads and response of long-span bridges in [31], using the simulation method developed in the following.

5. Conditional mean-field simulation

The simulation procedure is closely related to the concept of convected turbulence and is illustrated in figure 2, showing a stack of planes parallel to the yz-plane. The fluctuating wind

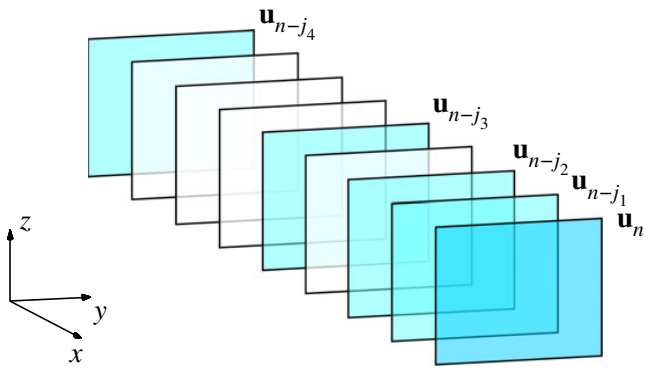

Figure 2. Conditional mean-field simulation procedure. (Online version in colour.)

velocity is represented at a set of fixed points $\mathbf{r}_j$ in the yx-plane represented by the global vector

$$\mathbf{x}^{\mathrm{T}} = [\mathbf{r}_1^{\mathrm{T}}, \mathbf{r}_2^{\mathrm{T}}, \ldots, \mathbf{r}_m^{\mathrm{T}}]. \tag{5.1}$$

The planes have the distance $\Delta x = U\Delta t$, and in a generic plane with index n the velocity vectors $\mathbf{v}_j$ from the individual points are collected in the global vector

$$\mathbf{u}_n^{\mathrm{T}} = [\mathbf{v}_1^{\mathrm{T}}, \mathbf{v}_2^{\mathrm{T}}, \ldots, \mathbf{v}_m^{\mathrm{T}}]_n. \tag{5.2}$$

At each step of the simulation algorithm, the index n is increased by one, corresponding to an increment Δx, and thus the simulation moves along the x-axis shown in figure 2.

The standard format of an auto-regressive vector process is

$$\mathbf{u}_n = \mathbf{A}_1\mathbf{u}_{n-1} + \mathbf{A}_2\mathbf{u}_{n-2} + \cdots + \mathbf{A}_j\mathbf{u}_{n-j} + \mathbf{B}\boldsymbol{\xi}_n, \quad n = 1, 2, \ldots. \tag{5.3}$$

where $\mathbf{u}_n$ is an array containing the new set of field variables, expressed as the sum of j previous sets $\mathbf{u}_{n-1}, \ldots, \mathbf{u}_{n-j}$ plus the set $\boldsymbol{\xi}_n$ of random variables. The random vectors $\boldsymbol{\xi}_n$ are here taken in the form of uncorrelated normalized normal components, whereby

$$\mathrm{E}[\boldsymbol{\xi}_i\boldsymbol{\xi}_j^{\mathrm{T}}] = \delta_{ij}\mathbf{I}. \tag{5.4}$$

When considering the process as a development in time, the time increment Δt between consecutive sets $\mathbf{u}_n$ defines the time discretization, and the depth of the filter generated by the j-term average defines the time interval $j\Delta t$, available for shaping the spectral properties of the process. As it turns out in the context of wind field simulation, a considerable gain in the efficiency of the auto-regressive process model is attained by selecting the distance between the previous steps to be increasing, thereby creating a longer filter length for a given number j of previous values of the field variables. With this modification, the process takes the form

$$\mathbf{u}_n = \mathbf{A}_1\mathbf{u}_{n-i_1} + \mathbf{A}_2\mathbf{u}_{n-i_2} + \cdots + \mathbf{A}_j\mathbf{u}_{n-i_j} + \mathbf{B}\boldsymbol{\xi}_n, \quad n = 1, 2, \ldots. \tag{5.5}$$

The particular case $i_i = 1, 2, 4, 8$ is illustrated in figure 2.

It is convenient to write the modified auto-regressive recurrence relation (5.5) in the form

$$\mathbf{u}_n = \mathbf{A}\,\mathbf{w}_n + \mathbf{B}\,\boldsymbol{\xi}_n, \quad n = 1, 2, \ldots. \tag{5.6}$$

in terms of the compound matrix and vector

$$\mathbf{A} = [\mathbf{A}_1, \ldots, \mathbf{A}_j] \quad \text{and} \quad \mathbf{w}_n^{\mathrm{T}} = [\mathbf{u}_{n-i_1}^{\mathrm{T}}, \ldots, \mathbf{u}_{n-i_j}^{\mathrm{T}}]. \tag{5.7}$$

The matrices $\mathbf{A}$ and $\mathbf{B}$ are now determined from the covariance properties of $\mathbf{u}_n$ and $\mathbf{w}_n$. For this purpose, the following notation for covariance matrices is introduced:

$$\mathbf{C}_{\mathbf{uu}} = \mathrm{E}[\mathbf{u}_n\mathbf{u}_n^{\mathrm{T}}], \quad \mathbf{C}_{\mathbf{uw}} = \mathrm{E}[\mathbf{u}_n\mathbf{w}_n^{\mathrm{T}}] \quad \text{and} \quad \mathbf{C}_{\mathbf{ww}} = \mathrm{E}[\mathbf{w}_n\mathbf{w}_n^{\mathrm{T}}]. \tag{5.8}$$

It is observed that these covariance matrices are independent of the subscript n for stationary fields, and for the turbulent wind field in question they are given explicitly in terms of the velocity component covariance functions in §2.

First, the matrix $\mathbf{A}$ is determined from (5.6) by observing that $\boldsymbol{\xi}_n$ is independent of $\mathbf{w}_n$, and post-multiplication by $\mathbf{w}_n^{\mathrm{T}}$ leads to the following equation:

$$\mathbf{C}_{\mathbf{uw}} = \mathbf{A}\,\mathbf{C}_{\mathbf{ww}}. \tag{5.9}$$

Post-multiplication of this equation with the inverse of $\mathbf{C}_{\mathbf{ww}}$ gives the explicit expression for the compound regression matrix $\mathbf{A}$,

$$\mathbf{A} = \mathbf{C}_{\mathbf{uw}}\mathbf{C}_{\mathbf{ww}}^{-1}. \tag{5.10}$$

When there are j regression terms, the size of $\mathbf{w}_n$ is j times larger than that of $\mathbf{u}_n$, and thus it may be numerically advantageous to avoid forming the inverse matrix and simply solve the equation system arising from taking the transpose of (5.9),

$$\mathbf{C}_{\mathbf{ww}}\mathbf{A}^{\mathrm{T}} = \mathbf{C}_{\mathbf{uw}}^{\mathrm{T}}. \tag{5.11}$$

It is observed that the conditional expectation of $\mathbf{u}_n$ for given $\mathbf{w}_n$ follows from (5.6) as

$$\mathrm{E}[\mathbf{u}_n|\mathbf{w}_n] = \mathbf{A}\mathbf{w}_n, \tag{5.12}$$

and thus the auto-regressive format (5.6) defines the new variable $\mathbf{u}_n$ as the conditional mean value for the given regression variables $\mathbf{w}_n$, plus a zero-mean stochastic term $\mathbf{B}\boldsymbol{\xi}_n$.

The matrix $\mathbf{B}$ that distributes the stochastic input is determined from the regression equation (5.6) by moving the term $\mathbf{A}\mathbf{w}_n$ to the left side of the equation and multiplying each side from the right by its transpose,

$$[\mathbf{u}_n - \mathbf{A}\,\mathbf{w}_n][\mathbf{u}_n - \mathbf{A}\,\mathbf{w}_n]^{\mathrm{T}} = \mathbf{B}\,\boldsymbol{\xi}_n\boldsymbol{\xi}_n^{\mathrm{T}}\mathbf{B}^{\mathrm{T}}. \tag{5.13}$$

When taking the expectation of this equation, using that the components of $\boldsymbol{\xi}_n$ are uncorrelated and normalized, and substituting the regression matrix $\mathbf{A}$ from (5.10), the following equation is obtained

$$\mathbf{B}\mathbf{B}^{\mathrm{T}} = \mathbf{C}_{\mathbf{uu}} - \mathbf{C}_{\mathbf{uw}}\mathbf{C}_{\mathbf{ww}}^{-1}\mathbf{C}_{\mathbf{wu}}. \tag{5.14}$$

Recalling the remarks concerning the undesirability of evaluating the inverse matrix $\mathbf{C}_{\mathbf{ww}}^{-1}$ in connection with the evaluation of the regression matrix $\mathbf{A}$, the equation is reformulated by introducing the matrix $\mathbf{A}$ from (5.10), yielding the more convenient expression

$$\mathbf{B}\mathbf{B}^{\mathrm{T}} = \mathbf{C}_{\mathbf{uu}} - \mathbf{A}\mathbf{C}_{\mathbf{ww}}\mathbf{A}^{\mathrm{T}}. \tag{5.15}$$

The solution can be obtained either by factorization into triangular matrices or by an eigenvalue analysis.

The expression on the right side of (5.13) is recognized as the conditional variance of $\mathbf{u}_n$ for given $\mathbf{w}_n$, whereby

$$\mathrm{Cov}[\mathbf{u}_n, \mathbf{u}_n|\mathbf{w}_n] = \mathbf{B}\mathbf{B}^{\mathrm{T}}. \tag{5.16}$$

This formula and the corresponding conditional mean formula (5.12) assign specific roles to the matrices $\mathbf{A}$ and $\mathbf{B}$: the recurrence matrix $\mathbf{A}$ defines the conditional mean field, and the matrix product $\mathbf{B}\mathbf{B}^{\mathrm{T}}$ determines the intensity and correlation of the fluctuations around this mean.

6. Wind field simulation

An application area of considerable current interest is that of turbulent wind load on structures. Specific applications range from structures like towers, high-rise buildings and long-span bridges to wind turbines. Traditionally, the level of ambition regarding the representation of the turbulent wind load in these applications has been very different, with structural applications often using simple analytical approximations for the resulting load, whereas wind turbine design typically uses rather detailed wind field simulation, often based on FFT techniques, see e.g. [4,5]. A field of growing interest is the representation of wind loads on long-span bridges with lengths

of up to 2000–3000 m. These applications require simulations of very long and narrow areas, not immediately suitable for frequency representation and Fourier methods. Furthermore, these applications require a realistic representation of the transverse length scale as considerably shorter than the equivalent axial length scale. This can be accomplished by suitable stretching as described in §4 and illustrated in [31]. As the stretched field can be generated directly from a corresponding isotropic field, the following simulations are limited to isotropic fields.

(a) Isotropic wind field correlation

The simulations are performed by using the recurrence relation (5.5) in which the compound recurrence matrix **A** and the input matrix **B** are evaluated from the correlation matrices for the points at all the involved cross-sections by (5.11) and (5.15). The correlation matrix for two cross-sections with distance j is of the form

$$\mathbf{C}_j = \mathrm{E}[\mathbf{u}_n \mathbf{u}_{n-j}^{\mathrm{T}}] = \begin{bmatrix} \vdots & \vdots & \vdots \\ \vdots & \mathrm{E}[\mathbf{v}_{p,n}\mathbf{v}_{q,n-j}^{\mathrm{T}}] & \vdots \\ \vdots & \vdots & \vdots \end{bmatrix} = \begin{bmatrix} \vdots & \vdots & \vdots \\ \vdots & \mathbf{R}(\mathbf{r}_{p,n} - \mathbf{r}_{q,n-j}) & \vdots \\ \vdots & \vdots & \vdots \end{bmatrix}. \tag{6.1}$$

where the subscripts p and q identify the points in the two cross-sections. The final form consists of the 3×3 block matrices representing the covariance between the point $\mathbf{r}_p$ in layer n and the point $\mathbf{r}_q$ in layer $n - j$.

For an isotropic field, the covariance function is given in terms of the axial and transverse correlation functions $f(r)$ and $g(r)$ by (2.1). According to Kolmogorov's cascade theory, the high-frequency behaviour of the spectral density gives $\gamma = 5/6$, and the axial and transverse correlation functions then follow from (2.7) and (2.10) as

$$f(r) = \frac{2}{\Gamma(1/3)} \left(\frac{r}{2\ell}\right)^{1/3} K_{1/3}\left(\frac{r}{\ell}\right) \quad \text{and} \quad g(r) = f(r) - \frac{2}{\Gamma(1/3)} \left(\frac{r}{2\ell}\right)^{4/3} K_{-2/3}\left(\frac{r}{\ell}\right) \tag{6.2}$$

with the length parameter ℓ calculated from (2.14) as $\ell = 1.339\lambda$. For a detailed analysis of the simulated wind field, the transverse coherence functions are available from §3 in terms of $K_{5/6}(\kappa_1 r)$ and $K_{-1/6}(\kappa_1 r)$.

If only considering the simulation, the axial and transverse correlation functions $f(r)$ and $g(r)$ can alternatively be expressed in terms of Airy functions [32]. This formulation uses a non-dimensional transformed variable z to represent the distance,

$$z = \left(\frac{3r}{2\ell}\right)^{2/3}, \tag{6.3}$$

whereby

$$f(r) = \frac{\mathrm{Ai}(z)}{\mathrm{Ai}(0)} \quad \text{and} \quad g(r) = f(r) + \frac{z}{3}\frac{\mathrm{Ai}'(z)}{\mathrm{Ai}(0)}. \tag{6.4}$$

Here, $\mathrm{Ai}(z)$ is the Airy function and $\mathrm{Ai}'(z)$ its derivative. Like the modified Bessel functions $K_\nu(r/\ell)$, the Airy function $\mathrm{Ai}(z)$ and its derivative $\mathrm{Ai}'(z)$ are directly available in several programming environments.

A simple approximate formulation of the spatial correlations can be obtained by using the exponent $\gamma = 1$, whereby

$$f(r) = \mathrm{e}^{-r/\lambda} \quad \text{and} \quad g(r) = \left(1 - \frac{1}{2}\frac{r}{\lambda}\right)\mathrm{e}^{-r/\lambda}. \tag{6.5}$$

This formulation improves on the classic exponential engineering approximation by retaining the integral zero mean property (2.3). A simple exponential format may also be obtained for the transverse coherence functions by selecting $\gamma = 1/2$, [23], but it is noted that this value represents the limit to a non-integrable spectral density (2.5). The resulting exponential coherence format has recently been compared with measured records in [21] and [22], confirming the general feature of

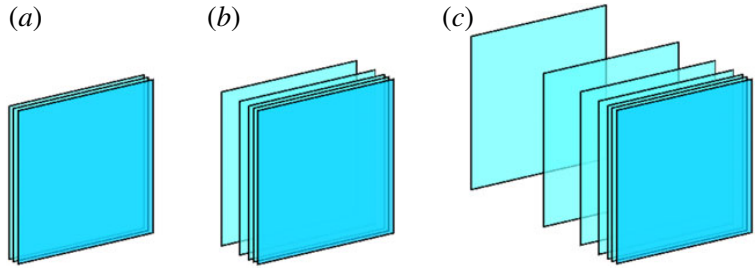

Figure 3. Regression planes, (*a*) $j = 1, 2$, (*b*) $j = 1, 2, 4, 8$, (*c*) $j = 1, 2, 4, 8, 16, 32$. (Online version in colour.)

Table 1. Simulation parameters: square field. Lengths in metres.

σ_u	λ	L_y	L_z	Δx	Δy	Δz	N_x	N_y	N_z
1.0	300	100	100	5.0	5.0	5.0	10^6	21	21

the $\kappa_1 r$ dependence. In view of the limit on the general consistency of the exponential coherence format, these results deserve a comparison with the consistent coherence functions from §3 with $\gamma = 5/6$.

(b) Square cross-section field

First an isotropic wind field with square cross-section area of dimension $L_y = L_z = 100\,\mathrm{m}$ is considered. The length scale is $\lambda = 300\,\mathrm{m}$, and the spatial increments are taken to be equal, $\Delta x = \Delta y = \Delta z = 5.0\,\mathrm{m}$. This corresponds to the along-wind resolution of $\lambda/\Delta x = 60$, and cross-section resolution $L_y/\Delta y = L_z/\Delta z = 20$. The record length is $N_x = 10^6$ steps, and the standard deviation of the velocity components is set to $\sigma_u = 1.0\,\mathrm{m\,s^{-1}}$, but appears only as a numerical scaling factor. The data, representative of e.g. a large wind turbine, are summarized in table 1.

In addition to the parameters in table 1, the simulation process also depends on the number and distribution of the regression terms. It turns out that a distribution of the regression intervals according to $j = 2^{i-1}$, $i = 1, 2, \ldots$ is quite effective. The cases with 2, 4 and 6 terms are illustrated in figure 3. The axes are defined as shown in figure 2. With the parameters from table 1, the intervals spanned by the regression terms are 0.033λ, 0.133λ and 0.533λ.

In many applications, such as e.g. response analysis of structures exposed to the wind field, the spectral density plays a central role, and thus the ability to reproduce the spectral density accurately in the simulated wind field is important. Here, the spectral density of the along-wind velocity component u at the centre of the cross-section square is chosen to illustrate the spectral characteristics of the simulated field. The results from the three sets of recurrence intervals just discussed are shown in figure 4*a*,*c*,*e* using the standard non-dimensional spectral density $k_1 S_{uu}(k_1)/\sigma_u^2$ in terms of the along-wind wavenumber k_1 in a double-logarithmic plot. It is seen that the simple two-step memory underestimates the maximum of the spectral density in the interval $k_1 \simeq 0.005$–0.01. This problem is nearly removed when using four regression planes, and finally a full representation is obtained with six regression planes. The right column contains the similar simulation results obtained by including the full set of regression steps with equal spacing Δx. The results are remarkably similar to those obtained by fewer steps with increasing intervals in the left column. Thus there is no visible improvement by including all the regression steps with interval Δx. All the simulated results show a slight overestimation of the spectral density for the largest wave numbers.

The results in figure 4 show that a quite accurate representation of the auto-spectral density of the along-wind component at the centre simulation point is obtained for the set of regression intervals $j = 1, 2, 4, 8, 16, 32$. This set of regression intervals is now used to simulate a wind field where all three wind velocity components are sampled at three points as illustrated in figure 5*a*, a

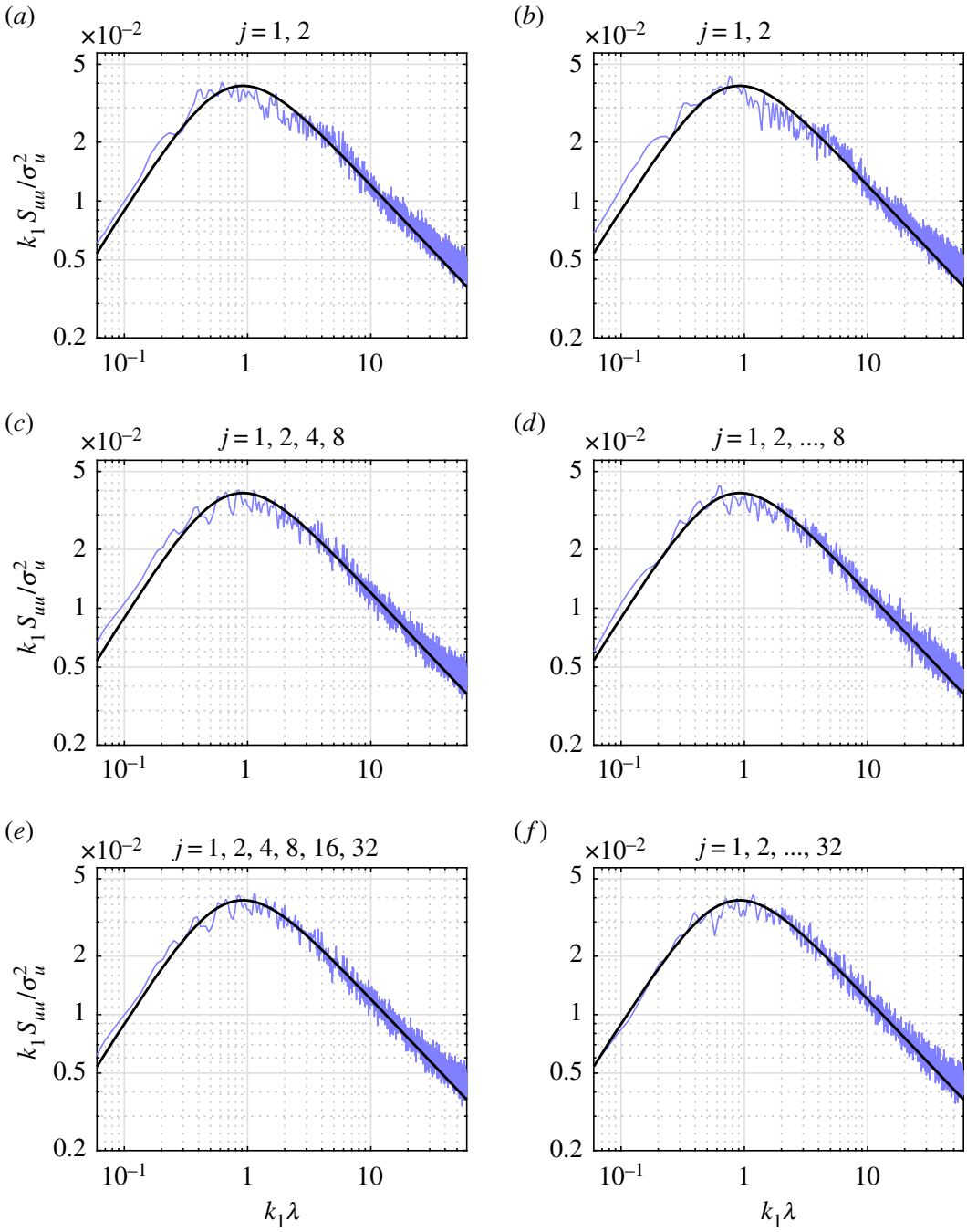

Figure 4. Estimated auto-spectral densities (blue line), target spectrum (black line). (*a*,*c*,*e*) Left column: exponentially spaced memory steps; (*b*,*d*,*f*) right column: full set of equally spaced memory steps. (Online version in colour.)

corner, a side centre and the centre node. The spectral densities $k_1 S_{uu}(k_1)$, $k_1 S_{vv}(k_1)$ and $k_1 S_{ww}(k_1)$ are shown in figure 5*b*–*d*, respectively. Each figure contains the simulated results at each of the three points, together with the relevant theoretical spectral density $F(k_1)$ from (3.11) or $G(k_1)$ from (2.12). The quality of the simulated results appears to be similar for each of the velocity components, and there is no notable difference between the records at the three points. Thus, the simulated results seem unbiased by the location of the sampling point and do not exhibit any boundary effects from the simulated cross-section domain.

The results in figures 4 and 5 have addressed properties of the individual simulated time records. In addition, there is the correlation properties between velocity components at points in the simulated cross-sections. Figure 6*a* shows the horizontal and vertical lines of points through the centre, and the correlations C_{uu}/σ_u^2, C_{vv}/σ_v^2 and C_{ww}/σ_w^2 evaluated from the simulated records along these lines. Figure 6*b* shows the correlation of the along-wind component u together with

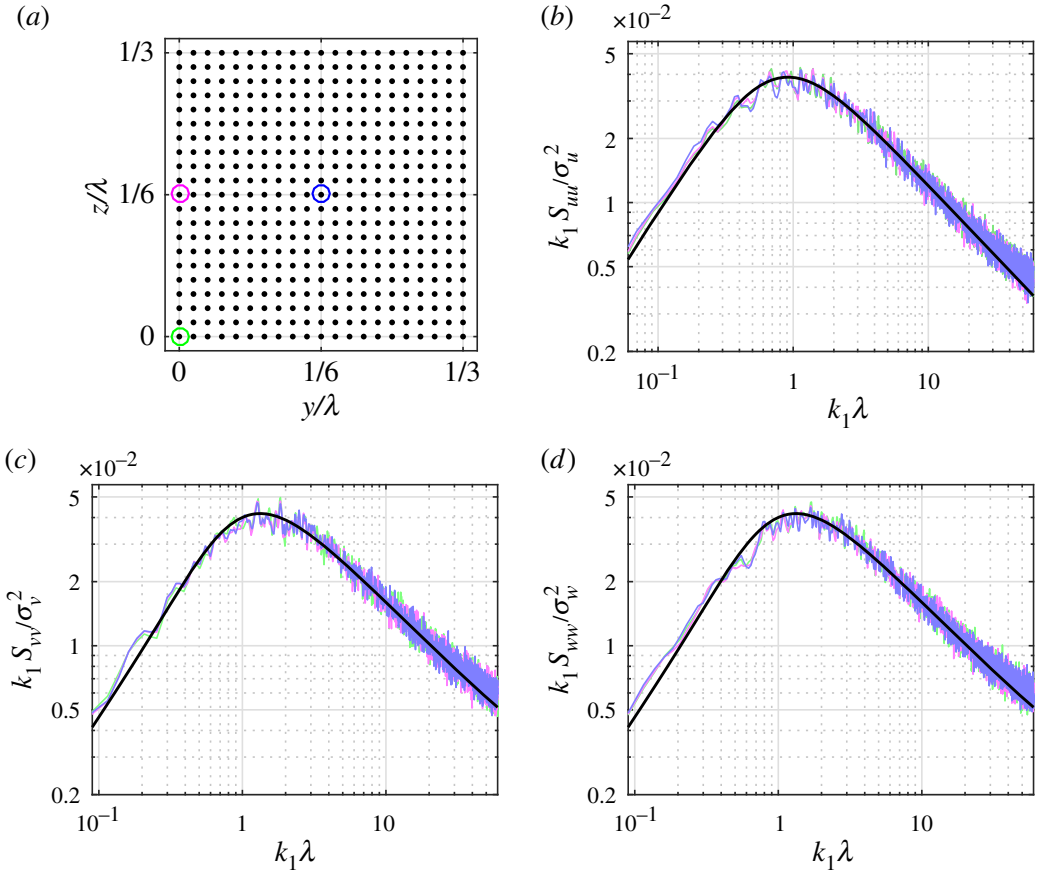

Figure 5. Target spectrum (black line), estimated auto-spectral densities in thin line (blue, magenta and green). (Online version in colour.)

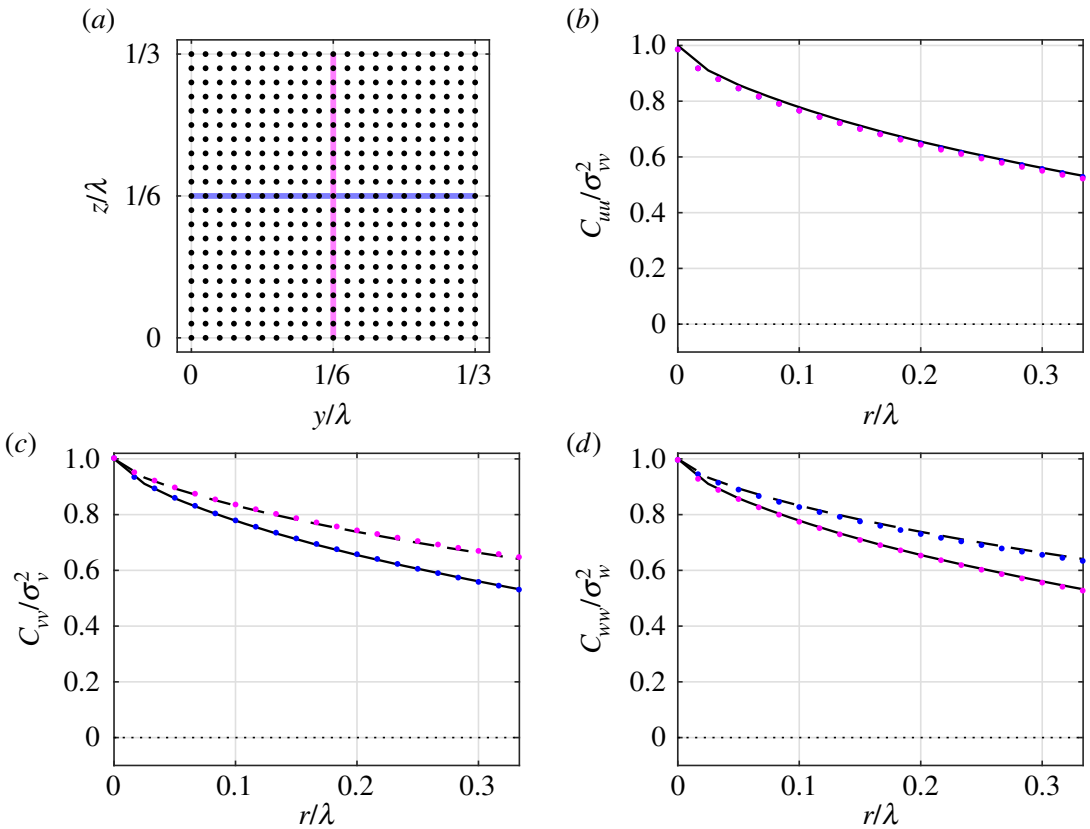

Figure 6. Theoretical transverse correlation $g(r)$ (full line) and axial correlation $f(r)$ (dashed line), estimated correlations (blue dotted, magenta dotted). (Online version in colour.)

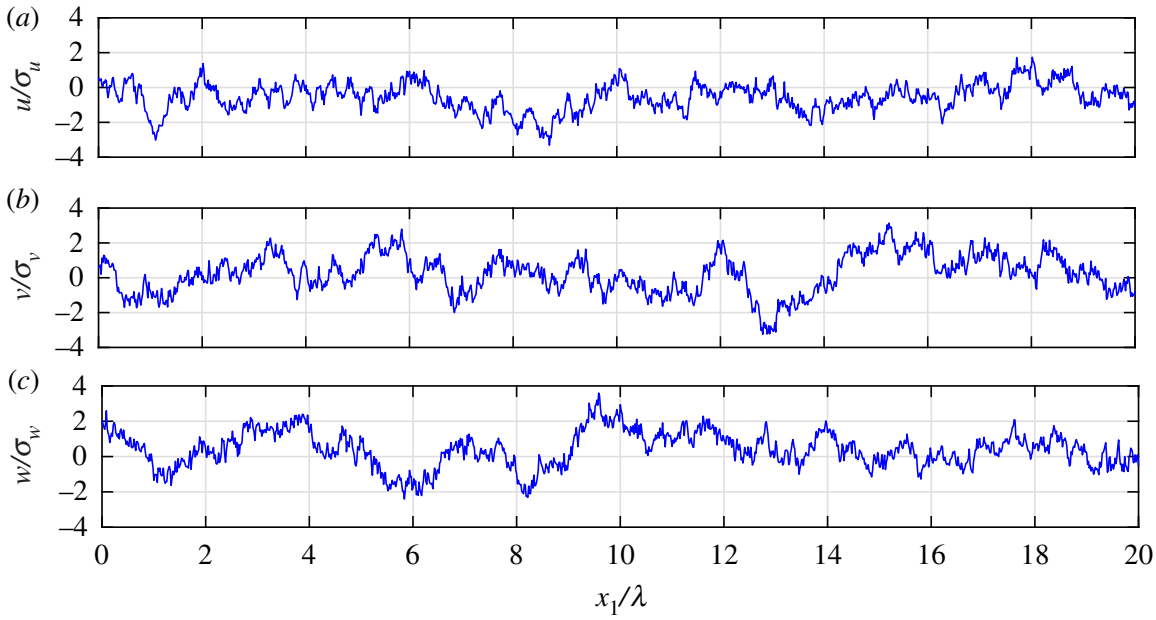

Figure 7. Equivalent time records of turbulent velocity components, $x_1/\lambda = (U/\lambda)t$. (Online version in colour.)

Table 2. Simulation parameters: horizontal line field. Lengths in metres.

σ_u	λ	L_y	L_z	Δx	Δy	Δz	N_x	N_y	N_z
1.0	300	1800	—	5.0	9.0	—	10^6	201	1

the theoretical value $g(r)$ from (6.2b) along the horizontal and vertical lines. The simulated results are indistinguishable and extremely close to the theoretical value. The correlation of the horizontal velocity component v is shown in figure 6*c* together with the theoretical value $f(r)$ from (6.2)*a* along the horizontal line and $g(r)$ along the vertical line. The agreement between simulated and theoretical results is very good. Finally, the similar results are shown for the vertical velocity component w in figure 6*d*. It is noted that the spatial correlations are significant over the whole area as the dimensions are less than the correlation length λ.

Figure 7 shows corresponding time records of the three wind components u, v and w at the centre point of the simulation grid. The time is represented via the non-dimensional equivalent time $x_1/\lambda = (U/\lambda)t$. The scale of the actual time depends on the mean wind speed U and the turbulence length scale λ. In the present case $\lambda = 300\,\mathrm{m}$, and thus for a mean wind speed of $U = 15\,\mathrm{m\,s^{-1}}$ a unit on the time axis corresponds to $\lambda/U = 20\,\mathrm{s}$.

(c) Horizontal line field

The present simulation scenario is representative of the turbulent wind field on a long-span bridge. The transverse length is $L_y = 1800\,\mathrm{m}$ and in order to test the capability of the simulation method the domain is taken as a single row of $N_y = 201$ points, corresponding to $N_z = 1$ and $L_z = 0\,\mathrm{m}$. The spectral properties of the wind are the same as in the previous example with $\sigma_u = 1.0\,\mathrm{m\,s^{-1}}$ and the axial integral length scale $\lambda = 300\,\mathrm{m}$. The parameters are summarized in table 2.

It was demonstrated in the previous example that an exponentially increasing distance to the regression planes in the simulation model leads to an efficient and accurate algorithm. In view of the much larger transverse dimension of the present model, 1800 m against 100 m, the need for additional depth of the memory is investigated. The general exponential representation $j = m^{i-1}$ with $i = 1, 2, \ldots, 5$ is investigated with basis $m = 2, 3, 4$, respectively. The simulated results are illustrated by their axial spectral density in figure 8. The figures to the left illustrate the regression

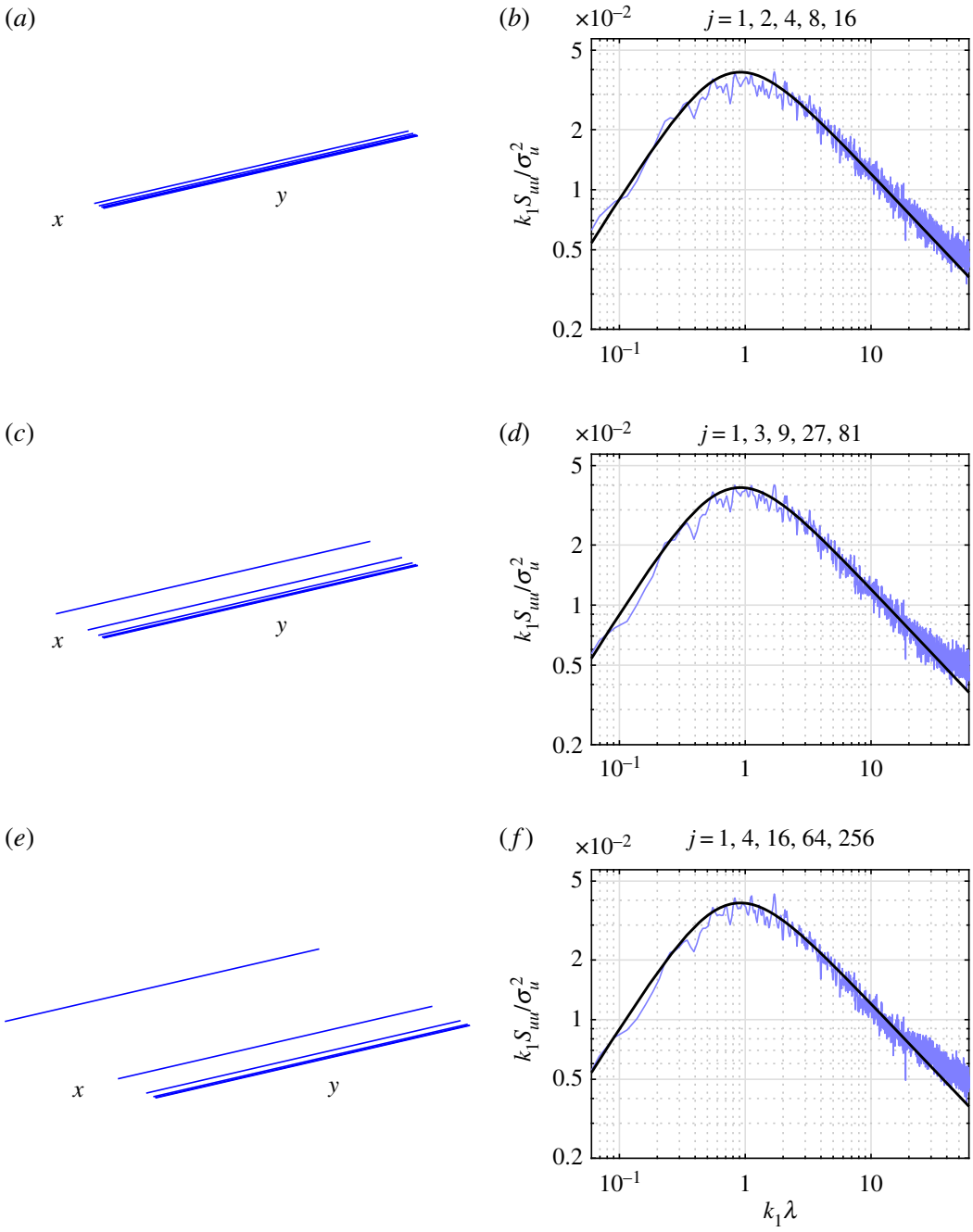

Figure 8. Estimated auto-spectral density (blue line), target spectrum (black line). (Online version in colour.)

lines, and the figures to the right the spectral density. It is observed that the accuracy of the spectral density around the peak increases with increasing total depth covered by the regression lines. However, this happens at the cost of a decreasing accuracy in the high-frequency domain, which is increasingly over-estimated.

A compromise is to keep the base 2, but to increase the number of regression terms to 9, whereby $j = 2^{i-1} = 1, 2, 4, 8, 16, 32, 64, 128, 256$. This set of regression lines contains the previous base 4 set in figure 8*e*, but with an intermediate line between each of those, and retains the fine discretization for small intervals. Simulation results are shown for the spectral density of all three velocity components in figure 9, sampled at the end, the quarter point and the mid-point, marked with blue, magenta and green, respectively. The spectral densities are represented with very good accuracy over the full frequency range. As in the previous example of the square, there is no notable dependence on the sampling point.

The spatial correlations are important characteristics of the simulated field. The correlation coefficients C_{uu}/σ_u^2, C_{vv}/σ_v^2 and C_{ww}/σ_w^2 are estimated from pairs of sampled records for the points

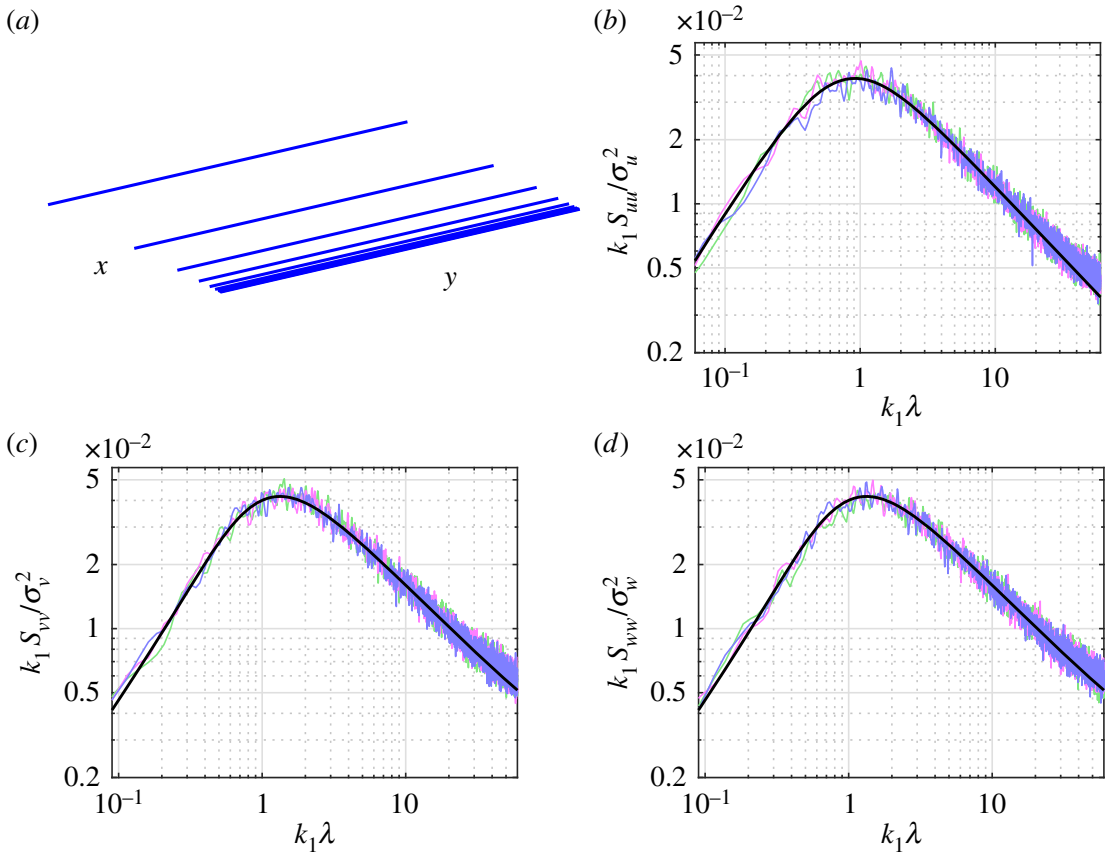

Figure 9. Estimated spectral densities at endpoint (blue line), quarter point (magenta line) and mid-point (green line), target spectrum (black line). (Online version in colour.)

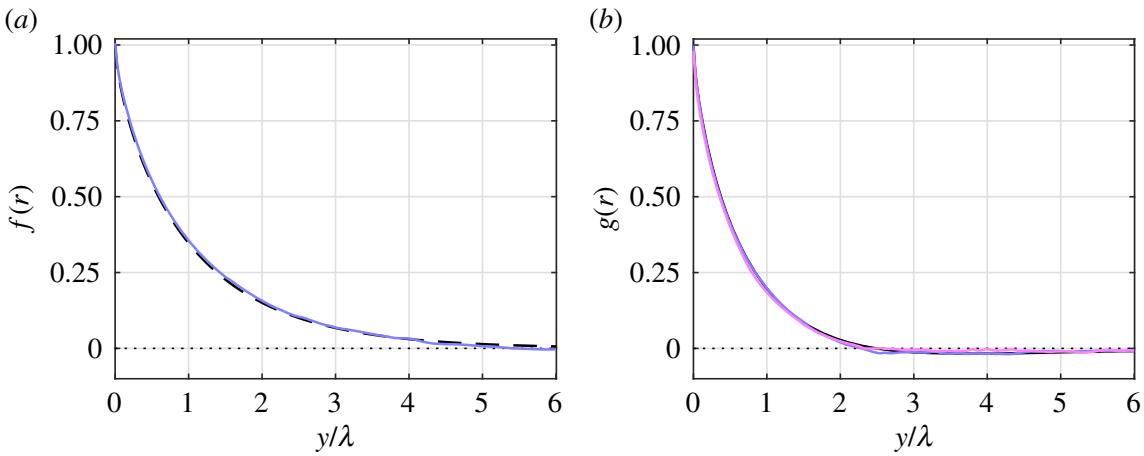

Figure 10. Transverse correlations: (*a*) $f(r)$ (black line), estimate C_{vv}/σ_v^2 (blue line); (*b*) $g(r)$ (black line), estimate C_{uu}/σ_u^2 (blue line) and C_{ww}/σ_w^2 (red line). (Online version in colour.)

along the line. The estimated axial and transverse correlations are shown in figure 10*a*,*b* together with the theoretical correlation functions $f(r)$ and $g(r)$ from (6.2), respectively. The agreement is seen to be very good over the full range up to $r = 6\lambda$, with no notable difference between the transverse correlation estimates for the along-wind velocity component u and the vertical velocity component w.

Finally, the ability of the simulation procedure to resolve the finer details of the turbulent wind velocity field is illustrated by considering the coherence functions $\psi_{11}(k_1 r)$ and $\psi_{33}(k_1 r)$ for spatial separations $r = 0.75\lambda, 1.5\lambda, 3.0\lambda$. The estimated coherence functions $\psi_{11}(k_1 r)$ and $\psi_{33}(k_1 r)$

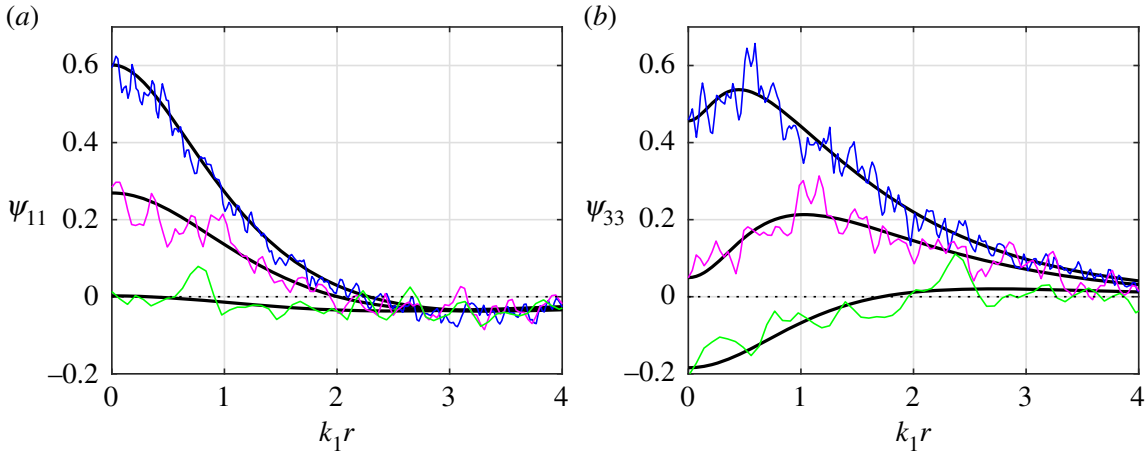

Figure 11. Estimated coherence: (*a*) ψ_{11}, (*b*) ψ_{33}. Separation 0.75λ top (blue line), 1.5λ middle (magenta line), 3λ bottom (green line). Target coherence (black line). (Online version in colour.)

are shown in figures 11*a*,*b* together with their theoretical counterparts from (3.14) and (3.21), respectively. In spite of statistical scatter, it is seen that the simulated field captures the underlying coherence structure quite well.

7. Conclusion

The theory for isotropic homogeneous turbulence has been summarized, and detailed results presented for both covariances and coherence functions in terms of modified Bessel functions for the case of a generalized von Kàrmàn spectrum, a common representation of the turbulence in natural wind. The typical differences observed in natural wind between the longitudinal, transverse and vertical length scales have been addressed by a simple procedure for generating consistent incompressible orthotropic turbulence by coordinate scaling with corresponding scaling of the velocity component standard deviations.

A procedure is then developed for numerical simulation of a convected turbulent wind field by a modified auto-regressive process, in which transverse regression planes are introduced at exponentially increasing distance from the current transverse plane. The format associated with this procedure is shown to represent the upcoming step of wind velocities as the sum of the conditional mean field and a stochastic part, represented by the conditional covariance matrix. The appropriate simulation matrices are expressed explicitly in terms of these conditional matrices, that in turn are determined explicitly by the homogeneous covariance properties determined in the first part of the paper.

Simulation results with exponentially increasing distance to the regression planes indicate the ability to attain very accurate results for a typical square area of size about one-third of the turbulence length scale and for a line of length six times the length scale, corresponding to a typical wind turbine field and a very long bridge, respectively. The results confirm high accuracy of the simulated frequency spectrum, the transverse correlation and the transverse coherence. Furthermore, the statistics of the simulated records appear to be independent of the particular points chosen in the cross-section. The sequential nature of the procedure and the rather free selection of simulation points in the cross-section plane make it highly competitive with Fourier-based spectral methods.

Data accessibility. This article has no additional data.

Authors' contributions. General theoretical results and the basic form of the simulation procedure were developed by S.K. Simulation code and examples were developed by R.N.M. Both S.K. and R.N.M. contributed to writing the final paper.

Competing interests. We declare we have no competing interests.

Funding. Partial support for RNM from Innovation Fund Denmark.

Acknowledgements. The paper is part of the project Aerodynamic Stability of Long Span Bridges, sponsored jointly by Innovation Fund Denmark, Rambøll and the Technical University of Denmark.

References

1. Shinozuka M, Deodatis G. 1996 Simulation of multidimensional Gaussian stochastic fields by spectral representation. *Appl. Mech. Rev.* **49**, 29–53. (doi:10.1115/1.3101883)
2. Deodatis G. 1996 Simulation of ergodic multivariate stochastic processes. *J. Eng. Mech.* **122**, 778–787. (doi:10.1061/(ASCE)0733-9399(1996)122:8(778))
3. Batchelor GK. 1953 *The theory of homogeneous turbulence*. Cambridge, UK: Cambridge University Press.
4. Mann J, Krenk S. 1994 Fourier simulation of non-isotropic wind field model. *Proceedings of ICOSSAR '93*, Innsbruck, Austria, August 9–13, 1993, vol. 3 (eds GI Schueller, M Shinozuka, JTP Yao), pp. 1669–1674. Rotterdam: Balkema.
5. Mann J. 1998 Wind field simulation. *Probab. Eng. Mech.* **13**, 269–282. (doi:10.1016/S0266-8920(97)00036-2)
6. Li Y, Kareem A. 1995 Stochastic decomposition and application to probabilistic dynamics. *J. Eng. Mech.* **119**, 162–174. (doi:10.1061/(ASCE)0733-9399(1995)121:1(162))
7. Di Paola M. 1998 Digital simulation of wind field velocity. *J. Wind Eng. Ind. Aerodyn.* **74-76**, 91–109. (doi:10.1016/S0167-6105(98)00008-7)
8. Di Paola M, Gullo I. 2001 Digital generation of multivariate wind field processes. *Probab. Eng. Mech.* **16**, 1–10. (doi:10.1016/S0266-8920(99)00032-6)
9. Chen X, Kareem A. 2005 Proper orthogonal decomposition-based modeling, analysis, and simulation of dynamic wind load effects on structures. *J. Eng. Mech.* **131**, 325–339. (doi:10.1061/(ASCE)0733-9399(2005)131:4(325))
10. Solari G, Carassale L, Tubino F. 2007 Proper orthogonal decomposition in wind engineering. Part 1: a state-of-the-art and some prospects. *Wind Struct.* **10**, 153–176. (doi:10.12989/was.2007.10.2.153)
11. Carassale L, Solari G, Tubino F. 2007 Proper orthogonal decomposition in wind engineering. Part 2: theoretical aspects and some applications. *Wind Struct.* **10**, 177–208. (doi:10.12989/was.2007.10.2.177)
12. Stefanou G, Papadrakakis M. 2007 Assessment of spectral representation and Karhunen–Loève expansion methods for the simulation of Gaussian stochastic fields. *Comput. Methods Appl. Mech. Eng.* **196**, 2465–2477. (doi:10.1016/j.cma.2007.01.009)
13. Hémon P, Santi F. 2007 Simulation of a spatially correlated turbulent velocity field using biorthogonal decomposition. *J. Wind Eng. Ind. Aerodyn.* **95**, 21–29. (doi:10.1016/j.jweia.2006.04.003)
14. Davenport AG. 1977 The prediction of the response of structures to gusty wind, In *Safety of structures under dynamic loading* (eds I Holand, D Kavlie, G Moe, R Sigbjörnsson), pp. 257–284. Trondheim, Norway: Tapir.
15. Yang WW, Chang TYP, Chang CC. 1997 An efficient wind field simulation technique for bridges. *J. Wind Eng. Ind. Aerodyn.* **67-68**, 697–708. (doi:10.1016/S0167-6105(97)00111-6)
16. Cao Y, Xiang H, Zhou Y. 2000 Simulation of stochastic wind velocity field of long-span bridges. *J. Eng. Mech.* **126**, 1–6. (doi:10.1061/(ASCE)0733-9399(2000)126:1(1))
17. Huang G, Liao H, Li M. 2013 New formulation of Cholosky decomposition and applications in stochastic simulation. *Probab. Eng. Mech.* **34**, 40–47. (doi:10.1016/j.probengmech.2013.04.003)
18. Peng L, Huang G, Kareem A, Li Y. 2013 An efficient space-time based simulation approach of wind velocity field with embedded conditional interpolation for unevenly spaced locations. *Probab. Eng. Mech.* **34**, 40–47. (doi:10.1016/j.probengmech.2013.04.003)
19. Benowitz BA, Deodatis G. 2015 Simulation of wind velocity on long span structures: a novel stochastic wave based model. *J. Wind Eng. Ind. Aerodyn.* **147**, 154–163. (doi:10.1016/j.jweia.2015.10.004)
20. Li Y, Hu P, Xu X, Qiu J. 2017 Wind characteristics at bridge site in a deep-cutting gorge by wind tunnel tests. *J. Wind Eng. Ind. Aerodyn.* **160**, 30–46. (doi:10.1016/j.jweia.2016.11.002)
21. Peng Y, Wang S, Li J. 2018 Field measurement and investigation of spatial coherence for near-surface strong winds in southeast China. *J. Wind Eng. Ind. Aerodyn.* **172**, 423–440. (doi:10.1016/j.jweia.2017.11.012)

22. Fenerci A, Øiseth O. 2018 Strong wind characteristics and dynamic response of a long-span suspension bridge during a storm. *J. Wind Eng. Ind. Aerodyn.* **172**, 116–138. (doi:10.1016/j.jweia.2017.10.030)
23. Krenk S. 1996 Wind field coherence and dynamic wind forces. *IUTAM symposium on advances in nonlinear stochastic mechanics* (eds A Naess, S Krenk), pp. 269–278. Dordrecht, The Netherlands: Kluwer.
24. Kristensen L, Jensen NO. 1979 Lateral coherence in isotropic turbulence and in the natural wind. *Bound. Layer Meteorol.* **17**, 353–373. (doi:10.1007/BF00117924)
25. von Kàrmàn T. 1948 Progress in the statistical theory of turbulence. *Proc. Natl Acad. Sci. USA* **34**, 530–539. (doi:10.1073/pnas.34.11.530)
26. Mignolet MP, Spanos PD. 1992 Simulation of homogeneous two-dimensional random fields: part I – AR and ARMA models. *J. Appl. Mech.* **59**, 260–269. (doi:10.1115/1.2899499)
27. Spanos PD, Mignolet MP. 1992 Simulation of homogeneous two-dimensional random fields: part II – MA and ARMA models. *J. Appl. Mech.* **59**, 270–277. (doi:10.1115/1.2899500)
28. Di Paola M, Zingales M. 2008 Stochastic differential calculus for wind-exposed structures with auto-regressive continuous (ARC) filters. *J. Wind Eng. Ind. Aerodyn.* **96**, 2403–2417. (doi:10.1016/j.jweia.2008.04.003)
29. Kareem A. 2008 Numerical simulation of wind effects: a probabilistic perspective. *J. Wind Eng. Ind. Aerodyn.* **96**, 1472–1497. (doi:10.1016/j.jweia.2008.02.048)
30. Krenk S. 2011 Explicit calibration and simulation of stochastic fields by low-order ARMA processes. *COMPDYN 2011. ECCOMAS thematic conference on computational methods in structural dynamics and earthquake engineering* (eds M Papadrakakis, M Fragiadakis, V Plevris), paper 550, pp. 1–10. Barcelona, Spain: ECCOMAS.
31. Møller RN, Krenk S, Svendsen MN. Submitted Turbulent wind response of long-span bridges including flutter. Department of Mechanical Engineering, Technical University of Denmark.
32. Olver FWJ, Lozier DW, Boisvert RF, Clark CW. 2010 *NIST handbook of mathematical functions*. Cambridge, UK: Cambridge University Press.

P2

Time simulation of turbulent wind response and flutter of long-span bridges

Randi Nøhr Møller, Steen Krenk & Martin Nymann Svendsen

Wind Engineering and Industrial Aerodynamics,
(submitted, 2019).

Time simulation of turbulent wind response and flutter of long-span bridges

Randi N. Møller[a,b,*], Steen Krenk[a], Martin N. Svendsen[b]

[a] *Department of Mechanical Engineering*
Technical University of Denmark, DK-2800 Lyngby, Denmark

[b] *Rambøll, Hannemanns Alle, DK-2300 Copenhagen, Denmark*

Abstract

An efficient procedure for simulation of time domain response analysis of long-span bridges to turbulent wind load is presented. The wind load is simulated by a convected three-dimensional orthotropic wind field with separate turbulence length-scales and intensities in the along wind and the two transverse directions. Efficiency of the simulation is obtained by using eight memory steps with exponentially increasing distance from current time, leading to a very accurate representation of the statistical properties of the wind field. The self-induced aerodynamic forces are implemented in the analysis via a discrete form of a local filter with one or two steps, and an efficient procedure is developed for determination of the filter parameters. The local form of the filter enables reduction of the total equation system to the size of the bridge model in still air. The detailed representation of the wind field automatically includes the feature that points with large horizontal separation exhibit reduced coherence of the low-frequency components, an important feature, verified in several recent measurement programs, that reduces the turbulent loading on long-span bridges and thereby increases the flutter velocity. Furthermore, the representation of the wind field contains a separate transverse length scale of importance for the resulting load. The simulation method is sufficiently general to permit response analysis of the full bridge structure with two layers of cables, but examples demonstrate rather small effect on the lower modes from the wind load on the cables.

Keywords: Long span bridge, Time domain response, Sequential wind field simulation, Quasi-static condensation, Momentum-based time integration.

1. Introduction

In the design of long span bridges the response due to wind loading plays an important role. In recent years, significant research attention has been given to this field which includes representation of turbulent wind, analysis of wind-structure interaction and simulation of both the wind load and the structural response in time domain response calculations. The time domain response calculations is of special interest when considering wind load on vehicles, fatigue and non-linear dynamics.

*Corresponding author

Email addresses: `rnm@ramboll.dk` (Randi N. Møller), `sk@mek.dtu.dk` (Steen Krenk), `mnns@ramboll.dk` (Martin N. Svendsen)

A correct representation of turbulent wind is crucial for representing the dynamic loading on wind-sensitive structures. The transverse coherence is of particular interest for long-span bridges where the integral length scale of the turbulence is smaller than the size of the considered structure. The turbulent wind field is most often represented by the auto-spectral density of the wind components of interest to give the stochastic single-point loading, supplemented by a coherence function representation to provide the transverse field properties. The covariance function is generally chosen on the empirical form $\exp(-C\omega\Delta y/U)$ suggested by Davenport [1]. This representation suggests a positive correlation at any separation Δy, which is in conflict with a full representation of an incompressible field, where it is evident that the turbulence components must be negatively correlated at certain distances to provide a zero mean flow. To address this issue an alternative covariance representation was suggested by Krenk [2] based on homogenious isotropic turbulence and a von Kàrmàn representation of the along wind spectral density [3, 4]. Recent data studies have demonstrated the improved representation of measured wind data [5, 6, 7], although only an exponential simplification was used.

The simulation of turbulent wind can either be done by an inverse Fourier transform of a spectral representation of the wind field or by sequential models as e.g. the auto-regressive moving-average (ARMA) models. The former has been widely used for time domain simulation of bridge loading [8, 9]. The basic format of a multi-component Fourier simulation was introduced by Shinozuka and Jan [10] and since then a number of contributions have been made in order to increase computational efficiency, applicability to large systems etc. [11, 12, 13]. For large systems the Fourier simulated wind fields are challenged by large storage requirements. Various formulations are discussed in [14]. Alternatively, application of sequential simulation methods allow for step-wise updates of the wind load based on a relatively short data memory. Early contributions concerning sequential multivariate random process simulations were made by Mignolet and Spanos [15, 16] and the multivariate ARMA representation of wind fields in relation to dynamic response of structures was discussed by Li and Kareem [17]. The idea of utilizing a full-field description of the turbulent wind to apply a low order auto-regressive model was introduced by Krenk [18], and recently a sequential conditional mean-field simulation procedure was proposed, in which the coefficient matrices are determined explicitly in terms of conditional means and conditional covariances of the wind field, using a compact non-uniformly spaced set of previous field values, [19].

The aerodynamic wind–bridge interaction is another main field of interest for bridge response as well as bridge stability calculations. The basic principles are carried over from Theodorsen's classic airfoil theory [20] that describes the actions on an oscillating flat plate in a fluid flow, and subsequent application to bridge deck flutter was introduced by Scanlan and Tomko [21]. The fluid–structure interaction is typically described by the frequency dependent aerodynamic derivatives, and thus it is necessary to transform this representation into time domain. This can be done by indicial functions as suggested by Scanlan et al. [22], or by the computationally more efficient use of rational function representations introduced by Eversman and Tewari [23] and used for bridge deck flutter by Chen et al. [24] and Høgsberg et al. [25, 26]. More recently the aero-elastic forces have been introduced in a finite element framework via additional degrees of freedom by Øiseth et al. [27]. Methods based on quasi-steady aerodynamics have also been suggested as a computationally efficient, although less accurate alternative [28, 29].

This paper presents a state-space formulation for a long suspension bridge, including self-excited aerodynamic forces. The bridge response is investigated using an anisotropic

full-field sequential simulation procedure, recently developed in [19]. The combination of the recursive wind field simulation procedure using a memory with 6–10 non-equally spaced steps and a momentum-based time integration of the extended state-space equations, including the aerodynamic derivatives via a first-order filter representation, results in a very flexible model formulation in which the points used for wind velocity simulation and aerodynamic loads can be configured freely, e.g. including bridge deck, cables and hangers, or a smaller model including only the bridge deck. The results demonstrate highly accurate representation of the characteristics of the three-dimensional wind field and illustrate the rather strong influence of the transverse correlation length on the bridge response. Furthermore, the computations demonstrate the high computational efficiency and moderate storage requirements of the proposed procedure.

2. Aerodynamic system

The aerodynamic system in relation to long span bridges can be understood as the structural system determined by mass, stiffness and damping of the structure and an aerodynamic load representation. The aerodynamic loading consists of contributions from both the mean wind and from the wind turbulence, where the turbulent wind components of main interest are the along wind component and the vertical component. State-of-the-art calculations of aerodynamic response is neglecting the higher order turbulence contribution leaving a pure mean wind contribution and a mixed mean wind and turbulence contribution. The mixed contribution is referred to as the buffeting load and is treated as a direct load determined solely by the wind speeds, static aerodynamic coefficients, bridge deck geometry and admittance functions. The mean wind contribution is influencing the dynamic system due to the vibrations of the bridge deck and the loading of the structure is therefore referred to as self-excited forces. Figure 1 shows the bridge cross-section with cross-sectional forces $\mathbf{f} = [f_1, f_3, f_\theta]^T$, the mean wind speed U, and the turbulence components u and w.

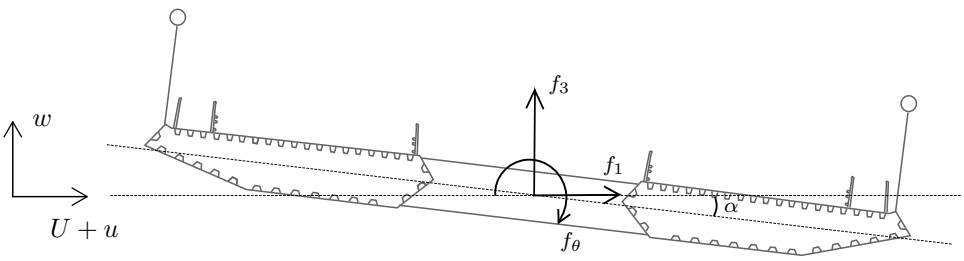

Figure 1: Aerodynamic forces.

The equation of motion of the full aerodynamic system is written with the structural terms on the left hand side and with the buffeting load and the self-excited forces on the right hand side of the equation

$$\mathbf{M}_s\ddot{\mathbf{q}}(t) + \mathbf{C}_s\dot{\mathbf{q}}(t) + \mathbf{K}_s\mathbf{q}(t) = \mathbf{f}_a(t) + \mathbf{f}_e(t). \tag{1}$$

Here $\mathbf{M}_s$, $\mathbf{C}_s$ and $\mathbf{K}_s$ are the structural mass, damping and stiffness matrices, respectively, and $\mathbf{q} = [q_1, q_3, q_\theta]^T$ is the displacement vector, $\mathbf{f}_e$ is the buffeting load, and $\mathbf{f}_a$ represents the self-excited aerodynamic forces. The self-excited forces depend on the displacement history

of the structure as expressed by the convolution integral

$$\mathbf{f}_a = \int_0^\infty \mathbf{Q}(\tau)\mathbf{q}(t-\tau)\, d\tau, \tag{2}$$

where $\mathbf{Q}(\tau)$ is the kernel function by which the self-excited forces are included as a sum of effects from time $t-\tau$, where τ is the time lag. Assuming a harmonic force and response

$$\mathbf{f}_a = \bar{\mathbf{f}}_a\, \mathrm{e}^{i\omega t}\,, \qquad \mathbf{q} = \bar{\mathbf{q}}\, \mathrm{e}^{i\omega t}, \tag{3}$$

where the bar denotes the complex amplitude, the self-excited forces can be expressed in the frequency domain by the relation

$$\bar{\mathbf{f}}_a = \bar{\mathbf{Q}}(\omega)\bar{\mathbf{q}}, \tag{4}$$

where $\bar{\mathbf{Q}}(\omega)$ is the Fourier transform of the kernel function. The aerodynamic, self-excited forces are most commonly defined by the geometry-specific, non-dimensional aerodynamic derivatives P_n^*, H_n^*, A_n^*, $n = 1, 2, ..., 6$, whereby the Fourier transform of the kernel function takes the form, [21],

$$\frac{\bar{\mathbf{Q}}}{\frac{1}{2}\rho U^2 B} = \frac{\omega_*^2}{B}\begin{bmatrix} P_4^* + iP_1^* & P_6^* + iP_5^* & B(P_3^* + iP_2^*) \\ H_6^* + iH_5^* & H_4^* + iH_1^* & B(H_3^* + iH_2^*) \\ B(A_6^* + iA_5^*) & B(A_4^* + iA_1^*) & B^2(A_3^* + iA_2^*) \end{bmatrix}, \tag{5}$$

with the reduced frequency $\omega_* = \omega B/U$ and with B and ρ as the reference width of the bridge deck and the air density.

The buffeting load is defined from geometrical considerations of how the turbulent wind affects the structure. For the geometrical considerations the deck is considered motionless wherefore the buffeting contribution is reduced by frequency dependent admittance functions to include effects of the dynamic structure. The frequency representation of the wind loading of the bridge is

$$\bar{\mathbf{f}}_e = \mathbf{B}_f(\omega)\bar{\mathbf{u}}(\omega) \tag{6}$$

where $\bar{\mathbf{u}} = [\bar{u}, \bar{w}]^T$ is the frequency representation of the the wind velocities found as the Fourier transform of the velocity vector $\mathbf{u}(t) = [u(t), w(t)]^T$. The matrix $\mathbf{B}_f(\omega)$ gives the relation between the relevant wind components and the bridge deck loads. From buffeting theory – see e.g. [30] – the relation is given as

$$\mathbf{B}_f(\omega) = \frac{\rho U B}{2}\begin{bmatrix} 2(D/B)\bar{C}_D A_{yu}(\omega) & ((D/B)C_D' - \bar{C}_L)A_{yw}(\omega) \\ 2\bar{C}_L A_{zu}(\omega) & C_L' + (D/B)\bar{C}_D A_{zw}(\omega) \\ 2B\bar{C}_M A_{\theta u}(\omega) & BD_M' A_{\theta w}(\omega) \end{bmatrix} \tag{7}$$

where $A_{yu}(\omega), ..., A_{\theta w}(\omega)$ are the frequency dependent aerodynamic admittance functions, $\bar{C}_D$, $\bar{C}_L$ and $\bar{C}_M$ are the static coefficients related to drag, lift and moment and $\bar{C}_D'$, $\bar{C}_L'$ and $\bar{C}_M'$ are the coefficient derivatives with respect to the angle α of the bridge deck as shown in Fig. 1.

2.1. Extended state space representation

The convolution integral in (2) is computationally expensive and a rational function approximation with increased efficiency has been suggested first for airfoil theory [23] and later

introduced in bridge flutter assessment [24, 25, 26]. The idea is to represent the aerodynamic force by instantaneous terms proportional to the displacement, velocity and acceleration as well as one or more memory terms that can be included in the equation of motion as additional state variables. This suggests writing the kernel function in the form

$$\mathbf{Q}(\tau) = -\mathbf{M}_a\ddot{\delta}(\tau) - \mathbf{C}_a\dot{\delta}(\tau) - \mathbf{K}_a\delta(\tau) + \sum_{j=1}^{J}\mathbf{Q}_j(\tau), \tag{8}$$

where $\delta(\ )$ is the generalized delta function, $\mathbf{M}_a$, $\mathbf{C}_a$ and $\mathbf{K_a}$ are referred to as the aerodynamic mass, damping and stiffness and the functions $\mathbf{Q}_j$ represent the memory part of the kernel function. Substitution of this into the convolution integral in equation (2) yields the aerodynamic forces

$$\mathbf{f}_a = -\mathbf{M}_a\ddot{\mathbf{q}}(t) - \mathbf{C}_a\dot{\mathbf{q}}(t) - \mathbf{K}_a\mathbf{q}(t) + \sum_{j=1}^{J}\mathbf{f}_j, \tag{9}$$

where

$$\mathbf{f}_j = \int_0^\infty \mathbf{Q}_j(\tau)\mathbf{q}(t-\tau)\,d\tau. \tag{10}$$

This representation of the self-excited forces suggests that the contribution from the mean wind can partly be considered as a modification of the overall system mass, damping and stiffness dependent on the mean wind speed. When introducing the expression of the aerodynamic self-excited forces (9) into the equation of motion (1), it takes the form

$$\mathbf{M}\ddot{\mathbf{q}}(t) + \mathbf{C}\dot{\mathbf{q}}(t) + \mathbf{K}\mathbf{q}(t) = \sum_{j=1}^{J}\mathbf{f}_j + \mathbf{f}_e(t), \tag{11}$$

with system mass, damping and stiffness matrices $\mathbf{M} = \mathbf{M}_s + \mathbf{M}_a$, $\mathbf{C} = \mathbf{C}_s + \mathbf{C}_a$ and $\mathbf{K} = \mathbf{K}_s + \mathbf{K}_a$, respectively. The memory part of the aerodynamic forces is causal, and this implies that $\mathbf{Q}_j = 0$ for $\tau < 0$. In the present paper the aerodynamic properties of each cross-section are identical. When the kernel functions are assumed of exponential form this corresponds to the format

$$\mathbf{Q}_j = \mathbf{D}_j \mathrm{e}^{-\gamma_j\tau}\,, \quad \tau \geq 0, \tag{12}$$

where the global matrix $\mathbf{D}_j$ contains identical diagonal block matrices, each representing the properties of the individual cross-section. If the aerodynamic properties of the cross-sections vary along the bridge deck, each diagonal block in the global matrix $\mathbf{D}_j$ may be different and associated with individual values of the decay parameter γ_j for different cross-sections.

When inserting the exponential representation of the kernel function into the convolution integral in (10), the memory part of the self-excited forces are found in the form

$$\mathbf{f}_j(t) = \int_0^\infty \mathbf{D}_j \mathrm{e}^{-\gamma_j\tau}\mathbf{q}(t-\tau)\,d\tau. \tag{13}$$

In order to represent the memory forces as additional state variables in the equation of motion the objective is to find a first order differential equation giving the relation between the memory forces and the displacements. The first time derivative of the memory force is found by differentiating the displacement vector, whereby integration by parts gives

$$\dot{\mathbf{f}}_j(t) = -\mathbf{D}_j\left[\mathrm{e}^{-\gamma_j\tau}\mathbf{q}(t-\tau)\right]_{\tau=0}^{\infty} - \gamma_j\int_0^\infty \mathbf{D}_j\mathrm{e}^{-\gamma_j\tau}\mathbf{q}(t-\tau)\,d\tau. \tag{14}$$

It follows from (13) that the integral defines the force $\mathbf{f}_j$, leading to the first-order differential equation

$$\dot{\mathbf{f}}_j + \gamma_j \mathbf{f}_j = \mathbf{D}_j \mathbf{q}. \tag{15}$$

Each memory term of the aerodynamic forces can then be introduced in the equation of motion as an additional state-space variable.

When introducing the velocity as a state-space variable $\mathbf{v}$ via the momentum relation $\mathbf{M}\mathbf{v} = \mathbf{M}\dot{\mathbf{q}}$ a convenient first order format of the equation of motion can be written as

$$\begin{bmatrix} \mathbf{C} & \mathbf{M} & \mathbf{0} \\ \mathbf{M} & \mathbf{0} & \mathbf{0} \\ \mathbf{0} & \mathbf{0} & \mathbf{I}_{J\times J} \end{bmatrix} \begin{bmatrix} \dot{\mathbf{q}} \\ \dot{\mathbf{v}} \\ \dot{\mathbf{f}} \end{bmatrix} + \begin{bmatrix} \mathbf{K} & \mathbf{0} & -\mathbf{I}_{1\times J} \\ \mathbf{0} & -\mathbf{M} & \mathbf{0} \\ -\mathbf{D} & \mathbf{0} & \mathbf{\Gamma} \end{bmatrix} \begin{bmatrix} \mathbf{q} \\ \mathbf{v} \\ \mathbf{f} \end{bmatrix} = \begin{bmatrix} \mathbf{f}_e \\ \mathbf{0} \\ \mathbf{0} \end{bmatrix}, \tag{16}$$

where the matrices $\mathbf{D}$ and $\mathbf{\Gamma}$, and the vector $\mathbf{f}$ from the J convolution integrals are defined as

$$\mathbf{D} = \begin{bmatrix} \mathbf{D}_1 \\ \vdots \\ \mathbf{D}_J \end{bmatrix}, \quad \mathbf{\Gamma} = \begin{bmatrix} \gamma_1 \mathbf{I} & \cdots & \mathbf{0} \\ \vdots & \ddots & \vdots \\ \mathbf{0} & \cdots & \gamma_J \mathbf{I} \end{bmatrix}, \quad \mathbf{f} = \begin{bmatrix} \mathbf{f}_1 \\ \vdots \\ \mathbf{f}_J \end{bmatrix}, \tag{17}$$

and the block diagonal unit matrix $\mathbf{I}_{J\times J}$ and the row of unit matrices $\mathbf{I}_{1\times J}$ complete the equations in a consistent way. If the aerodynamic properties vary along the deck, each diagonal block matrix $\mathbf{D}_j$ will consist of individual block matrices corresponding to each cross-section, and similarly the global matrix $\gamma_j \mathbf{I}$ is replaced by individual diagonal sub-matrices representing each cross-section. The implementation of the general format is quite straight-forward.

Stability of the system is closely related to the energy balance, and in the numerical integration of the system equations it is of interest to reproduce the energy balance equation as closely as possible. An energy balance equation for the wind-loaded structure is obtained by pre-multiplication of the equations of motion (16) with the block vector $[\dot{\mathbf{q}}^T, -\dot{\mathbf{v}}^T, \mathbf{0}^T]$, leading to

$$\frac{d}{dt}\left(\tfrac{1}{2}\mathbf{v}^T\mathbf{M}\mathbf{v} + \tfrac{1}{2}\mathbf{q}^T\mathbf{K}\mathbf{q}\right) = \mathbf{v}^T\left(\mathbf{f}_e + \sum_j \mathbf{f}_j\right) - \mathbf{v}^T\mathbf{C}\mathbf{v}\,, \tag{18}$$

where the velocity $\mathbf{v} = \dot{\mathbf{q}}$ has been introduced. The left hand side of the equation is the rate of change of the energy of the structure, consisting of the sum of the kinetic energy and the elastic energy. The right hand side contains the rate of work of the sum of the external force $\mathbf{f}_e$ and the contributions $\mathbf{f}_j$ to the aerodynamic forces, and the rate of dissipation induced by the damping matrix $\mathbf{C}$. It is noted that the system matrices $\mathbf{M}$, $\mathbf{K}$ and $\mathbf{C}$ contain aerodynamic contributions according to (11). In principle, a more detailed energy balance can be obtained by including self-induced aerodynamic forces $\mathbf{f}$ in the last position of the pre-multiplication vector. However, this has not been included here, as it is difficult to use directly due to its non-conservative character.

2.2. Aerodynamic matrices and parameter identification

The relation between the aerodynamic derivatives and the aerodynamic system parameter matrices, $\mathbf{M}_a$, $\mathbf{C}_a$, $\mathbf{K}_a$, $\mathbf{D}$ and $\mathbf{\Gamma}$ is now established, followed by the introduction of a simple algorithmic procedure for identifying the aerodynamic system parameters numerically. In this section the matrices represent the variables associated with an individual cross-section

without introducing a special notation for this. The parameter relations are found via the Fourier transform of the kernel function

$$\bar{\mathbf{Q}}(\omega) = \int_0^\infty \mathbf{Q}(\tau)\mathrm{e}^{-i\omega\tau}\, d\tau. \tag{19}$$

The exponential representation of the memory part of the kernel function is substituted from equation (12) whereby the Fourier transform of each memory part is found on the simple form

$$\bar{\mathbf{Q}}_j(\omega) = \mathbf{D}_j \int_0^\infty \mathrm{e}^{-(\gamma_j + i\omega)\tau}\, d\tau = \frac{\mathbf{D}_j}{\gamma_j + i\omega}. \tag{20}$$

The Fourier transform of the entire kernel function presented in equation (8) is then found using the same normalization as in (5)

$$\frac{\bar{\mathbf{Q}}}{\frac{1}{2}\rho U^2 B} = \omega_*^2 \mathbf{M}_a^* - i\omega_* \mathbf{C}_a^* - \mathbf{K}_a^* + \sum_j \frac{\mathbf{D}_j^*}{\gamma_j^* + i\omega_*}, \tag{21}$$

where the normalized aerodynamic system matrices and memory parameters are given as

$$\mathbf{M}_a^* = \mathbf{M}_a/(\tfrac{1}{2}\rho B^3), \quad \mathbf{C}_a^* = \mathbf{C}_a/(\tfrac{1}{2}\rho U B^2), \quad \mathbf{K}_a^* = \mathbf{K}_a/(\tfrac{1}{2}\rho U^2 B) \tag{22}$$

and

$$\mathbf{D}_j^* = \mathbf{D}_j/(\tfrac{1}{2}\rho U^3), \quad \gamma_j^* = \gamma_j B/U. \tag{23}$$

The relations between the aerodynamic derivatives and the aerodynamic system matrices can be established by comparing the Fourier transform of the kernel function in (5) with the expression in (21). For clarity the relation is split into the real part

$$\mathbf{M}_a^* - \frac{1}{\omega_*^2}\mathbf{K}_a^* + \frac{1}{\omega_*^2}\sum_j \frac{\gamma_j^*}{\gamma_j^{*2} + i\omega_*^2}\mathbf{D}_j^* = \frac{1}{B}\begin{bmatrix} P_4^* & P_6^* & BP_3^* \\ H_6^* & H_4^* & BH_3^* \\ BA_6^* & BA_4^* & B^2A_3^* \end{bmatrix} \tag{24}$$

and the imaginary part

$$-\frac{1}{\omega_*}\mathbf{C}_a^* - \frac{1}{\omega_*}\sum_j \frac{1}{\gamma_j^{*2} + i\omega_*^2}\mathbf{D}_j^* = \frac{1}{B}\begin{bmatrix} P_1^* & P_5^* & BP_2^* \\ H_5^* & H_1^* & BH_2^* \\ BA_5^* & BA_1^* & B^2A_2^* \end{bmatrix} \tag{25}$$

A method for parameter identification was presented by Scanlan et al. [22] using non-linear least squares fitting. This method has been adopted by Caracoglia and Jones [31] with a discussion of lack of robustness, and an improved iterative algorithmic approach for parameter fitting was later presented by Zhang et al. [32] providing a numerical scheme with multiple nested loops to search for the optimal exponentials. Here, a simple identification procedure is presented based on the least squares solution of an over-determined equation system. The equally weighted minimization process is written as

$$\min_{\gamma_j \in \mathbb{R}_+} \{(\mathbf{A}\mathbf{x} - \mathbf{b})^T(\mathbf{A}\mathbf{x} - \mathbf{b})\} \tag{26}$$

where $\mathbf{A}$ is the system matrix containing the relations between the aerodynamic derivatives and the aerodynamic system matrices as they appear of (24) and (25),

$$\mathbf{A} = \begin{bmatrix} \mathbf{I} & \mathbf{0} & -(1/\omega_*^2)\mathbf{I} & \gamma_1/(\gamma_1^{*2} + \omega_*^2)\mathbf{I} & \cdots & \gamma_n/(\gamma_n^{*2} + \omega_*^2)\mathbf{I} \\ \mathbf{0} & -(1/\omega_*)\mathbf{I} & \mathbf{0} & \gamma_1/(\gamma_1^{*2} + \omega_*^2)\mathbf{I} & \cdots & \gamma_n/(\gamma_n^{*2} + \omega_*^2)\mathbf{I} \end{bmatrix} \tag{27}$$

The number of rows in $\mathbf{A}$ is $18m$, where m is the number of data points. The vector $\mathbf{b}$ contains the frequency dependent aerodynamic derivatives via the Fourier transform of the kernel function

$$\mathbf{b}^T = \left[\mathrm{Re}[\widetilde{\widetilde{\mathbf{Q}}}^*]^T\,, \quad \mathrm{Im}[\widetilde{\widetilde{\mathbf{Q}}}^*]^T\right]. \tag{28}$$

Finally, the vector $\mathbf{x}$ is found by solving the overdetermined linear system $\mathbf{Ax} = \mathbf{b}$ and contains the elements of the aerodynamic system matrices for a particular set of γ_j^*, $j = 1, 2, ..., n$. This gives $\mathbf{x}$ in the form

$$\mathbf{x}^T = \left[\widetilde{\mathbf{M}}^{*T}, \quad \widetilde{\mathbf{C}}^{*T}, \quad \widetilde{\mathbf{K}}^{*T}, \quad \widetilde{\mathbf{D}}_1^{*T}, \quad \cdots, \quad \widetilde{\mathbf{D}}_n^{*T}\right]. \tag{29}$$

The tilde denotes a rearrangement of the matrix so that the columns in the matrix are stacked in a vector, here exemplified by a matrix $\mathbf{V}$ containing vectors $\mathbf{v}_j$, $j = 1, 2, ..., n$ as columns:

$$\mathbf{V} = \left[\mathbf{v}_1, \quad \mathbf{v}_2, \quad \cdots, \quad \mathbf{v}_n\right] \quad \Rightarrow \quad \widetilde{\mathbf{V}} = \left[\mathbf{v}_1^T, \quad \mathbf{v}_2^T, \quad \cdots, \quad \mathbf{v}_n^T\right]^T \tag{30}$$

The least square optimization requires an initial guess on the values of γ_j and from experience a good initial guess is $\gamma_j = 1$. Specific results are given in section 3

2.3. Time integration

Generalizing the momentum based time integration procedure, presented e.g. in [33], the discretized equations are obtained by integrating the extended first-order equations of motion (16) over a time interval h,

$$\begin{bmatrix} \mathbf{C} & \mathbf{M} & \mathbf{0} \\ \mathbf{M} & \mathbf{0} & \mathbf{0} \\ \mathbf{0} & \mathbf{0} & \mathbf{I}_{J\times J} \end{bmatrix} \begin{bmatrix} \int_h \dot{\mathbf{q}}\,dt \\ \int_h \dot{\mathbf{v}}\,dt \\ \int_h \dot{\mathbf{f}}\,dt \end{bmatrix} + \begin{bmatrix} \mathbf{K} & \mathbf{0} & -\mathbf{I}_{1\times J} \\ \mathbf{0} & -\mathbf{M} & \mathbf{0} \\ -\mathbf{D} & \mathbf{0} & \mathbf{\Gamma} \end{bmatrix} \begin{bmatrix} \int_h \mathbf{q}\,dt \\ \int_h \mathbf{v}\,dt \\ \int_h \mathbf{f}\,dt \end{bmatrix} = \begin{bmatrix} \int_h \mathbf{f}_e\,dt \\ \mathbf{0} \\ \mathbf{0} \end{bmatrix} \tag{31}$$

A discrete form is obtained by representing the integrals by the second order accurate trapezoidal rule in terms of the mean value, denoted by an overbar as e.g. $\bar{\mathbf{q}} = \frac{1}{2}(\mathbf{q}_n + \mathbf{q}_{n+1})$, where the subscripts $n+1$ and n refer to the end points of the time interval. When the increment is denoted by $\Delta\mathbf{q} = \mathbf{q}_{n+1} - \mathbf{q}_n$ the discretized form is

$$\begin{bmatrix} \mathbf{C} & \mathbf{M} & \mathbf{0} \\ \mathbf{M} & \mathbf{0} & \mathbf{0} \\ \mathbf{0} & \mathbf{0} & \mathbf{I}_{J\times J} \end{bmatrix} \begin{bmatrix} \Delta\mathbf{q} \\ \Delta\mathbf{v} \\ \Delta\mathbf{f} \end{bmatrix} + h \begin{bmatrix} \mathbf{K} & \mathbf{0} & -\mathbf{I}_{1\times J} \\ \mathbf{0} & -\mathbf{M} & \mathbf{0} \\ -\mathbf{D} & \mathbf{0} & \mathbf{\Gamma} \end{bmatrix} \begin{bmatrix} \bar{\mathbf{q}} \\ \bar{\mathbf{v}} \\ \bar{\mathbf{f}} \end{bmatrix} = h \begin{bmatrix} \bar{\mathbf{f}}_e \\ \mathbf{0} \\ \mathbf{0} \end{bmatrix}. \tag{32}$$

These equations serve as basis of the numerical time integration discussed below, but are also used for a linear stability analysis as discussed in Section 5.2.

An energy balance for the discretized equations is found by pre-multiplication of (32) by $[\Delta\mathbf{q}^T, -\Delta\mathbf{v}^T, \mathbf{0}^T]$. When the mean-value terms are expressed using the relation

$$\Delta\mathbf{q}^T\mathbf{K}\bar{\mathbf{q}} = \left[\tfrac{1}{2}\mathbf{q}^T\mathbf{K}\mathbf{q}\right]_n^{n+1}, \tag{33}$$

the energy balance equation of the descretized equations of motion takes the form

$$\left[\tfrac{1}{2}\mathbf{v}^T\mathbf{M}\mathbf{v} + \tfrac{1}{2}\mathbf{q}^T\mathbf{K}\mathbf{q}\right]_n^{n+1} = \Delta\mathbf{q}^T\left(\bar{\mathbf{f}}_e + \sum_j \bar{\mathbf{f}}_j\right) - \frac{1}{h}\Delta\mathbf{q}^T\mathbf{C}\Delta\mathbf{q}. \tag{34}$$

The discrete energy balance is a fairly direct reproduction of the differential form (18) in which the rate of change of the mechanical energy is replaced by its increment over the integration time interval h and the velocity is replaced by its integral mean $h^{-1}\Delta\mathbf{q}$ in the external work and dissipation terms on the right hand side of the equation.

When solving the full equations of motion with aerodynamic forces (32), the equations for the memory-based aerodynamic forces are expressed in terms of the individual contributions $\mathbf{f}_j$, and the corresponding equations are used to express the current unknown force $\mathbf{f}_{n+1}^j$ in terms of the value in the previous step $\mathbf{f}_n^j$ together with the displacement vectors $\mathbf{q}_{n+1}$ and $\mathbf{q}_n$. Similarly, the velocity $\mathbf{v}_{n+1}$ is expressed in terms of its previous value $\mathbf{v}_n$ and the displacement vectors $\mathbf{q}_{n+1}$ and $\mathbf{q}_n$. The first row in (32) can then be written as a set of equations for the displacement increment $\Delta\mathbf{q}$ in terms of the values of the state-space variables at step n. Thus, the size of the system of equations to be solved corresponds to the number of degrees-of-freedom in the structural model. The algorithm is presented in Table 1. It is noted that the inverse of the algorithmic stiffness matrix $\mathbf{K}_*$ should not be computed directly, but merely represents the solution of an equation system, conveniently solved in terms of the corresponding triangular factors, calculated outside the time-step loop.

Table 1: Numerical integration algorithm.

(1) System matrices: $\mathbf{K}, \mathbf{C}, \mathbf{M}, \mathbf{D}, \mathbf{\Gamma}$

$$\mathbf{K}_* = \mathbf{K} + \frac{2}{h}\mathbf{C} + \left(\frac{2}{h}\right)^2 \mathbf{M} - \sum_j \frac{1}{2/h + \gamma_j}\mathbf{D}_j$$

(2) Initial conditions:

$$\mathbf{q}_0,\ \mathbf{v}_0,\ \mathbf{f}_0$$

(3) Displacement increment:

$$\Delta\mathbf{q} = 2\mathbf{K}_*^{-1}\Big[\bar{\mathbf{f}}_e - \mathbf{K}\mathbf{q}_n + \frac{2}{h}\mathbf{M}\mathbf{v}_n + \sum_j \frac{1}{2/h + \gamma_j}\Big(\frac{2}{h}\mathbf{f}_n^j + \mathbf{D}_j\mathbf{q}_n\Big)\Big]$$

(4) State vector update:

$$\mathbf{q}_{n+1} = \mathbf{q}_n + \Delta\mathbf{q}$$

$$\mathbf{v}_{n+1} = \mathbf{v}_n + 2\Big(\frac{1}{h}\Delta\mathbf{q} - \mathbf{v}_n\Big)$$

$$\mathbf{f}_{n+1}^j = \mathbf{f}_n^j + \frac{2}{2/h + \gamma_j}\Big(\mathbf{D}_j\bar{\mathbf{q}} - \gamma_j\mathbf{f}_n^j\Big)$$

(5) Return to (3) for a new time step or stop

The discrete dynamic equations (32) and the corresponding time integration algorithm in Table 1 represent a direct discretization of the system differential equations (16). For models with high-frequency modes there may be a need for so-called algorithmic damping, a mechanism for dissipating energy from high-frequency modes close to or beyond their aliasing limit. As demonstrated in [33], algorithmic damping that specifically addresses the high-frequency modes may be introduced in the present integration format on two levels – either as a generalized viscous damping, or by additional damping forces generated by a first-order filter. The generalized viscous damping consists in introducing two balanced terms proportional to the stiffness matrix $\mathbf{K}$ and the mass matrix $\mathbf{M}$, respectively, in the diagonal of the first matrix

(a) (b)

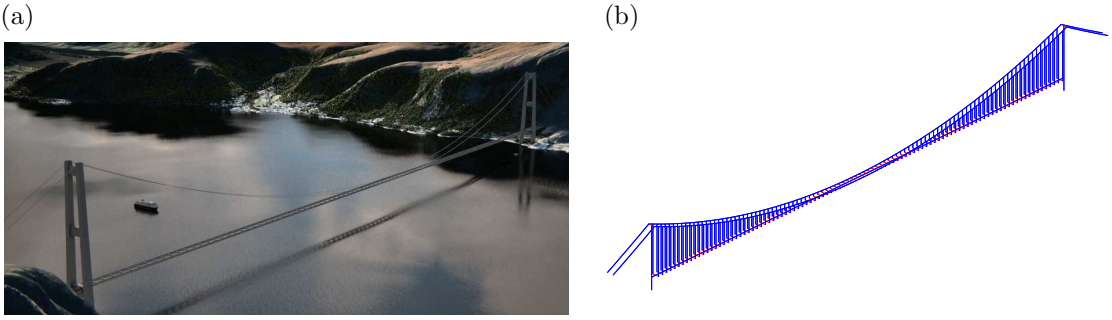

Figure 2: The Sulafjord Bridge: (a) Rendering [37], (b) Finite element model.

in (32),

$$\begin{bmatrix} \mathbf{C}+\frac{1}{2}\alpha h\mathbf{K} & \mathbf{M} & \mathbf{0} \\ \mathbf{M} & -\frac{1}{2}\alpha h\mathbf{M} & \mathbf{0} \\ \mathbf{0} & \mathbf{0} & \mathbf{I}_{J\times J} \end{bmatrix} \begin{bmatrix} \Delta\mathbf{q} \\ \Delta\mathbf{v} \\ \Delta\mathbf{f} \end{bmatrix} + h \begin{bmatrix} \mathbf{K} & \mathbf{0} & -\mathbf{I}_{1\times J} \\ \mathbf{0} & -\mathbf{M} & \mathbf{0} \\ -\mathbf{D} & \mathbf{0} & \mathbf{\Gamma} \end{bmatrix} \begin{bmatrix} \bar{\mathbf{q}} \\ \bar{\mathbf{v}} \\ \bar{\mathbf{f}} \end{bmatrix} = h \begin{bmatrix} \bar{\mathbf{f}}_e \\ \mathbf{0} \\ \mathbf{0} \end{bmatrix}. \tag{35}$$

The effect of the new terms can be seen from the energy balance equation, that now takes the form

$$\begin{aligned} \left[\tfrac{1}{2}\mathbf{v}^T\mathbf{M}\mathbf{v}+\tfrac{1}{2}\mathbf{q}^T\mathbf{K}\mathbf{q}\right]_n^{n+1} &= \Delta\mathbf{q}^T\left(\bar{\mathbf{f}}_e+\textstyle\sum_j\bar{\mathbf{f}}_j\right)-\frac{1}{h}\Delta\mathbf{q}^T\mathbf{C}\Delta\mathbf{q} \\ &- \alpha\left(\tfrac{1}{2}\Delta\mathbf{v}^T\mathbf{M}\Delta\mathbf{v}+\tfrac{1}{2}\Delta\mathbf{q}^T\mathbf{K}\Delta\mathbf{q}\right). \end{aligned} \tag{36}$$

It is seen that in contrast to the original viscous dissipation term the additional dissipation terms are scaled by the time-step h and contain a quadratic form of the velocity increment $\Delta\mathbf{v}$. Hereby the algorithmic damping dissipates energy at high frequencies relative to the time-step, while the other terms are system specific and dissipate energy at certain frequencies independent of the time-step. The balanced algorithmic damping is a simple and computationally inexpensive implementation that provides damping with the same frequency dependence as the numerical damping of a traditional Newmark algorithm, [34], however without the distortion of the mechanical energy represented in the damped Newmark algorithm. Alternatively, first-order filters can be applied to provide improved algorithmic damping with frequency dependence corresponding to the generalized-α method, in which the damping is shifted towards higher frequencies [35]. The filter representation of the algorithmic damping force is similar to the present representation of the memory dependent aerodynamic forces, but does not contain any matrices and can therefore be implemented with negligible computational overhead as demonstrated in [33].

3. Bridge model

The structural model used for response calculation is a 3000 m suspension bridge proposed for crossing Sulafjorden in Norway in relation to the Coastal Highway E39 project [36, 37]. In Fig. 2 a rendering of the bridge structure is shown to the left and the finite element model used for response calculations is shown to the right. The suspension cables as well as the hangers are modelled with Green strain bar elements to ease the cable calibration procedure. However, the response calculations are performed on a linearised model. The towers are

Table 2: Still-air frequencies, S/A: symmetric/asymmetric, D/H/T: drag/heave/torsion.

Type	f [Hz]	Type	f [Hz]	Type	f [Hz]	Type	f [Hz]
SD1	0.037	SD2	0.117	SD3/ST1	0.134	AD3	0.182
AD1	0.074	AT1	0.118	AH2	0.137	ST3	0.193
AH1	0.076	SH2	0.126	ST2	0.145	AH3	0.209
SH1	0.091	AD2/AT2	0.129	SH3	0.175	AT3	0.221

modelled with elastic beam elements and the bridge deck is modelled using aero-elastic beam elements with self-excited forces represented via additional degrees of freedom in the system as presented in Section 2.1.

The structural properties are presented here providing information about the overall geometry, structural damping and still-air frequencies. A more detailed description of the structural properties is found in [36]. The distance between the pylons is 3000 m, the sag to span ratio of the suspension cables is 1:10 and the clearance height of the bridge deck is 74 m. Table 2 gives the lowest 16 still-air natural frequencies of the bridge.

The structural damping is implemented in the form of Rayleigh damping

$$\mathbf{C}_s = \alpha \mathbf{M}_s + \beta \mathbf{K}_s \,, \tag{37}$$

corresponding to the modal damping ratios

$$2\zeta_j = \frac{\alpha}{\omega_j} + \beta\omega_j, \quad j = 1, 2, \cdots . \tag{38}$$

The parameters α and β are determined to provide a realistic level of damping with damping ratio $\zeta \simeq 0.32\%$ for the low modes, relevant for flutter, [38]. When setting the damping ratio to $\zeta_* = 0.32\%$ at two frequencies $\omega_a = \omega_1 = 0.232\,\mathrm{rad/s}$ and $\omega_b = \omega_{10} = 0.861\,\mathrm{rad/s}$, the parameters α and β are

$$\alpha = 2\frac{\omega_a\omega_b}{\omega_a + \omega_b}\zeta_* = 1.17 \cdot 10^{-3} s^{-1} \,, \quad \beta = \frac{2}{\omega_a + \omega_b}\zeta_* = 5.85 \cdot 10^{-3} s \tag{39}$$

when the angular frequencies ω_1 and ω_{10} are determined from Table 2.

The bridge deck is a twin-box girder as shown in Fig. 1. However, as no detailed measurements of the aerodynamic coefficients are available for this cross-section at the present stage, the self-excited forces for heave and torsional motion are treated by the Theodorsen theory [20] for a flat plate. The self-excited forces related to drag are implemented based on quasi-steady theory corresponding to instantaneous action, see e.g [30]. The drag, lift and torsion aerodynamic coefficients are set to $\bar{C}_D = 1.20$, $\bar{C}_L = -0.15$ and $\bar{C}_M = 0.30$, and their first derivative with respect to the deck angle α are $C'_D = 0$, $C'_L = 6.3$ and $C'_M = 1.0$. The length of the bridge deck is $L_b = 3000\,\mathrm{m}$, the height is $D = 2.5\,\mathrm{m}$, and the reference width is $B = 13\,\mathrm{m}$. Note, that this is the reference width for applying flat plate theory taking into account the expected effect of an aerodynamically shaped twin-box girder, [39]. The admittance functions are all set to one. The main suspension cables and the hangers have a diameter of $D_c = 1.19\,\mathrm{m}$ and $D_h = 0.10\,\mathrm{m}$, respectively, and the drag coefficient is set to 0.8 for all cables. The drag coefficient for the pylons is 2. Other aerodynamic coefficients are set to zero.

In order to determine the number of memory terms to be included in the representation of the self-excited forces the approximated aerodynamic derivatives for different number of

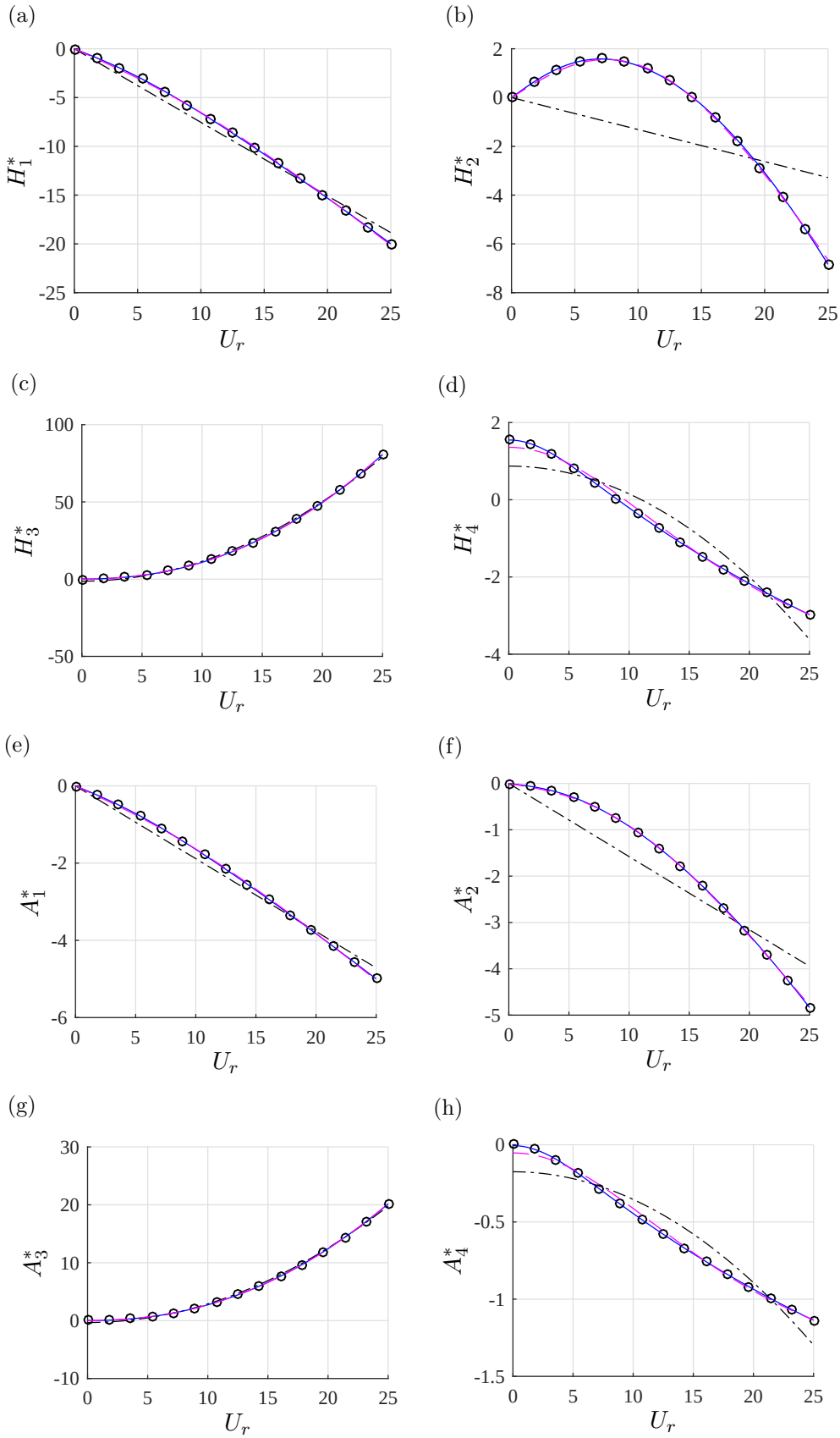

Figure 3: Aerodynamic derivatives, flat plate: (○) analytic plate, (·—,– –,—) 0,1,2 memory terms.

memory terms are shown in Fig. 3. The black dashed-dotted line is without memory terms, the magenta dashed line represents a single memory term, and the blue solid line corresponds to two memory terms. The approximated aerodynamic derivatives are shown together with their theoretical counterparts for flat plate theory shown as black circles. Figure 3 shows that the representation without memory terms results in a rather poor representation of H_2^*, H_4^*, A_2^* and A_4^*. Also, it is seen that the representation of the remaining functions H_1^*, H_2^*, A_1^* and A_2^* is linear, introducing considerable arbitrariness in H_2^* and A_2^*. The single memory term representation is seen to be quite good for all eight derivatives, with only a modest improvement in the two-term representation, visible in the representation of H_4^* and A_4^*. This indicates that a single memory term representation provides sufficient accuracy in the case of flat plate theory. The single memory representation for the considered flat plate is given by the normalized aerodynamic system matrices and memory parameters

$$\mathbf{M}_a^* = \begin{bmatrix} 0 & 0 & 0 \\ 0 & 0.105 & -0.019 \\ 0 & -0.053 & -0.060 \end{bmatrix}, \mathbf{C}_a^* = \begin{bmatrix} 0.036 & 0.012 & 0 \\ -0.023 & 0.281 & -2.051 \\ 0.600 & 0.913 & 3.545 \end{bmatrix}, \mathbf{K}_a^* = \begin{bmatrix} 0 & 0 & 0 \\ 0 & 0.055 & -3.953 \\ 0 & 0.177 & -12.848 \end{bmatrix} \tag{40}$$

and

$$\mathbf{D}_1^* = \begin{bmatrix} 0 & 0 & 0 \\ 0 & 0.017 & 0.593 \\ 0 & 0.056 & 1.927 \end{bmatrix}, \quad \gamma_1^* = 0.310, \tag{41}$$

where the normalization is defined in (22) and (23).

3.1. Reduced model

The structural model is reduced by quasi-static condensation to improve the computational efficiency. The method of quasi-static condensation consists of selecting a number of 'dynamic' degrees of freedom, here denoted $\mathbf{q}_d$, and the remaining 'static' degrees of freedom $\mathbf{q}_s$. In the equations of motion corresponding to the 'static' degrees of freedom the inertia and damping terms are neglected, leading to a representation entirely in terms of the 'dynamic' degrees of freedom,

$$\mathbf{q} = \begin{bmatrix} \mathbf{q}_d \\ \mathbf{q}_s \end{bmatrix} = \begin{bmatrix} \mathbf{I} \\ \mathbf{S} \end{bmatrix} \mathbf{q}_d \,, \quad \mathbf{S} = -\mathbf{K}_{ss}^{-1}\mathbf{K}_{sd} \tag{42}$$

The subscripts d and s on the stiffness matrix $\mathbf{K}$ refer to the blocks corresponding to dynamic or quasi-static degrees of freedom. Extending the method to include motion-induced forces suggests to treat the state proportional aero-elastic terms as the structural mass, damping and stiffness while the memory part of the motion-induced forces are reduced by considering the rate of work. The reduced mass matrix and force vector are found as

$$\bar{\mathbf{M}} = \mathbf{M}_{dd} + \mathbf{S}^T\mathbf{M}_{sd} + \mathbf{M}_{ds}\mathbf{S} + \mathbf{S}^T\mathbf{M}_{ss}\mathbf{S} \,, \quad \bar{\mathbf{f}} = \mathbf{f}_d + \mathbf{S}^T\mathbf{f}_s \tag{43}$$

and the reduction of the other system matrices and load vectors follows the same format.

The quality of the approximation depends on the difference between the quasi-static shape introduced between the master nodes, and the shape in the full dynamic model. Two different levels of reduction, 1:5 and 1:10, are considered to find a relevant level for the present structure. The methodology for the node selection is to choose every fifth or tenth node along the bridge deck and the corresponding nodes in the suspension cables as master nodes. Figure 4 shows

the principle of the master node selection for the case of the 1:5 reduction, with the master nodes indicated by black dots.

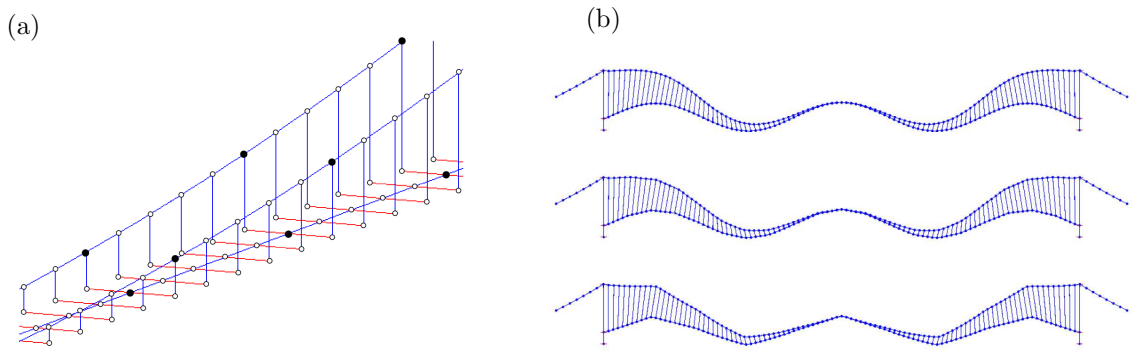

Figure 4: (a) Reduced system nodes, (b) second mode for reduction of 1:1, 1:5, 1:10.

Figure 4(b) shows the second symmetric heave mode determined with the full model at the top, with the 1:5 reduction in the middle, and the 1:10 reduction at the bottom. It is seen that the 1:5 reduction captures the mode shape well for this particular mode, whereas the 1:10 reduction is too coarse. Figure 5 shows the natural frequencies for the full model and the two reduced models. Figure 5(a) shows the natural frequencies for the still air system and Fig. 5(b) shows the natural frequencies for the aero-elastic system with wind speed $U = U_{cr}$, where $U_{cr} = 57\,\mathrm{m/s}$ is the critical wind speed at which the system becomes unstable. Both plots indicate that the 1:5 reduction gives a good representation of modes up to around mode number 15, whereas the 1:10 reduction shows differences at mode 9 and up. The frequencies shown in Fig. 5 suggest that a 1:5 reduction maintains considerable accuracy while decreasing the computational effort, whereas the 1:10 reduction might be too coarse.

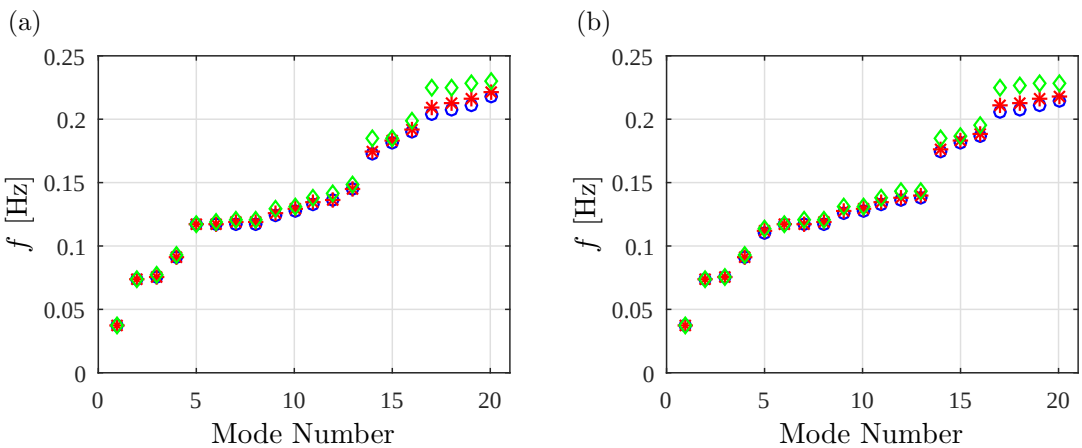

Figure 5: Modal frequencies: (a) Still-air, (b) at critical wind speed. Full model (∘), 1:5 (∗), 1:10 (◇).

4. Wind field model

The wind field description used in this paper consists of a three-dimensional full-field representation of the turbulence described in 3D space and convected across the structure with the mean wind velocity U. The covariance structure of the turbulent wind velocity field is generated by a transformation of an equivalent isotropic field, thereby accounting for the different length scales in the along-wind and transverse directions. This representation is supplemented by an efficient sequential simulation model based on convected 'frozen' turbulence. These aspects are briefly outlined in the following subsections, and a detailed description of the underlying theory can be found in [19].

4.1. Stretched isotropic turbulence

The representation of the turbulent velocity field is based on a transformation of an equivalent isotropic velocity field, and therefore a compact resume of the properties of the isotropic velocity field is first given. In the equivalent homogeneous isotropic field the covariance matrix of the velocity vectors at two points is expressed in terms the vector $\mathbf{r}$ of length $r = |\mathbf{r}|$ connecting the two points. According to the classical theory of isotropic turbulence, [3], the covariance matrix of the velocity vector $\tilde{\mathbf{v}}$ at two points separated by the vector $\mathbf{r}$ is of the form

$$\mathbf{R}(\mathbf{r}) \;=\; \mathrm{E}\big[\,\tilde{\mathbf{v}}(\mathbf{r}_0+\mathbf{r})\,\tilde{\mathbf{v}}(\mathbf{r}_0)^T\big] \;=\; \sigma^2_{\mathrm{iso}}\Big(\big[\,f(r)-g(r)\,\big]\frac{\mathbf{r}\,\mathbf{r}^T}{\mathbf{r}^T\mathbf{r}} \;+\; g(r)\,\mathbf{I}\Big), \tag{44}$$

where σ^2_{iso} is the variance of a single wind velocity component in the isotropic field. The functions $f(r)$ and $g(r)$ describe the lengthwise and transverse correlation, respectively.

The lengthwise correlation function $f(r)$ is introduced via its spectral wave-number representation

$$\sigma^2_{\mathrm{iso}} f(r) \;=\; \int_{-\infty}^{\infty} F(k)\,\mathrm{e}^{ikr}\,dk, \tag{45}$$

where k is the wave-number corresponding to the spatial separation r. For convection in the x_1-direction this defines a relation between the spatial x_1-coordinate and the time t of the form $x_1 = -Ut$, and thus the spatial x_1 variation corresponds to a time history and the corresponding spectral densities are easily scaled to frequency form. In the present context it is convenient to represent the spectral density function $F(k)$ in terms of the normalized form of the von Kàrmàn spectral density, [4],

$$F(k) \;=\; \frac{1}{\sqrt{\pi}}\,\frac{\Gamma(5/6)}{\Gamma(1/3)}\,\frac{\sigma_v^2\,\ell}{[\,1+(k\ell)^2]^{5/6}}\,, \tag{46}$$

where $\Gamma(\;)$ is the gamma function, and ℓ is a length parameter, determined by the integral length-scale λ as $\ell = 1.339\lambda$. The sequential simulation procedure used here does not use the spectral density directly, but the covariance matrix $\mathbf{R}(\mathbf{r})$ expressed in terms of the corresponding correlation functions

$$f(r) \;=\; \frac{2}{\Gamma(1/3)}\Big(\frac{r}{2\ell}\Big)^{1/3} K_{1/3}\Big(\frac{r}{\ell}\Big)\,, \qquad g(r) \;=\; f(r) \;-\; \frac{2}{\Gamma(1/3)}\Big(\frac{r}{2\ell}\Big)^{4/3} K_{-2/3}\Big(\frac{r}{\ell}\Big), \tag{47}$$

where the transverse correlation function $g(r)$ follows from incompressibility of the velocity field, and $K_\nu(\;)$ denotes the modified Bessel function of the second kind of order ν. These functions are available in many computer software libraries.

In the isotropic turbulence model the length scale is the same in all directions and similarly the the turbulence intensity σ^2_{iso} identical for each of three velocity components. A simple generalization that conserves incompressibility can be obtained by a linear transformation of the spatial coordinates and performing a similar transformation of the corresponding wind velocity components,

$$\mathbf{x} = \mathbf{F}\,\mathbf{r}\,, \qquad \mathbf{v} = \mathbf{F}\,\tilde{\mathbf{v}}. \tag{48}$$

In the present case orthotropic scaling, in which each of the axes are stretched, is used, corresponding to

$$\mathbf{F} = \frac{1}{\lambda}\begin{bmatrix} \lambda_x & & \\ & \lambda_y & \\ & & \lambda_z \end{bmatrix} \tag{49}$$

as illustrated in Fig. 6. The easiest way to implement this transformation is to transform the structure into the equivalent isotropic space, perform an isotropic wind field simulation, followed by the transformation (48) back to the physical coordinates and wind velocities.

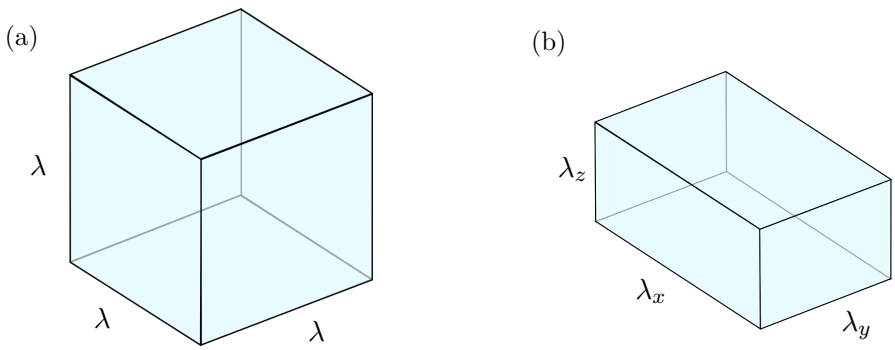

Figure 6: Wind field stretching: (a) isotropic, (b) stretched.

In the current context of long-span bridge loading it is important to introduce a representative ratio between the standard deviation of the along wind and vertical wind velocity components σ_u and σ_w, and a representative ratio of the horizontal transverse length-scale λ_y to the axial length-scale λ_x. The stretch of the isotropic wind field is chosen based on the Norwegian standard, N400 [40]. The ratio of the vertical to along-wind turbulence intensities is set to $\sigma_w/\sigma_u = 0.5$, thereby defining the vertical spatial stretch of the field λ_z/λ_x. The horizontal transverse horizontal stretch is defined by the length scale ratio $\lambda_y/\lambda_x = 0.5$, with the implication that $\sigma_v/\sigma_u = 0.5$. The wind field parameters are given in Table 3 with U representing the mean wind speed and $I_u = \sigma_u/U$ being the turbulence intensity of the along-wind component. Due to the stretching procedure the parameters in Table 3 provide the complete field input for the representation of the full turbulence field, illustrating the basic simplicity of the stretched isotropic wind field description.

Table 3: Wind field parameters

U [m/s]	I_u	λ [m]	λ_x/λ	λ_y/λ	λ_z/λ
44	0.13	300	1.0	0.5	0.5

4.2. Sequential wind field simulation

The wind-field is simulated with the sequential simulation procedure developed in [19], in which the wind velocity field at the current time is formed as the sum of the conditional mean for a given set of previous velocities and a stochastic contribution representing the random fluctuations. The wind velocity components at a set of selected points at the time step n are collected in the vector $\mathbf{u}_n$. The vector $\mathbf{u}_n$ is generated sequentially by the recurrence relation

$$\mathbf{u}_n = \mathbf{A}\mathbf{w}_n + \mathbf{B}\boldsymbol{\xi}_n\,, \quad n = 1, 2, ... \tag{50}$$

in which the vector $\mathbf{w}_n$ contains the extended velocity vector $\mathbf{u}_i$ at j previous times, and the matrix $\mathbf{A}$ collects the corresponding regression matrices according to the format

$$\mathbf{A} = [\mathbf{A}_1, ..., \mathbf{A}_j]\,, \qquad \mathbf{w}_n^T = [\mathbf{u}_{n-i_1}^T, ..., \mathbf{u}_{n-i_j}^T]. \tag{51}$$

The vector $\boldsymbol{\xi}_n$ is formed by independent normalized random variables, and scaling and correlation are introduced via the coefficient matrix $\mathbf{B}$. The format described by (50) and (51) describes an auto-regressive stochastic process, but in the present context of a convected wind velocity field there are two important special features: the convection concept permits explicit determination of the matrices $\mathbf{A}$ and $\mathbf{B}$, and the spectral characteristics of the wind are efficiently represented by an exponential regression layout with indices $[i_1, i_2, ..., i_j] = [2^0, 2^1, ..., 2^{j-1}]$, illustrated in Fig. 7.

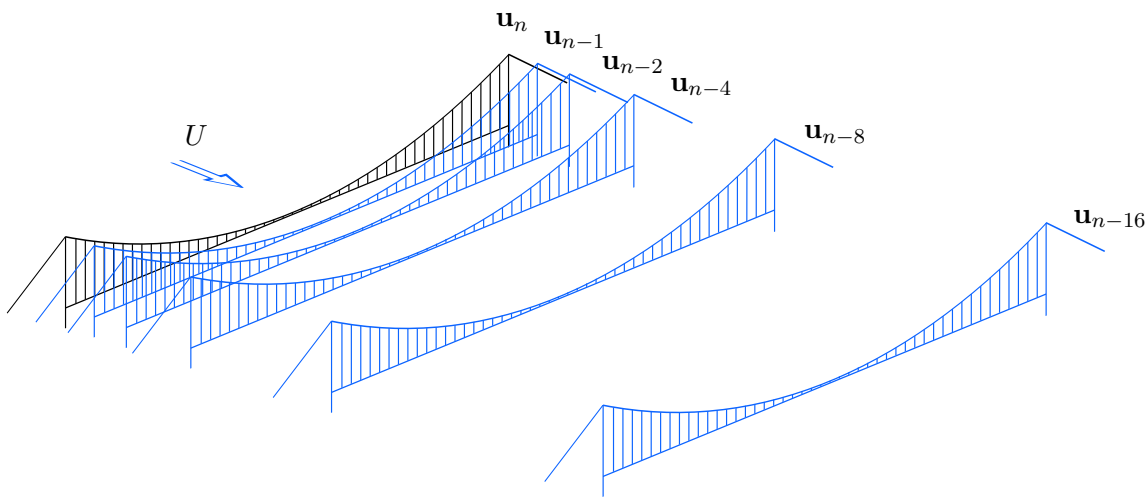

Figure 7: Wind simulation memory with 5 memory steps (distorted geometry).

Within the concept of a convected stationary wind field the turbulent wind velocity components are fully characterized by their covariance matrices

$$\mathbf{C}_{\mathbf{uu}} = \mathrm{E}[\mathbf{u}_n\mathbf{u}_n^T]\,, \quad \mathbf{C}_{\mathbf{uw}} = \mathrm{E}[\mathbf{u}_n\mathbf{w}_n^T]\,, \quad \mathbf{C}_{\mathbf{ww}} = \mathrm{E}[\mathbf{w}_n\mathbf{w}_n^T]. \tag{52}$$

These matrices are given directly in terms of the 3D spatial covariance function described in Section 4.1. The matrices $\mathbf{A}$ and $\mathbf{B}$ can then be determined by the following simple argument. It follows directly from the recurrence relation (50) that the first term on the right side is the conditional mean value of $\mathbf{u}_n$ for given $\mathbf{w}_n$. By moving this term to the left side of the equation and multiplying each side with its transpose it follows that the product $\mathbf{B}\mathbf{B}^T$ is

defined by the conditional covariance of $\mathbf{u}_n$ for given $\mathbf{w}_n$. These results can be expressed in the following compact form

$$\mathbf{A} = \mathbf{C}_{\mathbf{uw}}\mathbf{C}_{\mathbf{ww}}^{-1} \quad \text{and} \quad \mathbf{B}\mathbf{B}^T = \mathbf{C}_{\mathbf{uu}} - \mathbf{A}\mathbf{C}_{\mathbf{ww}}\mathbf{A}^T. \tag{53}$$

Full details of the wind field simulation procedure and its calibration have been given in [19].

4.3. Wind field simulation examples

Statistical properties of the wind field described by the data of Table 3 are here estimated from the simulated records and the performance and applicability of the sequential simulation method is discussed in relation to large scale bridge structures. Two different simulation fields are evaluated. Firstly, a full field simulation of all three wind components in 335 simulation points positioned according to the nodes of the three dimensional finite element bridge model including bridge deck, cables and towers. Secondly, a simulation record of a line of 101 simulation points located at the nodes along the bridge deck. For the second simulation record the along bridge wind component is considered redundant and due to symmetry the along wind and vertical wind component become statistically independent, thereby allowing separate simulations of the two remaining components.

For both simulation records the simulation frequency $f_s = 6\,\text{Hz}$, corresponding to an equivalent spatial separation of $\Delta x = U/f_s = 7.33\,\text{m}$, is used in order to obtain a suitable resolution in the time domain. The horizontal separation is $\Delta y = L_b/100 = 30\,\text{m}$. In order to permit predictions with low scatter the simulation time was 60 hours corresponding to $1.296 \cdot 10^6$ time steps. The regression layout is chosen with 8 memory steps, $[i_1, i_2, ..., i_8] = [1, 2, 4, 8, 16, 32, 64, 128]$. Thus, the depth of the 8-step memory is $128/6 = 21.33\,\text{s}$.

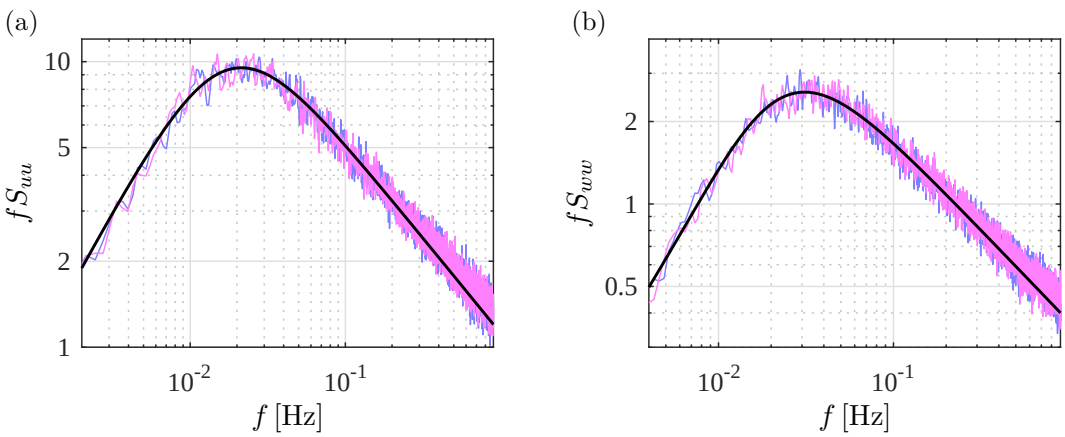

Figure 8: Auto-spectral densities: (a) $S_{uu}(f)$, (b) $S_{ww}(f)$. Full-structure (—), horizontal line (—), analytic (—).

The frequency content in a simulation point is illustrated by the auto-spectral densities. In Fig. 8 the estimated auto-spectral density of the along wind and the vertical wind component are plotted together with the theoretical spectrum. It is seen that both the full-structure and the horizontal line simulation represent the energy content very well over the full frequency interval, indicating negligible influence of the difference from the different simulation point distributions.

Finally, the transverse coherence is estimated from the simulation records. In Fig. 9 the estimated (root) coherence between simulation records at points with a transverse separation of $\frac{1}{2}\lambda$, λ and $\frac{3}{2}\lambda$,respectively, are plotted together with the theoretical coherence given in [19]. The coherence functions are plotted as function of the wave number k_1 times the distance between simulation points y. It is seen that the single-component and the full-field simulation both give a good representation of the target coherence. It is interesting to note, that coherence functions of the general shape illustrated in Fig. 9 have been measured and reported in the recent publications [5, 6, 7].

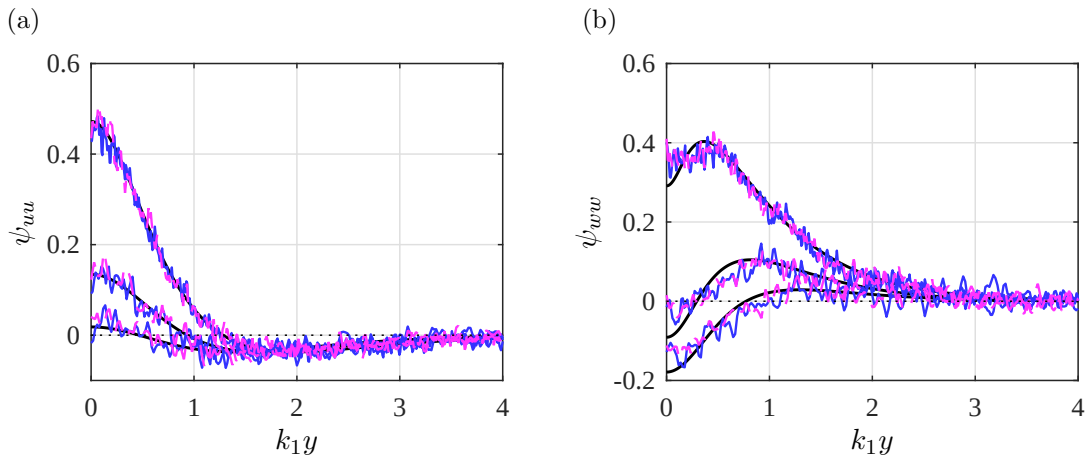

Figure 9: Transverse coherence for separation $\frac{1}{2}\lambda$, λ and $\frac{3}{2}\lambda$: (a) $\psi_{uu}(k_1 y)$, (b) $\psi_{uu}(k_1 y)$. Full structure (—), horizontal line (—), analytic (—).

The simulated wind velocity records do not show any quality differences between the full-field simulation and the use of two independently simulated single-component records for u and w for points along a horizontal line.

Table 4: Computational time for 3 hours simulated wind velocity record.

	Sequential [19]	Fourier [8]
Full Structure	233 s	-
Deck, field simulation	10 s	134 s
Deck, two-component simulation	2×2 s	2×11 s

Table 4 shows the computation time for 3 hours simulated records obtained with the sequential simulation method. The scenarios covered are points distributed on the full bridge including cable and pylons, all velocity components in points along the bridge deck, and a case in which the vertical and the along-wind components are simulated independently at points along the bridge deck. The third case permits separate simulation of the vertical and the along-wind velocity components because they uncouple for points in a horizontal plane due to spatial symmetry. The last column in the table gives the time of a standard Fourier simulation based on [8]. The computations were carried out on a desktop computer with 32 GB memory and 2.70 GHz Intel Core i7-6820HQ CPU. The 3 hours time record represents the limit for full-field deck Fourier simulation without memory swapping, leaving direct Fourier simulation of the wind velocity field for the full bridge out of the present range. In this context

it should be mentioned that the computation time of the Fourier simulation can be decreased and the storage requirements reduced e.g. by interpolation of the decomposed matrices or by system truncation [9, 14]. Also, super fast Fourier simulation methods have been developed for line-like structures [11, 12] applicable for bridge deck loading.

5. Model performance and results

In this section the model performance is discussed in relation to the quality of the structural response. The wind field is defined by the parameters given in Table 3. Time integration is performed using the second order momentum based time integration algorithm shown in Table 1 with time step $h = 1/6 = 0.166\,\mathrm{s}$.

5.1. Buffeting response

Figure 10 shows the standard deviation of the drag, heave and torsional response σ_y, σ_z and σ_θ at quarter span as function of the mean wind speed for loading of the full structure and loading of the deck only. The load is evaluated based on the wind speeds at the nodal locations and is assumed linearly distributed over the elements. It is seen that the influence of including full structural loading is only significant for the along wind response, whereas the heave and torsional response for the two load cases are very similar.

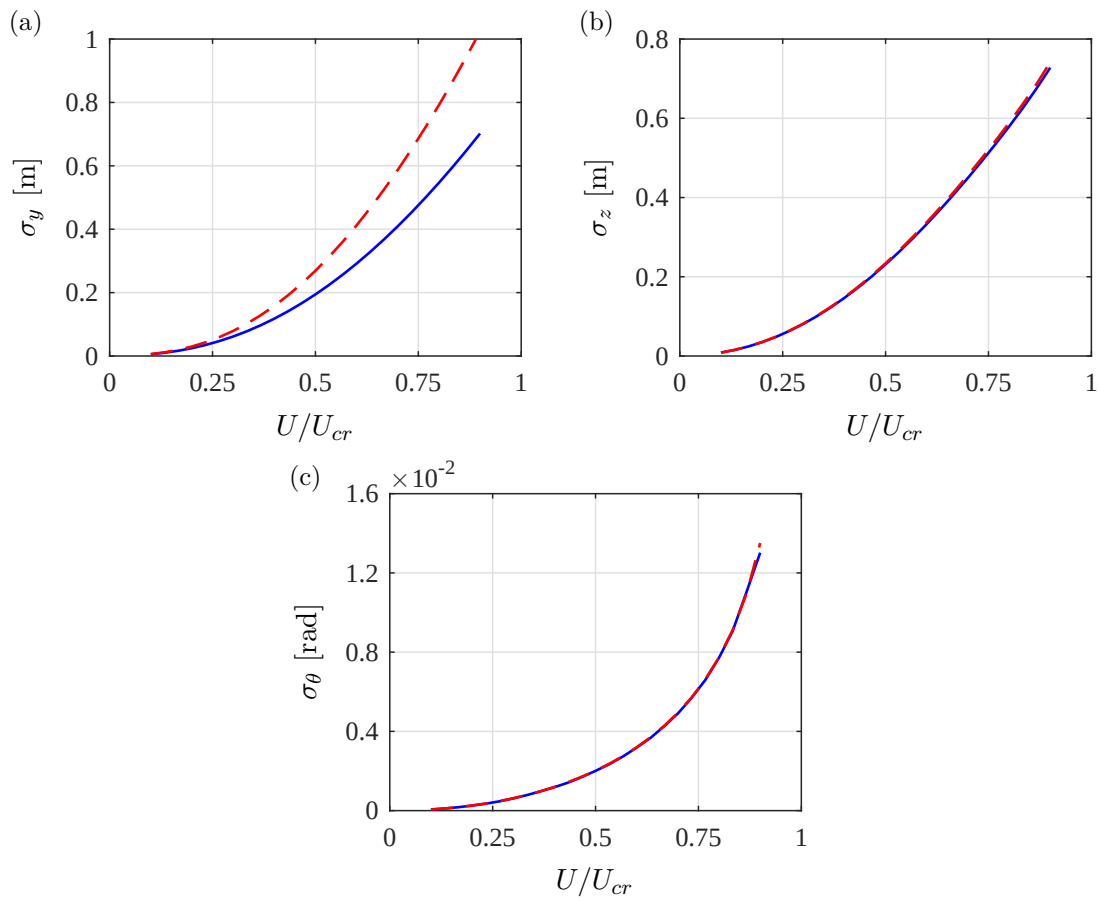

Figure 10: Response at quarter-span: deck loading (—), full bridge loading (– –).

Figure 11 shows the standard deviation of the displacement at quarter-span in terms of drag, heave and torsion as function of the normalized wind speed. Full structure turbulent loading is applied and the response is found using 0, 1 and 2 memory terms, respectively, in the representation of self-excited aerodynamic forces, corresponding to extending the state-space equation of motion in (16) with 0, 1 or 2 additional state-variable vectors $\mathbf{f}_j$. A quasi-steady representation was assumed for the wind-structure interaction related to drag motion, and thus the drag response is indifferent to the number of memory terms included in the representation of self-excited forces. Also, the heave response is seen to be only slightly influenced by including additional memory terms. However, the torsional response is seen to be overestimated using a zero memory representation of the self-excited forces. The difference in the response found with 1 and 2 memory terms, respectively, is seen to be small in the considered case of flat plate theory, suggesting the use of only one additional state-variable in the response calculations for this case. This result corresponds well with the representation of aerodynamic derivatives illustrated in Fig. 3.

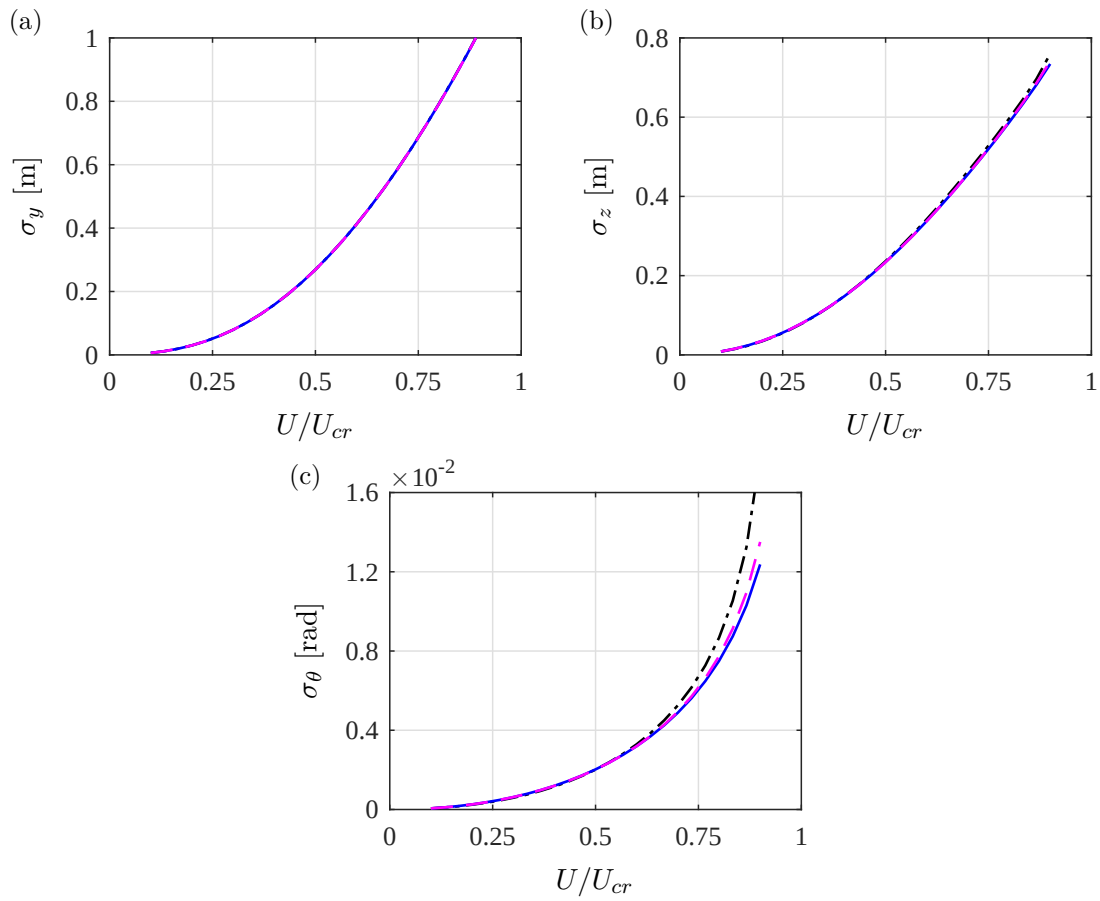

Figure 11: Response standard deviations at quarter-span: 0,1,2 memory terms (•—,−−, —) .

The time record of the full bridge model and the bridge model reduced by quasi-static condensation with a node selection ratio of 1:5 are shown in Fig. 12. The mean wind is set to $U = 0.6\,U_{cr}$ and full structure turbulent wind load simulation is applied. The time records show the drag q_y, the heave q_z and the torsional q_θ steady-state response at quarter-span

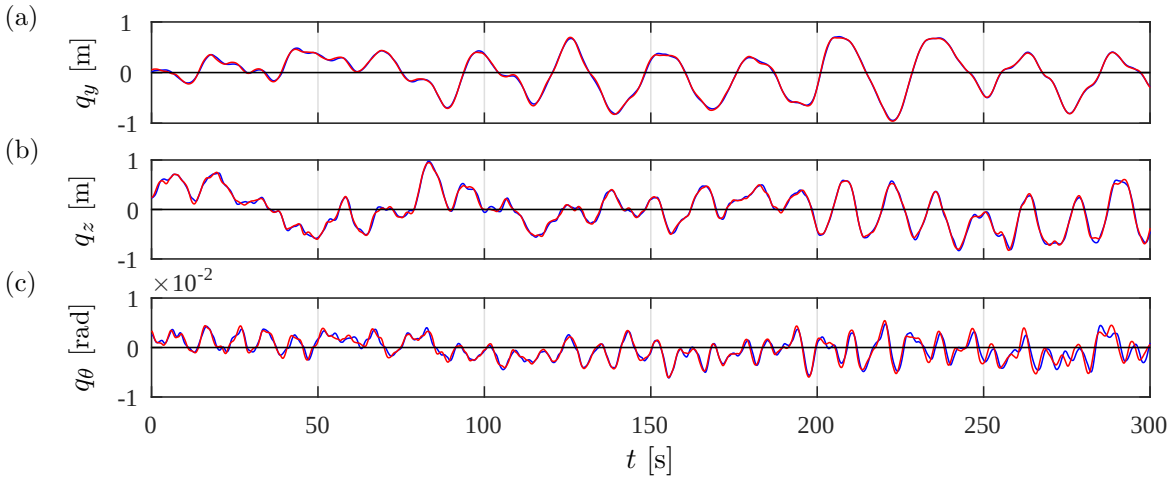

Figure 12: Time response at quarter span: full model (−), 1:5 reduction (−).

in a five minute time interval. It is seen that the response obtained by the reduced model corresponds well with the response found with the full model. The calculation time for the five minute time history is reduced significantly from 59.3 s to 0.7 s by making use of the reduced model instead of the full model.

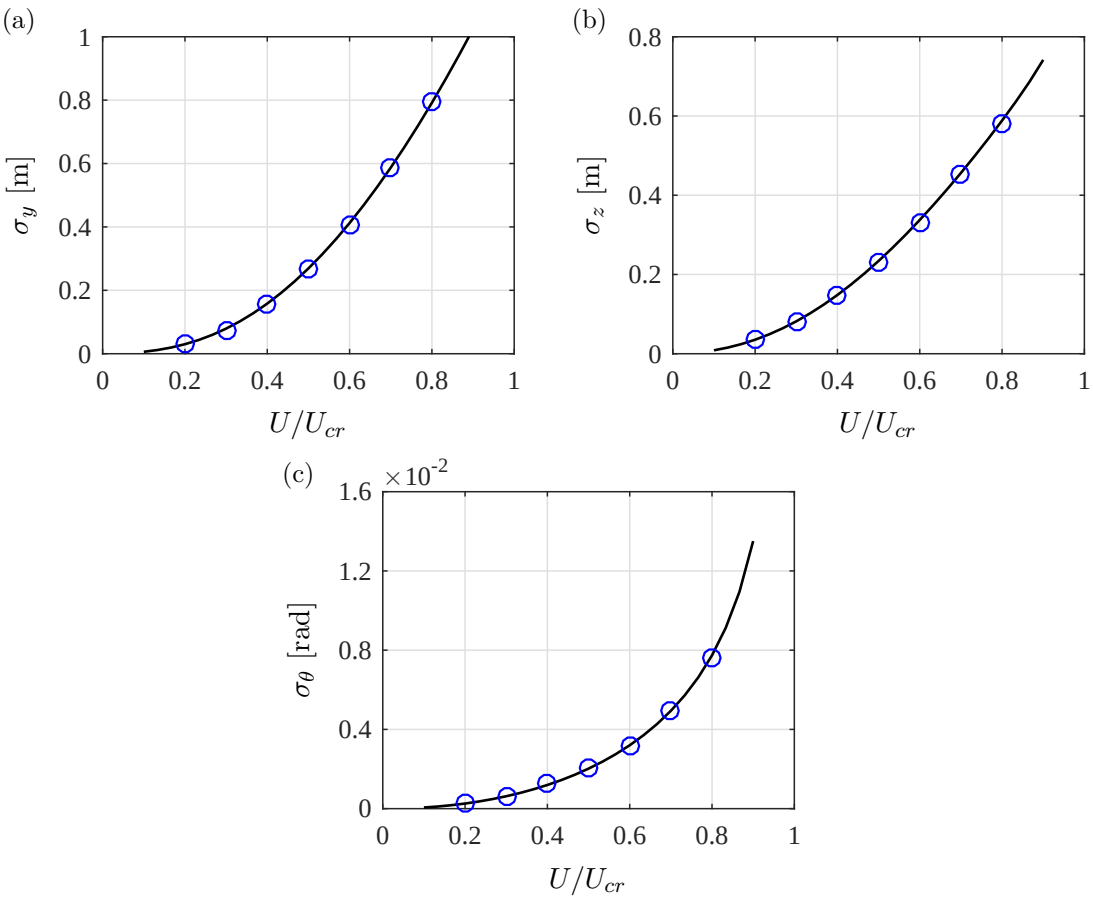

Figure 13: Response at quarter-span: frequency domain (−), time domain (○).

Figure 13 shows the response at quarter span as function of the mean wind speed for loading of the full structure. The solid line represents the response obtained with a frequency domain calculation based on the spectral representation of the isotropic turbulence field given in [2]. As for the time domain loading, stretching of the wind field is equivalent with inverse stretching of the structural model and the scaling of the turbulence component follows the scaling shown in (48). The response is evaluated for a number of frequencies in the interval $\omega = [0.001; 2]$ rad/s with a frequency interval of $\Delta\omega = 0.0014$ rad/s. This method is free of the approximations related to the auto-regressive simulation of the wind and the quality of the result is thereby only determined by the frequency interval and the discretization of the solution domain. For lightly damped systems a relatively fine resolution is needed around the system frequencies. The blue circles marks the time domain results evaluated based on 20 hours of steady-state response. Besides the approximations related to the wind field simulation using this method, the quality of the results also depend on the time-step size chosen for the time integration. The integration algorithm is second order accurate meaning the error introduced is proportional to $(\omega h)^2$, wherefore the number of time-steps per modal period of interest should be at least $2\pi \simeq 6$ to limit the time-step error. The results obtain by the two methods appear consistent as expected based on the statical properties estimated from the wind field, the simulation length, the time-step size and the frequency domain resolution.

5.2. Flutter

The critical wind speed, also referred to as the flutter wind speed, defining the stability limit of the aero-elastic system can be determined from the homogeneous form of the discrete equation of motion (32). The stability limit is found at the mean wind speed that will cause the magnitude of the complex valued amplification factor of the most critical mode of the combined aero-elastic system equations to exceed unity. This stability limit is independent of the external loading. However, in the design of long span bridges the flutter wind speed is sometimes defined as the wind speed at which the torsional and the vertical response exceed a certain limit [41]. In this particular reference the torsional and the vertical response limit is set to 0.035 rad and 1/500 times the span length, respectively.

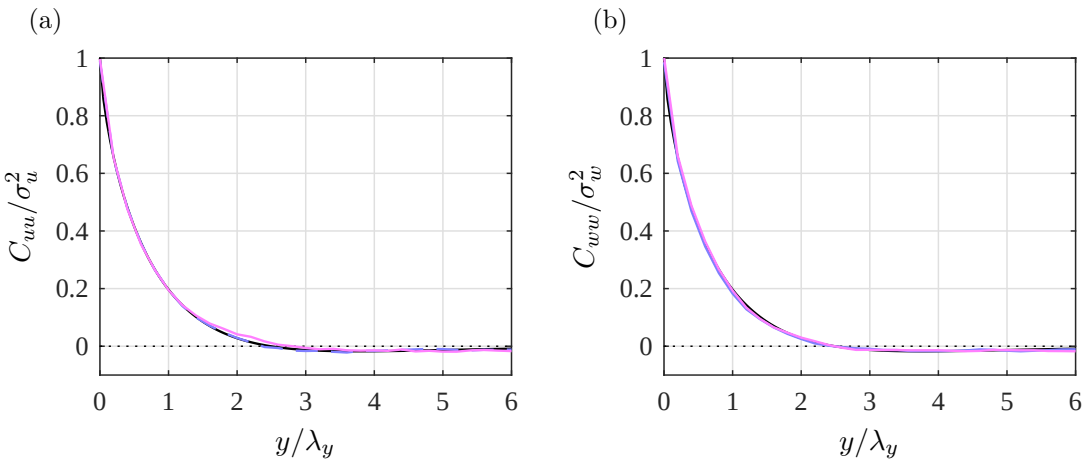

Figure 14: Transverse correlation functions: (a) $C_{uu}(y)$, (b) $C_{ww}(y)$. Full-field (−), single component(−), analytic (−).

For long-span bridges the span exceeds the turbulence length-scale along the bridge deck. This leads to two effects: the non-trivial form of the coherence function that describes the covariance of turbulence components around a particular frequency, and the limitation of the horizontal covariance to distances of around two times the transverse length-scale. The coherence characteristics are illustrated in relation to the sequential wind field simulation in Fig. 9. The most characteristic feature is that even the low-frequency components have limited correlation over large distances, a feature that would be lost if transverse statistics were represented by the classic non-dimensional combined frequency-length parameter $\omega y/U$. In addition to this feature, demonstrated in several recent measurement campaigns [5, 6, 7], the transverse correlations depend on the length-scale of the turbulent field in the transverse direction. This effect is illustrated in Fig. 14 showing the normalized correlation of the along-wind turbulent velocity component u as well as the vertical velocity component w as a function of the transverse separation, normalized by the transverse length-scale λ_y. It is seen that both the u- and the w-component are effectively uncorrelated for distances exceeding twice the transverse length-scale, $y > 2\lambda_y$. For fully correlated components the response corresponds to that following from a harmonic analysis, whereas the magnitude of the response to uncorrelated components is accumulated via what amounts to a root-mean-square analysis. Thus, limited correlation results in reduced response, and as a result a reduced transverse length-scale will lead to a reduced response.

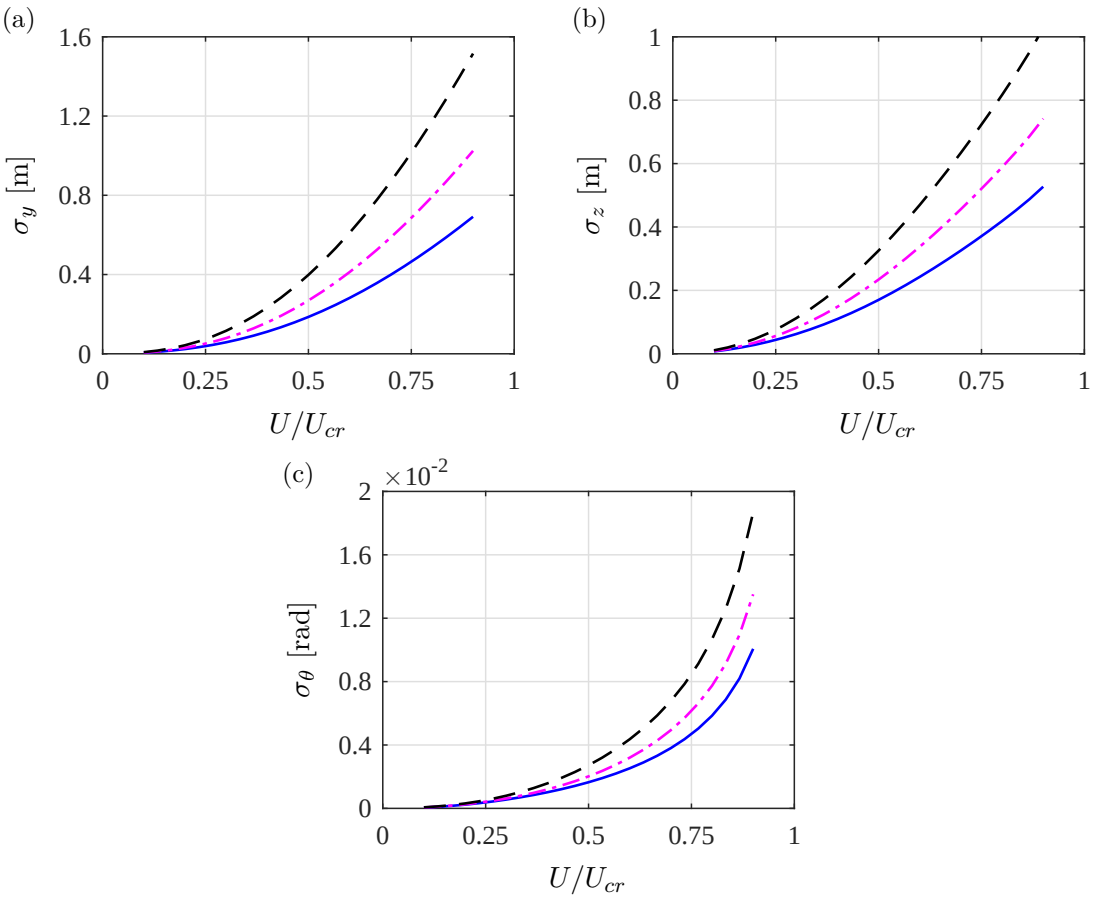

Figure 15: Response at quarter-span: $\lambda_y = 75\,\mathrm{m}$ (—), $\lambda_y = 150\,\mathrm{m}$ (–·–), $\lambda_y = 300\,\mathrm{m}$ (- -).

The influence of the across-wind turbulence length-scale on the response is illustrated in Fig. 15. The plots show the standard deviation of the response as function of the normalized mean wind speed. The response is calculated with simulated wind load on the full structure and is shown for three different transverse length scales, $\lambda_y = 75, 150, 300\,\mathrm{m}$, while the along wind length scale is held constant at $\lambda_x = 300\,\mathrm{m}$. As discussed, above a shorter transverse length-scale leads to a smaller part of the wind field being correlated and therefore results in a smaller response. The effect is quite noticeable, and it is seen that a doubling of the length scale results in around 50% increase of the response. This emphasizes that a representative value of the transverse turbulence length-scale is important in the design of long span-bridges.

6. Conclusions

A procedure has been presented for time-domain aerodynamic response analysis of long-span bridges subjected to turbulent wind. The wind load is generated by the mean-field simulation procedure recently developed in [19]. The procedure is based on convection of an isotropic homogeneous turbulent velocity field, which is generalized to orthotropic form by a simple stretching procedure. Based on data from the Norwegian standard [40] the transverse length-scale is set to half of the along-wind scale, and vertical turbulence component intensity is set to half of the along-wind component intensity. The structural model combines beam elements for bridge deck and pylons with bar elements for cables and hangers. It is demonstrated that a 1:5 reduction of the nodes along the deck and main cables leads to a quite accurate representation of the dynamics of the first 13 modes. The self-excited aerodynamic loads are represented via first-order filter terms in the equation of motion, and the full system is represented by a set of equations in which these filter variables are included as auxiliary degrees of freedom. The full equation system is discretized based on momentum considerations, and the discretized equations serve both as a tool for simulation via time integration and as basis for a linear eigenvalue analysis, determining the flutter velocity.

Three procedures were investigated for the simulated wind load: full 3D simulation at all nodes of the structure, full 2D simulation of the wind velocity components on the bridge deck, and a reduced form simulating only the vertical and along-wind components at the nodes of the bridge deck. It was found that the wind load on the cables had only minor influence on the response in relation to low-frequency deck response and flutter. This in turn permits to use the reduced two-component simulation method, in which the two components are statistically independent, hereby reducing the simulation effort further. The direct time-simulation procedure of both wind field and response is considerably faster than FFT-based simulation procedures, and permits simulation of wind fields with a larger number of simulation points, because the storage requirements are much smaller than for the FFT methods. The simulated wind field gives a very detailed representation of the transverse coherence, and examples demonstrate the quite large influence of this in combination with the use of a representative transverse turbulence length scale on the response magnitude.

7. Acknowledgements

This paper is part of a project sponsored jointly by Innovation Fund Denmark, Rambøll and the Technical University of Denmark.

References

[1] A.G. Davenport, The prediction of the response of structures to gusty wind, in *Safety of Structures under Dynamic Loading*, (eds. I. Holand, D. Kavlie, G. Moe and R. Sigbjörnsson), Tapir, Trondheim, Norway, 257–284, (1977).

[2] S. Krenk, Wind field coherence and dynamic wind forces. *IUTAM Symposium on Advances in Nonlinear Stochastic Mechanics*, (eds. A. Naess, S. Krenk), Kluwer, Dordrecht, 269–278, (1996).

[3] G.K. Batchelor, *The Theory of Homogeneous Turbulence*, Cambridge University Press, Cambridge, U.K. (1953).

[4] T. von Kàrmàn, Progress in the statistical theory of turbulence, *Proceedings of the National Academy of Science*, **34**, 530–539, 1948.

[5] A. Fenerci, O. Øiseth, Measured buffeting response of a long-span suspension bridge compared with numerical predictions based on design wind spectra, *Journal of Structural Engineering*, **143**, 04017131 (pp. 15), 2017.

[6] J.D. Zeng, Z.G. Li, M.S. Li, Coherence of simulated atmospheric boundary-layer turbulence, *Fluid Dynamics Research*, **49**, 2017.

[7] Y. Peng, S. Wang, J. Li, Field measurement and investigation of spatial coherence for near-surface strong winds in southeast China, *Journal of Wind Engineering and Industrial Aerodynamics*, **172**, 423–440, 2018.

[8] K. Aas-Jakobsen, E. Strømmen, Time domain buffeting response calculations of slender structure. *Journal of Wind Engineering and Industrial Aerodynamics*, **89**, 341–364, 2012.

[9] L. Carassale, G. Solari, Monte Carlo simulation of wind velocity fields on complex structures, *Journal of Wind Engineering and Industrial Aerodynamics*, **94**, 323–339, 2006.

[10] M. Shinozuka, C.-M. Jan, Digital simulation of random processes and its applications, *Journal of Sound and Vibrations*, **25**, 111–128, 1972.

[11] B.A. Benowitz, G. Deodatis, Simulation of wind velocity on long span structures: A novel stochastic wave based model, *Journal of Wind Engineering and Industrial Aerodynamics*, **147**, 154–163, 2015.

[12] L. Peng, G. Huang, A. Kareem, Y.Li, An efficient space-time based simulation approach of wind velocity field with embedded conditional interpolation for unevenly spaced locations. *Probabilistic Engineering Mechanics*, **43**, 156–168, 2016.

[13] Y. Song, J. Chen, Y.Peng, P.D. Spanos, J. Li, Simulation of nonhomogeneous fluctuating wind speed field in two-spatial dimensions via an evolutionary wavenumber-frequency joint power spectrum. *Journal of Wind Engineering and Industrial Aerodynamics*, **179**, 250–259, 2018.

[14] A. Kareem, Numerical simulation of wind effects: A probabilistic perspective, *Journal of Wind Engineering and Industrial Aerodynamics*, **96**, 1472–1497, 2008.

[15] M.P. Mignolet, P.D. Spanos, Recursive simulation of stationary multivariate random processes – Part I, *Journal of Applied Mechanics*, **54**, 674–680, 1987.

[16] P.D. Spanos, M.P. Mignolet, Recursive simulation of stationary multivariate random processes – Part II, *Journal of Applied Mechanics*, **54**, 681–687, 1987.

[17] Y. Li, A. Kareem, ARMA systems in wind engineering, *Probabilistic Engineering Mechanics*, **5**, 50–59, 1990.

[18] S. Krenk, Explicit calibration and simulation of stochastic fields by low-order ARMA processes. *COMPDYN 2011. ECCOMAS Thematic Conference on Computational Methods in Structural Dynamics and Earthquake Engineering*, (eds. M. Papadrakakis, M. Fragiadakis, V. Plevris), paper 550, 1–10, 2011.

[19] S. Krenk, R.N. Møller, Turbulent wind field representation and conditional mean simulation, Proceedings of the Royal Society A, **475**: 20180887, 2019.

[20] T. Theodorsen, General theory of aerodynamic instability and the mechanism of flutter, *NACA Report*, **496**, Washington, DC (1934).

[21] R.H. Scanlan, J.J. Tomko, Airfoil and bridge deck flutter derivatives, *Journal of the Engineering Maechanics Division – ASCE*, **97**, 1717–1737, 1971.

[22] R.H. Scanlan, J.-G. Beliveau, K.S. Budlong, Indicial aerodynamic functions for bridge decks, *Journal of the Engineering Maechanics Division – ASCE*, **100**, 657–672, 1974.

[23] W. Eversman, A. Tewari, Modified exponential series for the Theodorsen function, *Journal of Aircraft*, **28**, 553–557, 1991.

[24] X. Chen, M. Matsumoto, A. Kareem, Time domain flutter and buffeting response analysis of bridges, *Journal of Engineering Mechanics*, **126**, 7–16, 2000.

[25] J.R. Høgsberg, J. Krabbenhøft and S. Krenk, State space representation of bridge deck aeroelasticity, 13'th Nordic Seminar on Computational Mechanics (NSCM-13), Oslo University, Norway, 109–112, (2000).

[26] J.R. Høgsberg, *Aerodynamics of Bridge Decks*, M.Sc. thesis, Department of Mechanical Engineering, Technical University of Denmark, 2002.

[27] O. Øiseth, A. Rönnquist, R. Sigbjörnsson, Finite element formulation of the self-exited forces for time-domain assessment of wind-induced dynamic response and flutter stability limit of cable-supported bridges. *Finite Elements in Analysis and Design*, **50**, 173–183, 2012.

[28] C. Borri, C. Costa, Quasi-steady analysis of a two-dimensional bridge deck element, *Journal of Computers and Structures* **82**, 993–1006, 2004.

[29] O. Øiseth, A. Rönnquist, R. Sigbjörnsson, Simplified prediction of wind-induced response and stability limit of slender long-span suspension bridges, based on modified quasi-steady theory: A case study. *Journal of Wind Engineering and Industrial Aerodynamics*, **98**, 730–741, 2012.

[30] E. Strømmen, *Theory of Bridge Aerodynamics*, Springer, Berlin (2006).

[31] L. Caracoglia, N.P. Jones, Time domain vs. frequency domain characterization of aeroelastic forces for bridge deck sections, *Journal of Wind Engineering and Industrial Aerodynamics*, **91**, 371–402, 2003.

[32] Z. Zhang, Z. Chen, Y. Cai, et al., Indicial functions for bridge aeroelastic forces and time-domain flutter analysis, *Journal of Bridge Engineering*, **16**, 546–557, 2011.

[33] S. Krenk, Extended state-space time integration with high-frequency energy dissipation, *International Journal for Numerical Methods in Engineering*, **73**, 1767–1787, 2008.

[34] M. Géradin, D.J. Rixen, *Mechanical Vibrations – Theory and Application to Structural Dynamics, Third Edition*, Wiley, Chichester, U.K. (2015).

[35] J. Chung, G.M. Hulbert, A time domain algorithm for structural dynamics with improved numerical dissipation - the generalized-α method. *Journal of Applied Mechanics*, **60**, 371–375, 1993.

[36] Rambøll, for the Norwegian Public Roads Administration, Konseptrapport Hengebru i Korridor 1, November 2015.

[37] Norwegian Public Roads Administration, Statens vegvesen – E39 Sulafjorden K1, Elverum, Norway, Link: https://youtu.be/VUUPLido31Q (2015).

[38] S.O. Hansen, R.G. Srouji, B. Isaksen, K. Berntsen, Vortex-induced vibrations of streamlined single box girder bridge decks. *14th International Conference on Wind Engineering*, Porto Alegra, Brazil, June 21–26, 2015.

[39] H. Sato, S. Kusuhara, K. Ogi, H. Matsufuji, Aerodynamic characteristics of super long-span bridges with slotted box girder, *Journal of Wind Engineering and Industrial Aerodynamics*, **88**, 297–306, 2000.

[40] Statens Vegvesen, *N400 Handbook for Bridge Design*, Elverum, Norway (2009).

[41] Forth Replacement Crossing (Queensferry Crossing), Principal Contract for the Design, Construction and Completion of the Forth Replacement Crossing, Employer's Requirements, TS/MTRIPS/WKS/2009/02, Transport Scotland (2011).

P3

Damping system for long-span suspension bridges

Randi Nøhr Møller, Steen Krenk & Martin Nymann Svendsen

Structural Control and Health Monitoring,
(submitted, 2019).

Received: Added at production | Revised: Added at production | Accepted: Added at production

DOI: xxx/xxxx

RESEARCH ARTICLE

Damping system for long-span suspension bridges

Randi N. Møller*[1,2] | Steen Krenk[1] | Martin N. Svendsen[2]

[1]Department of Mechanical Engineering, Technical University of Denmark, DK-2800 Lyngby, Denmark
[2]Rambøll, DK-2300 Copenhagen, Denmark

Correspondence
*Randi N. Møller, Department of Mechanical Engineering, Technical University of Denmark, Nils Koppels Allé, Building 404, DK-2800 Kgs. Lyngby, Denmark Email: rnm@ramboll.dk

Summary

A damping system targeting flutter instability motions of long-span suspension bridges is presented. The damping system consists of four symmetrically located and equally tuned passive devices extracting energy from the structural system, based on the relative displacement between the pylons and the main suspension cables. Each device consists of a viscous damper and a spring in parallel, connecting the pylon to the suspension cable via a pre-tensioned cable. The tuning of the damping system is based on the asymptotic solution to a two-component subspace approximation, using still-air modes as input. It is shown that the simple tuning approach provides accurate results and that the damping system is capable of providing a relatively high amount of damping on the modes relevant for flutter. The efficacy of the damping system is illustrated numerically on a full aero-elastic model of a single-span suspension bridge with and without mid-span cable clamps and it is found that the stability limit of both structural systems can be increased significantly. Also, the buffeting response is evaluated and especially the torsional response is lowered. Different device configurations are investigated by shifting the anchorage point on the pylon and on the suspension cable and the influence of the flexible connecting cable is assessed. Finally, design considerations concerning spring deformations, pre-tensioning of the system as well as in-service displacements and forces are discussed.

KEYWORDS:
Long-span bridges, Passive flutter control, Passive damping, Suspension bridges, Damper calibration.

1 | INTRODUCTION

For long span suspension bridges the aerodynamic stability limit is an important design factor typically setting the limit for the maximum span length. The self-excited forces causing the system to become unstable are primarily generated by the mean wind flow around the bridge girder, whereby aerodynamic shaping of the girder is a key issue in the design process. However, as there is a need for longer and longer spans, installation of external damping to increase the stability limit further has continually been investigated. A general investigation of the influence of modal damping on the flutter and buffeting response was carried out by Jain et al. [1], where it was found that higher damping would increase the stability limit as well as lower the buffeting response. Two main damper concepts have been widely considered in relation to long span bridges. One is the tuned mass damper, where structural vibrations are suppressed by one or more oscillating masses connected to the structure via a suitably tuned parallel spring-damper connection. The other is the aerodynamic movable flaps or winglets that control the wind flow around the bridge girder to suppress vibrations.

The installation of passive tuned mass dampers for increasing the flutter wind speed of long span suspension bridges was studied analytically and experimentally on a cross-sectional model by Gu et al.[2] where it was found that a significant improvement of the bridge stability characteristics could be obtained by tuning of the dampers in the neighbourhood of the flutter frequency. An improved tuning of standard tuned mass dampers in relation to flutter motion was discussed by Chen and Kareem[3] and non-linear hysteretic tuned mass dampers for multi-mode flutter mitigation was suggested by Casalotti et al.[4], providing the ability to improve post flutter behaviour. To address the concern of the weight penalty related to installation of tuned mass dampers in long span bridges, a tuned mass damper with two degrees of freedom targeting mitigation of a vertical and a torsional mode simultaneously was discussed by Mokrani et al.[5]. The suggested two degrees of freedom damper was numerically and experimentally tested showing the ability to damp both torsional and vertical vibrations. However, it was concluded that installation of the damper in a real bridge with a wide deck would be challenging. The use of multiple tuned mass dampers to limit the oscillations of the top of the pylons was analyzed by Casciati and Giuliano[6] using slightly different tuning to cover a wider frequency interval. Installation of semi-active tuned mass dampers for suppression of flutter motion was considered by Gu et al.[7], where a tuned mass damper with adjustable frequency was found to provide efficient control, and finally numerical and experimental investigations of active tuned mass dampers for flutter suppression was carried out by Körlin and Starossek[8]. Semi-active and especially fully active devices are providing high control performance, but require high maintenance, and failure of the system can be fatal for the structure, thus limiting their use.

Control of flutter motion via winglets or flaps has also been widely studied, including both passive and active systems. An active control system was first proposed by Kobayashi and Nagaoka[9] where section model experiments showed that the flutter wind speed could be increased by a factor of two. The setup included two symmetrically located wings located above the main girder. An improved control algorithm was suggested by Wilde and Fugino[10], and a setup with control surfaces placed underneath the bridge deck clear of the bridge cable system was shown to provide a stable system at any wind speed. Since then, the concept has been further developed with more recent contributions by Li et al.[11] providing a new theoretical framework for feedback control and by Bakis et al.[12] with a full model implementation and a multimodal flutter evaluation. A passive control system was proposed and numerically tested by Omenzetter et al.[13,14], showing that an antisymmetrical setup was able to suppress aeroelastic response efficiently. However, this system is then only fully active for wind from one particular direction. A corresponding symmetric setup showed limited effectiveness. A passive system with winglets controlled by tuned mass dampers was suggested by Starossek and Aslan[15], thereby avoiding installation of an active system as well as the relatively high weight of traditional tuned mass dampers on long span bridges. Only few alternatives to tuned mass dampers and winglets for suppression of flutter motion are found in the literature. However, a study on the use of a liquid column damper was carried out by Suduo et al.[16] showing the ability to lower the buffeting response as well as increasing the flutter wind speed.

All of the above mentioned studies showed that the concept of introducing external damping is indeed a viable method for increasing the aerodynamic stability limit of long span bridges. However, for long-span bridges the tuned mass damper solutions are related to concerns regarding the added mass and the surface control systems are primarily effective with active control. This paper presents a passive damping system for long-span suspension bridges extending the results for sagging cables damped by a transverse force[17], where substantial damping can be obtained by applying the damper force near the cable support. The damping system consists of four identical devices located symmetrically near the supports of the two main cables at the pylons. The dampers are connected to the main cables by smaller cables, and in order to keep these in tension a pre-tensioning must be applied via a loaded spring in parallel with the damper. The damping system is targeting the lowest vertical and torsional modes to suppress flutter-type instability of the aero-elastic system. Tuning of the damping system is based on the two-component subspace method developed by Main and Krenk[18], where the frequency dependence and optimal tuning to a particular mode follows in a simple way from combining the two solutions corresponding to a system without dampers and a system in which the dampers are locked. The spring reduces the efficiency of the damper by decreasing the frequency increase following from a hypothetical locking of the damper as discussed by Krenk and Høgsberg[19]. In the present case the frequency shift needed for the design is obtained directly from analyzing the structure with a spring as part of the structural system. The tuning of the damping system is based on the still-air modes and the effectiveness is illustrated numerically for a full three-dimensional aero-elastic bridge model as presented by Møller et al.[20]. Different configurations and choices regarding the tuning are discussed, and the influence on both the buffeting response and the stability limit is illustrated. Also, the influence of the configuration and flexibility of the cables used to connect the dampers to the main cables of the bridge is discussed.

2 | SUSPENSION BRIDGE DAMPING

Figure 1 shows a beam-truss element model of a typical suspension bridge. The aerodynamic stability limit, also referred to as the flutter limit, is the point where the wind-structure interaction will cause the aero-elastic system to have negative damping, which is fatal for the structure. In order to increase the stability limit an external damper system can be applied to the system.

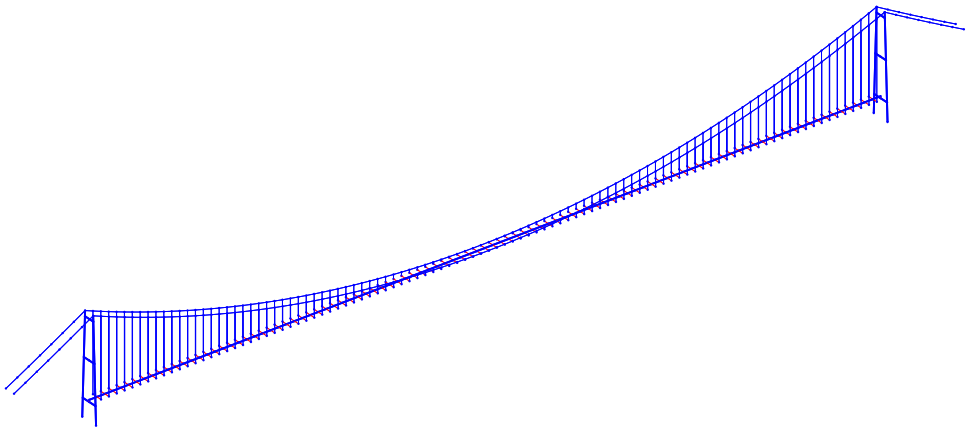

FIGURE 1 Suspension bridge model.

The typical instability motions of a suspension bridge are the low-frequency vertical and torsional deck motions. These deck motions are directly related to the first and second mode shape of a suspended cable with sag shown in Fig. 2a,b. The vertical deck motion is related to in-phase motion of the suspension cables while the torsional deck motion is related to out-of-phase motion of the suspension cables. Thereby, both the antisymmetric vertical and torsional deck motions are governed by the first antisymmetric cable mode and both the symmetric vertical and torsional deck motions are governed by the first symmetric cable mode. This observation shows that all modes of interest in relation to aerodynamic instability of the bridge can be addressed by four dampers placed in a double-symmetric setup, extracting energy from the system via viscous dampers working on the relative motion of the main suspension cables and the pylons. As the distance between the device attachment point on the pylon and on the suspension cable is relatively long, a connection via a pre-tensioned cable is considered. The cable connection only transfers tension forces and thus the viscous damper needs to be placed in parallel with a pre-tensioned spring.

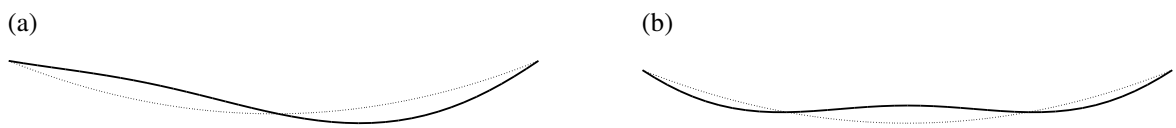

FIGURE 2 Cable modes: (a) antisymmetric mode, (b) Symmetric mode.

2.1 | Local spring-damper system

A conceptual sketch of a suspension bridge with external spring-damper devices between the pylons and the suspension cables is shown in Fig. 3. The damper system consists of four symmetrically placed identical devices with damping coefficient c and spring stiffness coefficient k. The pre-tensioned connecting cable is not shown.

FIGURE 3 External device positioning (distorted geometry).

The force acting on the structure due to local external damping devices as illustrated in Fig. 3 is represented in the form

$$\mathbf{f}(t) = -\sum_j \mathbf{w}_j f_j(t), \tag{1}$$

where $f_j(t)$ is the magnitude of the force of device $j = 1, .., 4$ and $\mathbf{w}_j$ is the corresponding connectivity vector providing the location of the external device in the global model. The connectivity vector contains zeros at all degrees of freedom unrelated to the device attachment nodes, whereby

$$\mathbf{w}_j^T = \left[\cdots, \mathbf{w}_{A_j}^T, \cdots, \mathbf{w}_{B_j}^T, \cdots\right]. \tag{2}$$

The dots indicate zeros and index A and B refer to the connected nodes as shown in Fig. 3, whereby $\mathbf{w}_A$ and $\mathbf{w}_B$ are nodal connectivity vectors with unit length providing the direction of the damper force in the particular structural node. The damper force at the points A and B are of opposite sign and the direction can be found by the vector connecting the two points $\mathbf{x}_{AB}$, whereby the nodal connectivity vectors are found as

$$\mathbf{w}_A = -\mathbf{w}_B = \frac{\mathbf{x}_{AB}}{\|\mathbf{x}_{AB}\|}. \tag{3}$$

The force-displacement relation of the the spring-damper device in the frequency domain is given as

$$f_j(\omega) = H_j(\omega) q_j(\omega), \tag{4}$$

where $H_j(\omega)$ is the frequency response function of device j and $q_j(\omega)$ is the actuator displacement found as the relative displacement of node A_j and B_j, whereby it can be expressed in terms of the connectivity vector and the global displacement vector $\mathbf{q}$ as $q_j(\omega) = \mathbf{w}_j^T \mathbf{q}$.

The global frequency domain force-displacement relation of the structure due to external damping devices can now be found as the sum of the contribution of each device

$$\mathbf{f}(\omega) = -\sum_j H_j(\omega) \mathbf{w}_j \mathbf{w}_j^T \mathbf{q}(\omega). \tag{5}$$

For a parallel spring-damper device the frequency function is a sum of a contribution from the spring and from the damper, whereby the frequency function takes the form

$$H_j(\omega) = k_j + i\omega c_j \tag{6}$$

Introducing this into equation (5) each term $H_j(\omega)\mathbf{w}_j\mathbf{w}_j^T$ appears as an additional stiffness and damping matrix from the corresponding device attached to the structure,

$$\mathbf{C}_d = \sum_j c_j \mathbf{w}_j \mathbf{w}_j^T, \quad \mathbf{K}_d = \sum_j k_j \mathbf{w}_j \mathbf{w}_j^T. \tag{7}$$

This result implies that the damper design consists of to steps: a decision on the positioning of the device giving the connectivity vector $\mathbf{w}_j$ followed by a tuning process to obtain the device parameters k_j and c_j.

2.2 | Two-component subspace approximation

In the following the device damping parameters are taken to be equal, $c_j = c$, and similarly for the device stiffness parameters, $k_j = k$. The calibration of the damping and stiffness parameters c and k can then be done based on the two-component subspace method[18]. This method is applicable when the implemented devices do not introduce substantial changes to the considered modes. The displacement is assumed to be described by a linear combination of the relevant free vibration mode shape vector

$\mathbf{u}_0$ and a modified shape vector $\mathbf{u}_\infty$ corresponding to clamped dampers,

$$\mathbf{q}(t) = \mathbf{u}_0\xi_0(t) + \mathbf{u}_\infty\xi_\infty(t) = \mathbf{S}\boldsymbol{\xi}(t), \tag{8}$$

The response variables ξ_0 and ξ_∞ determine the magnitude of the contribution from each of the two modes combined in the matrix $\mathbf{S} = [\mathbf{u}_0, \mathbf{u}_\infty]$. The representation is illustrated for the first antisymmetric cable mode in Fig. 4.

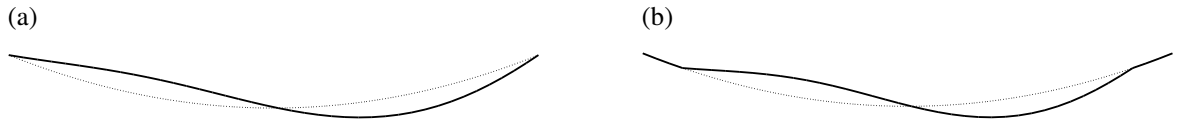

FIGURE 4 First antisymmetric mode shape: (a) without dampers $\mathbf{u}_0$, (b) clamped dampers $\mathbf{u}_\infty$.

Making use of the subspace assumption, the additional stiffness from the external spring-damper devices are counted as part of the original structure which is assumed to be without structural damping in the present context. Hence the equation of motion of the structural system for assumed harmonic load and response takes the form

$$\left[\mathbf{K} - \omega^2\mathbf{M} + \textstyle\sum_j H_j(\omega)\mathbf{w}_j\mathbf{w}_j^T\right]\mathbf{q} = \mathbf{f}. \tag{9}$$

Introducing the two-component subspace assumption into equation (9) and pre-multiplying by the transpose of the real valued shape vector $\mathbf{S}\boldsymbol{\xi}$ the following reduced equation of motion is obtained

$$\left[\mathbf{S}^T\mathbf{K}\mathbf{S} - \omega^2\mathbf{S}^T\mathbf{M}\mathbf{S} + \textstyle\sum_j H_j(\omega)\mathbf{S}^T\mathbf{w}_j\mathbf{w}_j^T\mathbf{S}\right]\boldsymbol{\xi} = \mathbf{S}^T\mathbf{f}. \tag{10}$$

It is seen that each term within the square brackets is a two by two matrix with components obtained by pre-and post-multiplication with the vectors $\mathbf{u}_0$ and $\mathbf{u}_\infty$.

In the present context it is convenient to normalize the mode shape vectors $\mathbf{u}_0$ and $\mathbf{u}_\infty$ such that they correspond to unit modal mass,

$$\begin{aligned} \mathbf{u}_0^T\mathbf{M}\mathbf{u}_0 &= 1\,, \quad \mathbf{u}_0^T\mathbf{K}\mathbf{u}_0 = \omega_0^2 \\ \mathbf{u}_\infty^T\mathbf{M}\mathbf{u}_\infty &= 1\,, \quad \mathbf{u}_\infty^T\mathbf{K}\mathbf{u}_\infty = \omega_\infty^2 \end{aligned} \tag{11}$$

whereby, ω_0 and ω_∞ are the real valued eigenfrequency of the free and clamped system, respectively. The off-diagonal terms in the two structural matrices in (10) are represented by the non-dimensional coefficient

$$\kappa = \mathbf{u}_\infty^T\mathbf{M}\mathbf{u}_0 = \omega_0^{-2}\,\mathbf{u}_\infty^T\mathbf{K}\mathbf{u}_0, \tag{12}$$

where the last equality follows from pre-multiplication of the original undamped eigenvalue problem by $\mathbf{u}_\infty^T$.

The clamping condition corresponds to $\mathbf{w}^T\mathbf{u}_\infty$, and thus the damping contribution in (10) is expressed in terms of the single scalar frequency function

$$H(\omega) = \textstyle\sum_j H_j(\omega)u_j^2\,, \quad u_j = \mathbf{w}_j^T\mathbf{u}_0, \tag{13}$$

where u_j denotes the displacement across device no. j, described entirely by the original undamped mode $\mathbf{u}_0$.

With this notation the frequency equation of the two degrees of freedom system can be determined from the determinant of (10) as

$$\begin{vmatrix} \omega_0^2 - \omega^2 + H(\omega) & \kappa(\omega_0^2 - \omega^2) \\ \kappa(\omega_0^2 - \omega^2) & \omega_\infty^2 - \omega^2 \end{vmatrix} = 0. \tag{14}$$

It is easily verified that when introducing the difference between the two normalized mode shapes $\Delta\mathbf{u}_\infty = \mathbf{u}_\infty - \mathbf{u}_0$ the coefficient κ can be expressed in the form

$$\kappa = 1 - \frac{1}{2}\Delta\mathbf{u}_\infty^T\mathbf{M}\Delta\mathbf{u}_\infty. \tag{15}$$

This formula suggests that when the locked mode shape vector $\mathbf{u}_\infty$ constitutes only a modest modification of the original mode shape vector $\mathbf{u}_0$ the parameter κ is close to unity. Thus, it is assumed in the following that $\kappa = 1$, a representative assumption[18].

With this assumption the determinant equation (14) can be rearranged into the form

$$\frac{\omega^2-\omega_0^2}{\omega_\infty^2-\omega_0^2}=\frac{H(\omega)/(\omega_\infty^2-\omega_0^2)}{1+H(\omega)/(\omega_\infty^2-\omega_0^2)}. \tag{16}$$

It is seen that introducing damping into the system will cause the frequency ω to become complex valued, corresponding to a decaying vibration with damping ratio $\zeta = \mathrm{Im}[\omega]/|\omega|$.

This formula may also be used to estimate the frequency increase caused by introducing a spring at the location of the damping device. In this case the frequency shift before mounting the damper is given in terms of the non-dimensional parameter

$$\xi = \frac{H(\omega)}{\omega_\infty^2-\omega_0^2} = \frac{\sum_j k_j u_j^2}{\omega_\infty^2-\omega_0^2} \tag{17}$$

as

$$\frac{\omega^2-\omega_0^2}{\omega_\infty^2-\omega_0^2} \simeq \frac{\xi}{1+\xi}. \tag{18}$$

Naturally, the frequency increase from introducing a spring at each device location can also be calculated from an additional eigenvalue problem. The calibration of the dampers can be carried out either by including the spring component in the system determining the undamped frequency ω_0, or by an eigenvalue analysis of the system without the spring, followed by introducing the correction of ω_0 given by (18).

2.3 | Asymptotic results

For design of external damper devices it is convenient to consider the asymptotic result. This result has been shown[18] to provide good accuracy for small perturbation where the frequency shift imposed by a locked device is small relative the original system frequency $\Delta\omega_\infty \ll \omega_0$, where $\Delta\omega_\infty = \omega_\infty - \omega_0$. The left hand side of the result presented in (16) can be approximated as

$$\frac{\omega^2-\omega_0^2}{\omega_\infty^2-\omega_0^2} = \frac{\Delta\omega}{\Delta\omega_\infty}\frac{\omega+\omega_0}{\omega_\infty+\omega_0} \simeq \frac{\Delta\omega}{\Delta\omega_\infty}, \tag{19}$$

where $\Delta\omega = \omega - \omega_0$ is the frequency change imposed by the damper. This gives the linearised relation between the damped complex frequency of the system and the devise frequency function

$$\frac{\Delta\omega}{\Delta\omega_\infty} \simeq \frac{i\eta}{1+i\eta}, \tag{20}$$

with the non-dimensional damping parameter

$$\eta = \frac{1}{i}\frac{H(\omega)}{\omega_\infty^2-\omega_0^2} \tag{21}$$

For viscous dampers the damping parameter can be written in terms of the damping coefficients c_j as

$$\eta = \frac{\omega}{\omega_\infty+\omega_0}\frac{\sum_j c_j u_j^2}{\Delta\omega_\infty} \simeq \frac{\sum_j c_j u_j^2}{2\Delta\omega_\infty} \tag{22}$$

The asymptotic results are characterized by the frequency trace forming a semi-circle in the complex plan as illustrated in Fig. 5a and the corresponding damping curve shown in Fig. 5b. Here the dashed line represents the results obtain considering an external damper and the solid line represents the results obtained with a parallel spring-damper device, where the stiffness of the spring is resulting in a 10% reduction of the frequency shift $\Delta\omega_\infty$. The semicircular shape of the frequency trace yields a high utilization of the damping potential of a particular mode for $\mathrm{Re}[\Delta\omega]/\Delta\omega_\infty \in [0.25; 0.75]$ and from geometrical consideration the maximal damping can be approximated as

$$\zeta^{\max} \simeq \frac{\omega_\infty-\omega_0}{\omega_\infty+\omega_0}, \tag{23}$$

corresponding to the steepest line from the origin touching the circle. This corresponds to the top point of the semi-circular frequency trace and accordingly to a damping parameter $\eta = 1$. The damping ratio for modes with non-optimal damping can be estimated as $\zeta = \mathrm{Im}[\omega]/|\omega| \simeq \mathrm{Im}[\omega]/\omega_0$ and expressing the frequency as in (20) yields

$$\zeta \simeq \frac{\Delta\omega_\infty}{\omega_0}\frac{\eta}{1+\eta^2}. \tag{24}$$

A simple tuning procedure for damping of several modes with identically tuned dampers is to target optimal damping of a single mode and subsequently check the utilization of the damping potential of the other modes.

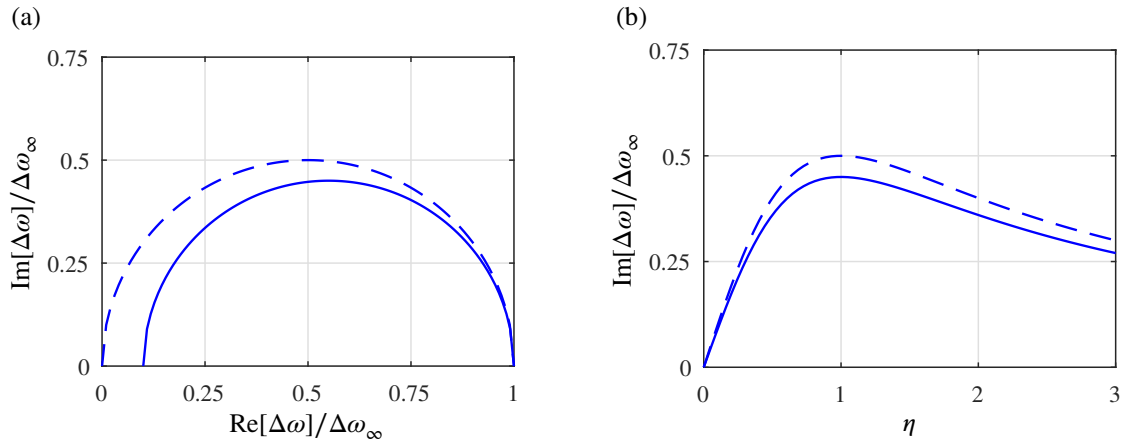

FIGURE 5 (a) Complex root locus, (b) normalized damping. Without spring (– –), parallel spring (–).

3 | AERO-ELASTIC MODEL

A three-dimensional aero-elastic finite element model is used for numerical evaluation of the effectiveness of the damper system. The bridge model is a typical single-span suspension bridge here examplified by model of a 3000 m suspension bridge proposed for crossing Sulafjorden in Norway as part of the Coastal Highway E39 project. The bridge model is shown in Fig. 1 and is implemented with beam elements for the towers and non-linear Green-strain truss elements for the cables to ease calibration, whereafter a linearized model is used for response calculations. The deck is modelled with aero-elastic beam elements where the aerodynamic self-excited forces are included via additional state-variables and the model size is reduced by quasi-steady reduction. A full description of the aero-elastic implementation has been presented by Møller et al.[20].

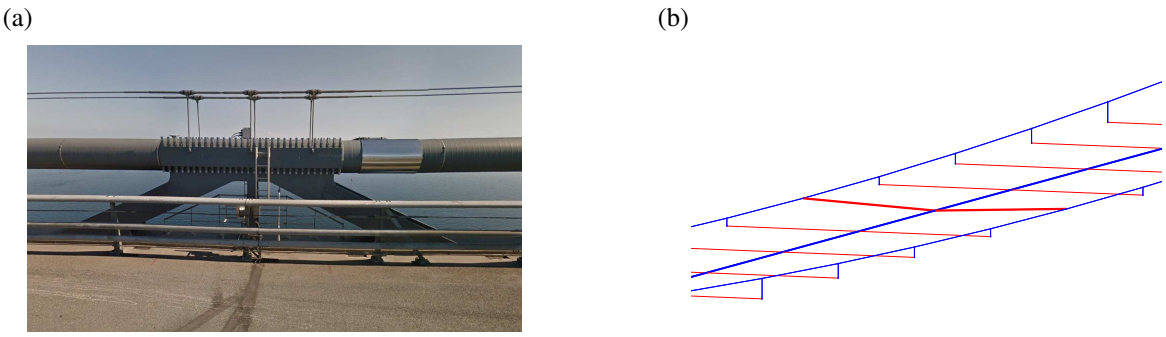

FIGURE 6 Mid-span cable clamp: (a) picture, Great Belt Bridge[24], (b) model implementation.

A detailed description of the geometry and structural properties is given by Rambøll[21] and is summarized here: The distance between the pylons is 3000 m, the sag to span ratio is 1:10 and the clearance hight of the bridge deck is 74 m. The distance between the suspension cables are 40 m and the distance between the hangers are 30 m. The bridge is considered without and with a mid-span cable clamp. The cable clamp is a stiff connection between the main suspension cables and the bridge girder and is a well established method to increase the stability limit of a suspension bridge, as it prevents lateral displacement of the cable relative to the girder which significantly increases the frequency of the first antisymmetric cable mode and thereby the frequency

TABLE 1 Still-air frequencies, S/A: symmetric/antisymmetric, D/H/T: drag/heave/torsion.

System 1		System 2		System 1		System 2	
ω [rad/s]	Type	ω [rad/s]	Type	ω [rad/s]	Type	ω [rad/s]	Type
0.233	SD1	0.233	SD1	0.756	SD2	0.791	SD1
0.473	AD1	0.477	AD1	0.791	SH2	0.812	AD2
0.476	AH1	0.572	SH1	0.813	AD2	0.861	AH2
0.572	SH1	0.605	AH1	0.860	AH2	0.914	ST1
0.743	AT1	0.756	SD2	0.911	ST1	1.053	AT1

of the first heave and torsional mode of the bridge. A picture of a cable clamp is shown in Fig. 6a and the corresponding model implementation is shown in Fig. 6b where the clamp is modelled as a rigid connection between the girder and main cables.

The still-air modal frequencies are given in Table 1 for a system without and with a cable clamp at mid span - System 1 and 2, respectively. The mode types are assigned abbreviations with A and S denoting antisymmetric and symmetric, respectively, and D, H and T denoting drag, heave and torsion. It is seen that the frequencies of the first anti-symmetric heave and torsional modes are significantly higher for System 2 including a cable clamp, while other modes have similar frequencies for the two different systems.

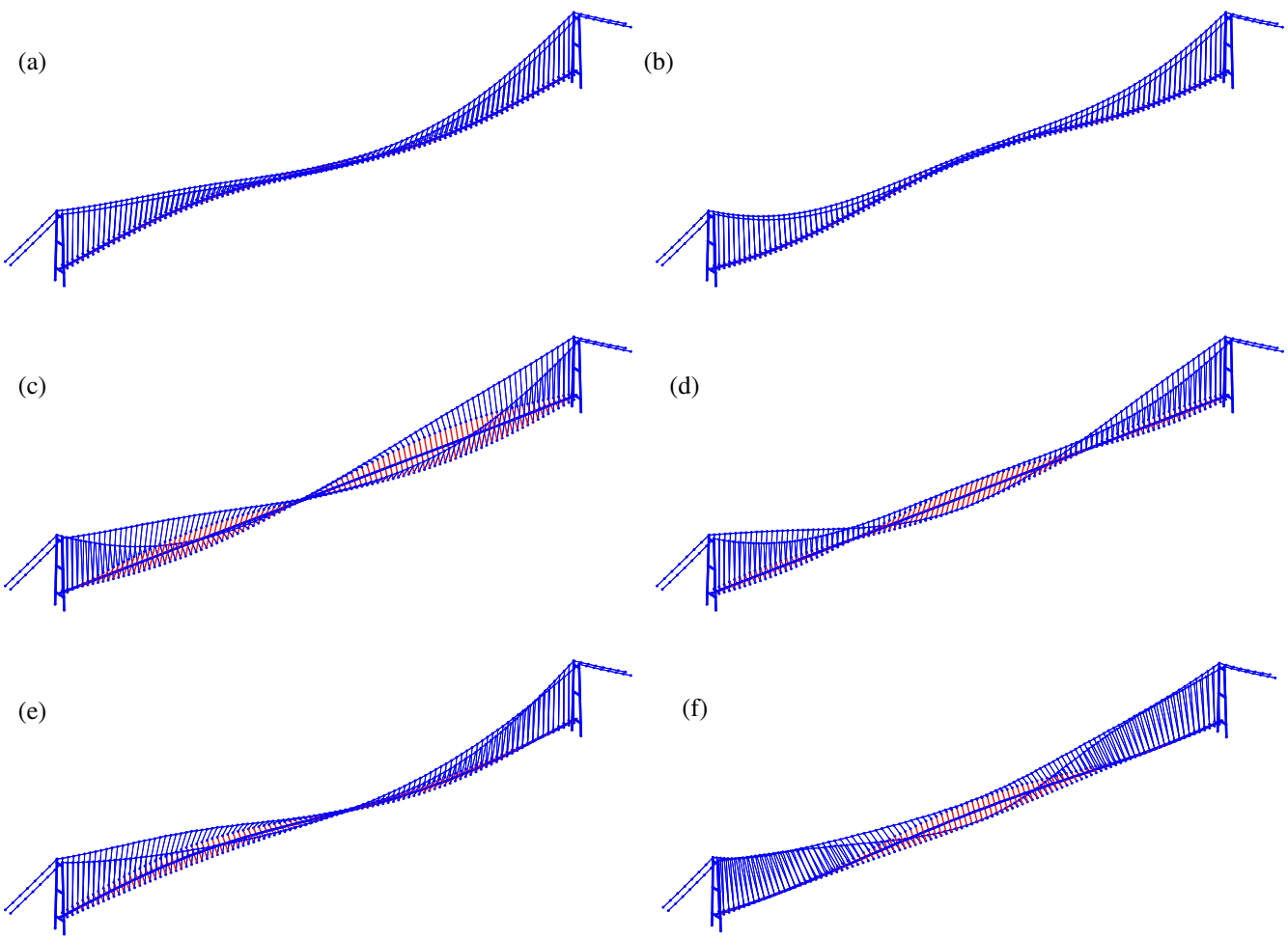

FIGURE 7 Mode shapes: (a) Anti-symmetric heave, (b) Symmetric heave, (c) Anti-symmetric torsion, (d) Symmetric torsion, (e) Anti-symmetric flutter, (f) Symmetric flutter.

The bridge deck is designed as a twin box girder, but at the current state the wind-structure interaction is treated by the Theodorsen theory for flat plates[22] with a reference width of the plate to account for the slotted hole[23]. The aero-elastic forces are implemented with a rational function approximation including a single exponential term to account for non-instantaneous effects. The aerodynamic coefficients of the bridge deck are set to $\bar{C}_D = 1.20$, $\bar{C}_L = -0.15$ and $\bar{C}_M = 0.30$, and their first derivative with respect to the deck angle are $C'_D = 0$, $C'_L = 6.3$ and $C'_M = 1.0$. The height and the reference width of the bridge girder is $D = 2.5$ m and $B = 13$ m. The diameter of the suspension cables and hanger cables are $D_{sc} = 1.19$ m and $D_h = 0.10$ m, and the drag coefficient of the cables is set to 0.8.

The structural damping of long-span bridges is very low and at the same time difficult to determine. In the current study it is of interest to investigate the effect of external dampers on different modes, different systems and at different aero-elastic states. To allow for a direct comparison of the results modal damping has been implemented with a damping coefficient of $\zeta_s = 0.32\%$ suggested by Hansen et al.[25]. The still-air mode shapes of main interest in relation to aerodynamic stability of the considered structure are shown in Fig. 7a–d being the first antisymmetric and symmetric heave mode and the first antisymmetric and symmetric torsional mode. Figure 7e,f shows the shape of the critical mode at the point of zero damping, and it is seen that these modes appear primarily as combinations of the displayed pairs of still-air modes.

The evolution of the modal properties of the four modes is now considered. Figure 8a shows the frequencies as function of the normalized mean wind speed for System 1 without a mid-span cable clamp. The heave modes are represented with dashed lines and the torsional modes are represented with solid lines. Symmetric and anti-symmetric modes are red and blue, respectively. Near the critical wind speed the frequencies of the torsional modes are decreasing, while the frequencies of the heave modes are more constant. In accordance with the still-air modal frequencies presented in Table 1, the anti-symmetric modes have the

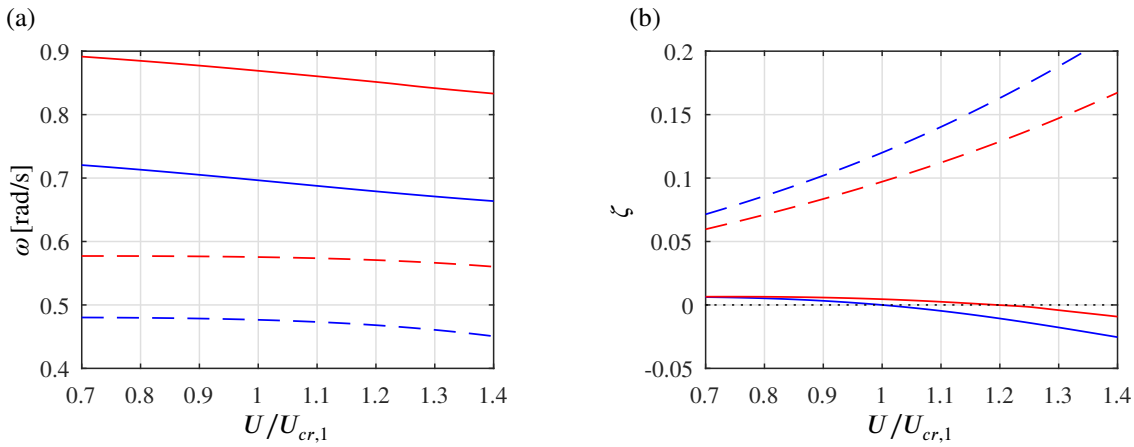

FIGURE 8 System 1: (a) Frequencies, (b) Damping ratios. — AH1, — SH1, — AT1, — ST1.

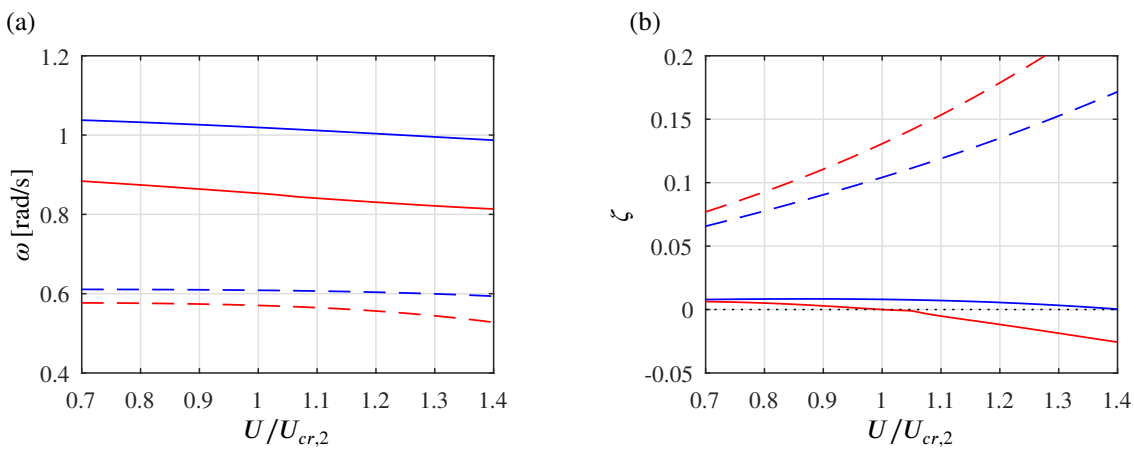

FIGURE 9 System 2: (a) Frequencies, (b) Damping ratios. — AH1, — SH1, — AT1, — ST1.

lowest frequencies. Figure 8b shows the damping of the four modes as function of the normalized wind speed. Near the critical wind speeds the damping of the original heave modes is very large, while the damping of the original torsional modes is low. At the mean wind speed $U = U_{cr,1}$, where $U_{cr,1} = 57.4$ m/s is the critical wind speed, the anti-symmetric torsional mode has zero damping, while the symmetric torsional mode becomes unstable at a mean wind speed 20% higher than the anti-symmetric torsional mode.

The evolution of the modal frequencies and the modal damping of System 2 with cable clamps is shown in Fig. 9a,b. In contrast to System 1 without cable clamps, the symmetric modes now have the lowest frequencies. Also, the damping curves have shifted, so that now the damping ratio of the first symmetric torsional mode crosses the zero damping line first at $U_{cr,2} = 1.2U_{cr,1}$, while the instability limit of the anti-symmetric modes is shifted to a wind speed around 40% higher than the critical wind speed of the symmetric mode.

3.1 | Damper design

The configuration investigated in detail in the following consists of four parallel spring-damper devices placed symmetrically at the middle cross beam of the pylons and connected to the main suspension cables at the third hanger connection by a cable, as shown in Fig. 10a. The devices are attached to the center of the pylons to ensure that they are free of the hanger cables. The height of the attachment point to the pylon is chosen based on the existing pylon geometry, and the horizontal distance to the suspension cable attachment corresponds to 3% of the span length which for a cable with sag would provide approximately 3% damping on the first anti-symmetric cable mode[17]. Figure 10b shows a sketch of the spring-damper-cable system. Initially, the cable connecting the parallel spring-damper device to the main suspension cable is considered infinitely stiff in comparison to the spring, whereby the the clamped frequency ω_∞ is found by inserting an infinitely stiff bar element between the pylon and the suspension cable.

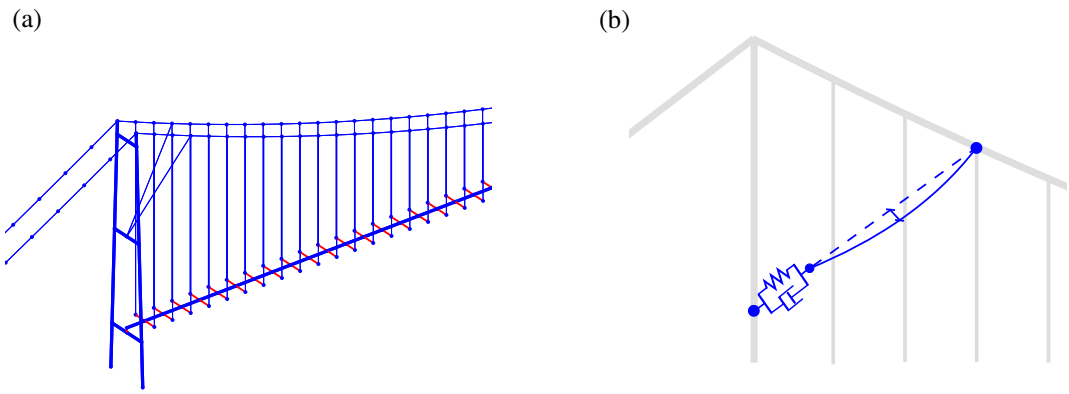

FIGURE 10 (a) Damper position, (b) Damper system sketch (distorted geometry).

Table 2 shows the still-air natural frequencies ω_0 and ω_∞ of the model with free and clamped devices, respectively. The frequencies are shown for the four most relevant modes in relation to stability of the suspension bridge and for the system without and with mid-span cable clamps, referred to as System 1 and 2, respectively. These frequencies are the basis of the design of the spring-damper system together with the structural frequency ω_k found when the stiffness of the spring is included in the model. In the design the stiffness of the spring is determined to provide a 10% reduction of the frequency interval $\omega_\infty - \omega_0$ of the mode chosen for design. This corresponds to the case with asymptotic solution illustrated in Fig. 5.

The asymptotic result of the two-component subspace approximation is shown for the four modes of interest in Fig. 11 for System 1. The dashed semi-circle represents the approximated frequency trace in the situation where the devices consist solely of a viscous damper, while the solid semi-circle is the approximated frequency trace of the modes including a spring with stiffness determined via the frequency shift of the first antisymmetric torsional mode. The axes are normalized by the corresponding frequency ω_0 of the undamped system. The plots clearly reveal that the relative frequency increment from zero

TABLE 2 Still-air angular frequencies [rad/s], S/A: symmetric/antisymmetric, H/T: heave/torsion.

System	State	AH1 (I)	SH1 (II)	AT1 (III)	ST1 (IV)
1	Free ω_0	0.476	0.572	0.743	0.911
1	Clamped ω_∞	0.495	0.594	0.779	0.941
2	Free ω_0	0.605	0.572	1.053	0.914
2	Clamped ω_∞	0.613	0.593	1.060	0.943

to infinite damping varies between modes. The normalization also entails that the y-axis is now an approximated damping ratio as $\zeta = \mathrm{Im}[\omega]/|\omega| \simeq \mathrm{Im}[\omega]/\omega_0$. From the plots it is seen that the damping potential is largest for the anti-symmetric modes, as expected because these modes are governed by the first antisymmetric cable modes where the relative displacement of the cable at the damper connection point is larger.

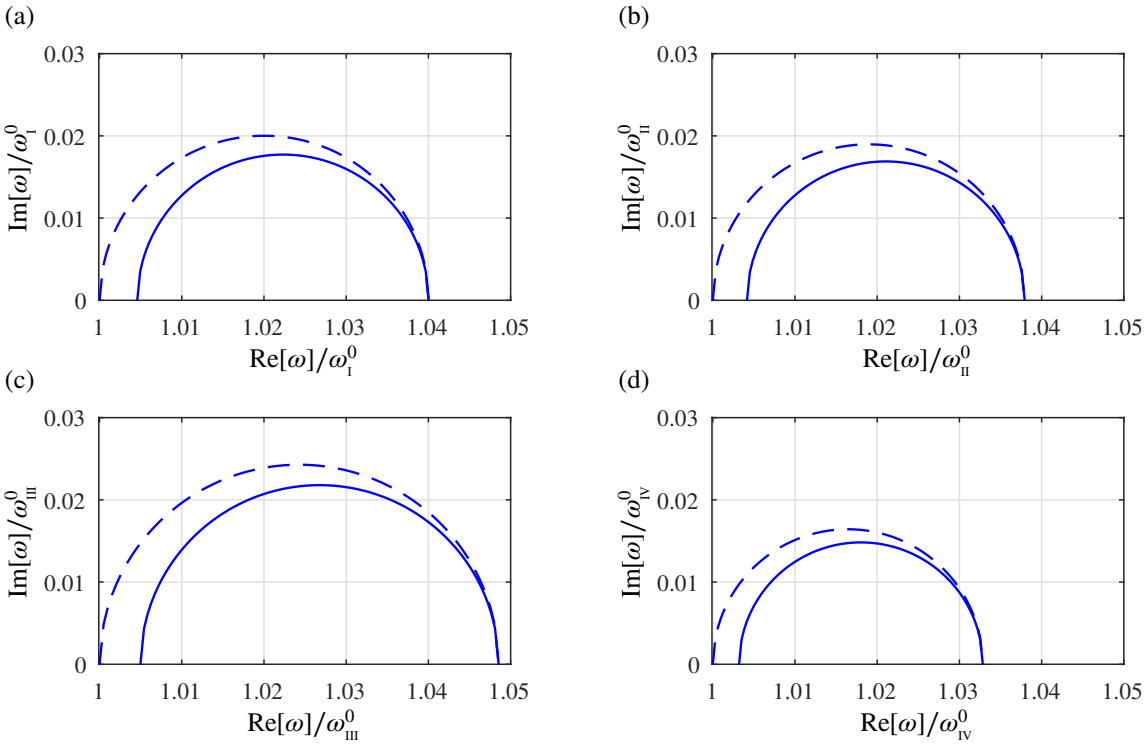

FIGURE 11 Complex frequency locus, (a) AH1, (b) SH1, (c) AT1, (d) ST1.

The devices are now calibrated to provide optimal damping of a single mode based on the asymptotic result of the two-component subspace method presented in (22). The stiffness and damping coefficients providing optimal damping of each of the considered modes are presented in Table 3. The damping coefficient that is optimal for the first anti-symmetric torsional mode is used throughout this section to illustrate the modal damping of all the four modes of interest.

Figure 12 shows the normalized design curves including the estimated frequencies of the four considered modes marked with blue circles. The estimated frequencies are found for the damping coefficient optimal for the first antisymmetric torsional mode, mode III, whereby the estimated frequency of this particular mode is seen to be at $\eta = 1$ and accordingly at the top of the frequency trace semicircle. Furthermore, the results clearly show that the other three modes exhibit damping relatively close to their optimal potential. This shows that four equally tuned and symmetrically located dampers are indeed capable of efficient damping of all the four modes.

TABLE 3 Optimal design parameters of each mode.

System	Parameter	AH1 (I)	SH1 (II)	AT1 (III)	ST1 (IV)
1	k [10^6 N/m]	0.950	0.990	1.091	1.135
1	c [10^6 kg/s]	19.772	17.173	14.556	12.366
2	k [10^6 N/m]	0.886	1.040	0.976	1.247
2	c [10^6 kg/s]	14.546	18.103	9.268	13.681

The actual damping ratios of the four modes are found by evaluating the complex frequencies of the bridge model including the external devices with the design tuning parameters. Figure 13 shows the asymptotically estimated frequencies marked with blue circles and the actual frequencies from the full model marked with red crosses. The frequency intervals are here normalized by the undamped frequency providing an estimate of the modal damping ratio of the considered modes. It is seen that the damping ratios obtained for each of the four modes vary considerably due to the dependence of the real part of the modal frequency as well as the frequency shift between a undamped mode and a locked mode. It is observed that as the damping of a particular mode is defined by its particular curve, the chosen tuning of the device will only shift the damping along its own curve. Tuning of a damper system to more than a single mode is therefore a trade-off between optimizing the damping of the mode with the highest damping potential or to provide more equal damping at more modes.

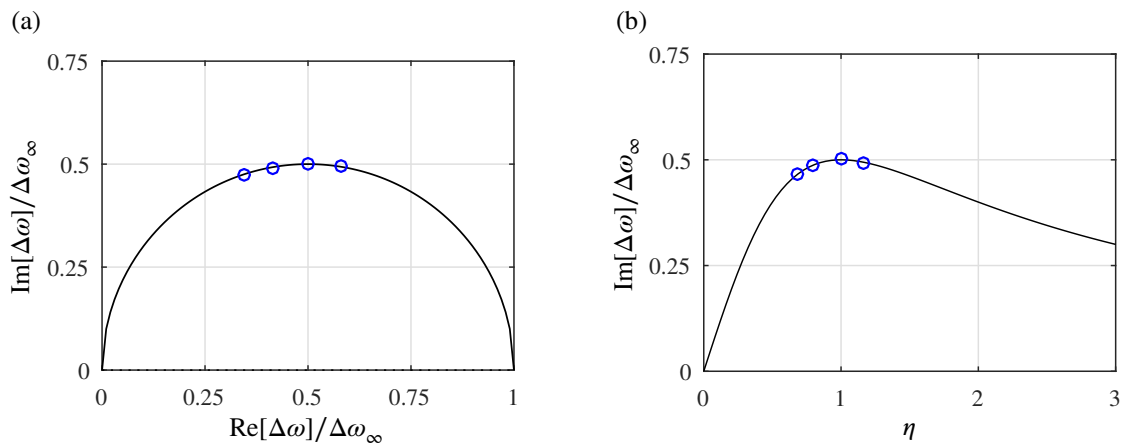

FIGURE 12 Individually normalized design curves: (a) Frequency trace (b) Damping curve.

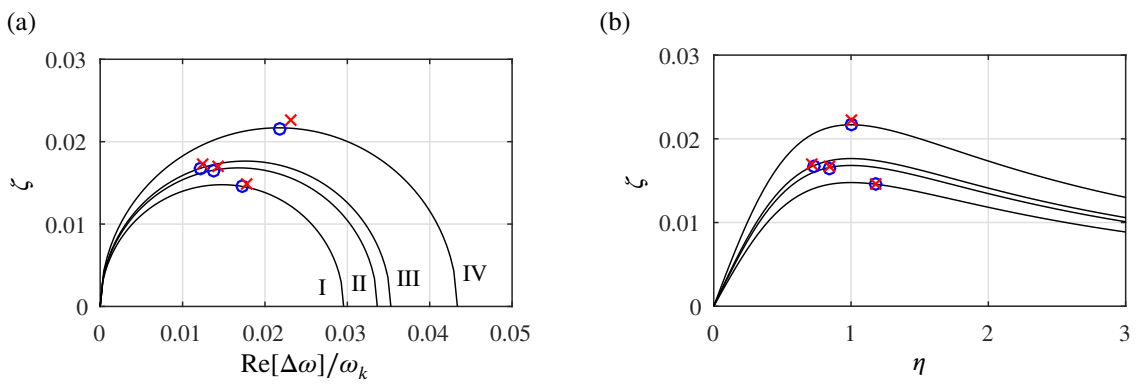

FIGURE 13 Common normalization of design curves: (a) Frequency trace (b) Damping curve.

3.2 | Effect of dampers on the stability limit

The damping coefficients are set according to the estimated optimal values shown in Table 3 and the spring stiffnesses are chosen based on a frequency shift of 10% of the same mode. Figures 14a and 14b show the angular frequency and damping ratio of the first anti-symmetric torsional mode (III) as function of the normalized mean wind speed of the model of System 1 without mid-span cable clamps. The dashed black curve indicates the reference system without external damping and the gray and blue curves represent the damped system with different tuning of the devices. The frequency plot shows the expected frequency increase due to the external devices. The damping plot shows a significant increase of the damping ratio which results in an increase of the stability limit of around 41% to 43% depending on the chosen damping parameters. The blue curve corresponds to optimal damping of the first symmetric heave mode (II) and provides the best stability conditions of the considered system. However, optimal tuning of each of the four modes result in an almost equal stability improvement.

Figures 15a and 15b show the frequency and damping evolution for increasing wind speeds of the first symmetric torsional mode (IV) for System 2 including mid-span cable clamps. Again, the dashed line indicate the system without external damping, while the red and gray curves represent the system with external damping with damper tuning as shown in Table 3. The expected shifts of the frequency and the damping are seen together with an increase of the stability limit of around 27% to 28%. This is lower than the increase for the system without a mid-span cable clamp, corresponding well with the lower damping potential of symmetric modes by the particular damping configuration. However, the stability increase is still substantial. The red curve

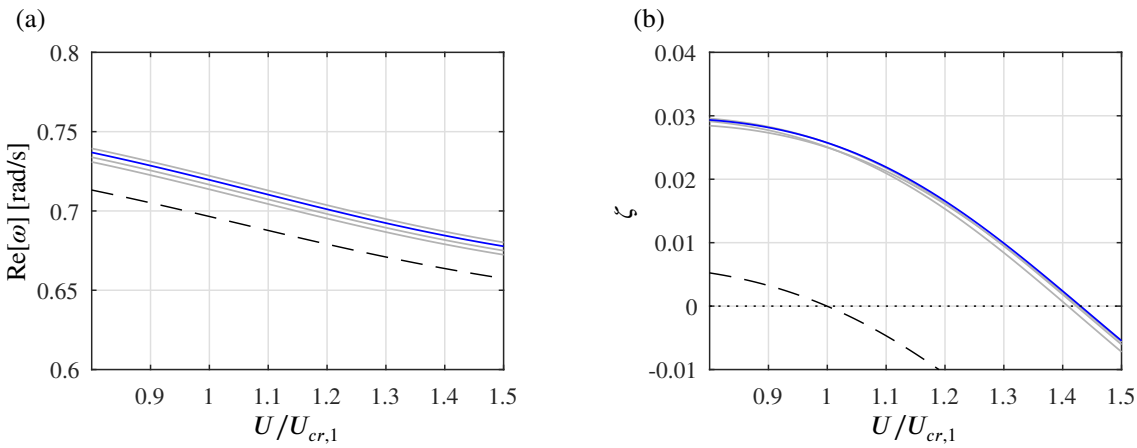

FIGURE 14 System without cable clamp: (a) Frequency, (b) Damping ratio of mode AT1 (III) as function of mean wind speed. (−−) undamped, (−,−) damped.

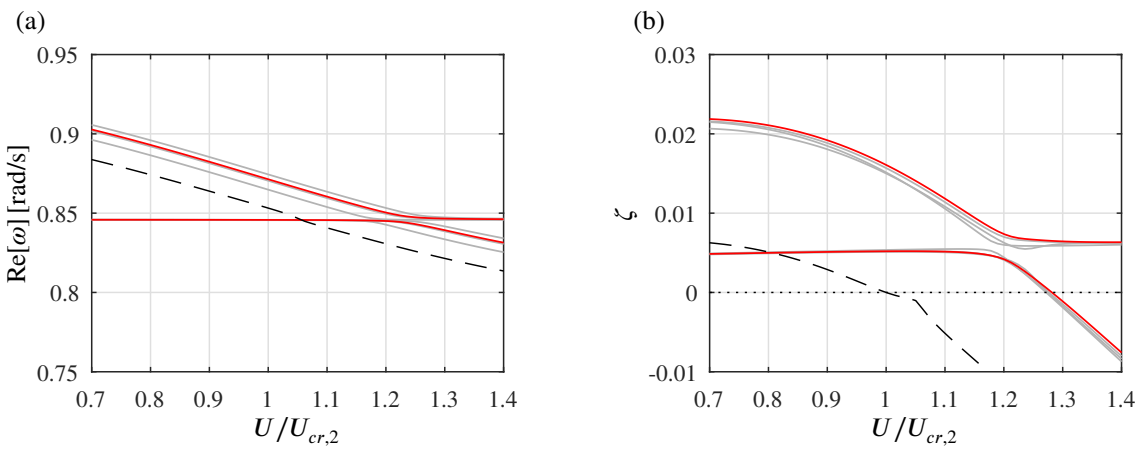

FIGURE 15 System with cable clamp: (a) Frequency, (b) Damping ratio of mode ST1 (IV) as function of mean wind speed. (−−) undamped, (−,−) damped.

represents results obtained for optimal tuning of the first antisymmetric mode (I), but again the chosen tuning has only slight influence on the stability limit.

3.3 | Device configuration

The position of the device in terms of attachment to the pylon and to the main cable will determine the effectiveness of the device. Figure 16a shows three different configurations in which the device is connected to hanger position 2, 3 and 4, respectively. Figure 16b shows three alternative configurations of the external dampers, now shifting the attachment at the pylon plus/minus 30 meters from the original location.

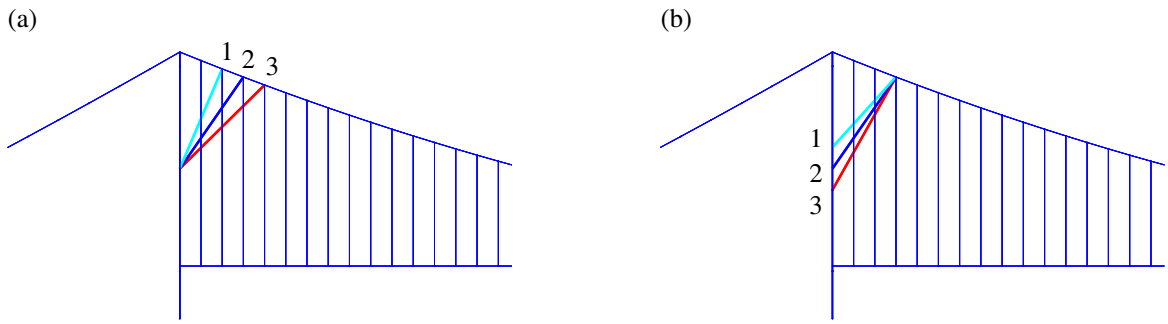

FIGURE 16 Damper configuration: (a) cable attachment, (b) tower attachment.

The stability analysis of System 2 with tuning based on each of the four modes showed that optimal tuning of the first antisymmetric heave mode (I) led to the highest stability limit increase. The current investigation is therefore carried out for optimal tuning of mode I. Table 4 shows the design parameters for each of the six damper configurations. It is noted that configurations a2 and b2 are identical, and that the free vibration frequency ω_0 is identical for all configurations as this refers to the vibration modes of the original structure without any external device. Going from configuration a1 to a3 the cable is attached further away from the pylon on the suspension cable. This leads to a higher clamped frequency ω_∞, whereby a higher damping ratio can be attained. The spring stiffness k is set to provide a reduction of the frequency shift of 10%, and it is found that less stiffness is required when the damper connection is moved further away from the pylon. Finally, the damping coefficient also becomes smaller going from configuration a1 to a3. Changing the location of the damper connection on the pylon and thereby changing the angle of the damper relative to the cable motion only appears to have a small influence on the damping parameters. However, a tendency is seen where a smaller angle between the cable and the pylon provides a more direct connection and thereby a higher clamped frequency.

The damping ratios of the four modes estimated using (24) are shown in Table 5 for all of the six damper configurations together with the similar parameters obtained from the full numerical model given in normalized form. As expected the damping of all four modes are increased going from configuration a1 to a3 and only slight differences are seen going from configuration b1 to b3. It is especially noted that the damping of the anti-symmetric modes is increased, whereas the damping of the symmetrical

TABLE 4 System with cable clamp: Design parameters for optimal damping of mode I.

Configu-ration	ω_0 [rad/s]	ω_k [rad/s]	ω_∞ [rad/s]	k [10^6 N/m]	c [10^6 kg/s]
a1	0.6053	0.6058	0.6100	1.394	22.917
a2	0.6053	0.6061	0.6129	0.886	14.546
a3	0.6053	0.6064	0.6160	0.723	11.847
b1	0.6053	0.6061	0.6126	0.946	15.526
b2	0.6053	0.6061	0.6129	0.886	14.546
b3	0.6053	0.6061	0.6131	0.863	14.170

TABLE 5 System with cable clamp: Modal damping for optimal damping of mode I.

Configu-ration	$\zeta_{\mathrm{I}}^{\mathrm{est}}$ [%]	$\zeta_{\mathrm{I}}/\zeta_{\mathrm{I}}^{\mathrm{est}}$	$\zeta_{\mathrm{II}}^{\mathrm{est}}$ [%]	$\zeta_{\mathrm{II}}/\zeta_{\mathrm{II}}^{\mathrm{est}}$	$\zeta_{\mathrm{III}}^{\mathrm{est}}$ [%]	$\zeta_{\mathrm{III}}/\zeta_{\mathrm{III}}^{\mathrm{est}}$	$\zeta_{\mathrm{IV}}^{\mathrm{est}}$ [%]	$\zeta_{\mathrm{IV}}/\zeta_{\mathrm{IV}}^{\mathrm{est}}$
a1	0.35	1.001	1.12	1.013	0.16	0.986	0.98	0.969
a2	0.56	1.003	1.69	1.020	0.27	0.987	1.47	0.985
a3	0.79	1.005	2.22	1.028	0.38	0.987	1.94	0.998
b1	0.53	1.003	1.66	1.019	0.24	0.987	1.55	0.988
b2	0.56	1.003	1.69	1.020	0.27	0.987	1.47	0.985
b3	0.58	1.003	1.69	1.020	0.29	0.986	1.44	0.983

modes is decreased going from configuration b1 to b3. The estimated damping ratio is generally providing an accuracy within 3% with larger perturbations of the original system causing larger deviations from the numerical results.

The modal damping ratio of the first anti-symmetric torsional mode (IV) is plotted as a function of the mean wind speed for configurations a1–a3 in Fig. 17a and for configurations b1–b3 in Fig. 17b. The graphs are color coded according to Fig. 16a,b. The dashed black curve is the reference damping ratio of the system without external damping. It is seen that the stability limit is significantly affected by shifting the location of the damper on the main cable changing from a stability increase of around 21% to 34%. Shifting the damper position on the tower is seen to have no effect on the stability limit.

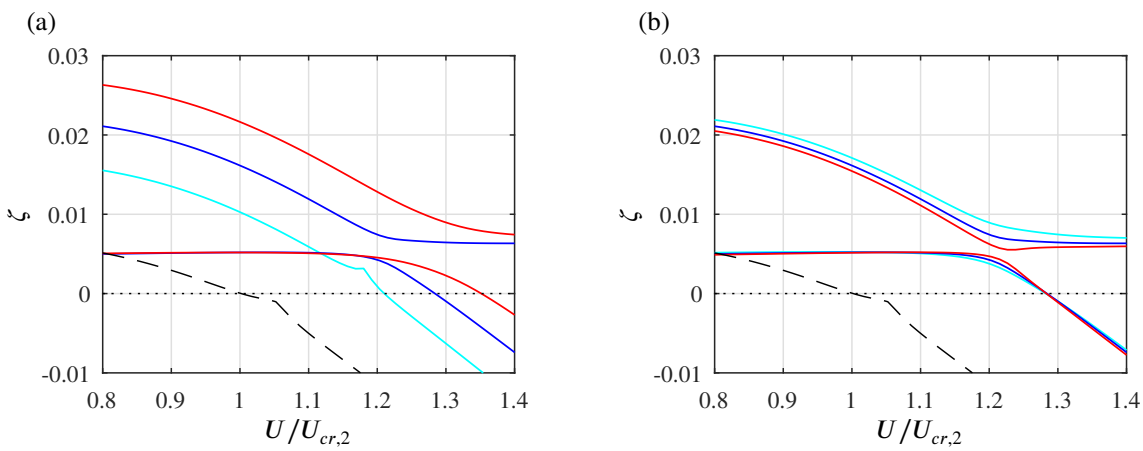

FIGURE 17 Damping ratios of ST1 (IV): (a) configuration 1a–3a, (b) configuration 1b–3b.

4 | DAMPED RESPONSE

The response due to turbulent wind loading is now evaluated. The wind field is represented as stretched isotropic turbulence[26]. The along-wind component is represented by the von Kàrmàn spectral density with the integral length scale $\lambda_x = 300\,\mathrm{m}$ and the two transverse length scales $\lambda_y = \lambda_z = 0.5\lambda_x$. The turbulence intensity is $I_u = 0.135$ and the standard deviation of the along-wind turbulence component is found as $\sigma_u = I_u/U$ where U is the mean wind speed. Direct time simulations of the three-dimensional wind field are carried out by the conditional mean field method[26]. The method is an auto-regressive procedure using non-uniform spacing of the regression terms and direct evaluation of the coefficients from conditional correlation functions. A basic step size $h = 0.6\,\mathrm{s}$ is used and an exponential memory layout with time intervals scaled by $k = [2^0, 2^1, ..., 2^8]$, providing a rather accurate representation of the statistical properties of the wind field. Numerical integration of the aero-elastic system is performed using a momentum based, second order method[20].

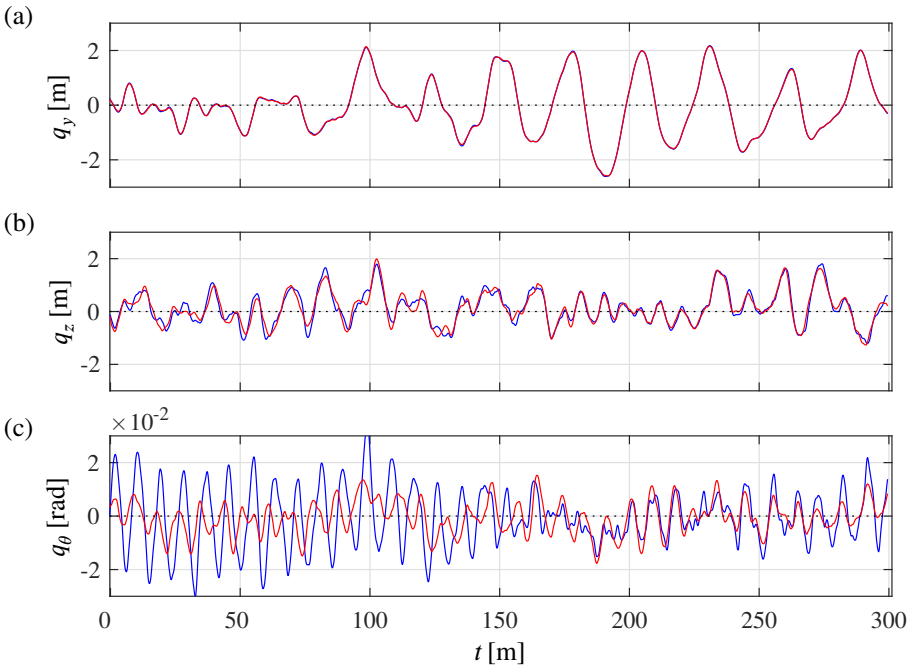

FIGURE 18 Response at quarter-span of system without cable clamp. (—) undamped, (—) damped.

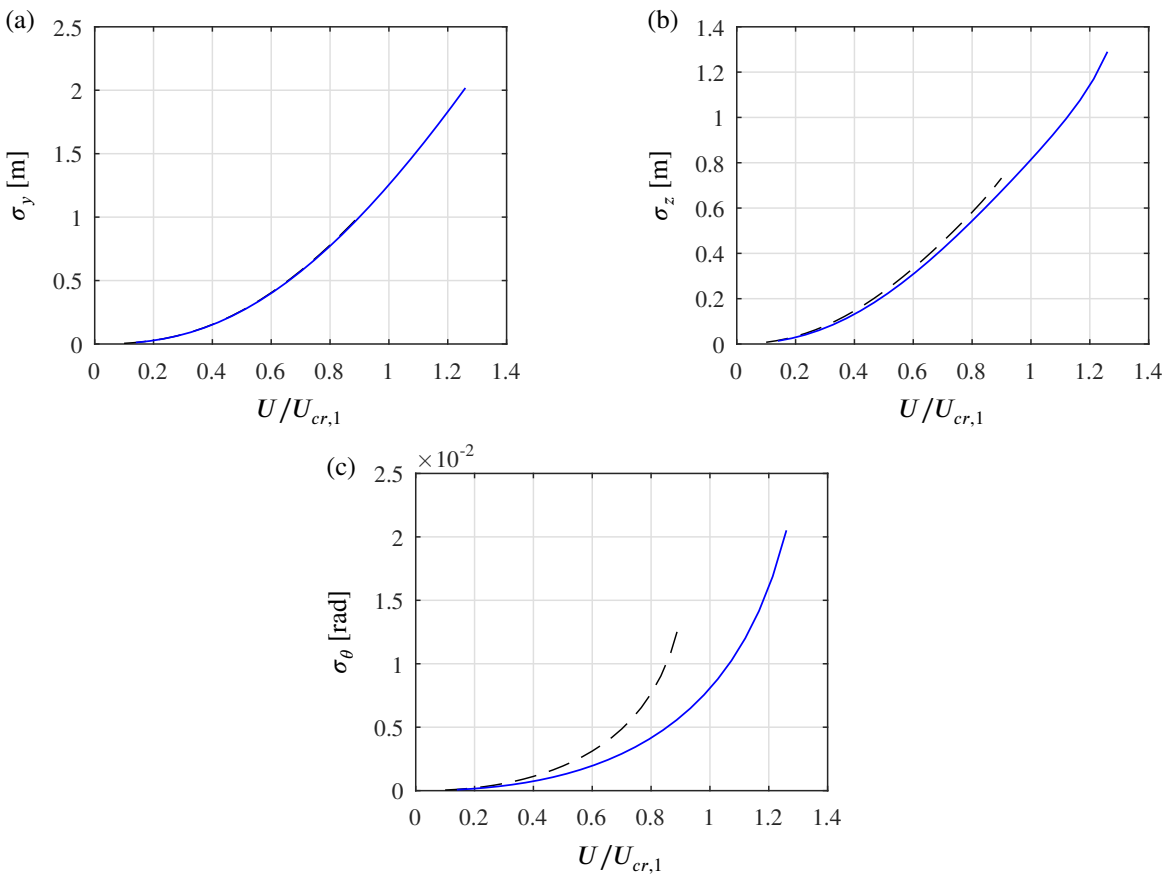

FIGURE 19 Response at quarter-span of system without cable clamp. (– –) undamped, (—) damped.

A five-minute steady state time record of the structural response of System 1 without a mid-span cable clamp is shown in Figs. 18a–c. The time records are shown at quarter span for a mean wind speed of 90% of the critical wind speed of the system without external damping. The blue curve represents the system without external damping and the red curve represents the system with external damping with device coefficients optimal for the first symmetric heave mode, mode II. The drag response, q_y, is unaffected by the external damping, the heave response q_z is slightly affected, while the torsional response, q_θ is significantly decreased by the added damping.

Figures 19a–c show the standard deviation of the drag, heave and torsional response σ_y, σ_z and σ_θ as function of the mean wind speed for System 1 without a mid-span cable clamp. The black dashed curves are results for the system without external damping and the blue curves are results with external damping and device coefficients optimal for the first symmetric heave mode, mode II. As for the time records shown in Fig. 18 the external dampers has no effect on the drag response, only modest effect on the vertical response and significant effect on the torsional response. It is seen that the vertical asymptomatic value of the torsional is shifted according to the stability limit increase discussed in relation to Fig. 14.

Figure 20a shows the standard deviation of the torsional response at mid-span for System 2 including mid-span cable clamps. The response is shown for the reference system without external damping marked with a dashed black curve and for the damper configuration a1–a3 as shown in Fig. 16a. The damping coefficients are set according to Table 4 and the graphs are colored as in to 16a. Figure 20b shows the standard deviation of the torsional response at mid-span for the same system for results obtained with device configuration b1–b3 as shown in Fig. 16b. As before the black dashed graph marks the results obtained with the reference model without external damping. It is seen that the torsional response obtained going from configuration a1 to a3 is decreasing and that the asymptotic value at the instability limit is shifted toward higher wind velocities. The torsional response is virtually unaffected by shifting the position of the device on the pylon, obtained for configuration b1–b3. These results correspond well with the damping results shown in Fig. 17.

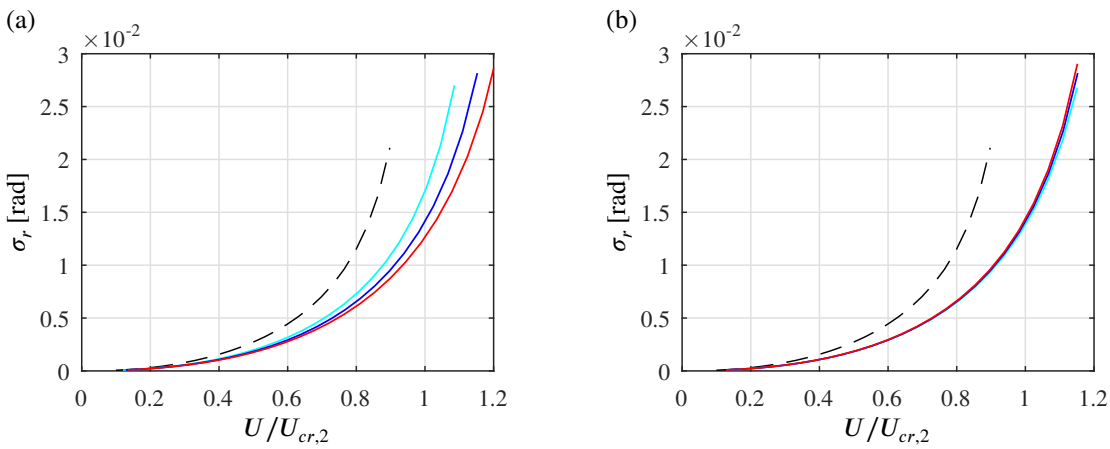

FIGURE 20 Torsional response at mid-span for system with cable clamp: (a) configuration a1–a3, (b) configuration b1–b3.

4.1 | Cable flexibility

The flexibility of the cable connecting the spring-damper device to the suspension cable as illustrated in Fig. 10b is now considered. As a first step the tension force in the cable T is determined as the sum of the damper force $c\dot{q}_d$ and the spring force $kq_d + \bar{T}$, where q_d is the damper displacement for a rigid connecting cable, $\dot{q}_d$ is the first time derivative of the relative displacement and $\bar{T}$ is the pre-tension force. As basis for the cable design the oscillating part of the cable tension force $T - \bar{T}$ is determined at a mean wind speed of 90% of the critical wind speed of the considered damped system. A five-minute time record of the force in an upstream connection and a downstream connection are shown in Fig. 21a,b for configuration a2. The aero-elasticity introduces an asymmetry in the system, whereby the force in the downstream connection is higher. Comparing the standard deviation of the response of a 20 hours time series, the downstream cable force is found to be 18.2% higher, and the damper system should therefore be designed based on a downstream device.

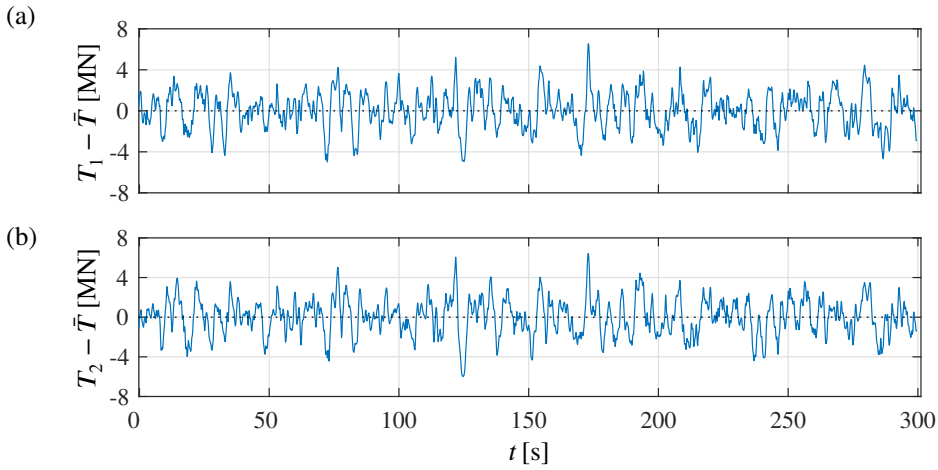

FIGURE 21 Cable force: (a) upstream device, (b) downstream device.

For the damper system to be working, the cable should be in tension at all times, corresponding to a positive cable force. Furthermore, the cross-section area of the cable as well as the tension force should be sufficient to provide a high axial cable stiffness relative to the spring stiffness to ensure effectiveness of the damper system. The cable stiffness k_c can be estimated from the so-called Dischinger formula[27,28]

$$k_c = \frac{E_{eq} A_c}{L}, \quad E_{eq} = \frac{E_c}{1 + w^2 L_h^2 A_c E_c / (12 T^3)} \tag{25}$$

where A_c is the cross-section area of the cable, L is the length of the cable and E_{eq} is the equivalent stiffness modulus of the cable taking into account the cable weight per unit length w, the horizontal span length L_h and the tension force in the cable T. The stiffness modulus is $E_c = 195$ GPa.

A cable design matching the damping and stiffness coefficients of the different cable configurations in Fig. 16 is carried out. A consistent design approach is applied in two steps: First, the cross-section area of the cable is determined to provide a stiffness ratio between the spring and the cable of $k_c/k = 20$ assuming $E_{eq} = E_c$. Then the pre-tension, and thereby the initial deformation of the spring, is determined to provide a ratio $E_{eq}/E_c = 0.95$ for the minimum tension occurring in the cable $T_{\min} = \bar{T} - \Delta T$, where ΔT is the expected peak value of the oscillating part of the cable force. This ensures a high cable stiffness within the operating tension range. The cable design parameters are shown in Table 6. The parameter Δx is the peak elongation/compression of the spring-damper device determined based on the structural response. The peak response is estimated as the standard deviation of the response multiplied by a peak factor $p = 4$. $\bar{x}$ is the initial spring deformation, D_c is the cable diameter and $\sigma_{\max}/f_y$ is the utilization ratio of the cable, where $\sigma_{\max}$ is the maximum stress and $f_y = 1640$ MPa is the yield stress. Finally, the stiffness ratio k_c/k is provided, where k_c is the cable stiffness at $x = \bar{x}$.

Considering the cable design for configuration a1 to a3, the cable length is only increasing slightly while the horizontal length is increased significantly. Also, it is seen that the required pre-tension of the cable as well as the peak value of the oscillating part

TABLE 6 Cable parameters.

Configuration	L [m]	L_h [m]	ΔT [MN]	Δx [m]	$\bar{T}$ [MN]	$\bar{x}$ [m]	D_c [m]	$\sigma_{\max}/f_y$	k_c/k
a1	153.8	62.8	8.16	0.62	12.54	9.0	0.167	0.57	19.95
a2	158.1	91.6	8.64	1.04	12.31	13.9	0.135	0.89	19.97
a3	168.7	120.9	9.69	1.44	13.51	18.7	0.126	1.13	19.97
b1	134.8	91.6	8.75	1.00	12.10	12.8	0.129	0.97	19.98
b2	158.1	91.6	8.64	1.04	12.31	13.9	0.135	0.89	19.97
b3	183.4	91.6	8.60	1.06	12.77	14.8	0.144	0.80	19.96

of the cable force are increased slightly, while the initial displacement and the in-service elongation increase significantly. This can be explained by the decreasing stiffness and damping coefficients shown in Table 4. The stiffness decrease also explains the decreasing cross-section diameter needed to achieve the same stiffness ratio between the cable and the spring. For configuration a3 it is seen that the utilization ratio exceeds one. This factor is lowered by choosing a larger cross-section diameter. From the damping plots in Fig. 17a it was evident that a larger increase of the stability limit was obtained by moving the device attachment point on the suspension cable further away from the pylon. The results presented in Table 6 show that this is also the configuration that requires the largest initial deformation of the spring as well as the largest in-service deformations. From the cable design for configuration b1 to b3, it is seen that a shorter cable requires less initial deformation of the spring as well as slightly lower in-service deformations of the spring-damper device. From the stability results shown in Fig. 17b it was seen that the stability limit increase was similar for the three configurations, and a shorter cable is then to be preferred. For all of the configurations the stiffness ratio k_c/k is seen to be very close to 20, used as design input. Figure 22 shows the equivalent stiffness modulus as function of the tension force. The red cross marks the stiffness at $T = \bar{T}$ and the black crosses mark the stiffness at $T \pm \Delta T$ for configuration a2. For the design choices applied the cable stiffness is almost constant in the operating range.

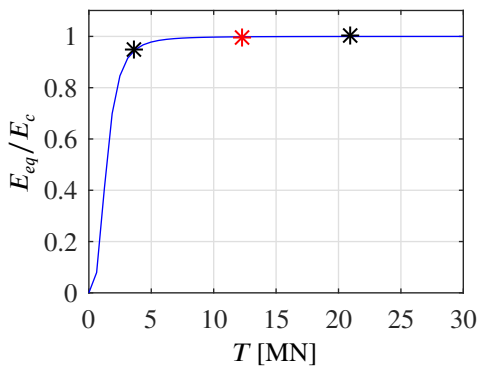

FIGURE 22 Cable stiffness modulus.

The effect of including cable flexibility in the model is evaluated by including an additional node between the structural attachment points, whereby the spring-damper device is now connecting the tower to the intermediate point and a linear bar element with stiffness k_c is connecting the intermediate point to the suspension cable. The tuning of the damper is re-evaluated as the frequency for locked dampers is now lower due to the flexibility of the cable. The spring stiffness is not updated, giving tuning parameters of $k = 0.886 \cdot 10^6$ N/m and $c = 9.586 \cdot 10^6$ kg/s. Figure 23a,b shows the frequency traces and the damping curves of configuration a2 including cable flexibility. The blue circles indicate the frequencies predicted based on the asymptotic solution for the two-component subspace method and the red crosses mark the frequencies obtained with the numerical model. The design results correspond well to the frequencies and damping ratios obtained with the numerical model.

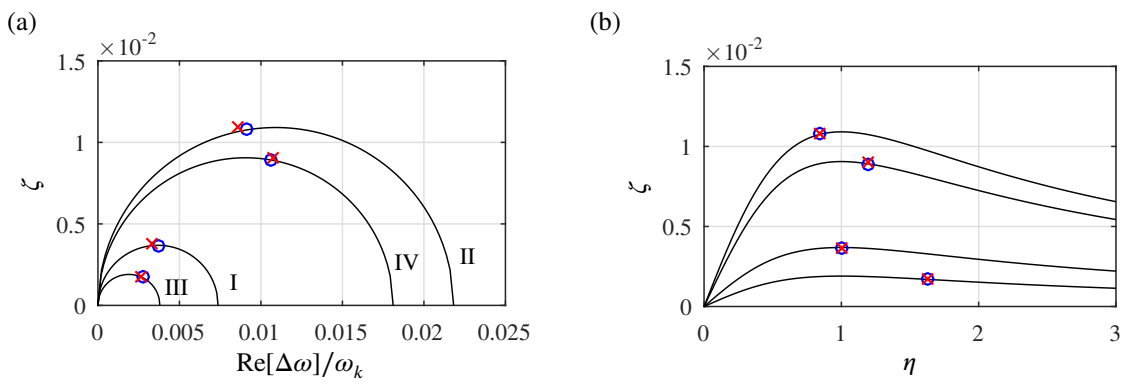

FIGURE 23 Design curves for configuration a2: (a) Frequency trace (b) Damping curve.

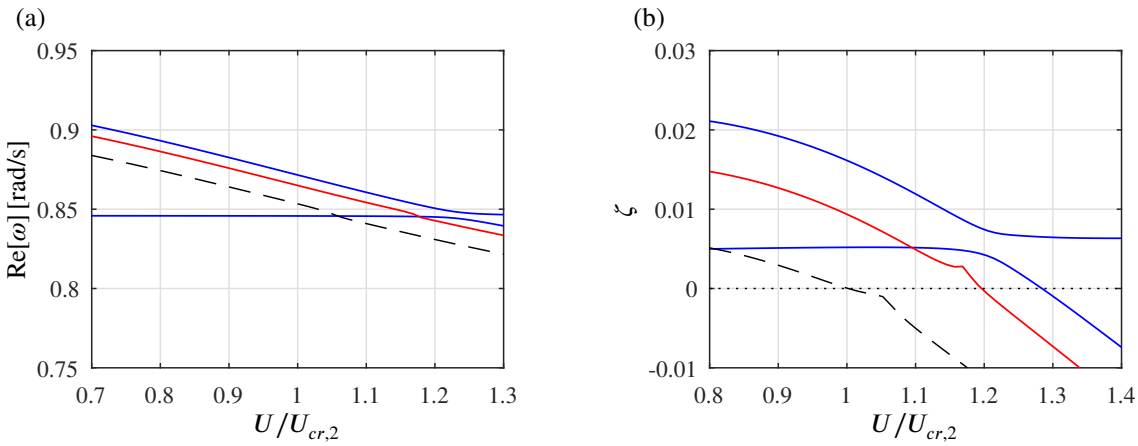

FIGURE 24 Effect of cable stiffness for system with cable clamp: (a) Frequency, (b) Damping ratio of mode ST1 (IV) as function of mean wind speed. (−−) undamped, (−) stiff damper cable, (−) flexible damper cable.

The change of the natural frequency and damping for increasing wind speeds are shown for the first symmetric torsional mode for configuration a2 in Fig. 24a,b. The dashed black line is the reference result for the system without external damping, the blue curves mark results obtained with the idealized model assuming an infinitely stiff cable and the red curves are results obtained with the model including cable flexibility. It is seen that the modal frequency is smaller when the cable flexibility is included. Also, the modal damping ratio is smaller, whereby the stability limit is reduced by 7.4% relative to the idealized case. The stiffness of the cable is a design choice and by accepting a larger initial deformation of the spring a stiffer cable can be used, providing a more effective damper system.

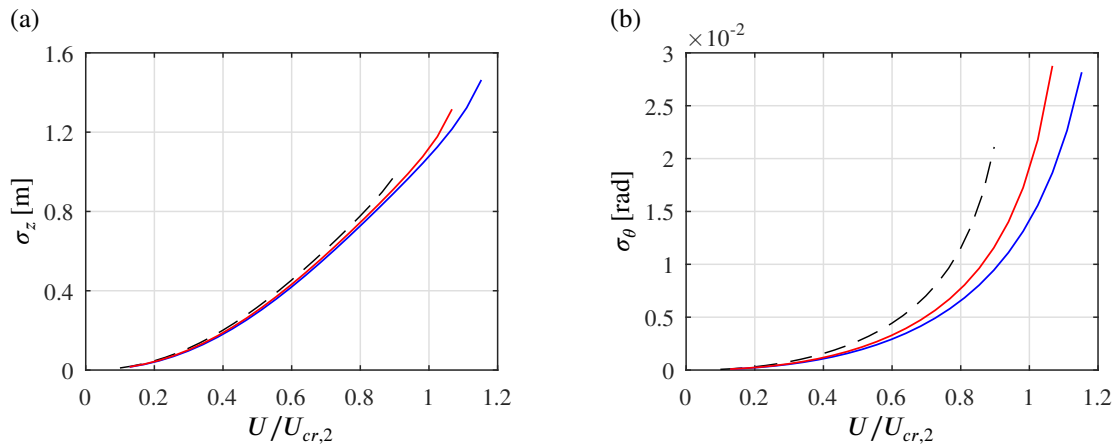

FIGURE 25 Response at mid span, (−−) undamped, (−) damped - stiff cable, (−) damped - flexible cable.

Finally, the effect of including the cable flexibility is considered in relation to the buffeting response. Figure 25a,b shows the vertical and torsional response at mid-span for System 2. The black dashed curves are results obtained with the reference system without external damping, the blue curves are results obtained with the idealized system with an infinitely stiff cable and the red curves are results including the cable flexibility. The dampers are placed according to configuration a2. It is seen that both the heave and the torsional response is higher when the cable flexibility is included.

The cable force can now be evaluated as the cable stiffness multiplied by the elongation of the bar element connecting the parallel spring-damper to the main suspension cable. Hereby, the peak value of the oscillating part of the cable force is found to $\Delta T = 5.33$ MN which is 38% lower than the cable force obtained for the idealized system. Repeating the design approach the initial deformation becomes $\bar{x} = 9.8$ m and the utilization ratio is $\sigma_{\max}/f_y = 0.66$. The initial deformation of the spring appears

large, but should be compared to the depth of the pylon leg which is around 16 m. The initial deformations can advantageously be conducted as compression by attaching the cable to the far end of the spring and thereby gaining a compact design.

4.2 | Damper operation characteristics

The in-service damper operation characteristics are now considered for the structure with a mid-span cable clamp and external dampers in configuration a2 including cable flexibility. The response is evaluated at a mean wind speed equal to 90% of the critical wind speed of the damped system. Figure 26a shows a five-minute steady-state displacement time record of the parallel spring-damper device evaluated as the relative displacement of the device end nodes. A downstream device is considered. Figure 26b shows the force in the viscous damperm $f_d = c\dot{q}_d$, $c = 9.586 \cdot 10^6$ kg/s. The standard deviation of displacement and damping force are found based on a 20-hour time simulation. Multiplication by a peak factor of 4 gives the peak values $\Delta q_d = 0.811$ m and $\Delta f_d = 5.18$ MN.

A five-minute time record of the energy dissipation rate $P_d = f_d \dot{q}_d$ in the device is shown in Fig. 27. The red line marks the mean value at $P_d = 0.18$ MW. Requirements to energy dissipation are typically part of a damper specification. This is for the design of the thermal capacity of the damper, as the mechanical energy is dissipated by transformation into heat. Location of the damper at the outside of the tower indicates that a relatively compact damper design may be necessary, i.e. concentrated heat build-up may be an issue. However, at this location, effective wind cooling can be assumed. An alternative may be to locate the

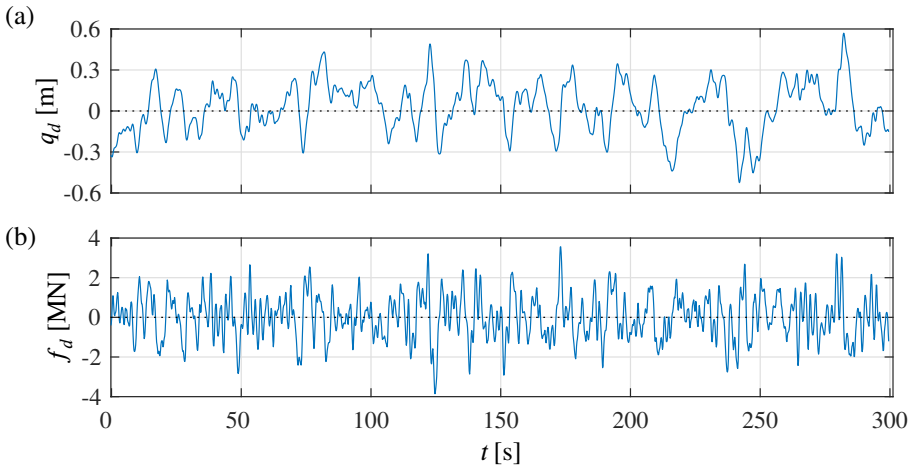

FIGURE 26 (a) Damper displacement (b) damper force.

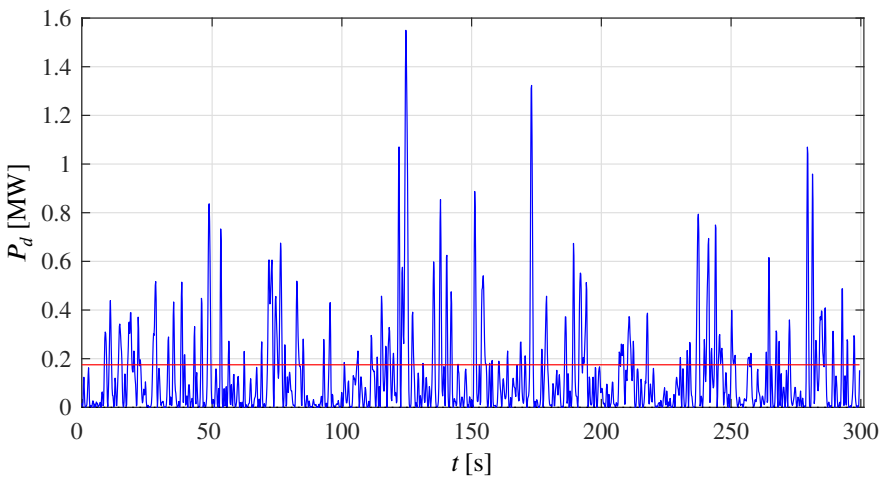

FIGURE 27 Energy dissipation.

damper inside the tower, where space is plenty to distribute the energy dissipation over more devices. Another benefit would be improved accessibility for inspection and maintenance. Drawbacks would be the absence of wind cooling and the need for a more complicated mechanism to transform the relative displacements of the main cable and the tower into displacements over the damper units.

5 | CONCLUSIONS

A damping system for long-span suspension bridges has been presented and the performance has been numerically tested on a full aero-elastic model with emphasis on the aerodynamic stability limit. The tuning of the dampers is based on the asymptotic results to a two-component subspace approximation with still-air modes as calibration input and the simple procedure was seen to provide very accurate results. Also, it was shown that the system of four symmetrically located identical dampers is able to damp all modes related to instability of the bridge effectively. The performance of the damping system was illustrated for two suspension bridge concepts: a single-span suspension bridge without cable clamps, where unstable flutter motions are governed primarily by the anti-symmetric modes, and a similar single-span suspension bridge with a mid-span cable clamp, for which flutter motions are governed primarily by the symmetric modes. It was found that under the assumption of an infinitely stiff connecting cable the system is able to provide an increase of the critical wind speed of around 40% for the system without cable clamps and an increase of around 28% for the system with mid-span cable clamps, when the device is attached to the suspension cable at a distance from the pylon of 3% of the bridge span length. It is also shown that the modal damping ratio, and thereby the critical wind speed, can be increased further by shifting the device attachment point on the suspension cable further away from the pylon. However, this comes at a cost of larger device deformations and larger required pre-tension forces in the damping system. Shifting the anchorage point of the device on the pylon was seen to have little effect. The damping system was shown to significantly reduce the torsional buffeting response, while having little impact on the lateral and vertical response. When including the flexibility of the pre-tensioned cable connecting the spring-damper device to the structure it was found that a cable with a stiffness of 20 times the spring stiffness would lower the critical wind speed with 7.4% relative to the critical wind speed of the damped system with an infinitely stiff connecting cable. Damper operation characteristics relevant for device design were shown for a realistic case, considering stroke, force and energy dissipation rate.

ACKNOWLEDGMENTS

This paper is part of a project sponsored jointly by Innovation Fund Denmark, Rambøll and the Technical University of Denmark.

References

1. A. Jain, N.P. Jones, R.H. Scanlan, Effect of modal damping on bridge aeroelasticity, *Journal of Wind Engineering and Industrial Aerodynamics*, **77-8**, 421–430, 1998.

2. M. Gu, C.C. Chang, W. Wu, H.F. Xiang, Increase of critical flutter wind speed of long-span bridges using tuned mass dampers, *Journal of Wind Engineering and Industrial Aerodynamics*, **73**, 111–123, 1998.

3. X. Chen, A. Kareem, Efficacy of tuned mass dampers for bridge flutter control, *Journal of Structural Engineering - ASCE*, **129**, 1291–1300, 2003.

4. A. Casalotti, A. Arena, W. Lacarbonara, Mitigation of post-flutter oscillations in suspension bridges by hysteretic tuned mass dampers, *Engineering Structures*, **69**, 62–71, 2014.

5. B. Mokrani, Z. Tian, D. Alaluf, F. Meng, A. Preumont, Passive damping of suspension bridges using multi-degree of freedom tuned mass dampers, *Engineering Structures*, **153**, 749–756, 2017.

6. F. Casciati, F. Giuliano, Performance of multi-TMD in the towers of suspension bridges, *Journal of Vibration and Control*, **15**, 821–847, 2009.

7. M. Gu, S.R. Chen, C.C. Chang, Control of wind-induced vibrations of long-span bridges by semi-active lever-type TMD, *Journal of Wind Engineering and Industrial Aerodynamics*, **90**, 111–126, 2002.

8. R. Körlin, U. Starossek, Wind tunnel test of an active mass damper for bridge decks, *Journal of Wind Engineering and Industrial Aerodynamics*, **95**, 267–277, 2007.

9. H. Kobayashi, H. Nagaoka, Active control of flutter of a suspension bridge, *Journal of Wind Engineering and Industrial Aerodynamics*, **41**, 143–151, 1992.

10. K. Wilde, Y. Fujino, Aerodynamic control of bridge deck flutter by active surfaces, *Journal of Engineering Mechanics*, **124**, 718–727, 1998.

11. K. Li, Y.J. Ge, Z.W. Guo, L. Zhao, Theoretical framework of feedback aerodynamic control of flutter oscillation for long-span suspension bridges by the twin-winglet system, *Journal of Wind Engineering and Industrial Aerodynamics*, **145**, 166–177, 2015.

12. K.N. Bakis, M. Massaro, M.S. Williams, D.J.N. Limebeer, Aeroelastic control of long-span suspension bridges with controllable winglets, *Structural Control and Health Monitoring*, **23**, 1417–1441, 2016.

13. P. Omenzetter, K. Wilde, Y. Fujino, Suppression of wind-induced instabilities of a long span bridge by a passive deck-flaps control system Part I: Formulation, *Journal of Wind Engineering and Industrial Aerodynamics*, **87**, 61–79, 2000.

14. P. Omenzetter, K. Wilde, Y. Fujino, Suppression of wind-induced instabilities of a long span bridge by a passive deck-flaps control system Part II: Numerical simulations, *Journal of Wind Engineering and Industrial Aerodynamics*, **87**, 81–91, 2000.

15. U. Starossek, H. Aslan, Passive control of bridge deck flutter using tuned mass dampers and control surface. *EURODYN 2008. 7th Eurepean Conference on Structural Dynamics*, Southampton, England, July 7-9, 2008.

16. X. Suduo, J.M. Ko, Y.L. Xu, Wind-induced vibration control of bridges using liquid column damper, *Earthquake Engineering and Engineering Vibrations*, **1**, 271–280, 2002.

17. S. Krenk, S.R.K. Nielsen, Vibration of a shallow cable with a viscous damper, *Proceedings of the Royal Society A*, **458**, 339–357, 2001.

18. J.A. Main, S. Krenk, Efficiency and tuning of viscous dampers on discrete systems, *Journal of Sound and Vibration*, **286**, 97–122, 2005.

19. S. Krenk, J.R. Høgsberg, Damping of cable by a transverse force, *Journal of Engineering Mechanics – ASCE*, **131**, 340–348, 2005.

20. R.N. Møller, S. Krenk, M.N. Svendsen, Turbulent wind response of long-span bridges including flutter, Department of Mechanical Engineering, Technical University of Denmark, 2018. (submitted for publication)

21. Rambøll, for the Norwegian Public Roads Administration, Konseptrapport Hengebru i Korridor 1, November 2015.

22. T. Theodorsen, General theory of aerodynamic instability and the mechanism of flutter, *NACA Report*, **496**, Washington, DC (1934).

23. H. Sato, S. Kusuhara, K. Ogi, H. Matsufuji, Aerodynamic characteristics of super long-span bridges with slotted box girder, *Journal of Wind Engineering and Industrial Aerodynamics*, **88**, 297–306, 2000.

24. Google Street View, Great Belt Bridge, Retrieved from https://www.google.dk/maps/@55.3418599,11.0356435,3a,75y,168.1h,78.95t/data=!3m6!1e1!3m4!1s5czNql8Nl_AWIqMa0RNcLA!2e0!7i13312!8i6656 (n.d.)

25. S.O. Hansen, R.G. Srouji, B. Isaksen, K. Berntsen, Vortex-induced vibrations of streamlined single box girder bridge decks. *14th International Conference on Wind Engineering*, Porto Alegra, Brazil, June 21–26, 2015.

26. S. Krenk, R.N. Møller, Turbulent wind field representation and conditional mean simulation, *Proceedings of the Royal Society A*, **475**: 20180887, 2019.

27. F. Dischinger, Hängebrücken für schwerste Verkehrslasten (I and II), *Der Bauingenieur*, **24**(3/4), 65–75, 107–113, 1949. (in German)

28. P. Croce, Non-linear behavior of heavy stays, *International Journal of Solids and Structures*, **50**, 1093–1107, 2013.

□

C1

Bridge response analysis with ARMA simulated wind field

Randi Nøhr Møller, Steen Krenk & Martin Nymann Svendsen

Proceedings of the 12th International Conference on Structural Safety and Reliability, pp. 1589–1598

Vienna, Austria, August 6–10, 2017.

Safety, Reliability, Risk, Resilience and Sustainability of Structures and Infrastructure
12th Int. Conf. on Structural Safety and Reliability, Vienna, Austria, 6–10 August 2017
Christian Bucher, Bruce R. Ellingwood, Dan M. Frangopol (Editors)

Bridge Response Analysis with ARMA Simulated Wind Field

Randi N. Møller[1,2], Steen Krenk[1] and Martin N. Svendsen[2]

[1)] Department of Mechanical Engineering, Technical University of Denmark, DK-2800 Lyngby, Denmark.
[2)] Rambøll, Hannemanns Allé, DK-2300 Copenhagen, Denmark

Abstract: The paper describes a direct auto-regressive simulation method for wind fields. It makes use of the correlation of the wind field in the transverse direction to permit a single step multi-component formulation with free distribution of the simulation points in the transverse plane. While the simulated field will typically need a small time step for resolution of the turbulent fluctuations, the calibration is performed with respect to an accumulated time step the size of which is determined from a typical time scale of the total turbulence spectrum. The formulation depends on the availability of a consistent three-dimensional covariance description of the wind field, and is here illustrated for isotropic turbulence. It is demonstrated that the covariance structure of the velocity field is captured well and permits easy application to e.g. long-span bridges.

1 Introduction

In the design of long-span bridges wind load constitutes one of the essential design considerations - both in relation to buffeting response and to flutter, and simulated wind records have been used for several decades. The classic approach has been Fourier simulation of correlated wind velocity records for a set of points in space. The computational extent of the simulation easily becomes very large due to the need for long records at a considerable number of points in space, see e.g. [1], [2] and the discussion in [3]. An alternative is the use of sequential simulation based on the auto-regressive format with or without moving average white noise input (ARMA or AR format). An early presentation of ARMA simulation in connection to wind loading was given in [4]. A general overview of the wind simulation literature relating to structural response calculations was given in [5]. Common for this literature is that the simulation consists of a number of correlated scalar processes, typically with each velocity component having its own spectral density function, and with the processes at different points connected via spatial coherence functions, often represented empirically by exponential functions of the distance.

An alternative approach consists in considering the turbulent velocity components as constituting a vector field in three-dimensional space, e.g. in the form of convected isotropic turbulence, [6]. The underlying flow field introduces two features generally missing in the engineering literature: an integral condition on the correlation and coherence of transverse flow, and a combined wave-number parameter replacing the simple frequency-distance parameter typically assumed in the engineering literature, [7]. This paper presents a summary of a simple auto-regressive simulation procedure [8] formulated explicitly in terms of point correlations at two suitably separated instances in time and investigates the properties of the simulated wind field in relation to applications to long-span bridges.

2 Background Theory

The basic idea of auto-regressive moving-average (ARMA) simulation developing through states indexed by n is that the stochastic field variables $\mathbf{u}_n$ at step n are given as a linear combination of previous steps $n-j,\cdots,n-1$ supplemented by independent white noise variables corresponding to the previous steps $n-k,\cdots,n-1$ in the form

$$\begin{aligned}\mathbf{u}_n &= \mathbf{A}_1\mathbf{u}_{n-1}+\mathbf{A}_2\mathbf{u}_{n-2}+\cdots+\mathbf{A}_j\mathbf{u}_{n-j}\\ &+\ \mathbf{B}_1\xi_{n-1}+\mathbf{B}_2\xi_{n-2}+\cdots+\mathbf{B}_k\xi_{n-k}, \qquad n=1,2,\cdots\end{aligned} \tag{1}$$

where j denotes the number of regression terms, and k similarly the number of averaging terms. The process is illustrated in Fig. 1. The simulation process starts from zero at $\mathbf{u}_{0-s}$, passes through a non-stationary transient phase before reaching $\mathbf{u}_0$ from which the process is near-stationary until the current state $\mathbf{u}_n$.

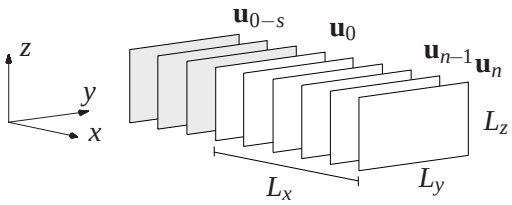

Figure 1: Simulation steps $\mathbf{u}_j,\cdots,\mathbf{u}_n$.

Traditionally, the frequency characteristics of the process have been obtained by using sufficiently long memory in terms of j previous values and k white noise input vectors. However the present goal is simulation of turbulent wind, and the correlation properties are therefore assumed to be available via observations in the transverse planes, and this suggests a single-step simulation procedure, although appropriate model parameter calibration requires the use of a suitable plane separated from the current state by a distance depending on the field properties, and not directly on the simulation step size. This corresponds to an auto-regressive (AR) process of the form

$$\mathbf{u}_n = \mathbf{A}\mathbf{u}_{n-1}+\mathbf{B}\xi_{n-1}, \qquad n=1,2,\cdots \tag{2}$$

The random vectors ξ_n are formed by uncorrelated normalized normal components, $\mathrm{E}[\xi_i\xi_j^T]=\delta_{ij}\mathbf{I}$, and the matrix $\mathbf{B}$ then generates the correlation between simultaneous input components.

2.1 Single-step calibration

The single-step format (2) produces a multi-dimensional Markov process. As this format does not correspond exactly to the properties of the simulated field a certain care must be exercised in the calibration of the two matrices $\mathbf{A}$ and $\mathbf{B}$. First, a simple calibration procedure is described based on the properties of two consecutive steps, e.g. $\mathbf{u}_n$ and $\mathbf{u}_{n-1}$. The covariance structure of this type of field can be generated from the single-step covariance properties, contained in the two matrices

$$\mathbf{C}_0 = \mathrm{E}[\mathbf{u}_n\mathbf{u}_n^T], \qquad \mathbf{C}_1 = \mathrm{E}[\mathbf{u}_n\mathbf{u}_{n-1}^T]. \tag{3}$$

In the single-step procedure these two covariance matrices determine the AR coefficient matrices $\mathbf{A}$ and $\mathbf{B}$. However, a more robust calibration is obtained by using the correlation between the current state and a previous state, separated from the current by several steps. That calibration is summarized in the next section as a generalization of the present single-step procedure. The details of the calibration procedures are given in [8].

The two system matrices $\mathbf{A}$ and $\mathbf{B}$ are determined by rearranging the recurrence relation (2) in the form

$$\mathbf{u}_n - \mathbf{A}\mathbf{u}_{n-1} = \mathbf{B}\xi_{n-1}. \tag{4}$$

This form permits direct determination of $\mathbf{A}$ and $\mathbf{B}$ by evaluation of the conditional mean value and covariance matrix of $\mathbf{u}_n$ for known $\mathbf{u}_{n-1}$. This is done in two different ways: directly from the relation (4), and by use of known relations for conditional mean and covariance. For the conditional mean value these two procedures give

$$\mathrm{E}[\mathbf{u}_n|\mathbf{u}_{n-1}] = \mathbf{A}\mathbf{u}_{n-1} = \mathbf{C}_1\mathbf{C}_0^{-1}\mathbf{u}_{n-1}. \tag{5}$$

This identifies the regression matrix $\mathbf{A}$ as

$$\mathbf{A} = \mathbf{C}_1\mathbf{C}_0^{-1}. \tag{6}$$

This equation gives the regression matrix $\mathbf{A}$ explicitly in terms of the covariance matrices $\mathbf{C}_0$ and $\mathbf{C}_1$ of the stochastic field.

The mean value of the terms on both sides of the relation (5) is equal to zero, and thus the conditional covariance is obtained by squaring the relation as

$$\mathrm{Cov}[\mathbf{u}_n\mathbf{u}_n^T|\mathbf{u}_{n-1}] = \mathbf{B}\mathrm{E}[\xi_{n-1}\xi_{n-1}^T]\mathbf{B}^T = \mathbf{C}_0 - \mathbf{C}_1\mathbf{C}_0^{-1}\mathbf{C}_1^T. \tag{7}$$

The expectation of the product of simultaneous values of the white noise vector ξ equals the unit matrix, thus giving the following relation

$$\mathbf{B}\mathbf{B}^T = \mathbf{C}_{0|1} = \mathbf{C}_0 - \mathbf{C}_1\mathbf{C}_0^{-1}\mathbf{C}_1^T. \tag{8}$$

This equation determines the product $\mathbf{B}\mathbf{B}^T$, and the matrix $\mathbf{B}$ can be extracted from Cholesky factorization or from the eigenvalues and eigenvectors of the conditional covariance matrix $\mathbf{C}_{0|1}$.

2.2 Multi-step calibration

In the multi-step calibration procedure the matrices $\mathbf{A}$ and $\mathbf{B}$ are obtained from the statistical properties of $\mathbf{u}_n$ and $\mathbf{u}_{n-k}$ via the covariance matrices $\mathbf{C}_0$ and

$$\mathbf{C}_k = \mathrm{E}[\mathbf{u}_n\mathbf{u}_{n-k}^T]. \tag{9}$$

This typically gives a more robust calibration, but is slightly more elaborate [8]. The current response vector $\mathbf{u}_n$ is expressed in terms of the previous step by the relation (4), and by expressing $\mathbf{u}_{n-1}$ by the similar formula for the previous step etc. k times, the following relation is obtained

$$\mathbf{u}_n - \mathbf{A}^k\mathbf{u}_{n-k} = \left(\mathbf{A}^{k-1}\mathbf{B}\xi_{n-k} + \cdots + \mathbf{A}\mathbf{B}\xi_{n-2} + \mathbf{B}\xi_{n-1}\right). \tag{10}$$

Using the same procedure as for the single-step calibration, the conditional mean for known $\mathbf{u}_{n-k}$ is expressed both from (10) directly and from the general result for correlated variables,

$$\mathrm{E}[\mathbf{u}_n|\mathbf{u}_{n-k}] = \mathbf{A}^k\mathbf{u}_{n-1} = \mathbf{C}_k\mathbf{C}_0^{-1}\mathbf{u}_{n-1}. \tag{11}$$

This identifies the recurrence matrix $\mathbf{A}$ via its k'th power as

$$\mathbf{A}^k = \mathbf{C}_k\mathbf{C}_0^{-1}. \tag{12}$$

The matrix $\mathbf{A}$ is determined by solving the non-symmetric eigenvalue problem

$$(\mathbf{A}^k)\mathbf{P} = \mathbf{P}\,\Gamma^k, \qquad (\mathbf{A}^k)^T\mathbf{Q} = \mathbf{Q}\,\Gamma^k, \tag{13}$$

where $\mathbf{P}$ and $\mathbf{Q}$ are the right and the left eigenvector matrices of $\mathbf{A}^k$, respectively. The eigenvalues are contained in the diagonal matrix $\Gamma^k = \lceil \gamma_1^k, \gamma_2^k, \cdots, \gamma_m^k \rfloor$. When normalizing the biorthogonality relations of the eigenvectors, $\mathbf{Q}^T\mathbf{P} = \mathbf{P}^T\mathbf{Q} = \mathbf{I}$, premultiplication of the original eigenvalue problem by $\mathbf{Q}^T$ gives

$$\mathbf{Q}^T\mathbf{A}^k\mathbf{P} = \Gamma^k. \tag{14}$$

It is seen that the biorthogonality relations immediately leads to the same relation for $k = 1$, and thereby to the desired matrix relation

$$\mathbf{A} = \mathbf{P}\Gamma\mathbf{Q}^T. \tag{15}$$

This generalizes the single-step result (6), corresponding to $k = 1$.

As in the single-step calibration procedure the calibration formula for the matrix $\mathbf{B}$ is determined from the squared recurrence relation (10). In spite of statistical independence of the white noise vectors ξ_n and ξ_{n-k} these terms result in a summation. The details are outside the scope of the present contribution, but may be found in [8]. The result of the analysis is the formula

$$\mathbf{B}\mathbf{B}^T = \mathbf{P}\mathbf{D}\mathbf{P}^T, \tag{16}$$

generalizing (8) for the single-step procedure. In this formula $\mathbf{P}$ is the right eigenvector matrix from (13), and the components of the symmetric matrix $\mathbf{D}$ is obtained from the conditional covariance matrix

$$\mathbf{C}_{0|k} = \mathbf{C}_0 - \mathbf{C}_k\mathbf{C}_0^{-1}\mathbf{C}_k^T \tag{17}$$

via the left eigenvector matrix $\mathbf{Q}$ and the eigenvalues γ_j as

$$D_{ij} = \frac{1-(\gamma_i\gamma_j)}{1-(\gamma_i\gamma_j)^k}\left[\mathbf{Q}^T\mathbf{C}_{0|k}\mathbf{Q}\right]_{ij}. \tag{18}$$

It is seen that for $k = 1$ the single-step formula (8) is recovered.

2.3 Correlations in isotropic turbulence

The present formulation is ideally suited to convected turbulence, where it is assumed that an instantaneous 'snap shot' of the wind velocity field in three-dimensional space defines a velocity field, that is then convected across the simulated cross-section plane. For isotropic turbulence the invariance of the correlation with respect to orientation in space implies the following generic form of the covariance function for the velocity vectors $\mathbf{v}_A$ and $\mathbf{v}_B$ at two points A and B, [6],

$$\mathbf{R}(\mathbf{r}) = \mathrm{E}[\mathbf{v}(\mathbf{r}_0+\mathbf{r})\mathbf{v}(\mathbf{r}_0)^T] = \sigma_u^2\Big([\,f(r)-g(r)\,]\frac{\mathbf{r}\mathbf{r}^T}{\mathbf{r}^T\mathbf{r}} + g(r)\,\mathbf{I}\Big), \tag{19}$$

where σ_u^2 is the variance of a single component at a point, and $r = |\mathbf{r}|$ is the distance between the two points A and B. The functions $f(r)$ and $g(r)$ describe the lengthwise and transverse correlation, respectively.

Incompressibility of the flow imposes a constraint condition between the longitudinal and transverse correlation functions $f(r)$ and $g(r)$ and the isotropic wind field can therefore be represented by a single normalized spectral density function $F(\kappa)$ corresponding to the two-sided

Fourier transform of $f(r)$ with κ as the wave-number corresponding to the distance r. It is here convenient to introduce a generic form of the normalized spectral density,

$$F(\kappa) = \frac{1}{\sqrt{\pi}} \frac{\Gamma(\gamma)}{\Gamma(\gamma - \frac{1}{2})} \frac{\ell}{[1+(\kappa\ell)^2]^\gamma}, \tag{20}$$

where ℓ is a length-scale of the turbulence, [7].

Two parameter values for γ are of particular interest: $\gamma = 5/6$ corresponding to the classic high frequency assumption of natural wind based on internal energy dissipation, and $\gamma = 1$ giving an exponential format for the covariance functions with similarities to assumptions often made in the engineering literature. For $\gamma = 5/6$ the correlation functions can be expressed in terms of modified Bessel functions [9] or in more compact form by Airy functions [8]. This formulation makes use of a non-dimensional transformed variable z to represent the distance,

$$z = \left(\frac{3r}{2\ell}\right)^{2/3}, \tag{21}$$

whereby the correlation functions take the form

$$f(r) = \frac{\mathrm{Ai}(z)}{\mathrm{Ai}(0)}, \qquad g(r) = f(r) + \frac{z}{3}\frac{\mathrm{Ai}'(z)}{\mathrm{Ai}(0)}. \tag{22}$$

Here $\mathrm{Ai}(z)$ is the Airy function and $\mathrm{Ai}'(z)$ its derivative, see e.g. [10]. A simpler approximate formulation can be obtained by using the exponent $\gamma = 1$, whereby

$$f(r) = \mathrm{e}^{-r/\lambda}, \qquad g(r) = \left(1 - \frac{1}{2}\frac{r}{\lambda}\right)\mathrm{e}^{-r/\lambda}. \tag{23}$$

The parameter λ is the integral spatial length-scale of the turbulence, defined by

$$\lambda = \int_0^\infty f(r)\,dr. \tag{24}$$

and substitution of the alternative form (22a) in terms of the Airy function leads to the relation $\ell = 1.339\lambda$ defining the length parameter ℓ. With either of these formulations the covariance function is given by (19) and this permits to build up the field covariance matrices $\mathbf{C}_0$, $\mathbf{C}_1$ and $\mathbf{C}_k$, used in the calibration procedure described above.

3 Simulated Wind Field

A number of tests are carried out to illustrate the performance of the present auto-regressive simulation procedure under various conditions. The primary focus is the applications to long bridges, where it is of interest to simulate wide fields, with limited height and free distribution of the simulation points in the transverse plane, permitting inclusion of towers and cables. To illustrate the performance of the wind field simulations, the cross correlation coefficients are evaluated from the simulated wind field and plotted together with the lengthwise and transverse correlation functions $f(r)$ and $g(r)$ used as input for the calibration of the wind field. The correlation coefficients are evaluated from the simulated time-record in the outermost point in the yz-plane and the simulation records with horizontal separation for all three wind components, u_x, u_y and u_z. The wind field dimensions are described by the lengths $L_i = l_i \cdot (n_i - 1)$, $i \in \{x, y, z\}$, where l_i is the distance between simulation points and n_i is the number of simulation points in the corresponding direction. For all simulations the along-wind length is $L_x = 10^5\lambda$,

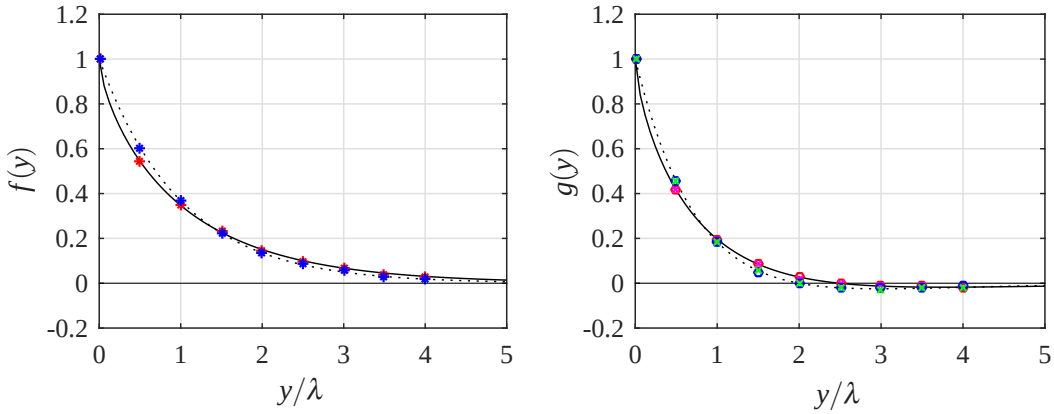

Figure 2: Correlation for y-separation: $(u_x, u_y, u_z)_{Ai}$ (∘, ∗, ×), $(u_x, u_y, u_z)_{exp}$ (∘, ∗, ×).

leading to a sufficiently small standard deviation on the estimated correlation coefficient. The integral length scale is $\lambda = 100\,\mathrm{m}$, and the simulation model is calibrated for each case using this length corresponding to $k = \lambda / l_x$.

Figures 2a-b show the correlation functions $f(y)$ and $g(y)$ estimated from a simulated wind field for a horizontal line with point spacing $l_y = \lambda/2$ and width of the simulated field $L_y = 4\lambda$, corresponding to $n_y = 9$. The equivalent along-wind interval length is $l_x = l_y = \lambda/2$, corresponding to a square mesh. The figure includes the results from both the von Kàrmàn ($\gamma = 5/6$)and the exponential ($\gamma = 1$) representation of the wind field correlation, shown by the full and dashed lines, respectively. It is observed that the simulated results lie very close to the analytical correlation functions, indicating the suitability of the auto-regressive procedure for simulating wind fields for line-like structures. Furthermore, the difference between the two representations of the wind field is quite small, suggesting the adequacy of the exponential approximation.

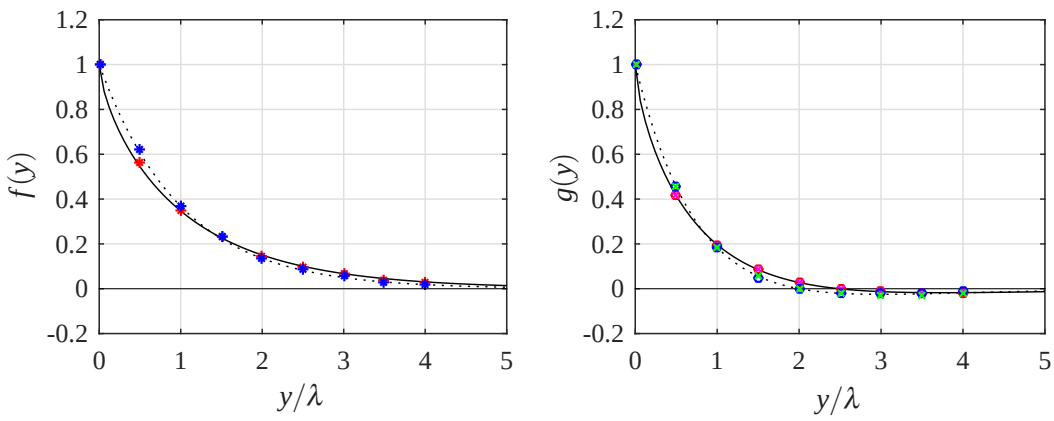

Figure 3: Correlation for y-separation: $(u_x, u_y, u_z)_{Ai}$ (∘, ∗, ×), $(u_x, u_y, u_z)_{exp}$ (∘, ∗, ×).

When evaluating dynamic structural response via time domain calculations it is important that the time integration steps are suitable for representing the characteristic structural behavior. This may imply different mesh intervals in the along-wind direction and in the transverse plane. Therefore the influence of mesh distortion is investigated. Figures 3a-b show results for a simulated wind field with the parameters: $l_x = \lambda/32$ and $l_y = \lambda/2$, corresponding to a distorted mesh with $l_x/l_y = 1/16$. As in the previous example a single row of $n_y = 9$ horizontally spaced points with $L_y = 4\lambda$ is considered. It is seen that all results estimated from simulation are very close to the analytical correlation function, indicating that the simulation method is insensitive to a refinement of the along-wind discretization, corresponding to a higher time-wise resolution.

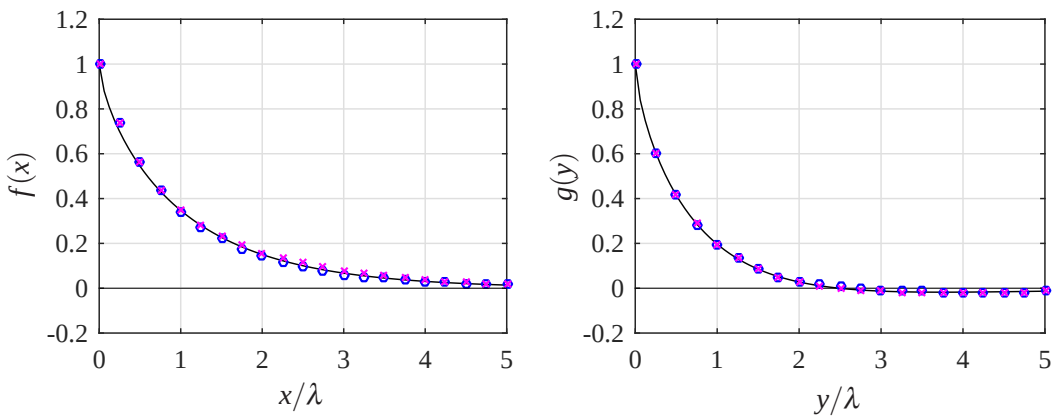

Figure 4: Correlation for x- and y-separation. Single component (×), three components (○).

A final test of the wind field simulation performance concerns simulation of only one or two wind components instead of the full three-component field. For many applications only one or two wind load components are needed in order to evaluate the structural response. This holds for long slender structures such as bridge decks or towers where two components are used to calculate the response or plane structures such as road signs where only one component is needed. In Figures 4a-b the estimated correlation functions of the u_x-component are plotted for a simulations performed with all three wind components and for only a single component. The simulation parameters are: $l_x = l_y = \lambda/4$, $L_y/\lambda = 5$ and $L_z = 0$. It is noted that the two simulations give equally good results for across wind correlation, while the simulation with only a single component shows a small error on the along wind correlation.

4 Structural Response

In this section the time domain buffeting response of a simple bridge structure subjected to turbulent wind loading is investigated. The investigation covers two issues of interest. First it is evaluated how the structural response is dependent on the wind simulation mesh. As shown in the previous section the auto-regressive simulation method showed no reduction of accuracy from time-interval refinement. However, the frequency content in the loading is of course diluted for a too coarse time discretization, and thus the spacing of the simulation points should be chosen carefully in order to represent the relevant loading frequencies. Secondly, the sensitivity of the structural response to the coherence length scale is investigated. The analyses are carried out with both the von Kàrmàn ($\gamma = 5/6$) and the exponential ($\gamma = 1$) representation of the wind field correlation.

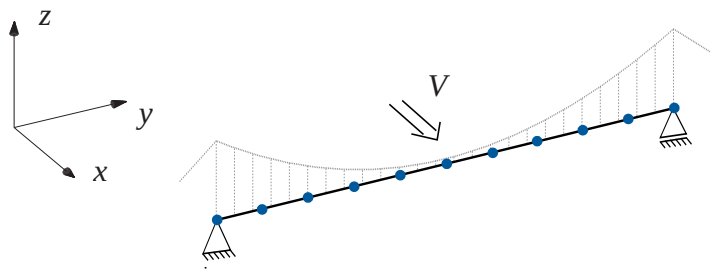

Figure 5: Idealized model of the Hardanger Suspension Bridge.

The structural response is evaluated for a simply supported beam with properties chosen to

represent an idealized model of the Hardanger Bridge [11]. The structure is shown in Figure 5. The length of the beam is $L_s = 1310\,\mathrm{m}$, the width is $B = 18.3\,\mathrm{m}$ and the height is assessed as $H = 3.1\,\mathrm{m}$. The distributed mass is $m = 12820\,\mathrm{kg/m}$ and the moment of inertia around the longitudinal axis is $I_p = 426000\,\mathrm{kgm^2/m}$. The elastic properties are $EA = 10^{11}\,\mathrm{N}$, $EI_x = 3.9 \cdot 10^{14}\,\mathrm{Nm^2}$, $EI_z = 6.2 \cdot 10^{13}\,\mathrm{Nm^2}$ and $GJ = 3.6 \cdot 10^{11}\,\mathrm{Nm^2}$, where E is the elastic modulus, A is the cross-section area and I_x and I_z are the moments of inertia about the x and z axis, respectively, and GJ is the torsion stiffness.

The analysis is limited to the horizontal, along-wind response. The modal frequencies and damping ratios for the horizontal modes are shown in Table 1. The wind load applied to the structure is a horizontal force component

$$q_x = \rho V H \bar{C}_D u_x \tag{25}$$

with air density $\rho = 1.25\,\mathrm{kg/m^3}$, drag coefficient $\bar{C}_D = 0.7$, mean wind speed $V = 40\,\mathrm{m/s}$, and longitudinal fluctuating wind component u_x with standard deviation $\sigma_u = 5.6\,\mathrm{m/s}$. The finite element model uses 10 three-dimensional two node beam elements, providing an adequate resolution up to the fifth vibration mode. The nodal load is obtained by the standard procedure of integration of the distributed load weighted by the displacement shape functions. The time stepping is performed using a second-order momentum based time integration with no algorithmic damping. Structural damping is implemented as Rayleigh damping $\mathbf{C} = 10^{-3}(10.1\mathbf{M} + 11.9\mathbf{K})$.

Table 1: Natural frequencies and damping ratios.

Mode:	Frequency ν [Hz]	Damping ratio ξ
1	0.064	0.015
2	0.255	0.013
3	0.573	0.023
4	1.020	0.039
5	1.593	0.060

Figure 6 shows the simulated wind velocity of the longitudinal fluctuating wind component, u_x, together with the structural response, r_x, at mid-span as a function of time. The parameters used for the simulation are $\lambda = L_s/10$, $n_y = 41$ and $dt = 1.25$ s. It is seen that the bridge structure acts as a filter so only low frequency response is observed despite the high frequency input, and the structural response at mid-span is dominated by the the first mode.

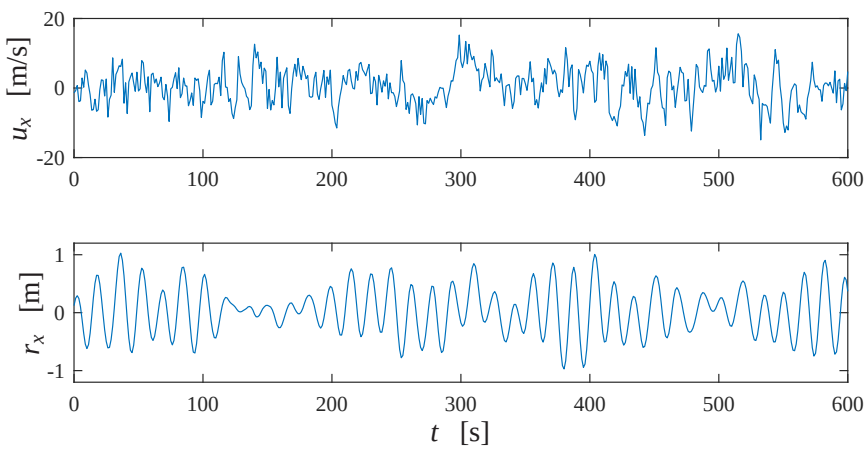

Figure 6: Velocity u_x and mid-span displacement r_x. $\lambda = L_s/10$.

In Table 2 the standard deviation of the simulated along-wind response at mid-span, σ_x, is tabulated for varying refinement of the wind loading. The results are based on simulations of length $20 \cdot 6000$ s. Results are shown for both the Airy function representation (Ai) of the wind correlation function and the approximate formulation using exponential functions (exp). It is noted that the time domain simulations seem to overestimate the response if the refinement of the wind simulation is too coarse. Furthermore, it is seen that the exponential formulation of the wind correlation functions results in a higher response in the order of 4%.

Table 2: Standard deviation of mid-span response, $\lambda = L_s/10$, $dt = 1.25\,s$.

λ/l_y	1	2	4	8	16
σ_x [m], (Ai)	0.587	0.495	0.479	0.452	0.443
σ_x [m], (exp)	0.595	0.501	0.486	0.482	0.485

Table 3 shows the along-wind response at mid-span for different time-steps with equivalent refinement of the wind loading as $l_x = Vdt$. The results are relatively independent of the size of the time-step within the investigated range. This indicates that the simulation time increment can be chosen solely to match the time integration step needed to represent the characteristic structural response.

Table 3: Standard deviation of mid-span response, $\lambda = L_s/10$, $\lambda/l_y = 4$.

λ/l_x	1	2	4	8	16
σ_x, [m], (Ai)	0.466	0.467	0.467	0.464	0.478
σ_x, [m], (exp)	0.479	0.475	0.495	0.491	0.483

Table 4 shows the along-wind response at mid-span for different integral length scale λ relative to the length L_s of the structure. The number of simulation points, $n_y = 41$, along the bridge is held constant. A clear tendency of decreasing response is seen for decreasing correlation length.

Table 4: Standard deviation of mid-span response, $n_y = 41$, $dt = 1.25\,s$.

L_s/λ	2	4	8	16	32
σ_x [m], (Ai)	0.499	0.483	0.470	0.447	0.328
σ_x [m], (exp)	0.532	0.523	0.509	0.438	0.316

5 Discussion

An auto-regressive model has been presented for simulation of stochastic turbulent wind fields. The wind field is perceived as 'frozen turbulence' convected across the structure by the mean wind speed V. Hereby time is represented via the length $x = -Vt$, and the discretization consists of a set of points $(y,z)_j$ in a transverse plane with velocities generated at the time increments $dt = -dx/V$. This time increment must be sufficiently small to permit correct representation of the dynamic response. The present model is calibrated from the correlation properties of the velocities at the selected simulation points at the current time and a suitable prior time. The time separation used for calibration is chosen from the integral length scale λ as $\Delta t = \lambda/V$. This calibration time interval is typically larger than the time increments dt in the simulation, and an explicit multi-step calibration procedure has been developed and implemented for convected isotropic turbulence.

Two representations have been implemented for the wind field: a field represented by the von Kàrmàn spectrum, and a field characterized by exponential type correlation functions. It is

demonstrated that when using the same integral length scale λ in the two models, they lead to vary similar results for the correlation functions. It is furthermore demonstrated that the correlation in the transverse plane is insensitive to a refinement of the time-discretization, thereby permitting the representation of high-frequency components in the wind. In the present model the correlation structure of the wind is represented via a set of points $(y,z)_j$ in a transverse plane at only two points in time. Thus, the results depend on the three-dimensional structure of the turbulent flow. In spite of this, tests indicate that the use of only one or two of the full three-component representation of the wind field retains the high accuracy of the covariance properties in the simulated field. Simulation of buffeting load on a simple bridge model indicate that the response is fairly insensitive to different time intervals, provided these permit representation of the periods of the relevant vibration modes. The simulations also demonstrate reduced response for bridges with spans considerably longer than the integral length scale of the turbulence. In this context it is to be noted that the present isotropic turbulence model leads to a reduced transverse length-scale due to the incompressibility of the flow. However, it may be necessary to modify the basic assumption of isotropy to account for differences in the magnitude of the turbulent velocity components and different length scales in the different directions.

Acknowledgment. This paper is part of a project sponsored jointly by the Innovation Fund Denmark, Rambøll and the Technical University of Denmark.

References

[1] K. Aas-Jakobsen and E. Strømmen, "Time domain buffeting response calculations of slender structures". *Journal of Wind Engineering and Industrial Aerodynamics* 89 (2001), 341–364.

[2] L. Carassale and G. Solari, "Monte Carlo simulation of wind velocity fields on complex structures". *Journal of Wind Engineering and Industrial Aerodynamics* 94 (2006), 323–339.

[3] X. Chen and A. Kareem, "Discussion on 'Time domain buffeting response calculations of slender structures' by K. Aas-Jakobsen and E. Strømmen". *Journal of Wind Engineering and Industrial Aerodynamics* 90 (2002), 639–642.

[4] Y. Li and A. Kareem, "ARMA systems in wind engineering". *Probabilistic Engineering Mechanics* 5 (1990), 50–59.

[5] A. Kareem, "Numerical simulation of wind effects: A probablistic perspective". *Journal of Wind Engineering and Industrial Aerodynamics* 96 (2008), 1472–1497.

[6] G.K. Batchelor, The Theory of Homogeneous Turbulence, Cambridge: Cambridge University Press, 1953.

[7] S. Krenk, "Wind field coherence and dynamic wind loading". In: *IUTAM, Symposium on Advances in Nonlinear Stochastic Mechanics* (1995), 269–278.

[8] S. Krenk, "Explicit calibration and simulation of stochastic fields by low-order ARMA processes". In: *COMPDYN 2011, ECCOMAS Thematic Conference on Computational Methods in Structural Dynamics and Earthquake Engineering*, Corfu, Greece, 2011.

[9] L. Kristensen and N.O. Jensen, "Lateral coherence in isotropic turbulence and in the natural wind". *Boundary Layer Meteorology* 17 (1979), 353–373.

[10] F.W.J. Olver, D.W. Lozier, R.F. Boisvert, C.W. Clark, NIST Handbook of Mathematical Functions, Cambridge: Cambridge University Press, 2010.

[11] O. Øiseth, A. Rönnquist and R. Sigbjörnsson, "Finite element formulation of the self-excited forces for time-domain assessment of wind-induces dynamic response and flutter stability limit of cable-supported bridges". *Finite Elements in Analysis and Design* 50 (2012),173–183.

C2

Quasi-static condensation of aeroelastic suspension bridge model

Randi Nøhr Møller, Steen Krenk & Martin Nymann Svendsen

Proceedings of the 30th Nordic Seminar on Computational Mechanics, pp. 129–132

Kongens Lyngby, Denmark, October 25–27, 2017.

30th Nordic Seminar on Computational Mechanics
NSCM-30
J. Høgsberg. N.L. Pedersen (Eds.)
2017

QUASI-STATIC CONDENSATION OF AEROELASTIC SUSPENSION BRIDGE MODEL

RANDI N. MØLLER*†, STEEN KRENK* AND MARTIN N. SVENDSEN†

*Department of Mechanical Engineering, Technical University of Denmark
DK-2800 Lyngby, Denmark
e-mail: randinm@mek.dtu.dk,sk@mek.dtu.dk, web page: http://www.mek.dtu.dk

†Rambøll, Hannemanns Allé, DK-2300 Copenhagen, Denmark
e-mail: mnns@ramboll.dk, web page: http://www.ramboll.dk

Key words: Structural Dynamics, Quasi-static Condensation, Aerodynamic Stability, Long Span Bridges.

1 INTRODUCTION

For long span bridges the wind-induced dynamic response is a design driving factor and therefore continuously a subject for detailed analysis. Traditionally both buffeting and stability calculations have been considered in the frequency domain. However, this yields a limitation in accounting for turbulence when considering the stability limit and further it is not possible to account for non-linear effects. These limitations suggest to do simulations of the aeroelastic response of long span bridges in the time domain. For this it is of interest to have an efficient model while still maintaining sufficient accuracy.

This contribution is on quasi-static reduction of an aeroelastic finite element model of a 3000m suspension bridge proposed for crossing Sulafjorden in Norway[1]. The model is intended for stability limit calculation where the representation of higher modes is of less importance. The present contribution demonstrates the application of quasi-static condensation to long suspension bridges as well as introduces an extension of the method to include the full aeroelastic system. This includes considerations on reduction of external wind loading as well as motion-induced forces.

2 AEROELASTIC BRIDGE MODEL

The suspension bridge is depicted in Figure 1(a). The bridge is implemented as a finite element model in Matlab using 3D beam elements for the towers and Green strain truss elements for the cables. The deck to hanger connections are modelled with rigid links and the bridge deck elements are aeroelastic beam elements including aerodynamic properties through additional degrees of freedom in the system.

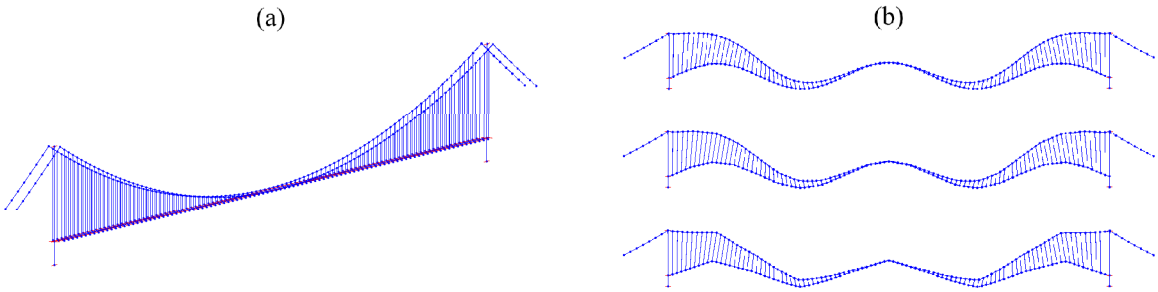

Figure 1: (a) Bridge model (b) Mode shapes: Full model, 1:5 and 1:10 reduction.

The equation of motion for the system including motion-induced forces can be written as

$$\mathbf{M}\ddot{\mathbf{q}}(t) + \mathbf{C}\dot{\mathbf{q}}(t) + \mathbf{K}\mathbf{q}(t) = \mathbf{f}_m(t) + \mathbf{f}_{ext}(t) \tag{1}$$

where $\mathbf{q}$ is the displacement vector. The coefficient matrices $\mathbf{M} = \mathbf{M}_s + \mathbf{M}_a$, $\mathbf{C} = \mathbf{C}_s + \mathbf{C}_a$ and $\mathbf{K} = \mathbf{K}_s + \mathbf{K}_a$ are the mass, damping and stiffness matrices. Here index s and a refers to structural and aerodynamic property matrices respectively. On the right hand side there is a contribution from the external forces $\mathbf{f}_{ext}$ and from the memory part of the motion-induced forces $\mathbf{f}_m$. To enable the memory part of the motion-induced forces to appear as additional degrees of freedom in the system, a number of j first order differential equations on the form

$$\dot{\mathbf{f}}_{m,j}(t) + \mathbf{D}_j\mathbf{f}_{m,j}(t) = \mathbf{A}_j\mathbf{q}(t) \tag{2}$$

are introduced[2,3]. Here the matrix $\mathbf{A}_j$ and the diagonal matrix $\mathbf{D}_j$ are shape specific property matrices. The aerodynamic properties are implemented as a single term approximation to the Theodorsen flat plate theory.

3 QUASI-STATIC CONDENSATION

The method of quasi-static condensation builds on the master-slave constraint principle, but instead of introducing rigid links between master and slave nodes a stiffness relation is used to describe the master-slave relation:

$$\mathbf{q} = \begin{bmatrix} \mathbf{q}_d \\ \mathbf{q}_s \end{bmatrix} = \begin{bmatrix} \mathbf{I} \\ \mathbf{S} \end{bmatrix} \mathbf{q}_d\,, \quad \mathbf{S} = -\mathbf{K}_{ss}^{-1}\mathbf{K}_{sd} \tag{3}$$

Here $\mathbf{q}_d$ and $\mathbf{q}_s$ are the displacement vectors of the master and the slave degrees of freedom respectively. The first and second index on the stiffness matrix $\mathbf{K}$ refer to master or slave rows and columns respectively. Extending the method to include motion-induced forces suggest to treat the state proportional aeroelastic terms as the structural mass, damping and stiffness while the memory part of the motion-induced forces are reduced by considering the rate of work. Hereby the reduced form of the equation of motion including motion-induced forces is

$$\bar{\mathbf{M}}\ddot{\mathbf{q}}_d(t) + \bar{\mathbf{C}}\dot{\mathbf{q}}_d(t) + \bar{\mathbf{K}}\mathbf{q}_d(t) = \bar{\mathbf{f}}_m(t) + \bar{\mathbf{f}}_{ext}(t) \tag{4}$$

and the differential equation describing the relation between the system displacements and the memory part of the motion-induced forces is found as:

$$\dot{\bar{\mathbf{f}}}_{m,j}(t) + \gamma_j \bar{\mathbf{f}}_{m,j}(t) = \bar{\mathbf{A}}_j \mathbf{q}_d(t) \tag{5}$$

The differential equation has maintained the form beneficial for implementation assuming that $\mathbf{D}_j = \gamma_j \mathbf{I}$. In equation (4) and (5) the reduced coefficient matrices, external forces and memory forces are found on the general form:

$$\bar{\mathbf{X}} = \mathbf{X}_{dd} + \mathbf{S}^T \mathbf{X}_{sd} + \mathbf{X}_{ds}\mathbf{S} + \mathbf{S}^T \mathbf{X}_{ss}\mathbf{S}\,, \quad \bar{\mathbf{x}} = \mathbf{x}_d + \mathbf{S}^T \mathbf{x}_s \tag{6}$$

where $\mathbf{X} \in \{\mathbf{M}, \mathbf{C}, \mathbf{K}, \mathbf{A}_j\}$ and $\mathbf{x} \in \{\mathbf{f}_{ext}, \mathbf{f}_m, \dot{\mathbf{f}}_m\}$.

4 ACCURACY OF REDUCED SYSTEM

The quasi-static system condensation has been applied to the bridge model and reduced model results are in this section compared to results obtained for the full system. Figure 1(b) shows mode shapes of the 14th still-air mode obtained with the full model, a model reduced to one fifth and to one tenth of the full model size respectively. It is seen that the mode shape obtained with the 1:5 model reduction is very similar to the mode shape obtained with the full model while the 1:10 reduction is resulting in a less smooth mode shape. This implies that the 1:10 reduction is too coarse and is no longer capturing the behaviour of the full model.

Figure 2 shows the natural frequencies for the full model (∘), the 1:5 reduction (∗) and the 1:10 reduction (◇). The left plot shows the natural frequencies for the still-air system and the right plot shows the natural frequencies for the aeroelastic system with wind speed $U = U_{cr}$. Both plots indicate that the 1:5 reduction gives a good representation of modes up to around mode number 15 while the 1:10 reduction shows divergence at mode 9 and up.

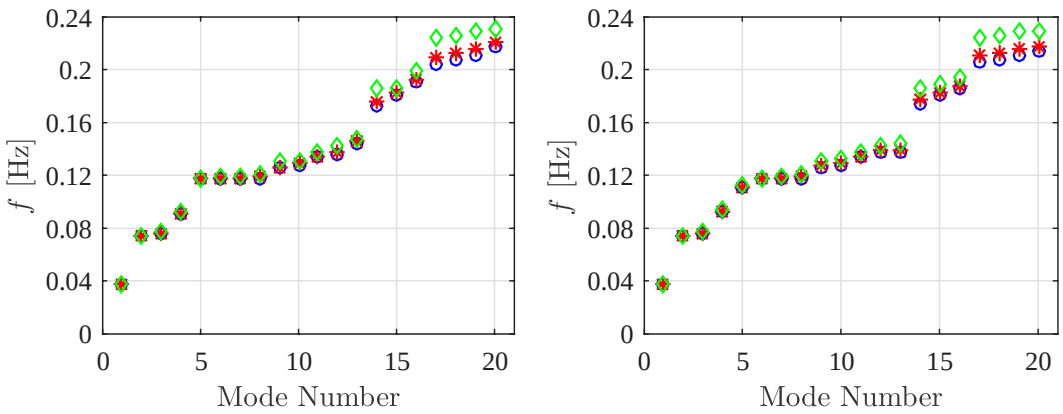

Figure 2: Modal frequencies: (left) still air (right) critical wind speed.

The time domain responses of the full bridge model and the 1:5 reduction are now considered when excited by turbulent wind loading. The mean wind loading influencing the aeroelastic terms is set to $U = 0.6U_{cr}$, the turbulence intensity is $I_u = 0.134$ and the integral length scale is $\lambda = 200$m. Figure 3 shows the drag q_y, the heave q_z and the torsional r_x response for a five minute time interval. It is seen that the response obtained by the reduced model is corresponding well with the response found by the full model. The calculation time for the five minute time history is significantly reduced from 59.3s to 0.7s making use of the reduced model instead of the full model.

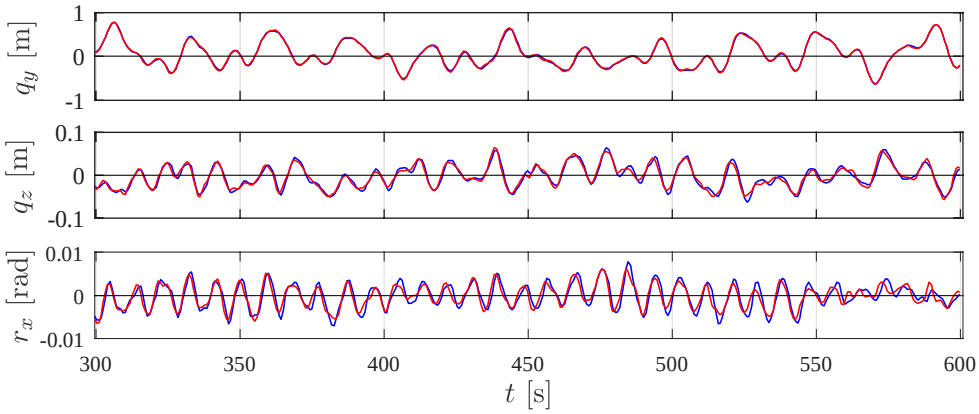

Figure 3: Time response at quarter span: Full model (−), 1:5 reduction (−).

5 CONCLUSIONS

It has been demonstrated that flutter analysis of a typical long suspension bridge can be performed using a model reduced by quasi-static condensation. A reduced model with a number of around 20 master nodes along the bridge deck and corresponding master nodes in the suspension cables has been shown to represent the behaviour of the bridge with sufficient accuracy. A further reduction of the model did not capture the essentials of relevant modes due to the coarseness.

REFERENCES

[1] Ramboll, for the Norwegian Public Roads Administration, Konseptrapport Hengebru i Korridor 1, November 2015.

[2] JR. Høgsberg, J. Krabbenhøft and S. Krenk, State space representation of bridge deck aeroelasticity, 13th Nordic Seminar on Computational Mechanics (NSCM-13), Oslo University, 109-112, (2000).

[3] O. Øiseth, A. Rönnquist and R. Sigbjörnsson, Finite element formulation of the self-excited forces for time-domain assessment of wind-induced dynamic response and flutter stability limit of cable-supported bridges. *Finite Elements in Analysis and Design*, **50**, 173-183, (2012)

DTU Mechanical Engineering
Section of Solid Mechanics
Technical University of Denmark

Nils Koppels Allé, Bld. 404
DK-2800 Kgs. Lyngby
Denmark

Tlf.: +45 4525 4250
Fax: +45 4525 1961

www.mek.dtu.dk

June 2019
ISBN: 978-87-7475-572-2

DCAMM
Danish Center for Applied Mathematics and Mechanics

Nils Koppels Allé, Bld. 404
DK-2800 Kgs. Lyngby
Denmark
Phone (+45) 4525 4250
Fax (+45) 4525 1961

www.dcamm.dk

DCAMM Special Report No. S264

ISSN: 0903-1685